

STAIR
(1+20)

(NASA-CR-169671) THE TELECOMMUNICATIONS AND
DATA ACQUISITION PROGRESS JOURNAL Progress
Report, Jul. - Sep. 1982 (Jet Propulsion
Lab.) 187 p HC A09/MF A01 CSCL 17B

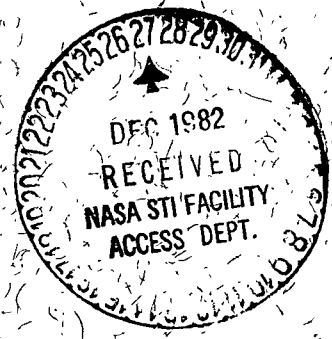
N83-14323
THRU
N83-14343
Unclas
02244

G3/32

The Telecommunications and Data Acquisition Progress Report 42-71

July - September 1982

N.A. Renzetti
Editor



November 15, 1982

NASA
National Aeronautics and
Space Administration

Jet Propulsion Laboratory
California Institute of Technology
Pasadena, California

The Telecommunications and Data Acquisition Progress Report 42-71

July - September 1982

N.A. Renzetti
Editor

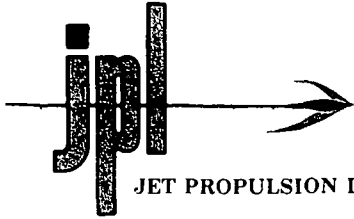
November 15, 1982

NASA

National Aeronautics and
Space Administration

Jet Propulsion Laboratory
California Institute of Technology
Pasadena, California

The research described in this publication was carried out by the Jet Propulsion Laboratory, California Institute of Technology, under contract with the National Aeronautics and Space Administration.



JET PROPULSION LABORATORY California Institute of Technology • 4800 Oak Grove Drive, Pasadena, California 91109

February 15, 1983

Recipients of Jet Propulsion Laboratory Telecommunications and Data Acquisition Progress Report 42-71

Subject: Errata

In the article entitled "Performance of Concatenated Reed-Solomon/Viterbi Channel Coding" by D. Divsalar and J.H. Yuen, in JPL TDA Progress Report 42-71, please note the following corrections:

In the seventh line from the bottom of page 83 the term $\pi/(M-1)$ should be replaced by $\pi_j/(M-1)$. Hence Eqs. (7), (12), (A-2), and (A-4) should read:

$$\Pr \{W_i = 0\} = \frac{\pi_j}{M-1} < \frac{\pi}{M-1} \quad (7)$$

$$\Pr \{W_i = 1\} = 1 = \frac{\pi_j}{M-1} < 1$$

$$\Pr \{W = i\} \leq \binom{n}{i} \left(\frac{\pi}{M-1}\right)^{n-i} \quad (12)$$

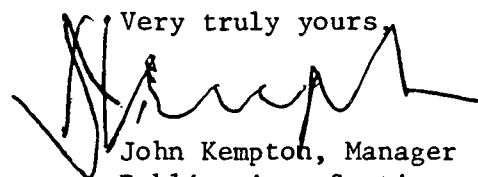
$$E\{e^{-\lambda W}\} \leq \left(\frac{\pi}{M-1} + e^{-\lambda}\right)^n \quad (A-2)$$

$$\Pr \{x_0 \rightarrow x_n\} \leq \min_{\lambda > 0} e^{\lambda t} \left(\frac{\pi}{M-1} + e^{-\lambda}\right)^n \cdot \left(1 - \pi + \pi e^{-\lambda}\right)^{N-n} \quad (A-4)$$

On page 85, Eq. (19) is an approximation. On page 89, in Fig. 3, the transition error probabilities should be $\pi_j/(M-1)$; $j = 1, 2, \dots, M-1$.

Since decoding error probability is very small with respect to decoding failure probability (see Eq. (22)), the results in the article are unaffected.

ORIGINAL PAGE IS
OF POOR QUALITY

Very truly yours,

John Kempton, Manager
Publications Section

Preface

This publication provides reports on developments in Earth-based radio technology with applications to several programs. In space communications it reports on activities of the Deep Space Network. In geodynamics it reports on the application of radio interferometry at microwave frequencies for geodynamic measurements. In the field of astrophysics the Deep Space Stations individually and in pairs as an interferometer have been applied to direct observation of celestial radio sources.

Each succeeding issue of this report will present material in some, but not necessarily all, of the following categories:

- Radio Astronomy
- Radio Interferometry at Microwave Frequencies

- Geodetic Techniques Development
 - Spacecraft Navigation
 - Orbiting Very Long Baseline Interferometry

- Deep Space Network

- Description
 - Program Planning
 - Advanced Systems
 - Network and Facility Engineering and Implementation
 - Operations
 - Spacecraft Radio Science
 - Planetary Radar

In each issue, there will be a report on the current configuration of one of the seven DSN systems (Tracking, Telemetry, Command, Monitor and Control, Test Support, Radio Science, and Very Long Baseline Interferometry).

The work described in this report series is either performed or managed by the Telecommunications and Data Acquisition organization of JPL.

Contents

RADIO INTERFEROMETRY AT MICROWAVE FREQUENCIES GEODETIC TECHNIQUES DEVELOPMENT

Determination of Intercontinental Baselines and Earth Orientation Using VLBI	1
O. J. Sovers, J. L. Fanselow, G. H. Purcell, Jr., D. H. Rogstad, and J. B. Thomas	
NASA Code 311-03-51-62	

ORBITING VLBI

Error Estimation for ΔVLBI Angle and Angle Rate Measurements Over Baselines Between a Ground Station and a Geosynchronous Orbiter	8
S. C. Wu	
NASA Code 311-03-58-33	

THE DEEP SPACE NETWORK DESCRIPTION OF THE DSN

DSN Monitor and Control System Mark III-82	20
G. L. Spradlin	
NASA Code 312-03-53-29	

PLANETARY AND INTERPLANETARY MISSION SUPPORT Planetary Flight Projects

Improved Downlink Frequency Calculations for Voyager 2	23
A. L. Ricardo	
NASA Code 311-03-22-30	
The Performance of VLA as a Telemetry Receiver for Voyager Planetary Encounters . .	27
L. J. Deutsch	
NASA Code 311-03-59-57	
Performance of Differenced Range Data Types in Voyager Navigation	40
T. H. Taylor, J. K. Campbell, R. A. Jacobson, B. Moultrie, R. A. Nichols, Jr., and J. E. Riedel	
NASA Code 312-03-51-56	

ADVANCED SYSTEMS Communications

Thermal Background Noise Limitations	53
S. Gulkis	
NASA Code 199-50-62-12	
KA-Band Weather-Dependent System Performance Estimates for Goldstone	60
R. C. Clauss, M. M. Franco, and S. D. Slobin	
NASA Code 310-20-66-15	
X-Band Noise Temperature Effects of Rain on DSN Antenna Feedhorns	66
S. D. Slobin, M. M. Franco, and R. C. Clauss	
NASA Code 310-20-66-15	

Viterbi Decoder Node Synchronization Losses in the Reed-Solomon/Viterbi Concatenated Channel	73
L. J. Deutsch and R. L. Miller	
NASA Code 310-20-67-60	

Performance of Concatenated Reed-Solomon/Viterbi Channel Coding	81
D. Divsalar and J. H. Yuen	
NASA Code 310-20-67-60	

NETWORK AND FACILITY ENGINEERING AND IMPLEMENTATION
Network

Electronic Simulation of a Barometric Pressure Sensor for the Meteorological Monitor Assembly	95
C. N. Guiar and L. W. Duff	
NASA Code 311-03-41-91	

The Fabrication and Surface Tolerance Measurements of the JPL Clear Aperture Microwave Antenna	104
J. Carpenter, S. Rocci, and C. T. Chian	
NASA Code 311-03-42-02	

Direct Comparison of Viking 2.3-GHz Signal Phase Fluctuation and Columnar Electron Density Between 2 and 160 Solar Radii	117
A. L. Berman, J. A. Wackley, and W. H. Hietzke	
NASA Code 311-03-24-00	

Deep Space Communications Complex Command Subsystem Mark IVA	129
W. G. Stinnett	
NASA Code 312-03-59-64	

A Compact Presentation of DSN Array Telemetry Performance	137
C. A. Greenhall	
NASA Code 311-03-41-82	

OPERATIONS
Network Operations

Deep Space Network Utilization for Flight Projects, Calendar Year 1981	143
C. L. Adkins and E. K. Goto	
NASA Code 311-03-13-50	

Mark IVA Microprocessor Support	148
A. L. Burford	
NASA Code 311-03-14-11	

A DSN Optimal Spacecraft Scheduling Model	154
W. A. Webb	
NASA Code 312-03-53-64	

ENERGY

Potential Availability of Diesel Waste Heat at Echo Deep Space Station (DSS 12)	166
R. D. Hughes	
NASA Code 312-03-44-08	

Determination of Intercontinental Baselines and Earth Orientation Using VLBI

O. J. Sovers, J. L. Fanelow, G. H. Purcell, Jr.,
D. H. Rogstad, and J. B. Thomas
Tracking Systems and Applications Section

A series of experiments has been conducted during the last decade to explore the capability of very long baseline interferometry (VLBI) to measure the crustal and rotational motions of the earth with accuracies at the centimeter level. The observing stations are those of NASA's Deep Space Network in California, Spain and Australia. A multiparameter fit to the observed values of delay and delay rate yields radio source positions, polar motion, universal time; the precession constant, baseline vectors, and solid earth tides. Source positions are obtained with formal errors of the order of $0''.01$. UT1-UTC and polar motion are determined at 49 epochs, with formal error estimates (1σ) for the more recent data of 0.5 msec for UT1-UTC and 2 to 6 mas for polar motion. Intercontinental baseline lengths are determined with formal errors of 5 to 10 cm. The Love numbers and earth tide phase lag agree with the commonly accepted values.

I. Introduction

Over the last few years, considerable progress has been made toward realizing the potential capability of radio interferometry to measure the crustal and rotational motions of the earth at the centimeter level (e.g., Refs. 1-5). Toward this goal, a series of experiments with NASA's Deep Space Network (DSN) antennas has been conducted over the last decade. In all, 48 sessions have been carried out using 8 different antennas on three continents. Delay and/or delay rate observables have been measured on two local baselines (at Goldstone, California and at Madrid, Spain), on a transcontinental baseline (California to Massachusetts, USA), and on two intercontinental baselines (Goldstone to Madrid and to Canberra, Australia). A multiparameter fit has been applied to these observables to extract astrometric and geophysical parameters.

These parameters include source positions, polar motion, universal time, the precession constant, baseline vectors and solid earth tides. This article summarizes the geophysical results obtained from the intercontinental measurements.

II. Interferometry Technique

In the present experiments, two separate interferometry systems were employed. The prototype system used in the early measurements recorded a single narrowband (24 kHz) channel at S-band (2.3 GHz) and therefore could only measure delay rate accurately (Ref. 6). To obtain measurements of delay as well, a new system was developed and implemented in 1977 (Ref. 7). It records six time-multiplexed frequency channels to permit calculation of delay by bandwidth synthesis

(BWS), a technique pioneered by Rogers (Ref. 8). Three 2-MHz-wide channels are placed at S-band and three at X-band (8.4 GHz) to allow dual-frequency calibration of charged-particle delays. This new system can measure delay with a precision (system noise error) of approximately 100 psec, given a correlated source strength of 0.5 Jy, an integration time of 3 minutes, a spanned bandwidth of 40 MHz, and two 64-m DSN antennas with system temperatures of 35 K.

III. Summary of Experiments

The need to optimize determination of each class of astrometric and geophysical parameters imposes stringent and sometimes conflicting requirements on the design of a VLBI observing schedule. Maximum sensitivity to polar motion and UT1 requires concurrent or consecutive sessions (within 24-48 hours) on the California/Spain baseline (essentially east/west) and the California/Australia baseline (with a large north/south component). Development of a reference frame requires complete coverage of the sky and several observations of each source during the period of mutual visibility for each pair of stations. Establishing accurate positions of enough radio objects to provide "nearby" reference points for navigating interplanetary spacecraft, as well as for measurements of earth orientation with only 3 hours of VLBI data in a subsequent operational mode, requires approximately 100 sources. Observations which meet the above requirements have been carried out between August 1971 and February 1980. In all, 117 extragalactic radio sources were observed in 48 sessions, which ranged in length from 2 to 24 hours. Of the 2414 individual observations, 692 were made at S-band only, 366 at X-band only, and 1356 were dual-frequency. The observations included 2399 measurements of delay rate and 2152 of delay.

IV. Model and Fit to Experimental Data

In considering the multitude of effects contributing to the delay model for VLBI, it is helpful to group them as either modeled or unmodeled effects, with the models containing parameters that may be either adjusted or fixed at their a priori values. Modeled quantities that were fixed at their a priori values include nutation (Wahr series, Ref. 9) and the effects of the ionosphere. Effects of ocean loading and plate motion are unmodeled.

There are eight categories of modeled and adjusted parameters: station locations, tropospheric delays, clock offsets and rates, polar motion and UT1, source positions, the precession constant, the gamma factor of general relativity, and solid earth tides. The solution provided a catalog of approximately 100 positions of radio sources with declinations ranging between -40° and $+70^\circ$ (with formal error estimates of the order

of $0''.01$). A number of discontinuities and nonlinearities in the station clocks were detected and modeled in many of the sessions. There were 114 parameters describing delay due to the troposphere; these were constrained to agree with the Chao monthly mean model (Ref. 10) to within 3%. The long span of data enables us to solve for the luni-solar precession constant, in addition to UT1 and polar motion at 49 epochs.

A rotation about the polar axis of 2.37 milliarcsecond/year (mas/yr) is included in the model to correct UT1 for the new IAU expressions for Greenwich mean sidereal time and precession (Ref. 9). The BIH Circular D provides a reference point for earth orientation: the values of both components of polar motion and two values of UT1 (one for each intercontinental baseline) are constrained on December 20-21, 1979, during which period there were two intercontinental observing sessions. In total, the fit to the 1971-1980 data includes 744 adjusted parameters.

The observables in the fit were weighted in inverse proportion to the sum of squares of known random error sources, plus an additional noise term which is adjusted to make chi-square per degree of freedom equal to 1 for each session. The software used to perform parameter estimation is based on the square-root-information-filter method (Ref. 11) implemented for the VAX 11/780 computer. Approximately 8 CPU hours are required for a solution for the 1971-80 data. RMS residuals for the grand fit are 0.5 nsec for delay and 0.3 psec/sec for delay rate. The resulting geophysical parameters are discussed in some detail in the next section.

V. Results

A. Earth Orientation

The solution for universal time and polar motion produced the average formal error estimates given in Table 1 as functions of the date of observation. Clearly, the quality of the data improved substantially as the interferometric system evolved, with the 1980 data exhibiting formal uncertainties of 6 to 20 cm.

Figures 1 and 2 show comparisons of our x and y polar motion values for the latter part of the data (1977-80) with BIH Circular D. Taking into account the 4 mas error of the BIH data (Ref. 12), there are no outstanding discrepancies with the possible exception of three points that differ by ~ 1.5 to 2σ . For the UT1 results similarly plotted in Fig. 3, short-period tidal fluctuations have been removed from the VLBI data in order to permit comparison with the heavily smoothed BIH values. The solid curve represents lunar laser ranging (LLR) data as smoothed over a 15-day interval by Fliegel et al. (Ref. 13). These data originally consisted of several hundred points in the range of the plot.

Figure 3 shows that the UT1 values measured by VLBI, LLR and BIH generally agree with one another if the BIH values are assigned errors of approximately 2 msec, and the LLR values errors of 1 msec or less. Both the VLBI and LLR results suggest the same oscillation of ~ 2 msec amplitude about the BIH values. The three points of large discrepancy (~ 2 to 3σ) between VLBI and LLR in February 1977 and February 1980 require further investigation.

The value obtained for the luni-solar precession constant is smaller than the 1976 IAU value by 3.7 ± 0.9 mas/yr. This discrepancy may indicate the need for a revision of either the precession constant or of the long-period (18.6-year) term in the nutation series. Such an inference is supported by calculations in which the fit was repeated with a modified nutation constant, and the precession constant was solved for. The rms delay residual for the 1971-80 VLBI data reaches a minimum when the amplitude of the 18.6-year term in the Wahr nutation series is increased by ~ 7 mas (to $9''.210$ in obliquity), at which point the precession constant equals the 1976 IAU value within its error estimate.

B. Baselines and Earth Tides

On the premise that our data, especially the 1971-1977 portion, lack quality sufficient to detect plate motion, each station was initially assumed to have a single location for the entire span of data. Table 2 shows the lengths of the two intercontinental baselines obtained from such fits in 1978 and at present. Comparison of baseline lengths in this table is complicated by the substantially different modeling used in the two calculations (e.g., the 1978 fit did not use the Wahr nutation series). In spite of the lack of separation of the effects of improved data quality and improved modeling, Table 2 shows the qualitative enhancement in system performance over the past decade. The decrease by nearly a factor of 3 in the formal baseline errors between 1978 and the most recent solution suggests that future improved experiments will permit detection of plate motion within the next few years

A useful test of internal consistency is to divide the data into parts and to determine if fits to the parts lead to consistent values for theoretically constant parameters. To test

baseline repeatability, the span of data was divided into two portions containing nearly equal numbers of observations: 1971-78 (average epoch 1978.2) and 1979-80 (average epoch 1979.9). All of the data were again simultaneously fit, but the Spanish and Australian 64-m antennas were each allowed to have different locations in the two spans of data. As shown in Table 3, the resulting baseline lengths for the two parts are in good agreement.

The Spanish baseline errors in Table 3 again show the improvement of data quality with time. It is of interest to note that, even though our results are consistent with no motion, the differences for both the Spanish and Australian baselines in Table 3 are more consistent with the motion inferred from paleomagnetic data (Refs. 14, 15). For a 1.7-year span, Morabito's application (Ref. 15) of Minster and Jordan's model (Ref. 14) indicates changes of +4 and -6 cm respectively for the Spanish and Australian baselines.

Assuming that the vertical and horizontal Love numbers and the solid-earth-tide-phase lag values are identical at all stations we obtain 0.63 ± 0.03 , 0.063 ± 0.017 , and -1.7 ± 1.6 degrees respectively. These agree well with the commonly accepted values of $0.603 - 0.611$, $0.0832 - 0.0842$, and 0 degrees (Refs. 16, 17).

VI. Conclusions

The radio interferometric system under development at JPL during the past decade has improved continually in quality. By 1980 it had reached the point where earth orientation parameters could be determined with formal uncertainties of 6 to 20 cm, and source positions with formal uncertainties of the order of $0''.01$. Formal uncertainties of 5 to 10 cm in intercontinental baseline lengths promise detection of plate-tectonic motion in the near future.

The present set of results represents very nearly our final fit to the 1971-80 data. Minor changes in the model, such as improved ephemerides and earth tide models, as well as adoption of the J2000 system, will probably not have significant repercussions.

References

1. Thomas, J. B., et al., "A Demonstration of an Independent-Station Radio Interferometry System with 4-cm Precision on a 16-km Baseline," *J. Geophys. Res.*, 81, pp. 995-1005, 1976.
2. Rogers, A. E. E., et al., "Geodesy by Radio Interferometry: Determination of a 1.24-km Base Line with 5-mm Repeatability," *J. Geophys. Res.*, 83, pp. 325-334, 1978.
3. Ryan, J. W., et al., "Precision Surveying Using Radio Interferometry," *J. Surveying and Mapping Division*, Proc. ASCE, Vol. 104, No. SU1, pp. 25-34, 1978.
4. Niell, A. E., et al., "Comparison of a Radio Interferometric Differential Baseline Measurement with Conventional Geodesy," *Tectonophysics*, 52, pp. 49-58, 1979.
5. Herring, T. A., et al., "Geodesy by Radio Interferometry: Intercontinental Distance Determinations with Subdecimeter Precision," *J. Geophys. Res.*, 86, pp. 1647-1651, 1981.
6. Thomas, J. B., *An Analysis of Long Baseline Radio Interferometry*, Technical Report 32-1526, Volume VII, 37-50, Volume VIII, 29-38, Volume XVI, 47-64, Jet Propulsion Laboratory, Pasadena, Calif., 1972.
7. Thomas, J. B., *An Analysis of Radio Interferometry with the Block 0 System*, Publication 81-49, Jet Propulsion Laboratory, Pasadena, Calif., 1981.
8. Rogers, A. E. E., "Very Long Baseline Interferometry with Large-Effective Bandwidth for Phase-Delay Measurements," *Radio Science*, 5, p. 1239, 1970.
9. Kaplan, G. H., "The IAU Resolutions on Astronomical Constants, Time Scales, and the Fundamental Reference Frame," USNO Circular No. 163, United States Naval Observatory, Washington, D.C., 1981.
10. Chao, C. C., *The Tropospheric Calibration Model for Mariner Mars 1971*, Technical Report 32-1587, pp. 61-76, Jet Propulsion Laboratory, Pasadena, Calif., 1974.
11. Bierman, G. J., *Factorization Methods for Discrete Sequential Estimation*, New York, Academic Press, 1977.
12. Dickey, J. O., "Analysis of Lageos Polar Motion Results Using Lunar Laser Ranging," *EOS* 62, p. 841, 1981.
13. Fliegel, H. F., Dickey, J. O., and Williams, J. G., "Intercomparison of Lunar Laser and Traditional Determinations of Earth Rotation," IAU Colloquium Proc. No. 63, O. Calame, ed., Grasse, France, 1981.
14. Minster, J. B., and Jordan, T. H., "Present-Day Plate Motions," *J. Geophys. Res.*, 83, pp. 5331-5354, 1978.
15. Morabito, D. D., Claflin, E. S., and Steinberg, C. J., "VLBI Detection of Crustal Plate Motion Using DSN Antennas as Base Stations," *DSN Progress Report 42-56*, pp. 59-75, Jet Propulsion Laboratory, Pasadena, Calif., 1980.
16. Wahr, J. M., "The Tidal Motions of a Rotating, Elastic and Oceanless Earth," pp. 162-171, Thesis, University of Colorado, 1977.
17. Lambeck, K., *The Earth's Variable Rotation: Geophysical Causes and Consequences*, pp. 13, 111, Cambridge University Press, 1980.

**Table 1. Earth orientation parameter formal errors
in fit to 1971-1980 VLBI data**

Year	Polar motion, mas		UT1, msec
	x	y	
1971-4	2.1
1977	10	4	0.9
1978	10	3	0.7
1979	6	2	0.5
1980	6	2	0.5

Table 2. Baseline length results from VLBI data

Date	California to	
	Spain	Australia
1971-78	8 390 429.66 ± 0.16 m	10 588 965.85 ± 0.26 m
1971-80	8 390 429.84 ± 0.05 m	10 588 966.32 ± 0.11 m

Table 3. Baseline consistency test results

Average date	California to	
	Spain	Australia
1978.2	8 390 429.78 ± 0.09 m	10 588 966.36 ± 0.11 m
1979.9	8 390 429.85 ± 0.05 m	10 588 966.27 ± 0.11 m
Difference	7 ± 10 cm	-9 ± 15 cm

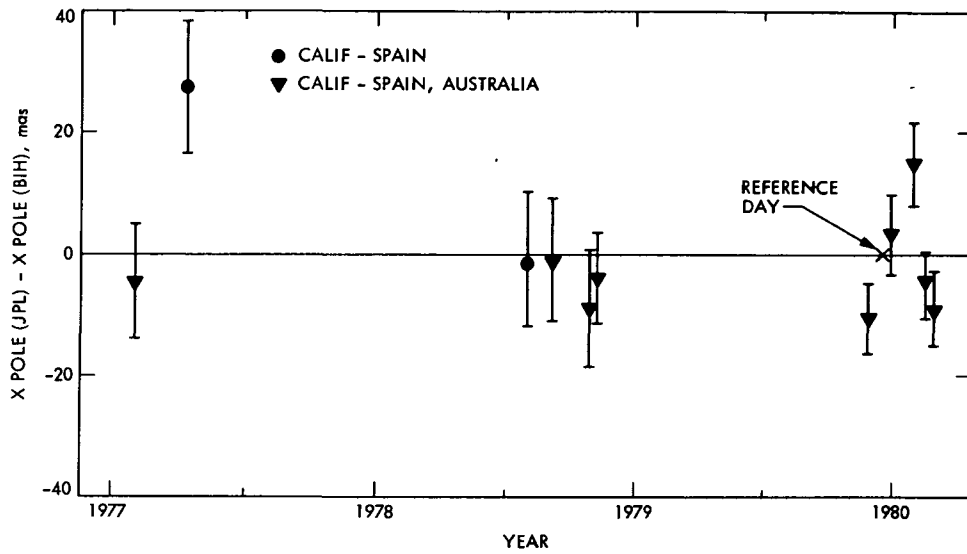


Fig. 1. Polar motion x-component results from 1977-1980 VLBI data

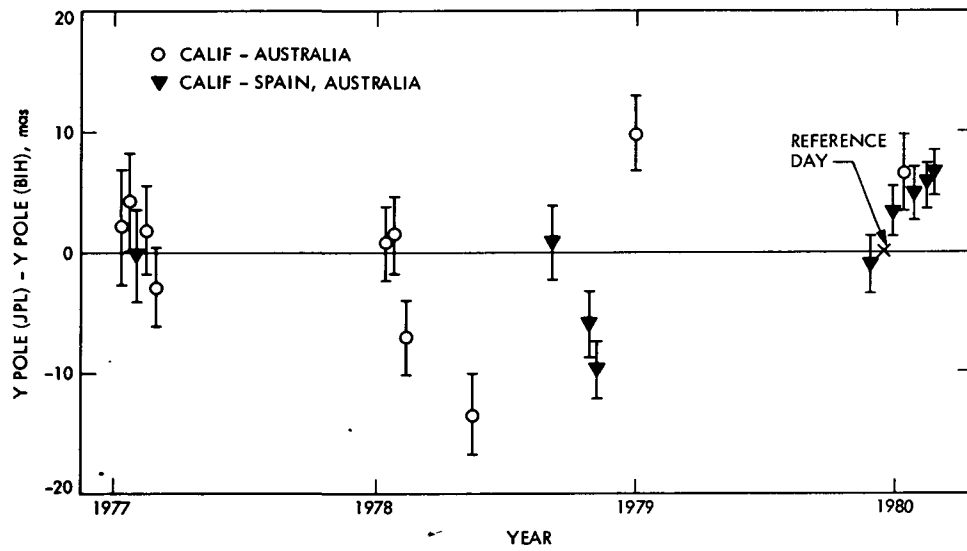


Fig. 2. Polar motion y-component results from 1977-1980 VLBI data

ORIGINAL PAGE IS
OF POOR QUALITY

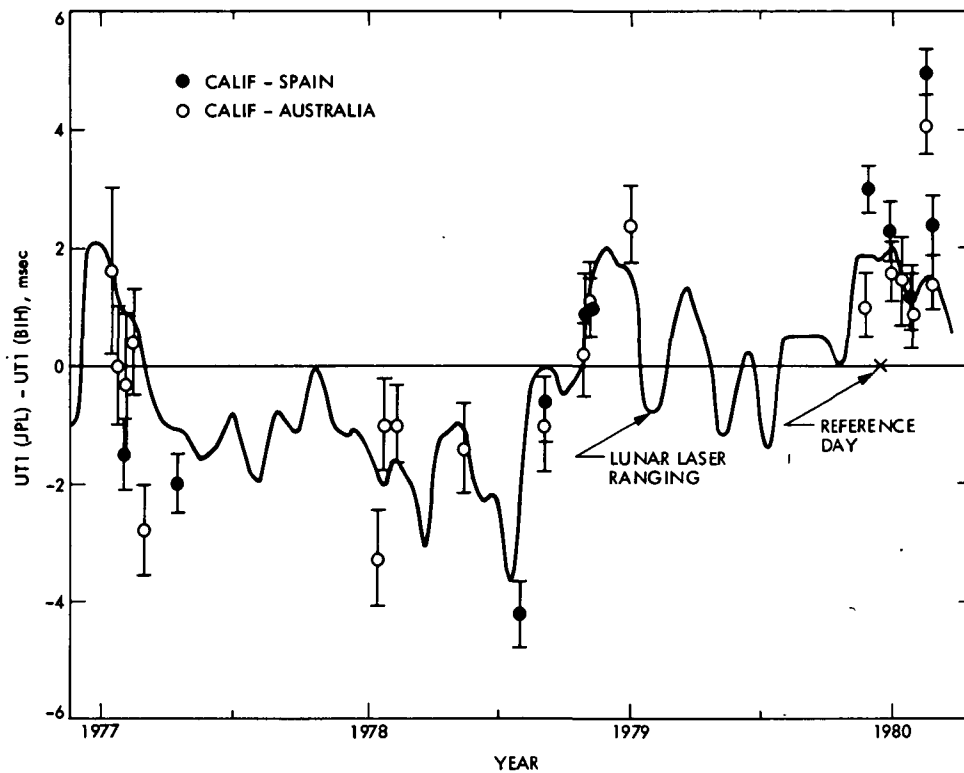


Fig. 3. UT1 results from 1977-1980 VLBI data. Short-period tidal terms have been removed to permit comparison with BIH values

Error Estimation for Δ VLBI Angle and Angle Rate Measurements Over Baselines Between a Ground Station and a Geosynchronous Orbiter

S. C. Wu

Tracking Systems and Applications Section

Baselines between a ground station and a geosynchronous orbiter provide high-resolution Δ VLBI data which is beyond the capability of ground-based interferometry. The effects of possible error sources on such Δ VLBI data for the determination of spacecraft angle and angle rate are investigated. For comparison, the effects on spacecraft-only VLBI are also studied.

I. Introduction and Assumptions

The technology of Δ VLBI over ground baselines for the measurements of deep space probe angle and angle rate has been well developed (Refs. 1-4). Wideband Δ VLBI (or Δ DOR) has been successfully demonstrated using Voyager telemetry subcarrier harmonics near Saturn encounters. It is well known that to resolve the two components of the spacecraft angular position, two nonparallel baselines are needed. These baselines have to be long for a high accuracy, but not too long to have either end of the baseline viewing below a minimum elevation angle ($\sim 10^\circ$). The intercontinental baselines between the three DSN sites at Goldstone, Madrid, and Canberra are nearly optimum in length, although not quite optimum in orthogonality.

To overcome the above limitation, thought has been given to baselines between ground stations and an Earth-orbiting satellite. With proper selection of the satellite geometry, one ground station will suffice. The baseline orthogonality will be furnished by the varying position of the satellite as it orbits around the Earth.

Here we shall investigate the effects of possible error sources on Δ VLBI measurements for the determination of

spacecraft angle and angle rate. The satellite is assumed to be geosynchronous for its unique feature of being in view at all time from a low- or mid-latitude station, provided the inclination of the satellite is not too high. The DSN site at Goldstone (latitude $\sim 35^\circ N$) is selected as the only ground station.

Since most deep space probe trajectories are near the ecliptic plane, which may assume a declination angle between -23 and 23° , an analysis at $\delta = 0^\circ$ will shed enough light on most cases to be encountered in deep space navigation. For this zero- δ case, a low-inclination satellite does not provide a long baseline component in the δ -direction. Therefore, a moderately high inclination angle is desirable. In the following analysis we shall assume a satellite inclination of 45° . For such geometry, the possible baseline projections onto the plane of the sky are shown in Fig. 1 for the two extreme cases and also for a more probable "general" case.

For the "general" case, the satellite orbit plane is inclined from the plane of the sky by an angle of $\sim 63^\circ$. The projections of the two orthogonal baselines are $\sim 40,000$ and $\sim 15,000$ km. These baselines will have error sensitivities of 0.25 and 0.67 nrad/cm, respectively, resulting in an RSS error sensitivity of 0.72 nrad/cm. The RSS error sensitivity will be used in the following estimation of the effects of most

error sources; when the delay (or delay rate) error is a function of the baseline projection length, the effects on angle (or angle rate) will be individually scaled by their component error sensitivities and then RSSed. Such error sources include solar plasma and satellite ephemeris error and spacecraft angular position error in the determination of angle rate.

Table 1 summarizes the assumed geometry and the quantities regarding the system performance and error sources. The rather large separation of 20° between the spacecraft and the quasar is assumed. Such a conservative choice is based on the fact that the number of quasars with correlated flux densities of 0.2 Jansky or higher, over the 40,000-km baseline, is yet to be investigated. We shall study first the effects on angle measurement with wide-band Δ VLBI (bandwidth synthesis) in Section II. Then, in Section III, we shall study the effects on angle rate measurement with narrow-band Δ VLBI. For comparison, we shall also study the cases of spacecraft-only VLBI. Table 2 lists all symbols to be used in the following calculation.

II. Spacecraft Angle Measurement

A. System Noise

The signal-to-noise of the correlated quasar signal can be derived from (Ref. 5)

$$SNR_Q = 2 \times 10^{-4} D_1 D_2 S_c \left(\frac{e_1 e_2 f_{ch} T_{obs}}{T_{s,1} T_{s,2}} \right)^{1/2}$$

$$= 6.8$$

The spacecraft signal is to be correlated individually at each end of the baseline with local models. The corresponding SNR are (Ref. 3)

$$SNR_S = 2 \left(\frac{P_t T_{obs}}{\pi k T} \right)^{1/2}$$

$$= 74.4 \text{ at satellite}$$

and

$$SNR_G = SNR_S \left(\frac{D_2}{D_1} \right) \left(\frac{\epsilon_2 T_1}{\epsilon_1 T_2} \right)^{1/2}$$

$$= 211.9 \text{ at Goldstone}$$

For S/C-only VLBI, the delay error is given by

$$\epsilon_\tau = \frac{\sqrt{2} c}{2\pi f_{span}} \left[\left(\frac{1}{SNR_S} \right)^2 + \left(\frac{1}{SNR_G} \right)^2 \right]^{1/2}$$

$$= 0.96 \text{ cm}$$

and the corresponding angle error is

$$\epsilon_\theta = 0.72 \epsilon_\tau = 0.69 \text{ nrad} \quad (1)$$

For Δ VLBI, the error is dominated by SNR_Q of the quasar signal. Hence the differenced delay error is

$$\epsilon_{\Delta\tau} = \frac{\sqrt{2} c}{2\pi f_{span}} \left(\frac{1}{SNR_Q} \right)$$

$$= 9.93 \text{ cm}$$

The corresponding angular separation error is

$$\epsilon_{\Delta\theta} = 0.72 \epsilon_{\Delta\tau} = 7.15 \text{ nrad} \quad (2)$$

B. Clock Offset

For S/C-only VLBI, the delay error is

$$\epsilon_\tau = c T_{off}$$

$$= 150 \text{ cm}$$

with a corresponding angle error of

$$\epsilon_\theta = 108 \text{ nrad} \quad (3)$$

The differenced delay measured by Δ VLBI is insensitive to clock offset.

C. Frequency Offset

Frequency offset between the two ends of a baseline has an effect on VLBI delay measurement of

$$\epsilon_\tau = \frac{1}{2} \frac{f_{off}}{f_{RF}} c T_{obs}$$

$$= 10.71 \text{ cm}$$

The corresponding angle error is

$$\epsilon_{\theta} = 7.71 \text{ nrad} \quad (4)$$

For Δ VLBI, the effect on the differenced delay is

$$\begin{aligned} \epsilon_{\Delta\tau} &= \frac{f_{off}}{f_{RF}} c T_{S/C-Q} \\ &= 25.71 \text{ cm} \end{aligned}$$

which gives

$$\epsilon_{\Delta\theta} = 18.51 \text{ nrad} \quad (5)$$

D. Clock Instability

For S/C-only VLBI, the delay error is

$$\begin{aligned} \epsilon_{\tau} &= \frac{\sqrt{2} c T_{obs}}{2} \left(\frac{\Delta f}{f} \right) \\ &= 1.28 \text{ cm} \end{aligned}$$

and the angle error is

$$\epsilon_{\theta} = 0.92 \text{ nrad} \quad (6)$$

For Δ VLBI, the differenced delay error is

$$\begin{aligned} \epsilon_{\Delta\tau} &= \sqrt{2} c T_{S/C-Q} \left(\frac{\Delta f}{f} \right) \\ &= 3.07 \text{ cm} \end{aligned}$$

and the angular separation error is

$$\epsilon_{\Delta\theta} = 2.21 \text{ nrad} \quad (7)$$

E. Troposphere

Troposphere (and ionosphere) affects only the ground observations; it has no effect on the observations made from the satellite. For S/C-only VLBI, the delay error is

$$\epsilon_{\tau} = \frac{\rho_z^t}{\sin \gamma_{S/C}} = 14.20 \text{ cm}$$

and the corresponding angle error is

$$\epsilon_{\theta} = 10.22 \text{ nrad} \quad (8)$$

For Δ VLBI, the differenced delay error due to a systematic calibration error is

$$\begin{aligned} \epsilon_{\Delta\tau} &= \rho_z^t \left| \frac{1}{\sin \gamma_{S/C}} - \frac{1}{\sin \gamma_Q} \right| \\ &= 4.86 \text{ cm} \end{aligned}$$

and that due to a horizontal inhomogeneity is

$$\begin{aligned} \epsilon_{\Delta\tau} &= \frac{\rho_{inh}^t}{\sin \gamma_{S/C}} \\ &= 4.73 \text{ cm} \end{aligned}$$

The corresponding angular separation error is

$$\epsilon_{\Delta\theta} = 4.89 \text{ nrad} \quad (9)$$

F. Ionosphere

For S/C-only VLBI, the delay error due to a calibration error in ionospheric peak delay is

$$\begin{aligned} \epsilon_{\tau} &= \rho_{peak}^i f(X_{S/C}) g(\gamma_{S/C}) \\ &= 2.35 \text{ cm} \end{aligned}$$

where the solar-zenith angle factor $f(X)$ and the elevation angle factor $g(\gamma)$ are given in Fig. 2 (Ref. 6).

The delay error due to a bias ionospheric error is

$$\begin{aligned} \epsilon_{\tau} &= \rho_{bias}^i g(\gamma) \\ &= 5.91 \text{ cm} \end{aligned}$$

The angle error is calculated to be

$$\epsilon_{\theta} = 4.58 \text{ nrad} \quad (10)$$

For Δ VLBI the differenced delay error due to an ionospheric peak error is

$$\begin{aligned}\epsilon_{\Delta\tau} &= \rho_{peak}^i [f(X_{S/C})g(\gamma_{S/C}) - f(X_Q)g(\gamma_Q)] \\ &= 0.66 \text{ cm}\end{aligned}$$

that due to a bias error is

$$\begin{aligned}\epsilon_{\Delta\tau} &= \rho_{bias}^i [g(\gamma_{S/C}) - g(\gamma_Q)] \\ &= 1.53 \text{ cm}\end{aligned}$$

and that due to a spatial fluctuation is

$$\begin{aligned}\epsilon_{\Delta\tau} &= \rho_{spa}^i f(X_{S/C})g(\gamma_{S/C}) \\ &= 4.73 \text{ cm}\end{aligned}$$

The angular separation error from these three error types is

$$\epsilon_{\Delta\theta} = 3.61 \text{ nrad} \quad (11)$$

G. Solar Plasma

The cancellation of solar plasma effect between two ray paths degrades as the ray path separation increases. Hence the effect on VLBI delay measurement is larger for longer baseline projection: For the longer baseline (40,000 km), the delay error is (Ref. 7)

$$\begin{aligned}\epsilon_{\tau} &= 0.052 \left(\frac{B}{V_{SW}}\right)^{0.75} [10 \sin(SEP)]^{-1.3} \\ &= 0.80 \text{ cm}\end{aligned}$$

which corresponds to an angle error of

$$\epsilon_{\theta} = 0.25 \quad \epsilon_{\tau} = 0.20 \text{ nrad}$$

For the shorter baseline (15,000 km)

$$\epsilon_{\tau} = 0.38 \text{ cm}$$

and

$$\epsilon_{\theta} = 0.67 \quad \epsilon_{\tau} = 0.26 \text{ nrad}$$

The 2-D angle error is

$$\epsilon_{\theta} = 0.33 \text{ nrad} \quad (12)$$

For Δ VLBI with a source separation of 20° , the separation at solar plasma distance (~ 1 AU) between ray paths observing S/C and quasar from the same site is much greater than that between the two sites observing the same source. Hence only common-source cancellation is effective. The Δ VLBI angle separation error is $\sqrt{2}$ as large as in the case of S/C-only VLBI:

$$\epsilon_{\Delta\theta} = \sqrt{2} \epsilon_{\theta} = 0.47 \text{ nrad} \quad (13)$$

H. Station Location Error

For S/C-only VLBI measurement,

$$\epsilon_{\tau} = \epsilon_{STN} = 50 \text{ cm}$$

and

$$\epsilon_{\theta} = 36.00 \text{ nrad} \quad (14)$$

For Δ VLBI measurement, it can be shown that

$$\begin{aligned}\epsilon_{\Delta\tau} &= [(\Delta\alpha \cos \delta)^2 + (\Delta\delta)^2]^{1/2} \epsilon_{STN} \\ &= 17.45 \text{ cm}\end{aligned}$$

and

$$\epsilon_{\Delta\theta} = 12.57 \text{ nrad} \quad (15)$$

I. Satellite Position Error

For S/C-only VLBI measurement, the delay error accompanying the longer baseline is

$$\begin{aligned}\epsilon_{\tau} &= [(\epsilon_L \sin \Omega)^2 + (\epsilon_C \cos \Omega)^2]^{1/2} \\ &= 271.13 \text{ cm}\end{aligned}$$

corresponding to an angle error of

$$\epsilon_{\theta} = 0.25 \quad \epsilon_{\tau} = 67.78 \text{ nrad}$$

The delay error accompanying the shorter baseline is

$$\begin{aligned}\epsilon_{\tau} &= [(\epsilon_H \sin \Omega)^2 + (\epsilon_C \cos \Omega)^2]^{1/2} \\ &= 100 \text{ cm}\end{aligned}$$

corresponding to an angle error of

$$\epsilon_{\theta} = 0.67 \epsilon_{\tau} = 67 \text{ nrad}$$

The 2-D angle error is

$$\epsilon_{\theta} = 95.31 \text{ nrad} \quad (16)$$

For Δ VLBI measurement, the angular separation error is reduced by the separation angle:

$$\epsilon_{\Delta\theta} = \Delta\theta \epsilon_{\theta} = 33.27 \text{ nrad} \quad (17)$$

J. Phase Instability

For S/C-only VLBI measurement, the effect is

$$\begin{aligned} \epsilon_{\tau} &= \frac{2c}{2\pi f_{span}} \epsilon_{\phi} \\ &= 3.33 \text{ cm} \end{aligned}$$

and

$$\epsilon_{\theta} = 2.40 \text{ nrad} \quad (18)$$

For Δ VLBI the effect is estimated to have the same magnitude as that on VLBI measurement:

$$\epsilon_{\Delta\theta} = \epsilon_{\theta} = 2.40 \text{ nrad} \quad (19)$$

K. Quasar Position Error

This error affects only Δ VLBI measurements:

$$\epsilon_{\Delta\theta} = \epsilon_{\theta,Q} = 5 \text{ nrad} \quad (20)$$

III. Spacecraft Angle Rate Measurement

A. System Noise

The effect on S/C-only VLBI measurement is very small and can be ignored. The effect on Δ VLBI is dominated by the correlated quasar signal-to-noise ratio,

$$\begin{aligned} \epsilon_{\Delta\dot{\tau}} &= \frac{4c}{2\pi f_{RF} T_{obs}} \left(\frac{1}{SNR_Q} \right) \\ &= 0.56 \times 10^{-3} \text{ cm/sec} \end{aligned}$$

and the corresponding angle rate error is

$$\epsilon_{\Delta\dot{\theta}} = 0.40 \text{ prad/sec} \quad (21)$$

B. Clock Offset

Clock offset between the two ends of a baseline has no effect on either VLBI or Δ VLBI measurements.

C. Frequency Offset

For S/C-only VLBI measurement, the delay rate error is

$$\epsilon_{\dot{\tau}} = \frac{f_{off}}{f_{RF}} c = 35.71 \times 10^{-3} \text{ cm/sec}$$

which corresponds to an angle rate error of

$$\epsilon_{\dot{\theta}} = 25.71 \text{ prad/sec} \quad (22)$$

Δ VLBI measurement is insensitive to frequency offset.

D. Clock Instability

For S/C-only VLBI measurement, the delay rate error is

$$\begin{aligned} \epsilon_{\dot{\tau}} &= \sqrt{2} c \left(\frac{\Delta f}{f} \right) \\ &= 4.26 \times 10^{-3} \text{ cm/sec} \end{aligned}$$

and the corresponding angle rate error is

$$\epsilon_{\dot{\theta}} = 3.07 \text{ prad/sec} \quad (23)$$

For Δ VLBI measurement, the differenced delay rate error can be shown to be

$$\begin{aligned} \epsilon_{\Delta\dot{\tau}} &= \sqrt{2} c \left(\frac{\Delta f}{f} \right) \left(\frac{T_{S/C-Q}}{T_{obs}} \right)^{1/2} \\ &= 4.67 \times 10^{-3} \text{ cm/sec} \end{aligned}$$

corresponding to an angle rate error of

$$\epsilon_{\Delta\dot{\theta}} = 3.36 \text{ prad/sec} \quad (24)$$

E. Troposphere

For S/C-only VLBI, the delay rate error is

$$\epsilon_{\dot{\tau}} = \left| \frac{\partial}{\partial t} \left(\frac{\rho_z^t}{\sin \gamma_{S/C}} \right) \right| = \rho_z^t \left| \frac{\cos \gamma_{S/C}}{\sin^2 \gamma_{S/C}} \dot{\gamma}_{S/C} \right|$$

Let

$$\dot{\gamma}_{S/C} = 0.7 \omega_e$$

then

$$\epsilon_{\dot{\tau}} = 1.56 \times 10^{-3} \text{ cm/sec}$$

corresponding to an angle rate error of

$$\epsilon_{\dot{\theta}} = 1.12 \text{ prad/sec} \quad (25)$$

For Δ VLBI, let $\dot{\gamma}_Q = 0.6 \omega_e$. The differenced delay rate error due to a systematic error is

$$\begin{aligned} \epsilon_{\Delta\dot{\tau}} &= \rho_z^t \left| \frac{\cos \gamma_{S/C}}{\sin^2 \gamma_{S/C}} \dot{\gamma}_{S/C} - \frac{\cos \gamma_Q}{\sin^2 \gamma_Q} \dot{\gamma}_Q \right| \\ &= 1.07 \times 10^{-3} \text{ cm/sec} \end{aligned}$$

and that due to a horizontal inhomogeneity is

$$\begin{aligned} \epsilon_{\Delta\dot{\tau}} &= \rho_{inh}^t \left| \frac{\cos \gamma_{S/C}}{\sin^2 \gamma_{S/C}} \dot{\gamma}_{S/C} \right| \\ &= 0.52 \times 10^{-3} \text{ cm/sec} \end{aligned}$$

The corresponding angular rate error is

$$\epsilon_{\Delta\dot{\theta}} = 0.86 \text{ prad/sec} \quad (26)$$

F. Ionosphere

On both VLBI and Δ VLBI angle rate measurements, only the temporal fluctuation component of the ionosphere has a significant effect. For S/C-only VLBI,

$$\begin{aligned} \epsilon_{\dot{\tau}} &= \frac{\rho_{temp}^i}{T_{obs}} f(X_{S/C}) g(\gamma_{S/C}) \\ &= 2.63 \times 10^{-3} \text{ cm/sec} \end{aligned}$$

and

$$\epsilon_{\dot{\theta}} = 1.89 \text{ prad/sec} \quad (27)$$

For Δ VLBI measurement,

$$\begin{aligned} \epsilon_{\Delta\dot{\tau}} &= \frac{\rho_{temp}^i}{T_{obs}} [f^2(X_{S/C}) g^2(\gamma_{S/C}) + f^2(X_Q) g^2(\gamma_Q)]^{1/2} \\ &= 3.24 \times 10^{-3} \text{ cm/sec} \end{aligned}$$

and

$$\epsilon_{\Delta\dot{\theta}} = 2.33 \text{ prad/sec} \quad (28)$$

G. Solar Plasma

For S/C-only VLBI, the delay rate measurement over the longer baseline has an error of

$$\begin{aligned} \epsilon_{\dot{\tau}} &= \frac{0.052 \sqrt{2}}{T_{obs}} \left(\frac{B}{V_{SW}} \right)^{0.75} [10 \sin(SEP)]^{-1.3} \\ &= 1.89 \times 10^{-3} \text{ cm/sec} \end{aligned}$$

which is corresponding to an angle rate error of

$$\epsilon_{\dot{\theta}} = 0.47 \text{ prad/sec}$$

Over the shorter baseline, the errors are

$$\epsilon_{\dot{\tau}} = 0.91 \times 10^{-3} \text{ cm/sec}$$

and

$$\epsilon_{\dot{\theta}} = 0.61 \text{ prad/sec}$$

The 2-D angle rate error is

$$\epsilon_{\dot{\theta}} = 0.77 \text{ prad/sec} \quad (29)$$

For Δ VLBI measurement, the error is $\sqrt{2}$ times larger; i.e.,

$$\epsilon_{\Delta\dot{\theta}} = 1.09 \text{ prad/sec} \quad (30)$$

H. Station Location Error

For S/C-only VLBI measurement, the delay rate error is

$$\begin{aligned}\epsilon_{\dot{r}} &= \omega_e \epsilon_{STN} \cos \delta & \epsilon_{\Delta\dot{\theta}} &= \Delta\theta \epsilon_{\dot{\theta}} = 3.33 \text{ prad/sec} & (34) \\ &= 3.65 \times 10^{-3} \text{ cm/sec}\end{aligned}$$

and the corresponding angle rate error is

$$\epsilon_{\dot{\theta}} = 2.63 \text{ prad/sec} \quad (31)$$

For VLBI measurement, the differenced delay rate error is

$$\begin{aligned}\epsilon_{\Delta\dot{r}} &= \omega_e \epsilon_{STN} [(\Delta\alpha \cos \delta)^2 + (\Delta\delta \sin \delta)^2]^{1/2} \\ &= 1.27 \times 10^{-3} \text{ cm/sec}\end{aligned}$$

and the corresponding angle rate error is

$$\epsilon_{\Delta\dot{\theta}} = 0.92 \text{ prad/sec} \quad (32)$$

I. Satellite Velocity Error

For S/C-only VLBI measurement, the effect on the delay rate measurement over the longer baseline is

$$\begin{aligned}\epsilon_{\dot{r}} &= [(\epsilon_{\dot{L}} \sin \Omega)^2 + (\epsilon_{\dot{C}} \cos \Omega)^2]^{1/2} \\ &= 27.11 \times 10^{-3} \text{ cm/sec}\end{aligned}$$

corresponding to an angle rate error of

$$\epsilon_{\dot{\theta}} = 6.78 \text{ prad/sec.}$$

The delay rate error over the shorter baseline is

$$\begin{aligned}\epsilon_{\dot{r}} &= [(\epsilon_{\dot{H}} \sin \Omega)^2 + (\epsilon_{\dot{C}} \cos \Omega)^2]^{1/2} \\ &= 10 \times 10^{-3} \text{ cm/sec}\end{aligned}$$

corresponding to an angle rate error of

$$\epsilon_{\dot{\theta}} = 6.70 \text{ prad/sec}$$

The 2-D angle rate error is

$$\epsilon_{\dot{\theta}} = 9.53 \text{ prad/sec} \quad (33)$$

For Δ VLBI measurement, the angle rate error is reduced by the S/C-quasar angular separation:

J. Phase Instability

For S/C-only VLBI measurement, the delay rate error is

$$\begin{aligned}\epsilon_{\dot{r}} &= \frac{2c}{2\pi f_{RF} T_{obs}} \epsilon_{\phi} \\ &= 0.06 \times 10^{-3} \text{ cm/sec}\end{aligned}$$

which is negligibly small. The error on Δ VLBI measurement is estimated to be of the same magnitude and is also negligible.

K. S/C Angular Position Error

It can be shown that the sensitivity of (differenced) delay rate to such error is equal to the rate of change of the baseline projection in the direction of the angular position (separation) error. That is,

$$\frac{\partial \dot{r}}{\partial \theta} = \hat{\theta} \cdot \dot{\mathbf{B}}, \quad \frac{\partial(\Delta\dot{r})}{\partial(\Delta\theta)} = \Delta\hat{\theta} \cdot \dot{\mathbf{B}}$$

For S/C-only VLBI, the delay rate error over the longer baseline is

$$\begin{aligned}\epsilon_{\dot{r}} &= \omega_e a \cos \Omega \epsilon_{\dot{\theta}} \\ &= 21.03 \times 10^{-3} \text{ cm/sec}\end{aligned}$$

corresponding to an angle rate error of

$$\epsilon_{\dot{\theta}} = 5.26 \text{ prad/sec}$$

Over the shorter baseline the errors are

$$\begin{aligned}\epsilon_{\dot{r}} &= \omega_e a \epsilon_{\dot{\theta}} \\ &= 46.32 \text{ cm/sec}\end{aligned}$$

and

$$\epsilon_{\dot{\theta}} = 31.03 \text{ prad/sec}$$

The 2-D angle rate error is

$$\epsilon_{\dot{\theta}} = 31.48 \text{ prad/sec} \quad (35)$$

For Δ VLBI measurement, the same calculation applies

except that ϵ_{θ} is replaced by $\epsilon_{\Delta\theta}$, which is assumed to be a factor of $(40/150)$ smaller. Hence,

$$\epsilon_{\Delta\dot{\theta}} = \left(\frac{40}{150}\right) \epsilon_{\dot{\theta}} = 8.39 \text{ prad/sec} \quad (36)$$

Note that the errors are dominated by a component resulting from S/C angular position error in the direction parallel to the longer baseline.

IV. Summary

Figures 3 and 4 summarize, respectively, the angle and angle rate errors for both S/C-only VLBI and S/C-quasar Δ VLBI data types. The VLBI angle measurement error is

dominated by clock offset and satellite position error, which are unlikely to be greatly reduced. For Δ VLBI angle measurement the major error sources are in satellite position and station location, both of which are scaled by the S/C-quasar angular separation. Hence the RSS error will also be scaled by such separation.

The determination of spacecraft angle rate is extremely sensitive to spacecraft angular position error. In the application to a planetary orbiter, where such data type will most probably be needed, the dynamics of the spacecraft trajectory allows the determination of the angular position. Therefore the effects of angular position error are removed. In the case of a cruising interplanetary spacecraft, the angle rate can be better determined from successive Δ VLBI angle measurements.

References

1. Melbourne, W. G., and Curkendall, D. W., "Radio Metric Direction Finding: A New Approach to Deep Space Navigation," paper presented at AAS/AIAA Astrodynamics Specialist Conference, Jackson Hole, Wyoming, Sep. 1977.
2. Brown, D. S., Hildebrand, C. E., and Skjerve, L. J., "Wideband Δ VLBI For Deep Space Navigation," paper presented at IEEE Position Location and Navigation Symposium, Atlantic City, N.J., Dec. 1980.
3. Brunn, D. L., Preston, R. A., Wu, S. C., Siegel, H. L., Brown, D. S., Christensen, C. S., and Hilt, D. E., " Δ VLBI Spacecraft Tracking System Demonstration: Part I. Design and Planning," *DSN Progress Report 42-45*, pp. 111-132. Jet Propulsion Laboratory, Pasadena, Calif., June 15, 1978.
4. Christensen, C. S., Moultrie, B., Callahan, P. S., Donovan, F. F., and Wu, S. C., " Δ VLBI Spacecraft Tracking System Demonstration: Part II. Data Acquisition and Processing," *TDA Progress Report 42-60*, pp. 60-67, Jet Propulsion Laboratory, Pasadena, Calif., Dec. 15, 1980.
5. Thomas, J. B., *An Analysis of Long Baseline Radio Interferometry, Part II*, Technical Report 32-1526, Vol. VIII, pp. 29-38, Jet Propulsion Laboratory, Pasadena, Calif. Apr. 1972.
6. Wu, S. C., "Atmospheric Media Effects on ARIES Baseline Determination," *TDA Progress Report 42-61*, pp. 1-6, Jet Propulsion Laboratory, Pasadena, Calif., Feb. 15, 1981.
7. Callahan, P. S., "An Analysis of Viking S-X Doppler Measurements of Solar Wind Columnar Content Fluctuation," *DSN Progress Report 42-44*, pp. 75-81, Jet Propulsion Laboratory, Pasadena, Calif., Apr. 15, 1978.

Table 1. Geometry and basic assumptions

Satellite inclination from equator plane = 45°
Satellite inclination from plane of sky = 63°
Station latitude = 35°
Spacecraft declination = 0°
S/C-quasar angular separation = 20°
Solar-earth-S/C angle = 10°
S/C elevation at station = 25°
Quasar elevation at station = 40°
Solar-zenith angles of ionospheric reference points = 50° (S/C) 52° (quasar)
Quasar angular position error = 5 nrad
S/C angular position error = 150 nrad (for angle rate determination)
S/C-quasar angular separation error = 40 nrad (for angle rate determination)
Satellite position error in HCL = (1 m, 1 m, 3 m)
Satellite velocity error in HCL = (0.1 mm/s, 0.1 mm/s, 0.3 mm/s)
Station location error (including polar motion and UT1) = 50 cm in each direction
Zenith troposphere errors: 6 cm systematic 2 cm inhomogeneity
Zenith ionosphere errors: 1.5 cm peak 3 cm bias 3 cm spatial fluctuation 1 cm temporal fluctuation (600 sec)
Clock offset = 5 nsec
Frequency offset = 10 mHz at X-band
Clock instability = 10^{-13} over 600 sec at satellite 10^{-14} over 600 sec at station
Phase instability = 2°
Quasar correlated flux density = 0.2 Jansky
S/C power at satellite receiver = -170 dBm
RF frequency = 8.4 GHz (X-band)
Spanned bandwidth = 100 MHz
Channel bandwidth = 2 MHz
Antenna diameters = 28 m at satellite 34 m at station
Antenna efficiencies = 0.40 at satellite 0.55 at station
System temperature = 100 K at satellite 25 K at station
Observation time per source per baseline = 600 sec
Separation time between S/C and quasar observations = 720 sec

Table 2. Definition of symbols

a = satellite orbit radius = 4.22×10^9 cm	$\Delta f/f$ = clock instability in terms of Allan variance (RSS of both sites)
B = length of baseline projection on plane of sky, km	ϵ_{STN} = station location error, cm
c = speed of light = 3×10^{10} cm/sec	$\epsilon_H \epsilon_C \epsilon_L$ = satellite position errors in altitude, cross-track and in-track, cm
D = antenna diameter, m	$\epsilon_{\dot{H}} \epsilon_{\dot{C}} \epsilon_{\dot{L}}$ = satellite velocity errors, cm/sec
e = antenna efficiency	ϵ_ϕ = phase instability, rad
f_{ch} = channel bandwidth, Hz	ϵ_θ = S/C angular position error, rad
f_{off} = frequency offset between ground station and satellite, Hz	$\epsilon_{\theta, Q}$ = quasar angular position error, rad
f_{RF} = nominal RF frequency, Hz	$\epsilon_{\Delta\theta}$ = error in S/C-quasar angular separation, rad
f_{span} = spanned bandwidth, Hz	ϵ_τ = error in delay, cm
$f(X)$ = solar-zenith angle factor of ionosphere	$\epsilon_{\Delta\tau}$ = error in differenced delay, cm
$g(\gamma)$ = elevation angle factor of ionosphere	$\epsilon_{\dot{\tau}}$ = error in delay rate, cm/sec
k = Boltzmann constant = 1.38×10^{-23} Joule/K	$\epsilon_{\Delta\dot{\tau}}$ = error in differenced delay rate, cm/sec
P_t = received S/C tone power, watt	$\epsilon_{\dot{\theta}}$ = error in angle rate, rad/sec
S_c = correlated flux density of quasar signal, Jansky	$\epsilon_{\Delta\dot{\theta}}$ = error in rate of angular separation, rad/sec
SEP = solar-Earth-S/C angle, radian	ρ_{peak}^i = zenith ionospheric peak error, cm
SNR = ratio of correlated fringe amplitude to RMS noise	ρ_{bias}^i = zenith bias ionospheric error, cm
T_{obs} = observation time per source per baseline, sec	ρ_{spa}^i = zenith ionospheric spatial fluctuation, cm
T_{off} = clock offset between ground station and satellite, sec	ρ_{temp}^i = zenith ionospheric temporal fluctuation, cm
$T_{S/C-Q}$ = separation time between the middles of S/C and quasar observations, sec	ρ_z^t = zenith tropospheric error, cm
T_S = system noise temperature, K	ρ_{inh}^t = zenith tropospheric horizontal inhomogeneity, cm
V_{SW} = solar wind velocity = 400 km/sec	Ω = satellite inclination angle from plane of sky
X = solar-zenith angle of ionospheric reference point	ω_e = Earth's spinning rate, also satellite rotation rate
α, δ = S/C right ascension and declination	= 73×10^{-6} rad/sec
γ = elevation angle	
$\Delta\alpha, \Delta\delta$ = angular separation in α and δ between S/C and quasar, radian	

ORIGINAL PAGE IS
OF POOR QUALITY

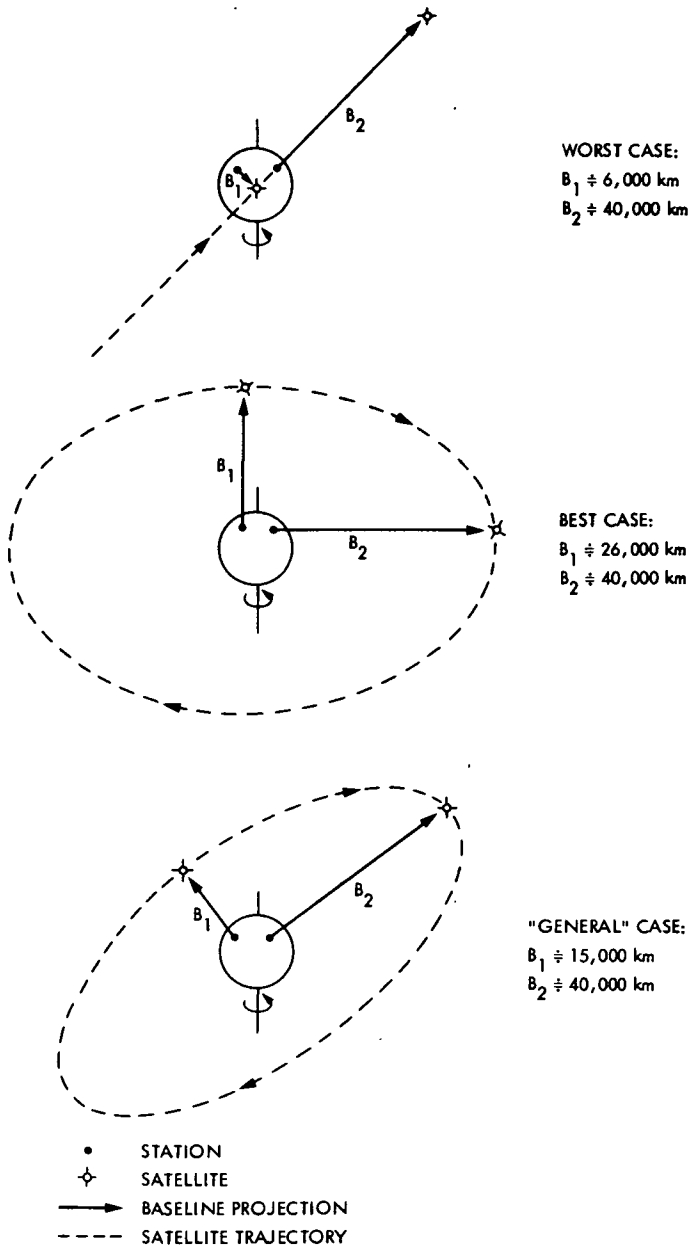


Fig. 1. Baseline projections on the plane of the sky

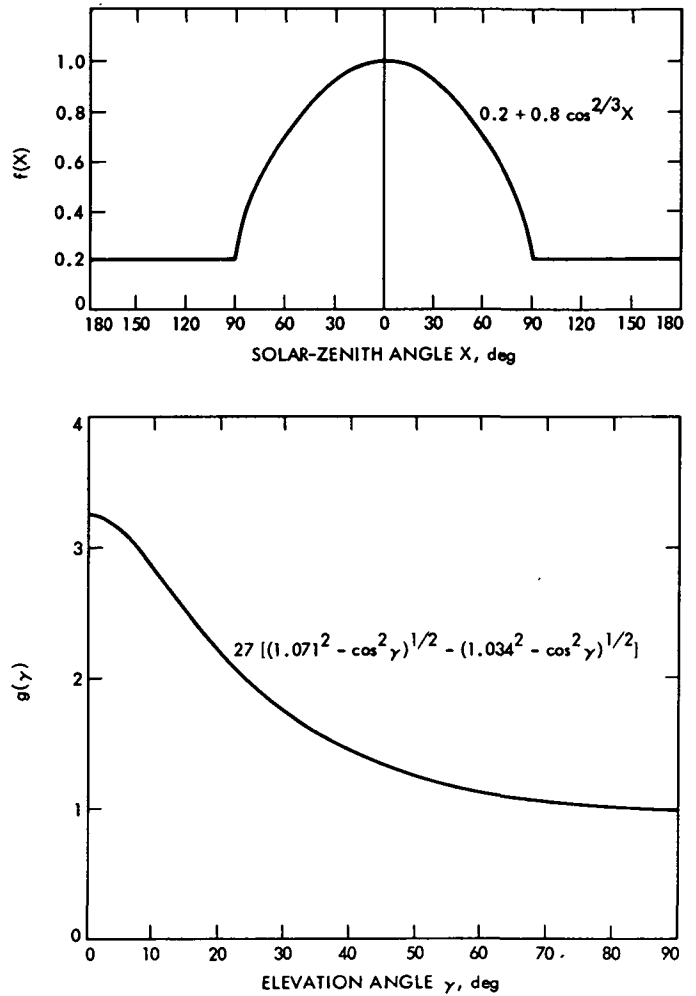


Fig. 2. Solar-zenith angle factor and elevation angle factor for ionospheric delay errors

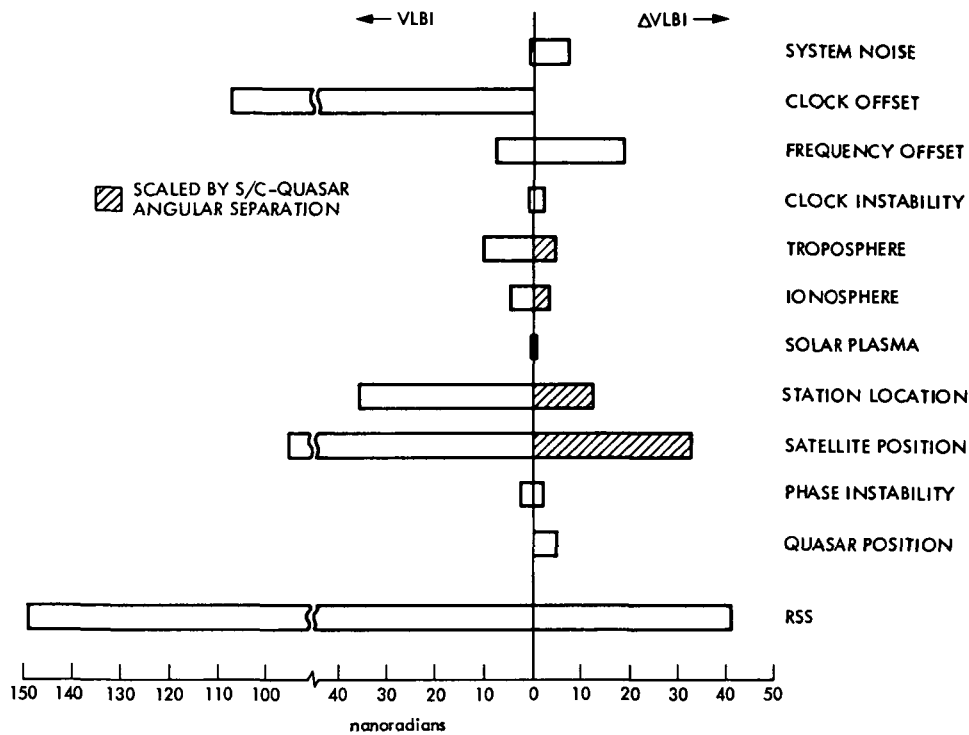


Fig. 3. Angle measurement errors from S/C-only VLBI and S/C-quasar Δ VLBI

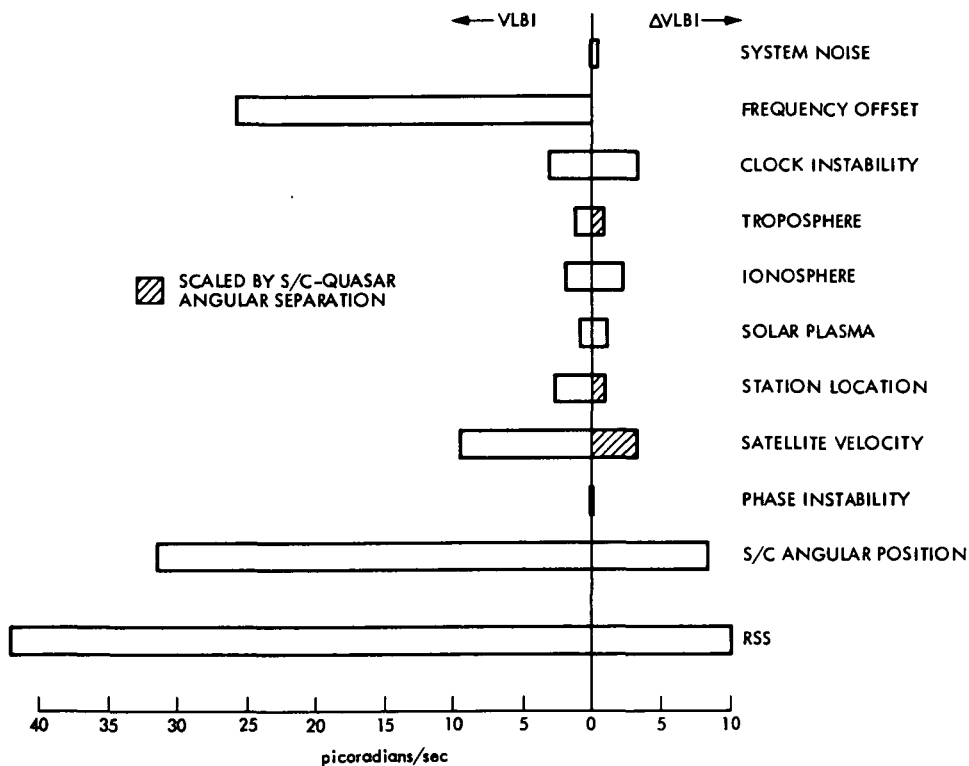


Fig. 4. Angle rate measurement errors from S/C-only VLBI and S/C-quasar Δ VLBI

DSN Monitor and Control System Mark III-82

G. L. Spradlin
TDA Engineering Office

A description of the DSN Monitor and Control System, Mark III-82 is presented. The major implementations required to evolve from the Mark III-80 to the Mark III-82 configuration are identified.

I. Introduction

The DSN Monitor and Control System, Mark III-82, is a multimission system utilized by the DSN to support Pioneers 6-11, Helios, Viking, Pioneer Venus, and Voyager missions. Figure 1 provides a block diagram of the DSN Monitor and Control System, Mark III-82 configuration.

Since 1980, implementation of equipment and software changes within the DSN facilities has resulted in enhanced capability within the DSN Monitor and Control System. The affected facilities are the Deep Space Stations and the Network Operations Control Center.

At the Deep Space Stations (DSS) a TDS Stand-Alone Host Processor has been implemented. Included are software ("host" software) changes which provide downline loading to the Stand-Alone Host Processor from a disc unit of any idle data system computer.

In the NOCC, changes have been made to functionally combine the elements of the NOCC Monitor and Control Subsystem (NMC) with the Display Subsystem that in effect redefines the NMC to include the man/machine interface for network operations. Some software and hardware modifications have also been accomplished.

II. Deep Space Station

As part of the DSN Monitor and Control System, the DSS Monitor and Control Subsystem (DMC) provides two primary functions: (1) The DMC provides the central control monitor capability for the DSS, and (2) the DMC receives control data from and furnishes monitor data to the NOCC for network control and monitor purposes.

There are four major assemblies of the DMC that accomplish the above functions. The four major elements are:

- (1) Digital Instrumentation Subsystem (DIS).
- (2) Stand-Alone Host Processor.
- (3) Station Monitor and Control Console.
- (4) Data System Terminal.

A. Digital Instrumentation Subsystem (DIS)

The DIS, (an XDS 920 computer) is utilized as a central collection point for station monitor data and for interfacing with the NOCC. For collecting station monitor data, the DIS has interfaces with all of the station subsystems. The station monitor data are accumulated by the DIS and displayed to the station operator located at the Station Monitor and Control

Console. Additionally, a subset of this station monitor data is sent to the NOCC for central monitoring purposes. New implementation within the DIS was limited to replacement of obsolete and hard-to-repair line printers. These printers are used to provide control data to the stations (e.g., predictions, sequence of events, and schedule data).

B. Stand-Alone Host Processor Assembly (SHP)

The SHP, which consists mainly of the Modcomp 7810 classic computer, has been installed in the DIS Monitor Interface Assembly (DMI) cabinet at all Deep Space Stations for the Mark III-82 configuration. Previously, the host software operated concurrently with the communications program in the Communications Monitor and Formatter Assembly (CMF). The SHP was implemented to remove constraints which arose from the use of the CMF to support data recalls and system performance tests. The SHP provides the interface for centralized operation of DSS data system computers.

The operational program is downline loaded using a disc drive of an idle data system computer (either the Command Processor Assembly, Metric Data Assembly, Communications Monitor and Formatter Assembly or Telemetry Processor Assembly). The SHP is interfaced to the data system computers via a Star Switch Controller (SSC) and operates in an unattended manner in conjunction with the Data System Terminal.

C. Station Monitor and Control Console (SMC IIA, SMC IIB)

The SMC IIA and SMC IIB were implemented for the purpose of providing a central monitor and control operator's position for some of the noncomputerized subsystems. Two different configurations, designated SMC IIA for the 64 m DSS and SMC IIB for all others, were developed for the DSN.

D. Data System Terminal Assembly (DST)

The DST is used as a central DSS input-output device for computers in the Command, Telemetry, Tracking, and Radio Science Subsystems, and for the Communications Monitor Formatter at the DSS. It consists of four elements: two keyboard-CRTs, a hardcopy printer, and "host" software capability. The keyboard-CRTs and printers interface with the host software, and the host software then interfaces with all of the data system computers via the Star Switch Controller. In this manner, the data system computers can be centrally controlled and monitored. The DST and the Station Monitor and Control console are collocated within the DSS control room and form a centralized operator position for monitor and control.

III. Network Operations Control Center (NOCC)

The NOCC Monitor and Control Subsystem (NMC) was re-defined to include all elements of what was formerly called the Display Subsystem. These elements, consisting of Digital Display Processor (DDP, a Modcomp II computer) and the Video Assembly Processor (VAP, a Modcomp II computer), are now referred to as the Display Group, and are functionally part of the NMC. In addition to the elements mentioned above, the NMC includes a Real-Time Monitor (also a Modcomp II computer with peripheral I/O devices).

The NMCs' primary functions are to provide overall network status, configuration, and performance visibility to the Network Operations Control Team. It provides the man/machine interface for displays and for operator controls. Recent modifications to the NMC have been in the area of the Display Group and include additional operational control terminals and display printers and software modifications to eliminate coupling between the Display Group and other NOCC Subsystems that has historically resulted in unnecessary complexity in software change implementation.

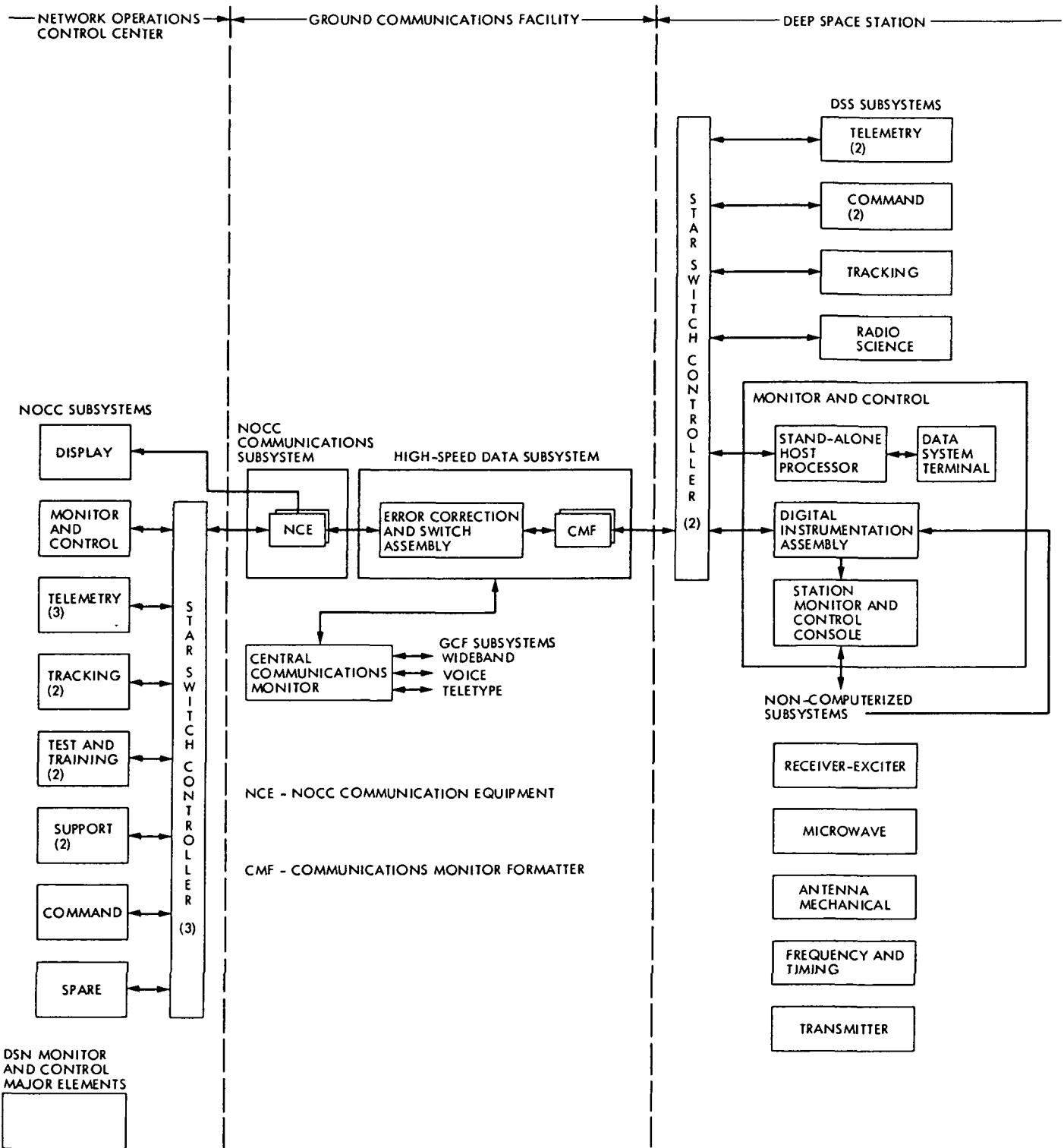


Fig. 1. DSN monitor and control system, Mark III-82

Improved Downlink Frequency Calculations for Voyager 2

A. L. Ricardo

Canberra Deep Space Communications Complex, Tidbinbilla

Voyager 2 and her sister ship Voyager 1 were launched, respectively, in August and September 1977. The object of these spacecraft was to conduct exploratory investigations of the Jupiter and Saturn planetary systems and the interplanetary medium between Earth and Saturn. In April 1978 the Voyager 2 redundant receiver and the loop capacitor in the prime spacecraft receiver failed, leaving the Voyager Project with a major problem: how to communicate with the spacecraft and get the data back.

I. Introduction

When Voyager 2 was launched on its modified Grand Tour of our Solar System, no one expected a spacecraft receiver failure in the phase locked loop (PLL) loop capacitor. A procedure to protect the loop capacitor on Voyager 1 has been developed and is working extremely well.

With Voyager 2's reduced receiver bandwidth (± 100 Hz) special procedures were developed to communicate with the spacecraft. At about the same time a procedure with limitations was developed to calculate the closed-loop voltage controlled oscillator (VCO) frequencies for the receivers of the Deep Space Stations. The method had an uncertainty term of ± 30 Hz due to uncertainties in the uplink.

Having been involved with both the Jupiter and Saturn Encounters, it seemed strange to personnel at DSS 43 that closed-loop receiver frequencies could not be calculated more accurately.

Prior to Voyager 2 Saturn Encounter a simple program was produced to calculate receiver ramps to maintain the receiver

static phase error at zero in the closed-loop receivers. The ramps were maintained throughout the entire occultation of the planet and allowed the receivers to be locked up quickly at exit occultation of the planet.

After Saturn Encounter serious thought was given to the possibility of improving the downlink lockup calculation accuracy.

II. Normal Operation

The system now in operation has no uncertainty terms as had the previous method, the only uncertainty now being the accuracy of the doppler predicts.

First, consider a spacecraft with a good loop capacitor (see Fig. 1). At the start of the uplink, and subsequent two-way downlink, the uplink is tuned to gain lock on the spacecraft receiver. It is then tuned to what is known as the track synthesizer frequency (TSF), where the exciter remains for the duration of the pass. One round-trip light time (RTLT) later the

DSS receivers drop lock. The signal is reacquired in a coherent mode (two-way) using two-way doppler (D2).

The basic equation for a two-way S-band signal is

$$Frs = 240/221 (48 \times TSF) \pm (D2 - 1 \times 10^6)$$

III. Voyager 2

Now look at Voyager 2. As a result of the receiver problem it is necessary to continuously tune the uplink to cancel out the doppler on the uplink, thus maintaining lock on the spacecraft receiver. With no apparent doppler in the uplink and the spacecraft appearing to see a constant frequency, we are left with a downlink that appears to have one-way characteristics. Take a snapshot at any point in time, at the uplink, follow it from the DSS to the spacecraft and back to Earth and it is not the case at all (see Fig. 2).

IV. Two-Way Acquisition

Consider a practical example. At 052506Z on day 246 the exciter is at a frequency of 44029327.082 Hz. This frequency is multiplied up to an S-band frequency to be radiated to the spacecraft. On the way it is frequency shifted by doppler. Upon reaching the spacecraft it is upconverted by the ratio 240/221 and retransmitted by the spacecraft as a coherent signal. After doppler shifting on the return, it reaches an Earth station as a two-way signal. Therefore, to calculate a correct DSS receiver frequency for two-way acquisition we need the following:

Exciter frequency one RTLT earlier = $XA0$

Two-way doppler from predicts = $D2$

Therefore the S-band equation is

$$Frs = 240/221 (48 \times XA0) \pm (D2 - 1 \times 10^6)$$

This gives the exact frequency for calculating VCO values for the DSS receivers.

V. Three-Way Acquisition

Next came the consideration of three-way acquisitions, and could the exciter ramp predicts as generated at JPL be extended back in time beyond the upcoming stations' rise times to a point one RTLT earlier. Jim Hodder and Steve Wissler of the Network Analysis Team at JPL carried out tests and determined that this method was not valid.

The next alternative was to have the three-way station ramp and doppler predicts sent to the upcoming station. The doppler predicts were of no value. However, using the three-way doppler from the upcoming station doppler predicts and the three-way station ramps, and converting the ramps to the local station theoretical ramps, accurate receiver lock frequencies were calculated. To achieve this required the following (see Fig. 3):

Three-way station $TSF = TSF3$

Local stations $TSF = TSF1$

Three-way station ramp predicts back one RTLT = $XA3$

Three-way doppler from predicts = $D3$

The equation is

$$Frs = 240/221 (48 \times [(TSF1 - TSF3) + XA3]) \pm (D3 - 1 \times 10^6)$$

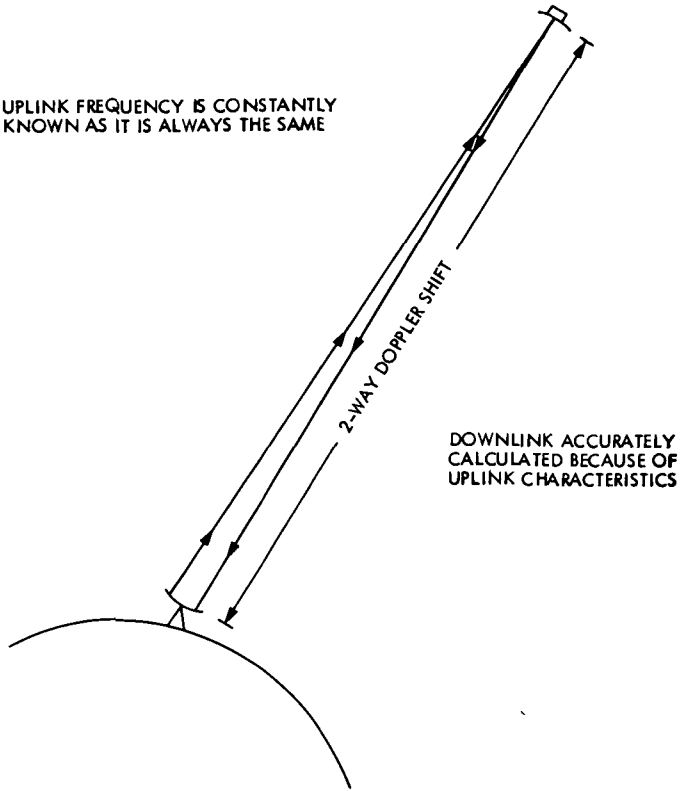
A calculator program suitable for use on Hewlett-Packard HP-9810A calculators has been produced which converts the ramp predicts to their two- or three-way times. The calculator output spaces the results on 10-minute centers. Times in between are simply interpolated.

VI. Conclusion

The method described is not as important at a 64-meter station, with a Spectral Signal Indicator, as it is at a 34-meter station. Since there is no Spectral Signal Indicator, there is no signal visibility. As we move deeper into space and a Uranus Encounter with lower signal levels it will allow speedier lock of receivers and greater data gathering during near encounter phases.

ORIGINAL PAGE IS
OF POOR QUALITY

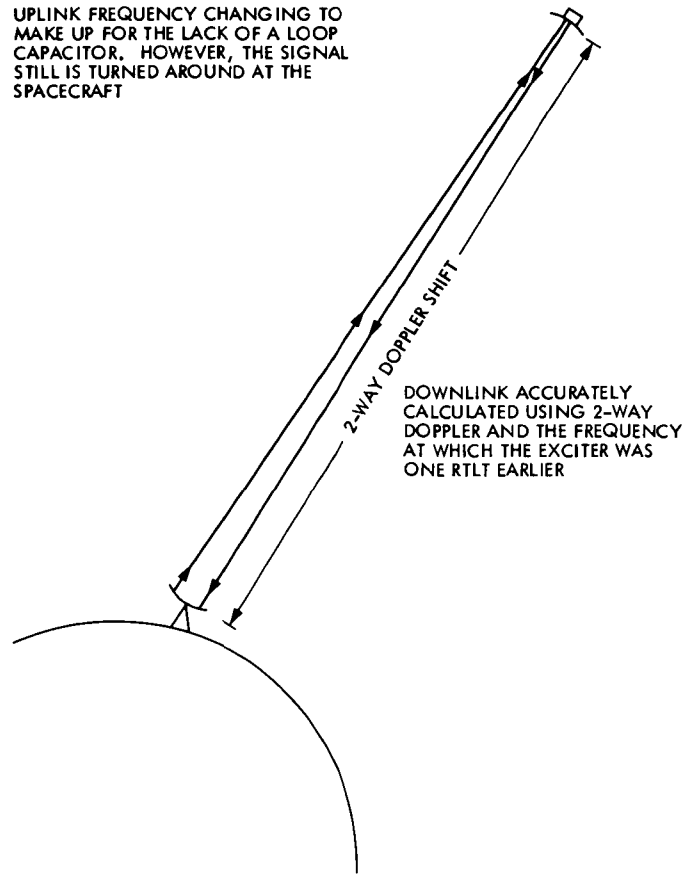
UPLINK FREQUENCY IS CONSTANTLY
KNOWN AS IT IS ALWAYS THE SAME



DOWNLINK ACCURATELY
CALCULATED BECAUSE OF
UPLINK CHARACTERISTICS

Fig. 1. Conventional spacecraft with good loop capacitor

UPLINK FREQUENCY CHANGING TO
MAKE UP FOR THE LACK OF A LOOP
CAPACITOR. HOWEVER, THE SIGNAL
STILL IS TURNED AROUND AT THE
SPACECRAFT



DOWNLINK ACCURATELY
CALCULATED USING 2-WAY
DOPPLER AND THE FREQUENCY
AT WHICH THE EXCITER WAS
ONE RTLT EARLIER

Fig. 2. Voyager 2 with no loop capacitor

ORIGINAL PAGE IS
OF POOR QUALITY

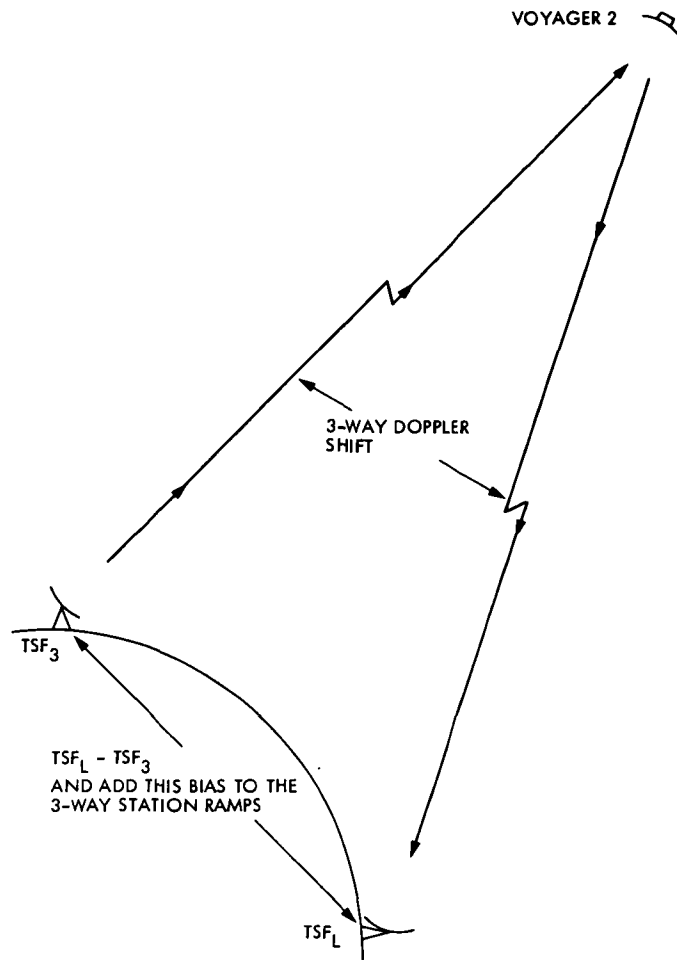


Fig. 3. Voyager 2 three-way acquisition

D5

N83 14328

The Performance of VLA as a Telemetry Receiver for Voyager Planetary Encounters

L. J. Deutsch

Communications Systems Research Section

The Very Large Array (VLA) has been proposed for use as a supplement to the Deep Space Network (DSN) for telemetry reception at Voyager 2 Uranus and Neptune encounters. The main problem with the use of VLA for telemetry is that it is not capable of producing a continuous stream of data. Gaps of one millisecond follow every 51 milliseconds of data. This report investigates the effect of these millisecond gaps on coded telemetry. An ungapped system of the same aperture as the VLA would be capable of handling data rates of 38.4 kbps at Uranus encounter and 19.2 kbps at Neptune encounter. It is shown here that VLA with (7, 1/2) convolutional coding (the baseline coding scheme for Voyager) will support a data rate of 10.8 kbps but not 19.2 kbps at both Uranus and Neptune. It is also shown that by implementing Voyager's concatenated Reed-Solomon/convolutional coding capability, data rates of 38.4 kbps and 19.2 kbps would be achievable at Uranus and Neptune respectively. Concatenation also offers a factor of 2 improvement in overall throughput.

I. Introduction

As Voyager 2 journeys toward Uranus and Neptune, a need for an increased telemetry receiving capability is arising. One way of increasing this capability is to increase the effective aperture of the DSN receiving sites. More antennas could be built or existing ones enlarged for use in antenna arrays. These efforts are expensive and time consuming. Even so, some additions and enlargements are planned before the 1986 encounter at Uranus (Ref. 1). Another way to increase telemetry reception capability is to use non-DSN facilities. These sites could be used independently or in arrays with DSN stations.

One of the prime candidate non-DSN facilities that is being considered for Voyager encounter enhancement is the Very Large Array (VLA) (Ref. 2). The VLA is a phased array consisting of 27 independently pointable parabolic dishes in the

New Mexico desert. Each dish measures 25 meters in diameter. The array is configured in three linear arrays of nine antennas each that radiate from a common center point. The antennas may be moved along these lines by means of railroad-type tracks. Communication between the antennas and the central processing site is by means of a connecting network of waveguides. The total aperture of the VLA is about twice that of a DSN array consisting of a 64-m antenna and three 34-m antennas. The VLA was designed for use as a radio astronomy observatory. Some additional front-end hardware will be needed in order for the VLA to receive the X-band Voyager telemetry transmissions.

The main problem with using the VLA as a telemetry receiver is that signals are not transmitted continuously from the antennas to the processing facility. Instead, the VLA has a duty cycle which consists of 51 ms of data gathering followed by a 1-ms calibration and control period. During these

1-ms intervals, which will be called "gaps," no data is gathered.

If uncoded telemetry data were received by the VLA, then, for data rates over a few thousand bits per second, the best possible bit error rate would be $(1/2)(1/52) = 0.95 \times 10^{-2}$. Coding must be used in order to achieve bit error rates below the 5×10^{-3} level required for good image quality. In this report it is shown that the use of the Viterbi-decoded (7, 1/2) convolutional code would allow the VLA to receive at a data rate of 10.8 kbps at both Uranus and Neptune encounters. It would not, however, support a data rate of 19.2 kbps at either encounter. It is further shown that the data rate can be improved by concatenating the (255, 233) Reed-Solomon code with the (7, 1/2) convolutional code. Such coding would allow the VLA to support a data rate of 38.4 kbps at Uranus and 19.2 kbps at Neptune. The reason for the improvement is that the Reed-Solomon code tends to correct the burst errors caused by the gaps. In terms of throughput (bits per day received at an acceptable average bit error rate), concatenated coding used in conjunction with source data compression provides for about a 100% increase over convolutional coding alone.

II. Mathematical Model of VLA Coded Performance

The performance of convolutional codes has always been difficult to model analytically. This is mainly due to the complex nature of the Viterbi decoding process. It is well known that when a Viterbi decoder makes a decoding error due to excessive channel noise, it has a tendency to produce a burst of decoded bit errors (Ref. 3). This is due to the fact that the Viterbi decoder is a multistate machine with a trellis structure that interconnects the states (Ref. 4). Each state corresponds to a possible sequence of decoded bits. A decoding error occurs when the decoder is in a state that corresponds to a sequence other than the one that was transmitted. Even if the channel bit signal-energy-to-noise-spectral-density ratio (E_b/N_0) is infinite from that time forward, it will still take the decoder several bit times, on average, to wander through the trellis from state to state until it returns to the correct one. During this period of wandering, a burst of errors occurs.

In the case that E_b/N_0 is infinite except during the gaps, an analysis can be performed. Suppose a convolutional code with constraint length k is used. Prior to encountering a gap, the Viterbi decoder always decodes correctly. During the gap, only noise is input to the decoder. Since received channel symbols are determined uniquely by the current data bit and the $k - 1$ previous data bits, no information is known about the bits in the gap with the exception of the final $k - 1$ bits. The decoder can correct these bits. This reasoning leads

to the following formula for the performance of Viterbi decoding in the presence of a periodically gapped channel and in the limit of high channel SNR.

$$P_b = 0.5 (R_b T_2 - k + 1) / [R_b (T_1 + T_2)] \quad (1)$$

In (1), R_b is data rate in bits per second, T_1 is the time in seconds spent in that portion of the cycle representing a perfect channel, and T_2 is the time in seconds spent in each gap. It is assumed that R_b is large enough so that the gaps are at least k bits long. A graph of P_b as a function of R_b for $T_1 = 51$ ms, $T_2 = 1$ ms, and $k = 7$ is shown in Fig. 1. This represents the best possible performance of the VLA with Viterbi-decoded (7, 1/2) convolutional coding. It is important to notice that even in the case of infinite channel SNR and with no other system losses, the VLA can support a data rate of at most 13.0 kbps at a bit error rate of $P_b = 5 \times 10^{-3}$.

For now, the only practical way to determine the performance of the VLA at finite channel SNRs and arrayed with other sites is through the use of simulations. The software simulations that were used in this study are described in the next section.

III. Software Simulations of VLA Performance

The starting point for the simulation software for this investigation was the software Viterbi decoder that was used in the studies of Viterbi decoder burst statistics and concatenated code performance (Refs. 3, 5, 6). This decoder is a modified version of a program written by J. W. Layland. The inputs to the program are the parameters of the convolutional code to be simulated, the channel E_b/N_0 , and the length of the simulation in terms of the number of bits to be processed. Any convolutional code of constraint length up to 12 and rate 1/2, 1/3, or 1/4 may be simulated. The software decoder assumes a 4-bit quantized input and has a path memory of 64 bits. It should be noted that the performance advantage of 4-bit quantization over the 3-bit quantization used by the DSN is negligible (Ref. 7). The outputs of the simulation include the Viterbi-decoded bit error probability, the error rate for 8-bit Reed-Solomon symbols (see Section IV), and various statistics concerning burst errors. A 90% confidence interval for the output error rates is also calculated. It should be noted that the software Viterbi decoder always maintains perfect node synchronization (for a discussion of node synchronization, Ref. 8). Also, no system losses other than the Gaussian noise of the channel are simulated.

For the purposes of this study, the software Viterbi decoder was modified so that the E_b/N_0 of the channel could be

changed periodically in order to simulate the gaps in VLA data reception. For example, simulation of the VLA system at a data rate of 19.2 kbps was achieved by alternating E_b/N_0 between one value for 979 bits and -9.99 dB for 19 bits. The output of the software decoder at the latter SNR is random to within the accuracy of the simulation.

Four scenarios were simulated in this fashion. For each of these, simulations were performed at three data rates that are typical of those that might be implemented for Voyager in conjunction with VLA telemetry reception (10.8, 19.2, and 38.4 kbps). These scenarios are as follows:

- (1) *Ideal performance.* In this scenario, it was assumed that no gaps were present in the data. This represents a best-possible case and it can be used to measure the magnitude of losses that occur in the other scenarios.
- (2) *Normal VLA.* This scenario represents the VLA as described in the introduction. The gaps are assumed to be periods of time where the channel E_b/N_0 is arbitrarily small. As was remarked above, an SNR of -9.99 dB was actually used for the gaps.
- (3) *VLA arrayed with an equal aperture.* The gaps in this scenario are 3.0 dB lower in E_b/N_0 than the rest of the data. Since there is no complex anywhere near the VLA of a comparable aperture, this scenario is best interpreted as arraying half of the VLA with the Goldstone DSN complex. The arraying is assumed to be perfect combined carrier referencing (CCR). Two different methods for achieving near ideal CCR performance have been described in Refs. 9 and 10.
- (4) *Rotated gaps.* In this scenario, the VLA is assumed to be reconfigured so that the three arms receive the 1-ms calibration signal at three different, equally spaced times. Each arm still has the same 51-ms/1-ms duty cycle. This is equivalent to a system with 1-ms periods of 1.76-dB signal attenuation every 17-1/3 ms.

For the purposes of displaying the results of the simulations, E_b/N_0 , refers to the bit SNR of the channel during the 51-ms periods of good reception whenever it appears in the figures.

Each scenario was simulated over a range of SNRs from 0.0 to 4.0 dB in 0.25-dB increments. At each SNR, one million bits of data were simulated for each data rate. The results of the simulations are shown graphically in Figs. 2 through 5. The asymptotes that appear in Fig. 3 agree with the performance that was predicted by Eq. (1) for high SNRs. Also, the burst statistics produced by these simulations corroborates the theory outlined in Section II. Notice that scenarios

3 and 4 both allow the VLA to support data rates higher than 10.8 kbps. In fact, arbitrarily high data rates can be supported provided the channel SNR is high enough. This is in contrast to scenario 2.

IV. Concatenated Coding

It was shown in section III that even at bit SNRs as high as 4 dB, the VLA as presently configured will not support a data rate of 19.2 kbps with only Viterbi-decoded (7, 1/2) convolutional coding. One way to improve this performance is to use Voyager's capability for a concatenated coded downlink. The Voyager project has the option of adding a (255, 223) Reed-Solomon code to the telemetry downlink coding system. This code would be the outer code, with the (7, 1/2) convolutional code being the inner code. The advantage to this concatenated scheme comes from the fact that the Reed-Solomon code has the ability to correct many errors provided that they occur in bursts. It was already remarked in section II that the errors produced by Viterbi decoding tend to be burst errors. Also, a gap may be considered to be a burst error.

A Reed-Solomon code is, in general, a nonbinary code. The role of the bit is played by the Reed-Solomon symbol. The (255, 223) code can correct up to 16 symbol errors in each 255-symbol codeword. Since each symbol is 8 bits long, a symbol error could represent a burst of errors from the inner convolutional code. If one assumes that symbol errors occur independently, then the bit error probability of the concatenated channel, without gaps, is given by (Refs. 5, 11),

$$P_{cb} = \frac{p}{\pi} \sum_{i=17}^{255} \binom{i}{255} \binom{255}{i} \pi^i (1-\pi)^{255-i} \quad (2)$$

where p is the bit error rate of the Viterbi decoder, and π is the average error rate for a Reed-Solomon symbol. Since both p and π are calculated in the software simulations described in section III, P_{cb} may be calculated in this case of independent symbol errors.

The Reed-Solomon symbols produced by Voyager will be interleaved to a depth of four before being convolutionally encoded, modulated, and transmitted. This means that since Viterbi decoder burst errors of 32 bits or more are unlikely (Ref. 5), the symbol errors produced by the Viterbi decoder will be very nearly independent. The effect of the gaps is to introduce a certain number of symbol errors in known positions in the data stream. For all the data rates that were investigated, these errors are uniformly distributed over the four levels of interleaving. This means that no Reed-Solomon codeword will receive an inordinate number of symbol errors

caused by gaps. Each Reed-Solomon codeword would be corrupted by no more than 6 symbol errors from the gaps. Since the Reed-Solomon code can correct this number of symbol errors, the asymptotic behavior of scenario 2 would be corrected by using concatenated coding. It should also be noted that a further, as yet undetermined, performance gain can be achieved by flagging the symbols that occur during gaps as erasures. The (255, 223) Reed-Solomon code can correct E errors and e erasures as long as $2E + e \leq 32$. Such an erasure handling decoder would have to be built to take advantage of this gain.

Graphs of P_{cb} for the four scenarios of section III are shown in Figs. 6 through 9. These were graphed using Eq. (2) and so, by the above remarks, should be viewed as an upper bound on the actual expected error rate, with the exception of the ideal reception case (scenario 1).

Some additional facts concerning concatenated coding should be mentioned at this point. The motivation for using concatenated coding in a mission like Voyager is to be able to achieve very low overall bit error rates at a lower SNR than convolutional coding alone. This is important if one is to implement source data compression. In source data compression, the number of bits needed to represent a Voyager image at Uranus and Neptune encounters will be reduced, through source coding techniques, by a factor of 2.5 (Ref. 12). Since the bits to be transmitted are less redundant, a compressed image is more vulnerable to channel bit errors than an uncompressed image. Concatenated coding allows source data compression to work by providing the low bit error rates required. A bit error rate of 10^{-5} is considered necessary for data compression. In comparing the performance of the VLA with and without Reed-Solomon coding, one must take into account the 255/223 overhead of the code, the factor of 2.5 in data throughput, and the lower bit error rate required for concatenated coding. This will be explained further in the following section.

V. VLA Throughput at Voyager Encounters

The most reasonable measure of performance for a telemetry receiving system such as the VLA is the amount of data throughput that it is capable of handling. The particular measure of throughput used in this study is the number of "good bits per day." During each day of an encounter, Voyager will be "visible" from the VLA for some number of hours. Depending on the data rate and coding that are implemented, only a fraction of this viewing time may support reception at the required bit error rate or better. This is due to the fact that received power is a function of the elevation angle of the antennas.

The raw data used in this section comes from design control tables for Voyager 2 Uranus encounter. The curve shown in Fig. 10 represents the total-power-to-noise-spectral-density ratio (P_T/N_0) that is expected to be incident on a three-element array at the Goldstone complex on day 34 of 1986 (Uranus encounter). This curve includes a 90% weather confidence level and the effects of antenna elevation angle. Since the VLA is at approximately the same latitude as Goldstone, the values of P_T/N_0 for the VLA at Uranus encounter were derived from these simply by scaling them up by the ratio of the apertures involved. For Neptune, 3.5 dB was subtracted to account for the additional space loss. It was assumed that the maximum viewing time is 8.3 hours.

For each data rate and scenario described in sections III and IV, the P_T/N_0 required for a bit error rate of 5×10^{-3} (for convolutional coding only) or 1×10^{-5} (for concatenated coding) was calculated from the corresponding E_b/N_0 given by Figs. 2 through 9. For convolutional coding,

$$P_T/N_0 = (E_b/N_0) \times R_b / \sin^2 \theta \quad (3)$$

and for concatenated coding,

$$P_T/N_0 = (223/255) (E_b/N_0) \times R_b / \sin^2 \theta. \quad (4)$$

The data rate R_b is the number of bits per second processed by the Viterbi decoder – hence the need for the factor 223/255 in Eq. (4). Modulation indices of $\theta = 76^\circ$ for Uranus and $\theta = 70^\circ$ for Neptune were assumed for this study. These insure that the carrier loop SNRs are at least 15 dB (see section VI). The length of time that the VLA can receive at the required bit error rate for each scenario was then calculated by observing how long the P_T/N_0 incident on the VLA is at least as high as that given by (3) or (4). Call this time T_0 . In the case of convolutional coding alone, the throughput of the system in terms of the number of good bits per day is given by

$$B = T_0 R_b. \quad (5)$$

In the case of concatenated coding, the throughput of the system is given by

$$B = 2.5 \times (223/255) \times T_0 R_b \quad (6)$$

where the factor of 223/255 is due to the Reed-Solomon coding overhead, the factor of 2.5 is due to the source data compression, and R_b is, again, the data rate of the inner convolutional channel.

Figures 11 and 12 show the expected number of good bits per day for the VLA at Uranus and Neptune encounters respectively. The four scenarios of section III are represented with scenario 2 (normal VLA) shown for 1/2 VLA aperture as well as full aperture. These histograms show clearly that the VLA, as presently configured, can support a convolutional-only channel at a rate of 10.8 kbps but not 19.2 kbps. Concatenated coding allows the VLA to be used at rates of 38.4 kbps at Uranus encounter and 19.2 kbps at Neptune encounter. Also, concatenated throughput is about twice that of the convolutional-only channel. Performance can also be improved by arraying the VLA with Goldstone or rotating the gaps.

VI. Other Degradations

Up to this point, the only degradations that were modeled or simulated were the space loss, the thermal noise in the receivers, and the gaps. Other sources of degradation may include radio loss (noisy carrier reference), imperfect sub-carrier tracking, imperfect symbol tracking, Viterbi decoder node synchronization losses, and Reed-Solomon frame synchronization losses.

The carrier margin, or the SNR in the design point bandwidth of the carrier tracking loop, is given by

$$m = (P_T/N_0) \cos^2 \theta / 2 B_{L0}$$

where B_{L0} is the two-sided threshold carrier loop bandwidth. For Block IV receivers, a typical value would be $B_{L0} = 15$ Hz. Average values of P_T/N_0 for the VLA at Uranus and Neptune encounters will be, according to section V, 47.5 and 44.0 dB respectively. For the assumed modulation indices of 76° and 70° , these lead to carrier margins of 20.4 and 19.9 dB. The loop SNR in the receiver, which is a function of the carrier margin (Ref. 13), will hence be 15.9 dB at Uranus and 15.5 dB at Neptune. These are high enough so that the carrier tracking loops will acquire on their own and cycle slip losses will be negligible. However, some radio loss will be evident.

The effects of a noisy carrier reference on the performance of the VLA were computed using the modified high rate model in Ref. 8. Figure 13 is an example of the results. It represents the normal VLA scenario at 10.8 kbps and various loop SNRs. It can be seen that the radio loss to be expected at the Voyager encounters is about 0.1 dB. Preliminary results on modeling the concatenated link with noisy carrier referencing show that the radio loss should be less than for convolutional coding alone.

The radio losses above were computed assuming a Viterbi decoder node synchronization threshold of 0.0 dB. They will

be about twice as large for a threshold of 2.0 dB. It is expected, however, that the threshold can be reduced in time for the Voyager encounters.

It was assumed, for this study, that carrier synchronization is maintained through the gaps. It was also assumed that the Subcarrier Demodulation Assembly (SDA) and the Symbol Synchronizer Assembly (SSA) perform perfectly. In general, losses occurring in the SDA and SSA are minimal compared to the radio loss. In the case of gapped reception, however, there could be additional losses due to timing inaccuracies.

One other "loss" that should be mentioned is that the DSN Viterbi decoder (MCD) performs about 0.2 dB worse than the software decoder used in this study, according to the DSN/Flight Project Interface Design Book (JPL Document 810-5). The origin of this discrepancy is not understood by the author. As remarked in section III, there is no significant difference in performance between the 3-bit quantization used in the hardware and the 4-bit in the software. A mission planner may choose to include this 0.2 dB loss in making predictions.

VII. Conclusions

The results of this study show that the VLA can be considered a viable telemetry receiving station for Voyager 2 Uranus and Neptune encounters. The problem of the 1-ms gaps can be solved in one of three ways. First, the VLA can be arrayed with a second site (such as the Goldstone complex) that does not exhibit this gapped behavior. Second, the VLA could be reconfigured so that the gaps occur at different times in each of the three arms. Third, concatenated coding may be implemented. These improvements each offer the capability of supporting data rates of 38.4 kbps at Uranus encounter and 19.2 kbps at Neptune encounter. The VLA, as presently configured and with convolutional coding alone, can support 10.8 kbps at each encounter but even with infinite SNR it can support only 13.0 kbps.

Concatenated coding is particularly attractive since, in addition to enabling the VLA to support higher data rates, it also offers a factor of 2 improvement in data throughput over arraying or reconfiguring. This is due to the fact that concatenated coding provides bit-error rates low enough to support the use of source data compression.

It is suggested that, before the VLA is actually used for this purpose, hardware simulations be performed in a facility such as the Telecommunications Development Laboratory (TDL) of JPL. The TDL channel simulator can be modified to mimic the gapped behavior of the VLA. In this way, the effect of gapped reception on the various DSN subsystems can be directly measured.

Acknowledgment

The author wishes to thank Jim Layland, who requested that this study be undertaken and provided essential background material for it. Jim also wrote the original Viterbi decoder software on which the simulations for this study are based.

References

1. Yeater, M. L., Herrman, D. T., and Sanner, G. E., "Networks Consolidation Program," *TDA Progress Report 42-59*, Jet Propulsion Laboratory, Pasadena, Calif., Oct. 15, 1980.
2. Thompson, A. R., Clark, B. G., Wade, C. M., and Napier, N. P., "The Very Large Array," *The Astronomical Journal Supplement Series of the American Astronomical Society*, Vol. 44, 151-167, Oct. 1980.
3. Deutsch, L. J., and Miller, R. L., "Burst Statistics of Viterbi Decoding," *TDA Progress Report 42-64*, Jet Propulsion Laboratory, Pasadena, Calif., Aug. 15, 1981.
4. McEliece, R. J., *The Theory of Information and Coding*, Addison-Wesley Publishing Co., Reading, Mass., 1977.
5. Butman, S. A., Deutsch, L. J., and Miller, R. L., *On the Error Statistics of Viterbi Decoding and the Performance of Concatenated Codes*, Publication 81-9, Jet Propulsion Laboratory, Pasadena, Calif., Sept. 1, 1981.
6. Miller, R. L., Deutsch, L. J., and Butman, S. A., "Performance of Concatenated Codes for Deep Space Missions," *TDA Progress Report 42-63*, Jet Propulsion Laboratory, Pasadena, Calif., June 15, 1981.
7. Gilhousen, K. S., Heller, J. A., Jacobs, I. M., and Viterbi, A. J., *Coding System Study for High Data Rate Telemetry Links*, NASA CR 114278, Jan. 1971.
8. Deutsch, L. J., and Miller, R. L., "The Effects of Viterbi Decoder Node Synchronization Losses on the Telemetry Receiving System," *TDA Progress Report 42-68*, Jet Propulsion Laboratory, Pasadena, Calif., Apr. 15, 1982.
9. Divsalar, D. D., and Yuen, J. H., "Improved Carrier Tracking Performance with Coupled Phase-Locked Loops," *TDA Progress Report 42-66*, Jet Propulsion Laboratory, Pasadena, Calif., Dec. 15, 1981.
10. Deutsch, L. J., Lipes, R. G., and Miller, R. L., "Virtual Center Arraying," *TDA Progress Report 42-65*, Jet Propulsion Laboratory, Pasadena, Calif., Oct. 15, 1981.
11. Liu, K. Y., and Lee, J. J., *An Experimental Study of the Concatenated Reed-Solomon/Viterbi Channel Coding System and Its Impact on Space Communications*, Publication 81-58, Jet Propulsion Laboratory, Pasadena, Calif., Aug. 15, 1981.
12. Rice, R. F., *Some Practical Universal Noiseless Coding Techniques*, Publication 79-22, Jet Propulsion Laboratory, Pasadena, Calif., Mar 15, 1979.
13. Deutsch, L. J., Miller, R. L., and Butman, S. A., "New Results on Antenna Arraying: Part 1," *TDA Progress Report 42-62*, Jet Propulsion Laboratory, Pasadena, Calif., Apr. 15, 1981.

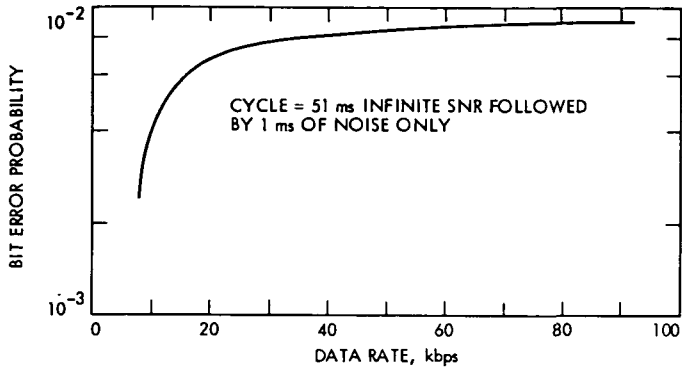


Fig. 1. Theoretical performance of VLA with Viterbi-decoded (7, 1/2) convolutional code at infinite SNR

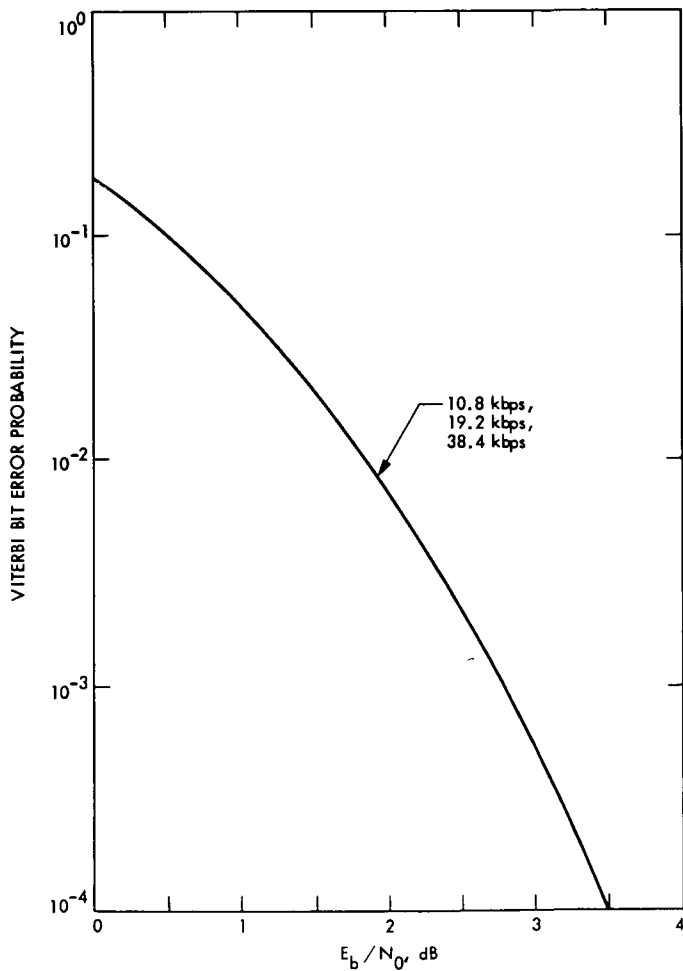


Fig. 2. Simulated performance of an ungapped receiving system, convolutional (7, 1/2) coding only

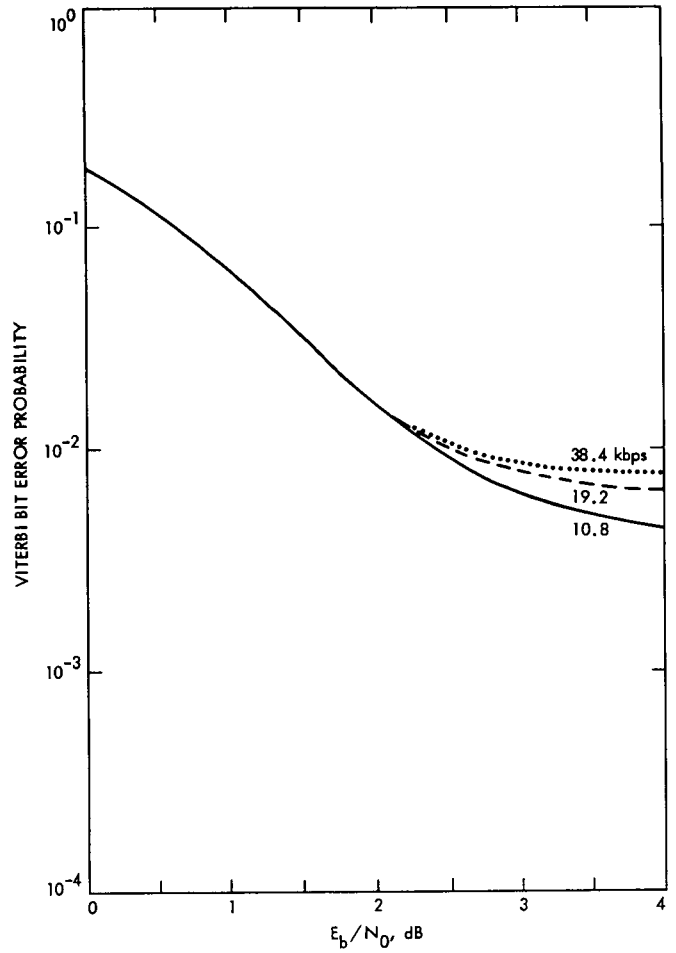


Fig. 3. Simulated performance of VLA with 1-ms gaps with no signal, convolutional (7, 1/2) coding only

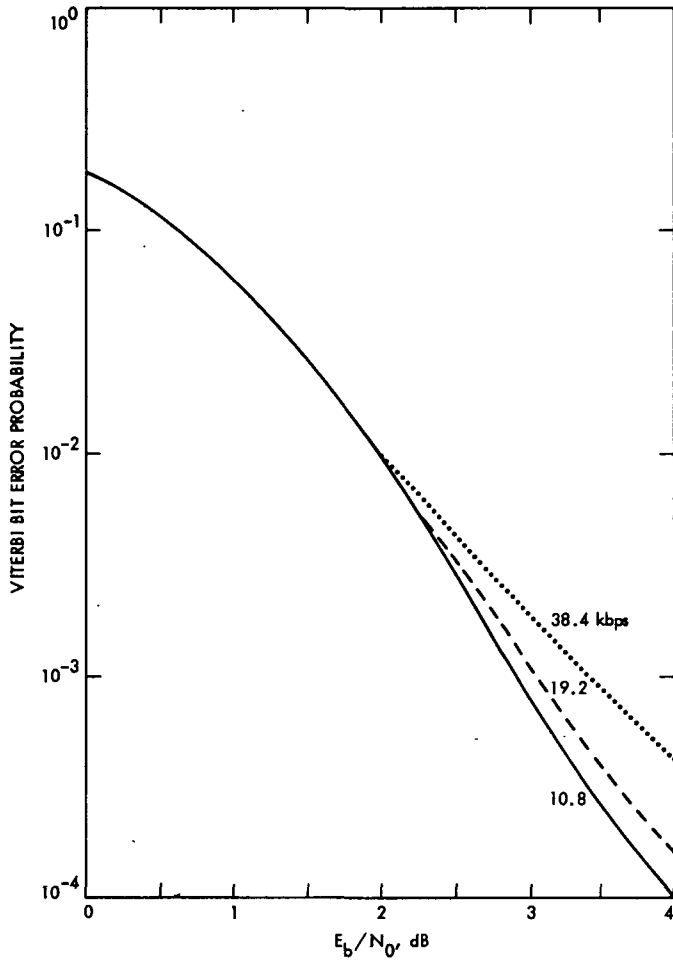


Fig. 4. Simulated performance of VLA with 1-ms gaps attenuated by 3-dB, convolutional (7, 1/2) coding only

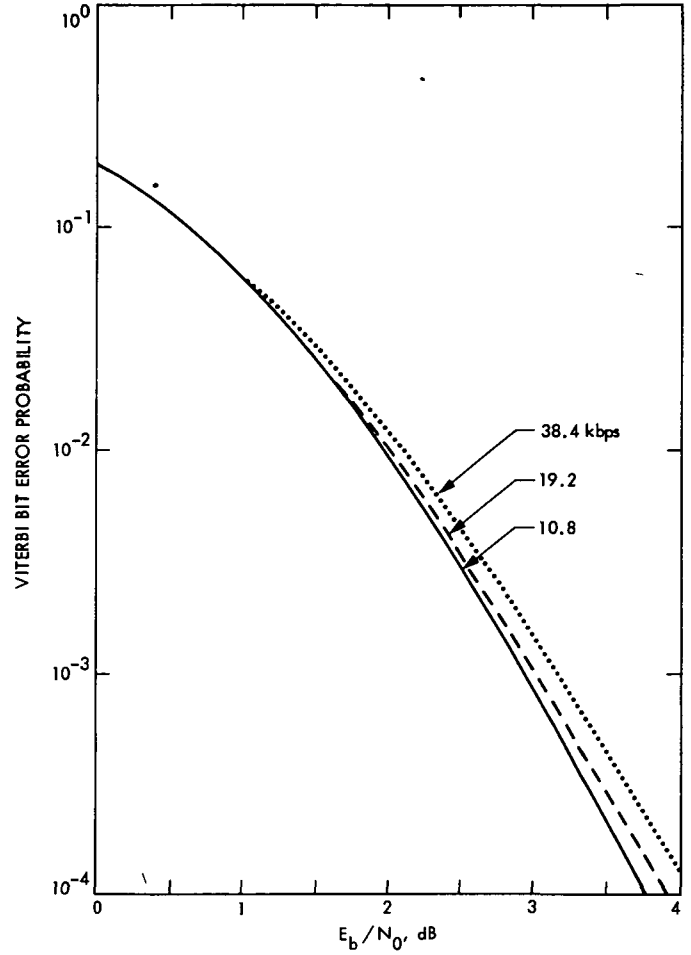


Fig. 5. Simulated performance of VLA with rotated gaps, convolutional (7, 1/2) coding only

ORIGINAL PAGE IS
OF POOR QUALITY

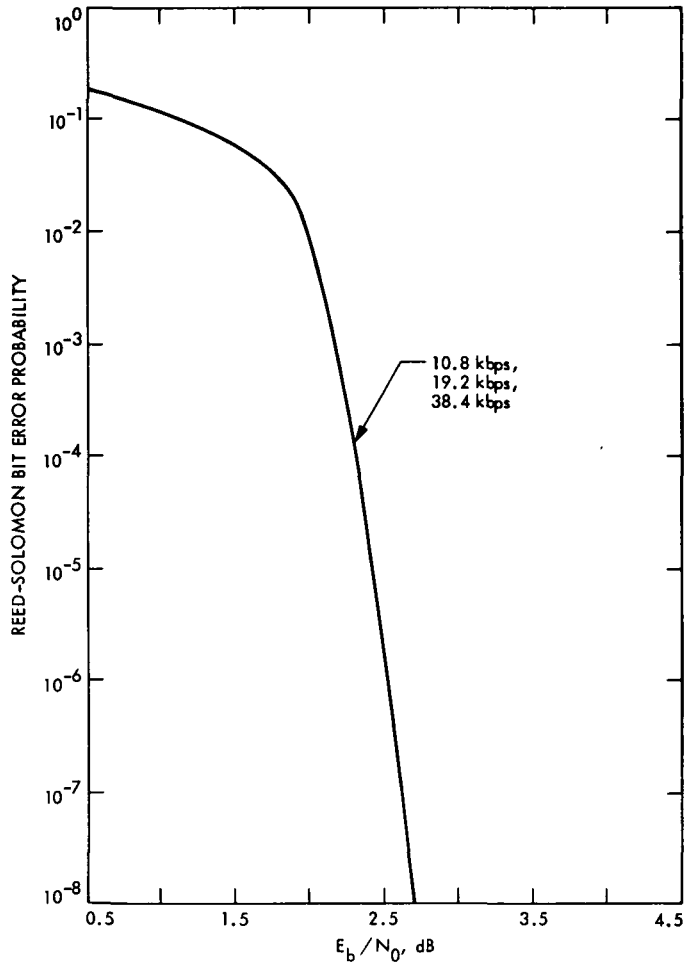


Fig. 6. Simulated performance of an ungapped receiving system, concatenated coding

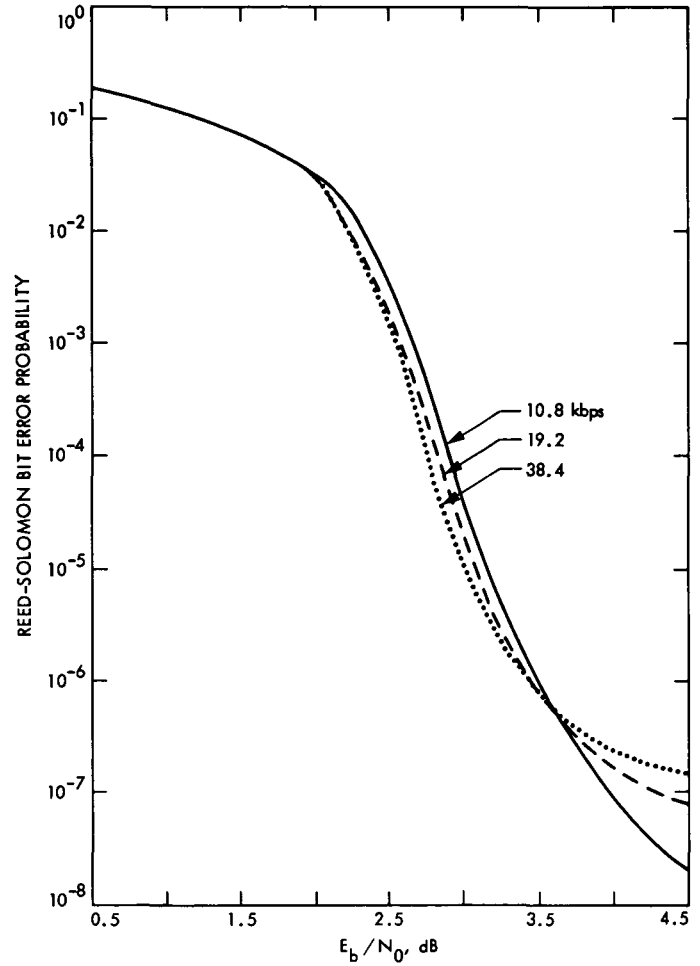


Fig. 7. Simulated performance of VLA with 1-ms gaps with no signal, concatenated coding

ORIGINAL PAGE IS
OF POOR QUALITY

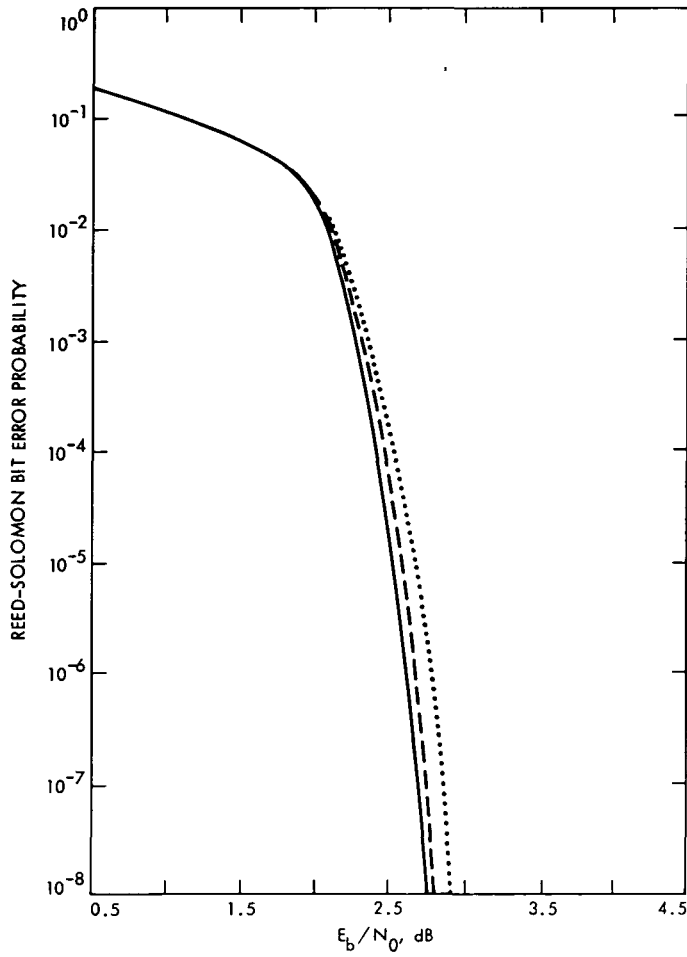


Fig. 8. Simulated performance of VLA with 1-ms gaps attenuated by 3 dB, concatenated coding

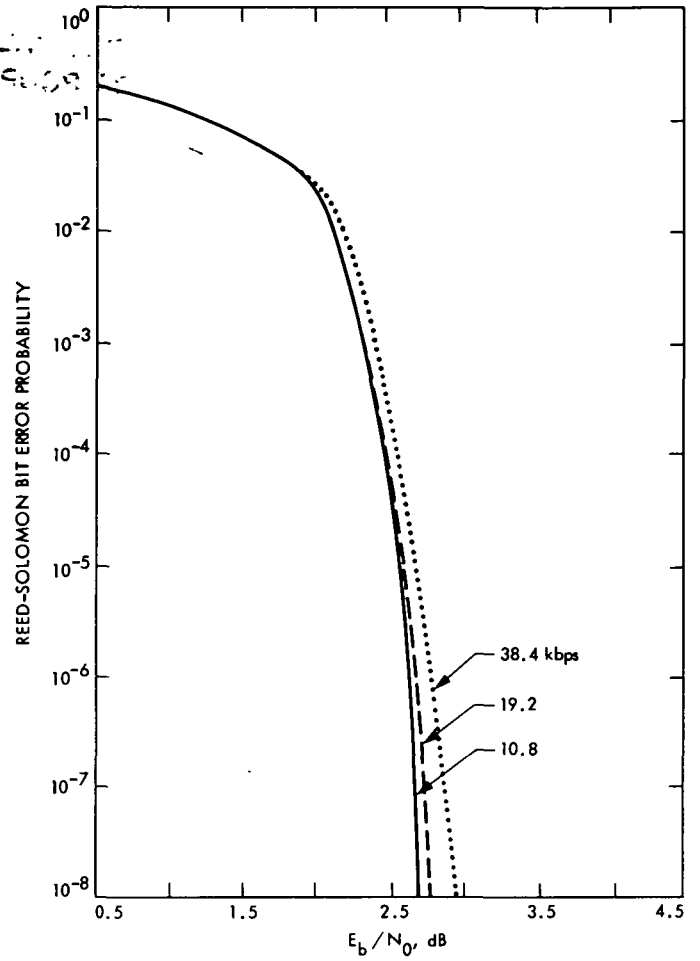


Fig. 9. Simulated performance of VLA with rotated gaps, concatenated coding

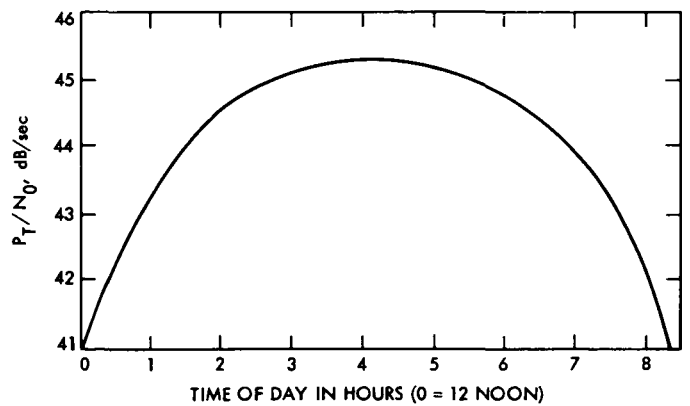


Fig. 10. Baseline performance of Goldstone array at Voyager 2 Uranus Encounter; array = 64 m + 34 m + 34 m; day 24, 1986, 90% weather

ORIGINAL PAGE IS
OF POOR QUALITY

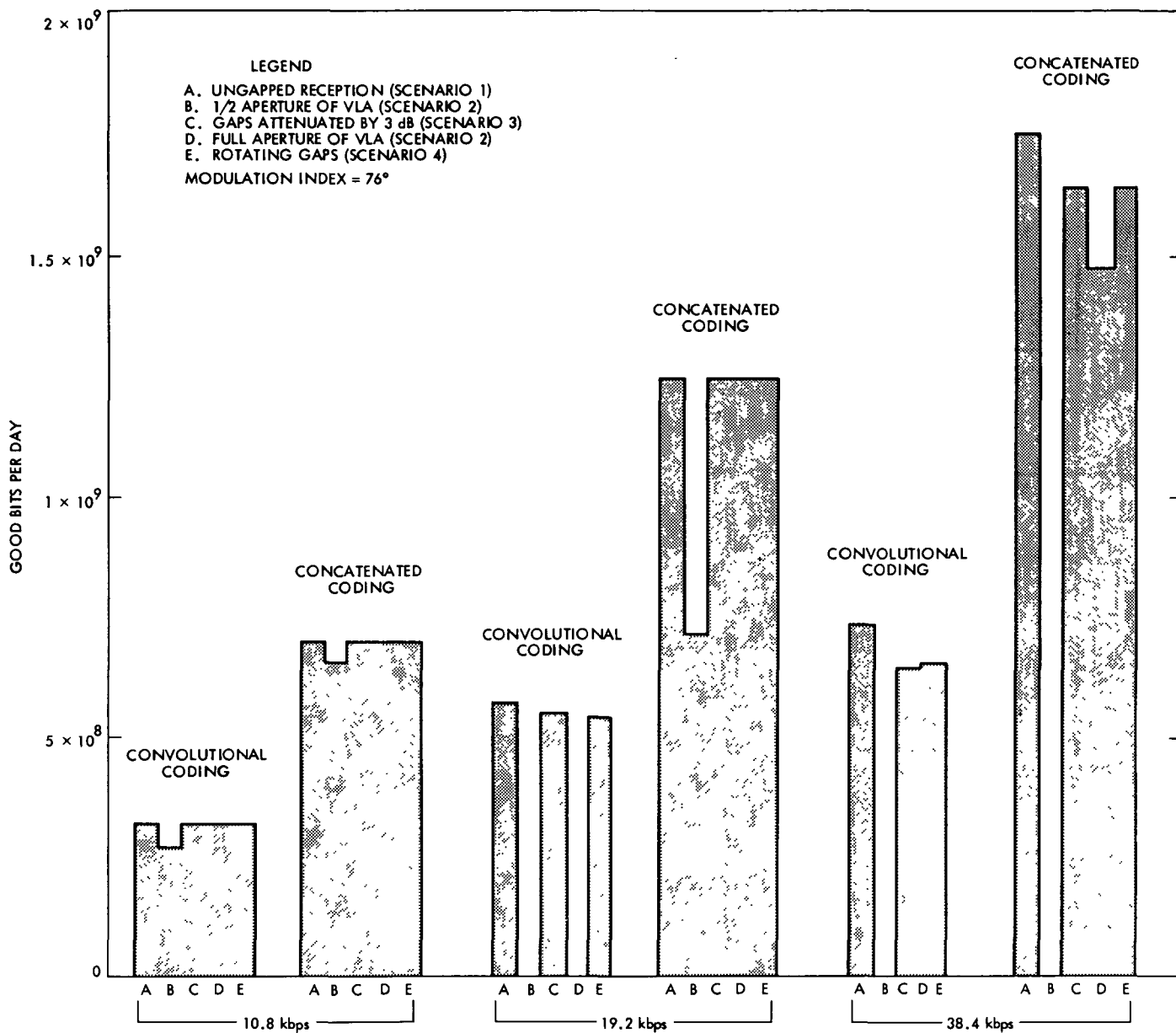


Fig. 11. Throughput of VLA at Voyager 2 Uranus Encounter

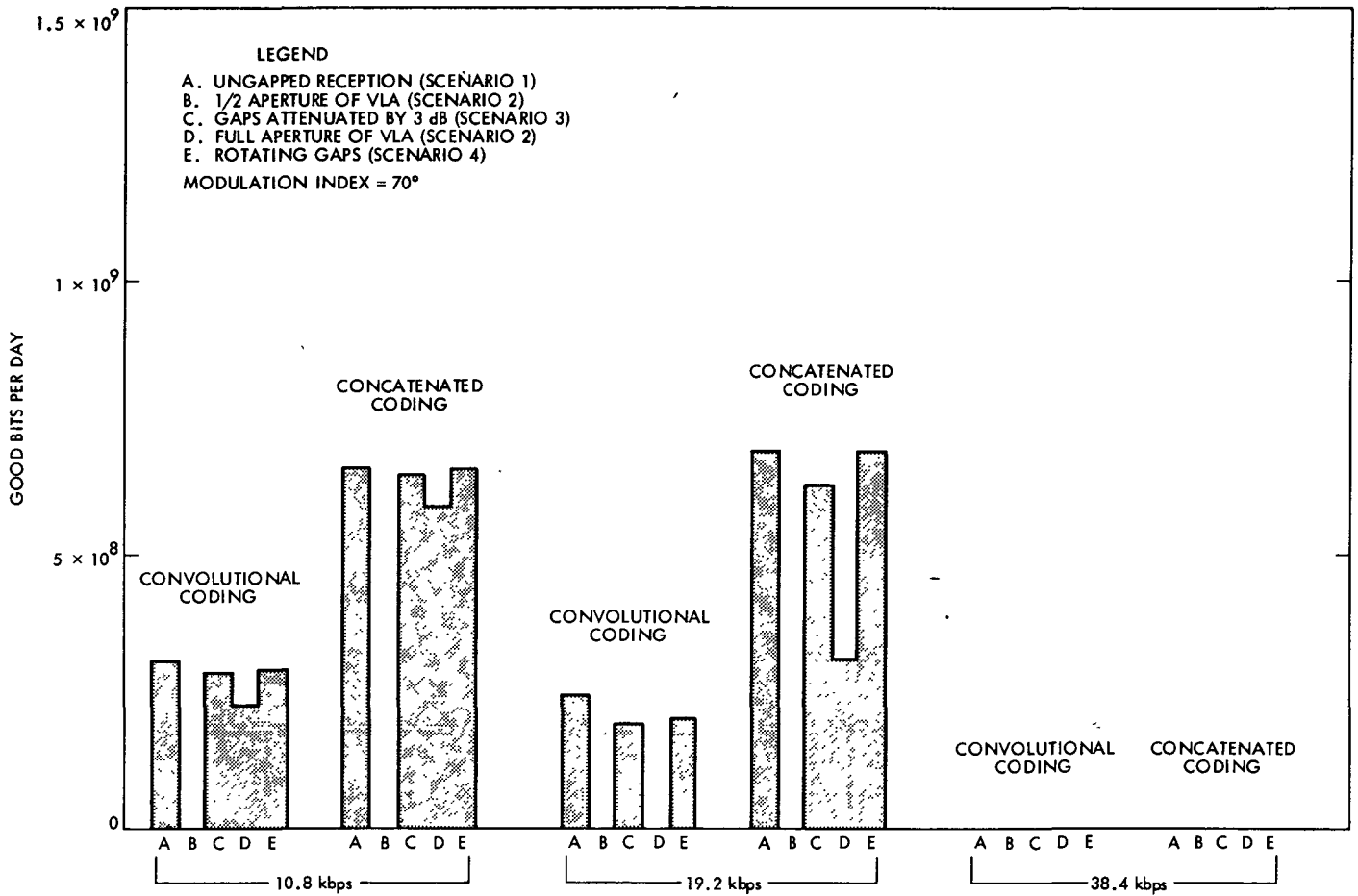


Fig. 12. Throughput of VLA at Voyager 2 Neptune Encounter

ORIGINAL PAGE IS
OF POOR QUALITY

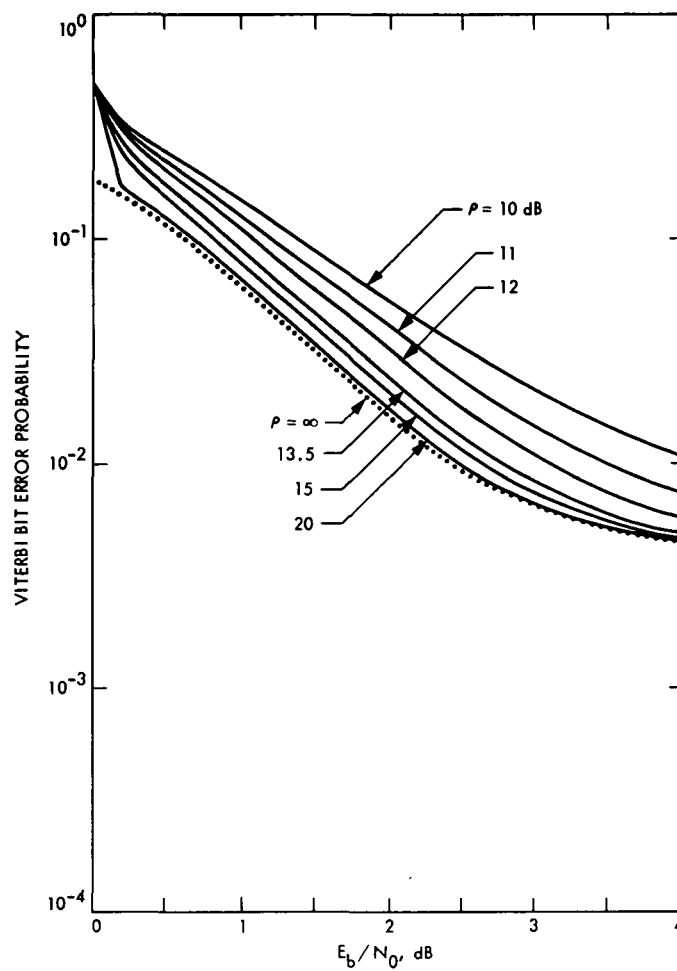


Fig. 13. The effects of noisy carrier referencing on the VLA,
carrier loop SNR = ρ

Performance of Differenced Range Data Types in Voyager Navigation

T. H. Taylor, J. K. Campbell, R. A. Jacobson,
B. Moultrie, R. A. Nichols Jr., and J. E. Riedel
Navigation Systems Section

Voyager radio navigation made use of a differenced range data type for both Saturn encounters because of the low declination singularity of doppler data. Nearly simultaneous two-way range from two-station baselines was explicitly differenced to produce this data type. Concurrently, a differential VLBI data type (DDOR), utilizing doubly differenced quasar-spacecraft delays, with potentially higher precision was demonstrated. Performance of these data types is investigated on the Jupiter-to-Saturn leg of Voyager 2. The statistics of performance are presented in terms of actual data noise comparisons and sample orbit estimates. Use of DDOR as a primary data type for navigation to Uranus is discussed.

I. Introduction

Spacecraft navigation during the Saturn encounters of Voyagers 1 and 2 was made more demanding by solar system geometry. For both spacecraft (S/C), late cruise and encounter occurred when the planet was near the line of nodes and thus at a geocentric declination of nearly zero (see Fig. 1). This caused special problems in S/C orbit determination using radio data because of the so called "low declination singularity": use of conventional doppler and range data in this geometry leaves the S/C declination poorly determined. Determination of right ascension, on the other hand, remains quite good when using conventional data.

No previous deep space mission had to contend with long periods of low declination, especially at such a critical time. To answer the potential loss of information, Voyager became the first mission to utilize explicitly differenced range as a basic data type. A fuller titular description might be "nearly simultaneous two-station two-way differenced range," but for

simplification it will be referred to here simply as differenced two-way range (DTR). As will be discussed, DTR relieves the declination problem by differencing data between two stations on an intercontinental baseline having an appreciable north-south projection. Because of this two-station feature, as well as other similarities with Very Large Baseline Interferometry (VLBI), DTR has also been called a "quasi VLBI" data type. DTR was adopted as the operational answer to the low declination problem.

Potentially more accurate than DTR is the true VLBI-based data type called "delta differential one-way range" (DDOR). As the name implies, this data type involves the differencing of one-way range from the spacecraft to each of two stations on an intercontinental baseline. The process is then repeated for a nearby quasar. Finally, these results are further differenced to provide a high accuracy spacecraft position with respect to the quasar. As with DTR, a declination determination depends on having a baseline with a large projection in the north-south

direction. DDOR was an experimental data type on the Jupiter-to-Saturn cruise legs of both Voyager 1 and Voyager 2, and was to be further demonstrated in the cruise of Voyager 2 beyond Saturn to Uranus. However, performance to date has been such that it is now to become an operational data type (in August 1982) for the remainder of the Uranus cruise.

We will give a brief description of the salient features of each of the radio data types used in Voyager navigation during the approximately 2-year Voyager 2 cruise from Jupiter to Saturn. Features of the data arc and trajectory are discussed, followed by analyses of solutions on this arc.

II. Description of Data Types

Four distinct data types are discussed: doppler, range, DTR, and DDOR.

A. Conventional Data (Doppler and Range)

“Two-way” doppler data are normally the workhorse of JPL deep space navigation. The uplink carrier frequency from a Deep Space Station is detected and coherently retransmitted by the spacecraft. Upon receipt of this downlink signal, frequency is detected and differenced with what was transmitted a “round-trip light time” earlier. This constitutes the doppler information. Typically, one-minute averaged samples are sufficient to resolve Voyager line-of-sight velocity to within a few tenths of 1 mm/sec.

Range data are acquired by phase modulating the uplink signal with a series of pure square wave tones. The spacecraft turns this modulation around, and the receiving station then correlates these tones with a local model to obtain a phase shift. This phase shift is equivalent to measurement of the total propagation delay, uplink and downlink, at the station. In the absence of strong media noise (e.g., more than 30 or 40 degrees away from a solar conjunction), 5 minutes of correlation is sufficient to resolve Voyager range to the 1-meter level. Absolute accuracy is typically at the 30-meter level.

Doppler and range data together yield both components of spacecraft state in the line-of-sight direction. In addition, angular information is obtainable from parallax effects resulting from motions of the earth, the spacecraft, and the earth’s rotation.

Hamilton and Melbourne (Ref. 1) analyzed the information content for a single pass of doppler data from a single tracking station. Angular information is contained in the sinusoidal modulation of the earth’s rotation onto range rate (doppler) (see Fig. 2). Right ascension (R.A.) is well determined from the phase of this modulation, while declination is determined

by its amplitude. The accuracy of R.A. is relatively unaffected by spacecraft or tracking station positions. On the other hand, declination accuracy is very poor when S/C declination is near zero because amplitude varies as the cosine of declination.

The amplitude is approximately given by:

$$A = \omega r_s \cos \delta$$

where

ω = earth’s rotation rate

r_s = spin radius (distance from polar axis) of tracking station

δ = spacecraft declination

This leads to an expression for accuracy of the estimated declination:

$$\sigma_\delta = \frac{\sigma_{r_s}}{r_s \tan \delta}$$

This is the source of the term “low declination singularity.” It is apparent that spin radius errors (or anything which masquerades like them) can have a large effect on low declination solutions.

When multiple passes of data are used, angular content of the doppler is augmented by earth and spacecraft motion in heliocentric space. For long arcs, this effect can dominate over the earth rotation information, at least in certain directions. For Voyager, angular information is strongest in the ecliptic R.A. direction partially because the S/C orbit is in the plane of the ecliptic. However, determination of geocentric declination is still fundamentally limited by the above considerations.

Conventional range data are generally inadequate to provide the same kind of angular information as doppler. Not only is range noisier, but inadequately modelled nongravitational accelerations (e.g., from minute gas leaks and from unbalanced thrusting of the attitude control system) can cause gross orbit errors when range is not used with care. For this reason it is usually used in combination with other data types, and is weighted much more loosely than its inherent accuracy would seem to warrant. Thus it usually provides only range information, while doppler provides range rate.

B. Differenced Two-Way Range

In the above discussion, attention was focused on single station tracking. When more than one station is used, doppler data are still hampered by the low declination problem. How-

ever, when data are gathered from widely separated stations on a large earth baseline, conventional range data could in principle be used for accurate angular determination. Unfortunately, the inadequately modelled acceleration problem still pertains and, additionally, solar plasma becomes a major concern.

The differenced two-way range data type was created to deal with these problems. A DTR point is simply generated by explicitly differencing two conventional range points from widely separated stations. The differencing eliminates errors common to both stations such as unmodelled spacecraft accelerations. If the conventional range points are close in time (simultaneous two-way ranging is not possible), then space plasma effects are also minimized.

A simplified geometric discussion loosely following Melbourne and Curkendall (Ref. 2) illustrates the ability of DTR to determine angles, and particularly declination. A delay measurement (e.g., a nearly simultaneous DTR point) provides S/C angular information by the relation

$$\tau = S \cdot B = |B| \cos \theta$$

where

τ = the geometric differential delay

S = the unit vector directed from the earth's center to the radio source

B = the baseline vector

θ = the angle between B and S .

In geocentric coordinates

$$\tau = B_e \cos \delta \cos(\alpha_B - \alpha) + B_z \sin \delta$$

where B_e and B_z are the baseline's equatorial and polar projections, respectively, α is the source's R.A., and α_B is the baseline's R.A. From this equation, the sensitivity of delay to declination as declination approaches zero is

$$\frac{\partial \tau}{\partial \delta} = B_z$$

That is, DTR retains sensitivity to declination in low declination geometries.

Figure 3 presents a simplified case of a baseline in the north-south direction. It is clear from this and from the above discussion that an expression of accuracy is given by

$$\sigma_\delta = \frac{\sigma_{\Delta\rho}}{|B| \cos \delta}$$

where $\sigma_{\Delta\rho}$ is the standard error in the difference of the two range measurements.

The NASA Deep Space Network (DSN) stations available for tracking are shown in Fig. 4. Notice that the Spain-Goldstone (S-G) baseline is nearly due east-west so that essentially no declination is available from that baseline. Declination is available primarily from the Goldstone-Australian (G-A) and Australia-Spain (A-S) baselines.

The range points chosen for explicit differencing are the last few at the end of the pass of the outgoing station and the first few of the incoming station. Ordinarily, the closest points are 15 minutes apart except for the A-S baseline where round-trip light time near Saturn exceeded the mutual visibility period and the closest possible points were 2 hours and 15 minutes apart. This was large enough to allow solar plasma effects to become significant in some instances, and so the value of this baseline for DTR was questionable.

The Voyager requirement on DTR was 6.4 meters accuracy (1 sigma). This is equivalent to about 600 nanoradians accuracy on the G-A baseline.

C. Delta Differential One-Way Range

The above equations for DTR apply to any differenced range data type, and this, of course, includes VLBI. DDOR is a differential data type generated by explicitly differencing a one-way S/C VLBI delay measurement with the corresponding measurement for an angularly nearby quasar. A detailed description is given by Border et al. (Ref. 3). Thus DDOR has some of the same attributes as DTR, particularly the ability to determine declination in similar geometries. It also shares the feature of "self-calibration" by cancellation (through the implicit differencing of a VLBI measurement) of errors common to each baseline (e.g., common path space plasma errors). Additionally, however, the second (explicit) differencing of S/C with quasar data allows further self-calibration in the cancellation of error sources such as dispersive transmission media, inaccurate station locations and earth platform parameters, and station clock differences. These features combined give DDOR potentially higher precision than DTR.

DDOR measurements typically require about a half-hour of tracking time: 10 minutes on the S/C, 10 on a quasar, and 10 minutes of antenna slewing time.

The expectation for DDOR accuracy on the Jupiter-to-Saturn cruise leg of Voyager 2 was about 4 m. This included allowance for 3.7 m of bias in quasar position.

III. Description of the Data Arc and Trajectory

The data arc is almost 2 years long, beginning 13 November 1979, about 4 months after the Voyager 2 Jupiter encounter, and ending 4 August 1981, 22 days before the Saturn encounter. The goal was to incorporate as much of the differenced data as possible on a single trajectory rather than in disjointed sets. It was not possible to use the original operational set of trajectories since they consisted of a series of shorter arcs.

The epoch state for the trajectory was initially derived from an operational solution obtained early in 1981. Three large Trajectory Change Maneuvers (TCMs) were modeled, as well as 25 smaller impulsive maneuvers due to delta Vs incurred during S/C attitude changes. Solar radiation pressure was modeled, but does not contribute significantly to the non-gravitational acceleration profile at 5 – 10 AU solar distance.

Processing the entire original data set was out of the question due to sheer volume (35,000 total range and doppler points) and the consequent computing costs. Also, there was a desire to see the effect of reducing conventional data to a minimum, letting the differenced data predominate. Thus, conventional data were severely edited, leaving about 670 doppler and 260 range points available. Data were selected so as to be evenly balanced among the three DSN sites. Doppler was selected at the rate of about 3 points per day (using 5 and 20 minute averaging periods), and range 1 point per day. These conventional data were calibrated for the effects of troposphere, ionosphere, and equipment group delays; but not for space plasma effects.

DTR was processed from a subset of the calibrated range data, from those tracking periods which had been scheduled specifically for generation of nearly simultaneous range points. Such periods were normally scheduled once each month, and usually consisted of 4 contiguous passes, beginning and ending at the Australian site. Thus 3 baselines were available each period. Generally, 4 points were chosen from each station for each baseline, and differencing order proceeded from the closest 2 points to the 2 most widely separated ones. Since points were 5 minutes apart, typical separations were 15 to 45 minutes for the S-G and G-A baselines, and from 2 hours 15 minutes to 2 hours 45 minutes for A-S. A total of 52 baselines was used, consisting of 203 differenced pairs.

DDOR was an experimental data type on this arc, and so coverage was more sporadic. Two baselines were used: S-G and G-A. Before February 1981, about 2 baselines per month were scheduled. After this, baselines were scheduled at an average rate of 1 every several days until encounter. During

the entire trajectory, only 2 quasars were used: P1055+01 until 27 August 1980, and 3C273 thereafter. After editing out bad data, 58 DDOR points (baselines) remained. These were calibrated for troposphere and ionosphere.

The JPL Orbit Determination Program (ODP) was used for solutions, using a conventional weighted least squares batch sequential filter with no correlation between batches. Batch length was 30 days, yielding 22 batches in the data arc. Estimated quantities were S/C state, bias and stochastic nongravitational accelerations, the earliest two TCMs, delta-Vs due to attitude changes, and quasar positions. Station location errors were considered for their effect on orbit uncertainty, but not estimated.

IV. Solutions and Results

For evaluation of performance it is necessary to compare data types – directly, in terms of their residuals, and indirectly in terms of the orbit solutions they generate. Table 1 gives a list of the combinations of data types and weights used to generate five solutions of interest.

Range is used in all of these, weighted loosely at 100 km. Doppler is used in three cases to provide strong determination of R.A. as well as highly accurate range rate. In the other two cases, doppler is left out and angles are determined solely by the differenced range data types.

Comparisons of solutions are made in the target planet "B-plane," illustrated in Fig. 5, where the B vector for the best current postencounter solution, the "reconstruction" solution, is plotted. Figure 6 compares the doppler solutions in the B-plane, relative to the above mentioned "best" solution. One-sigma error ellipses are drawn.

The most obvious feature is the disagreement in (ecliptic) declination between the doppler-range solution and solutions using differenced range. The differenced range solutions are in relatively good agreement in declination, each being within the other's error ellipse. The fact that all three agree in ecliptic R.A. is not surprising, since the doppler in each solution dominates the determination in that direction. Two solutions were done to entirely remove the influence of doppler by fitting only DDOR-range and DTR-range. They are shown in Fig. 7 along with error ellipses. Now the R.A. alignment is gone as each solution is allowed to float independently in that direction. The DDOR solution has moved north-east; and DTR, south-west.

Figures 8 and 9 plot residuals from the two DDOR baselines from the DDOR-doppler-range solution. Table 2 presents means and calculated 1-sigma noise for each case.

The fit seems good on both baselines as compared to the expected 4-meter accuracy. There is the possibility, of course, that the filter is simply "fitting out" some of the noise. This speculation is belied, however, by the dense data in the period from day 456 to 484. There, the noise on the S-G baseline is 0.6 m, while the G-A noise is 1.0 m. This span is too short for the filter to have significant effect, and so this result is commensurate with (in fact, better than) that of the entire data span.

DTR residuals are plotted in Figs. 10 through 12. Noise is good on two baselines. However, there is a poor fit on the A-S baseline. This one was expected to be poor due to the large time separation between points, allowing solar plasma variations to cause significant variations. The two points near -4 meters should probably have been deleted from the data set. However, they had little effect on the solution considering the total number of competing points on the S-G baseline. (The G-A baseline projection toward the S/C is nearly orthogonal to the A-S projection.) This was confirmed in a subsequent solution in which they were removed: the B-plane changed less than 100 km. (In fact, in another solution the entire A-S baseline was thrown out with, again, less than 100 km of difference in the B-plane.) Noise is quite good during the high-density period from day 576 through 611 (1.1 m on S/G and 1.2 m on G/A), making it unlikely that the filter is making noise overly optimistic over the entire arc.

The total separation between the two differenced range solutions (without doppler) is significant in terms of the residuals of those data types. To compare the solutions with the residuals, we use the DDOR residuals which were passed through in the DTR-range solution. They are plotted in Figs. 13 and 14. There is a clear bias of about -5 meters (at the end of the arc) in the S-G direction and -8 meters in the G/A direction. These biases should point, in some sense, from the DTR solution to the DDOR solution. To test a simple vector representation in the B-plane, we plot these biases in the diagonal coordinates of the projection of the baselines, using the approximation of 1 meter equals 150 kilometers at Saturn. The result is shown in Fig. 15. The correspondence of B-plane relative positions with this vector treatment of the residuals is obviously not perfect, but it is good enough to allow some experimentation. It holds up as a rule of thumb on the other solutions already plotted, and so we can use it to get a rough idea of the absolute biases of each data type.

The DTR-range and DDOR-range solutions disagree with each other and with the solutions containing doppler. Since

doppler dominates in R.A., it is easy to believe that the correct solution probably lies near a line connecting the doppler solutions¹. Taking the differenced range-doppler-range solutions themselves as extremes for the "correct" solutions and resolving vectors into baseline coordinates, we get the results listed in Table 3. Thus, a regime of biases is roughly determined for each data type and baseline, predicated on the hypothesis that — in R.A. at least — doppler knows best. For example, Table 3 indicates that the probable bias for DDOR on the G-A baseline is between -3.5 and -6.5 m. For DTR on the G-A baseline, it is between 2.0 and 5.0 m.

A single solution in the B-plane provides a limited picture of performance. Therefore, a history of solutions was formed for three of the data combinations already discussed by solving at 60-day (2-batch) intervals from the epoch, each interval containing all the information from epoch to the end of the corresponding batch. Figure 16 shows the B-plane history for doppler-range. This succinctly illustrates the weakness in declination. Figure 17 shows the DTR-range results. Note the change of scale. The tightening of the solution in declination can be seen in comparison to the doppler-range case. Results for the DDOR-range solutions are in Fig. 18. The tight declination is also seen here. Formal consider sigmas for these same cases are shown in Fig. 19 for B · T and Fig. 20 for B · R. The overwhelming early dominance of doppler is seen in the B · T plot. DTR and DDOR do not come close to matching this performance until late in the data arc. One reason for this is, of course, the sparsity of the differenced range data types until early 1981; whereas doppler data were used more uniformly throughout the arc. Superiority of the differenced range data types in declination is clearly seen in Fig. 20. Early in the plot S/C declination is around 8 deg. In August 1980 (batch 10), declination goes below 5 deg, staying close to 0 from then on through the encounter. Declination at encounter is about -2 deg. The effect on the doppler determination of B · R is apparent.

Comparison of the plots for the histories with plots for the uncertainties seems to show that the differential range types performed better than the curves would indicate. This may be due to larger than necessary a priori sigmas on nongravitational accelerations and impulsive maneuvers.

¹The "correct" solution might be thought to be the reconstruction solution at the origin. This is fortuitously close to the DTR-doppler-range solution. "Fortuitous," however, is the operative word, considering the size of the error ellipse and also the fact that the string of operational solutions which led to the reconstruction used primarily doppler, range, and DTR as the radiometric data types. The fact that the final reconstruction is close to the DTR solution simply expresses the fact that this data arc is compatible with the string of arcs which yielded the reconstruction. Given that compatibility, DTR is guaranteed to excel.

V. Discussion and Conclusions

Noise performance of each differenced range data type was good. The estimated 1-sigma noise for DDOR was 1.1 m overall, while DTR noise was 2.8 m. However, as seen in Table 3, there were significant biases for each data type if the assumptions in the above section are correct. This is reinforced by data from the current operational Voyager 2 trajectory where the relative bias (from DTR to DDOR) is -3.0 m on the S-G baseline and -5.5 m on the G-A baseline. This is compared with values of -5.0 m and -8.0 m in the pre-Saturn trajectory. Thus, it appears that errors have remained about the same despite the use of new quasars and some changes in the ranging system since the encounter. Expected accuracies prior to encounter were about 4.0 m for DDOR and 6.4 m for DTR. Noise for both data types compares very favorably with these numbers, but the assumed biases are less favorable. It appears that DTR probably met expectations, but that DDOR may have performed more poorly than expected.

From another viewpoint, the low data noise is the most significant feature for navigational purposes. Low noise allows good determination of S/C angular rate. It is this angular rate which will be the dominant feature in long mappings (e.g., from the present to the Uranus encounter), whereas positional errors will be relatively small and unchanged by mappings, especially considering the size of the Uranus ephemeris uncertainty which is the equivalent of about a 25-m bias in the R.A. direction, and 5.5 in declination. From this standpoint, DDOR excels.

Since Saturn, DDORs have been accomplished in the higher frequency X-band rather than the pre-encounter S-band. This results in increased signal strength for the S/C and decreased susceptibility to charged particle media errors. Additionally, the effective bandwidth has been increased. These have had the effect of decreased DDOR noise. The results are 0.6 m noise on the S-G baseline on 9 baselines since January 82, and an incredibly low 0.1 m on the 8 G-A baselines in the same period.

After having performed well on the Voyager 2 approach to Saturn, DTR was retired from Voyager service in March of 1982. Its use was becoming too unwieldy because of increased

round-trip light times and decreasing station overlaps due to decreasing declination. Indeed, the round-trip requirement of DTR is perhaps its worst drawback. At the least, it causes operational difficulties, and at the worst it destroys the requirement of near simultaneity. At Uranus the round-trip light time of 5.5 hours will exceed the effective overlap on all DSN baselines. In contrast, DDOR (by definition) requires only a short mutual visibility period of quasar and spacecraft over about a half-hour.

Since the Saturn encounter, S/C declination has been decreasing and is presently passing through about -10 deg. At Uranus, it will be near -23 deg. In this region, doppler becomes competitive with DDOR in determination of declination and, at first glance, there would seem to be no reason to continue the use of DDOR. There are, however, a few good reasons to continue. One of these is the fact that the same round-trip light time which renders DTR impractical also significantly reduces the amount of conventional data which can be gathered during the available S/C visibility periods at each station. At Spain, the tracking mode would have to be two-way for the entire 7-hour period (at Uranus) in order to receive 1.5 hours of data. At Goldstone, the margin is only 1 hour better. Only Australia will have a S/C visibility period (12 hours) significantly greater than the round-trip light time.

However, extended periods of two-way operation are becoming objectionable as the S/C distance increases because uplink noise begins to interfere with downlink telemetry. The downlink is phase-locked at a multiple of 11/3 to the uplink frequency, and so S/C received phase noise is actually amplified onto the downlink. Thus there is the desire to use less two-way data. DDOR is the ideal candidate to remedy this situation. This is especially true in light of the recently improved performance of DDOR. As a result, data accuracy for operational orbit determination is currently assumed to be 1 m. This allows a few baselines of DDOR to replace a great deal of doppler in determining angular position and rates. The present schedule calls for 2 doppler-range single station passes per week (about 8 hours per pass; this is as compared to nearly continuous tracking on previous interplanetary legs) and 3 DDOR measurements per month.

References

1. Hamilton, T. W., and Melbourne, W. G., "Information Content of a Single Pass of Doppler Data from a Distant Spacecraft," *Space Program Summary 37-39, Vol. III*, Jet Propulsion Laboratory, Pasadena, Calif., May 31, 1966.
2. Melbourne, W. G., and Curkendall, D. W., "Radio Metric Direction Finding: A New Approach to Deep Space Navigation," presented at AAS/AIAA Astrodynamics Specialist Conference, Jackson Hole, Wyoming, Sept. 7-9, 1977.
3. Border, J. S., Donovan, F. F., Hildebrand, C. E., Moultrie, B., Skjerve, L. J., and Finley, S. G., "Determining Spacecraft Angular Position with Delta VLBI: The Voyager Demonstration," presented at AIAA/AAS Astrodynamics Conference, San Diego, Calif., Aug. 9-11, 1982.
4. Curkendall, D. W., and Ondrasik, V. J., "Analytic Methods of Orbit Determination," presented at AAS/AIAA Astrodynamics Conference, Vail, Colo., July 16-18, 1973.
5. Siegel, H. L., Christensen, C. S., Green, D. W., and Winn, F. B., "On Achieving Sufficient Dual Station Range Accuracy for Deep Space Navigation at Zero Declination," presented at AAS/AIAA Astrodynamics Specialist Conference, Jackson Hole, Wyoming, Sept. 7-9, 1977.

Table 1. Data combinations and weights

1. Doppler-range (Dop-Rng)	
2. DDOR-doppler-range (DDOR-Dop-Rng)	
3. DTR-doppler-range (DTR-Dop-Rng)	
4. DDOR-range (DDOR-Rng)	
5. DTR-range (DTR-Rng)	
Doppler	1 mm/sec
Range	100 km
DDOR	2 m
DTR	5 m

Table 2. Noise and means

	DDOR			DTR		
	Noise	Mean	Baselines	Noise	Mean	Baselines
S-G	1.1	0.0	32	2.5	-0.5	18
G-A	1.1	0.0	26	1.3	0.1	24
A-S	-	-	-	4.3	3.4	10
All	1.1	0.0	58	2.8	0.5	52

Units = meters

Table 3. Resolution of solutions into biases

	DDOR		DTR	
	S-G	G-A	S-G	G-A
Ref. point				
DDOR-DOP-RNG	-3.5	-3.5	3.0	5.0
DTR-DOP-RNG	-4.0	-6.5	2.5	2.0

Units = meters

ORIGINAL PAGE IS
OF POOR QUALITY

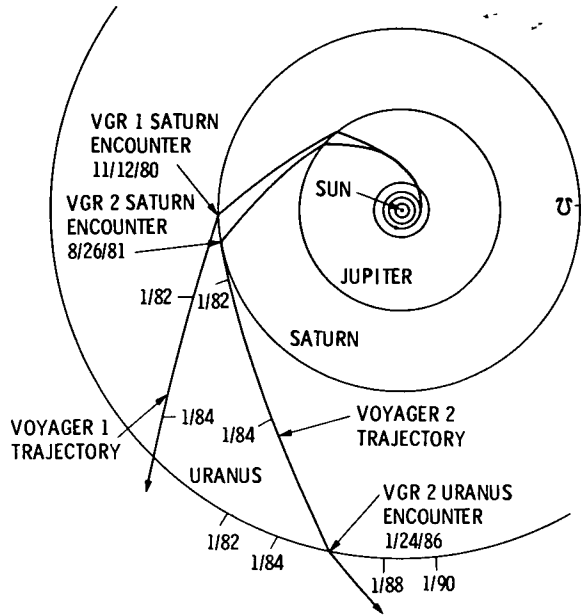


Fig. 1. Voyager trajectories

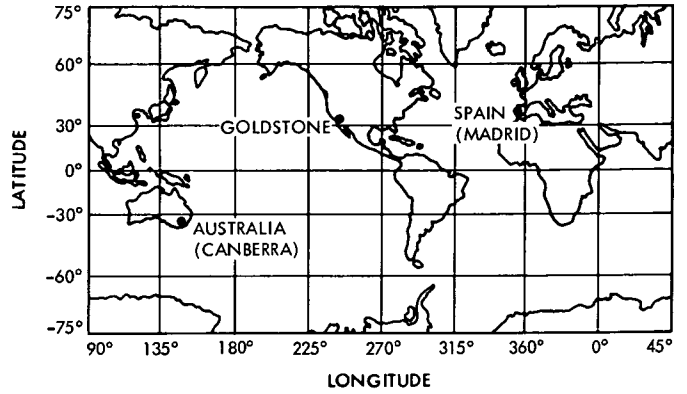


Fig. 4. DSN sites

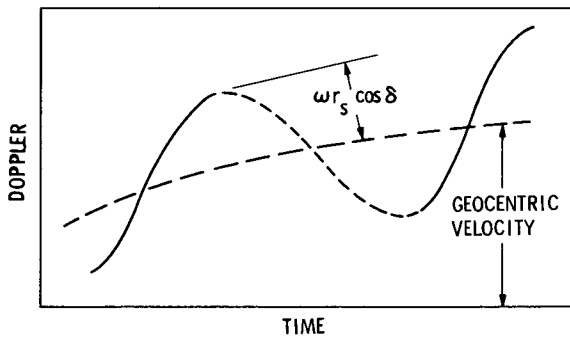


Fig. 2. Doppler signature

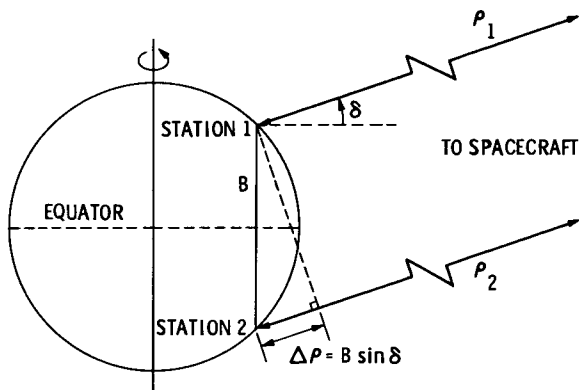


Fig. 3. Ranging from two stations

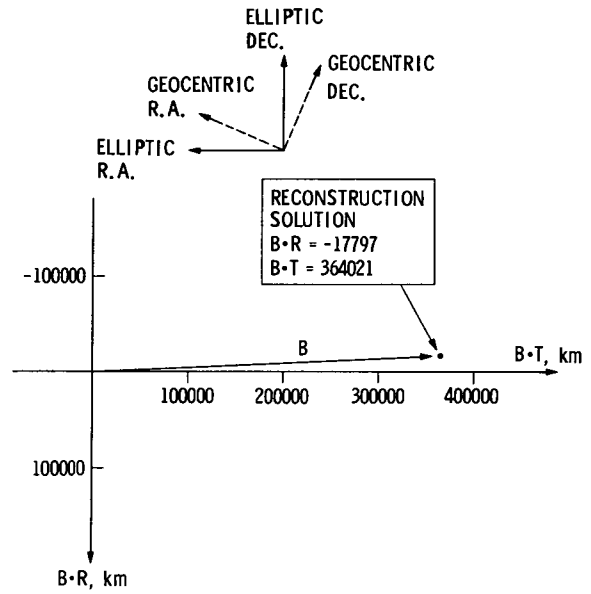


Fig. 5. B-plane orientation

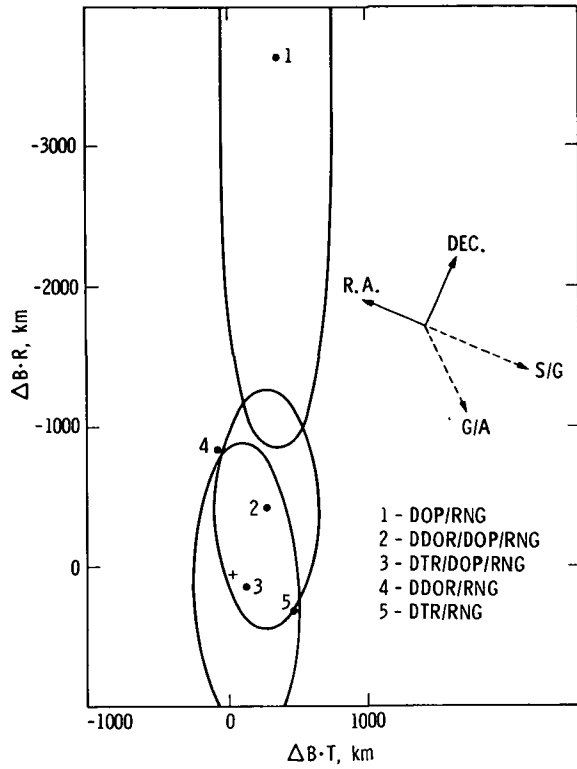


Fig. 6. B-plane solutions with doppler

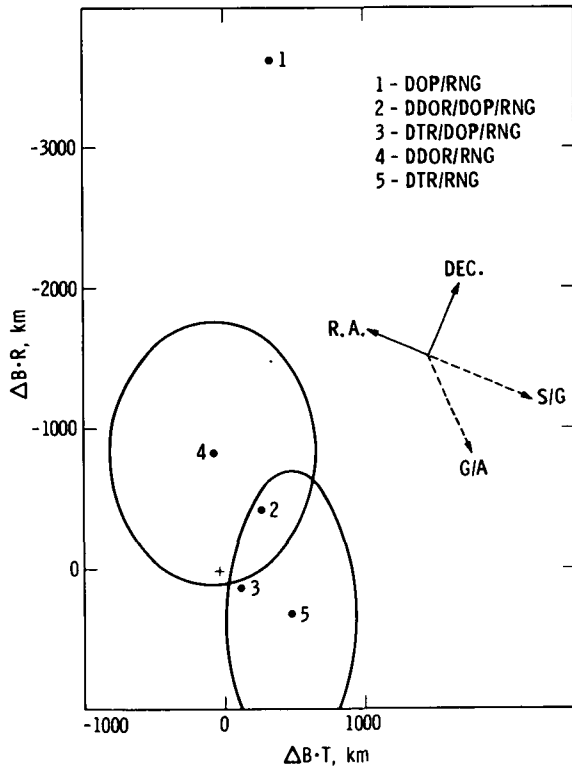


Fig. 7. B-plane solutions without doppler

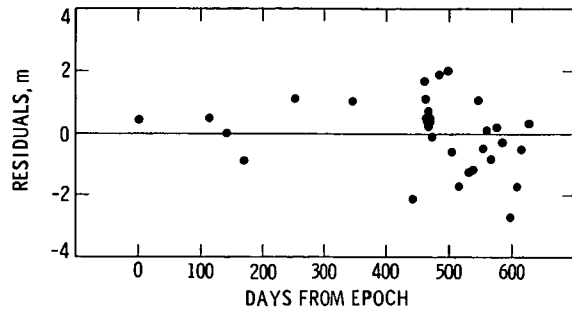


Fig. 8. DDOR residuals, S-G baseline

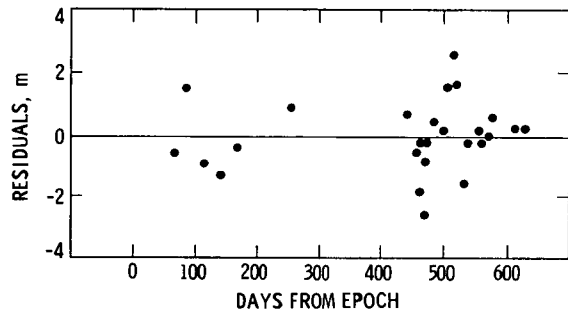


Fig. 9. DDOR residuals, G-A baseline

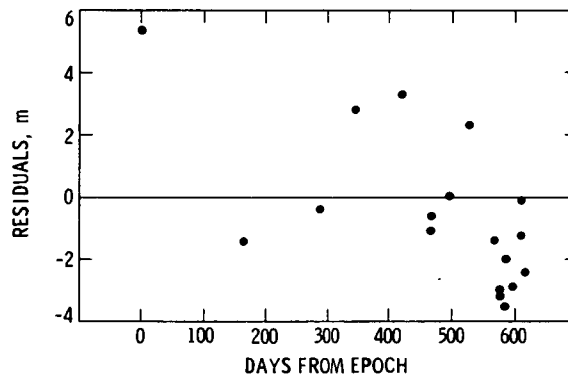


Fig. 10 DTR residuals, S-G baseline

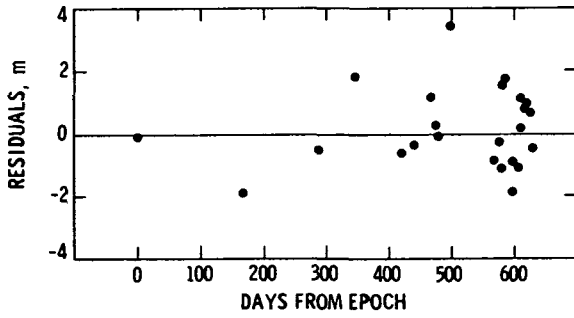


Fig. 11. DTR residuals, G-A baseline

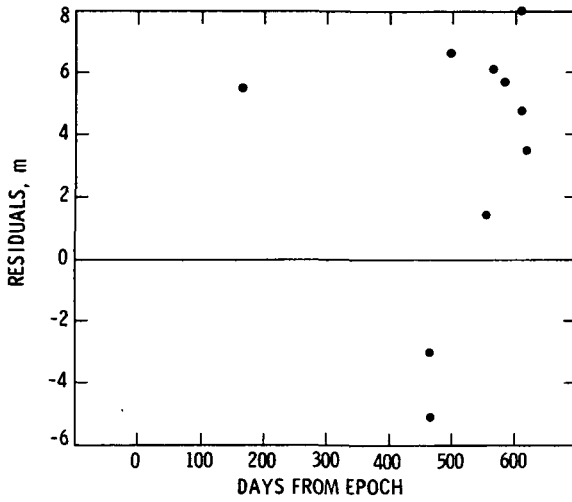


Fig. 12. DTR residuals, A-S baseline

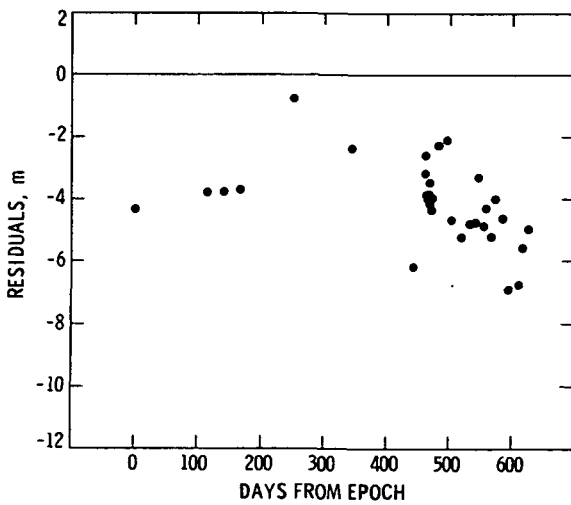


Fig. 13. DDOR residuals passed through, S-G baseline

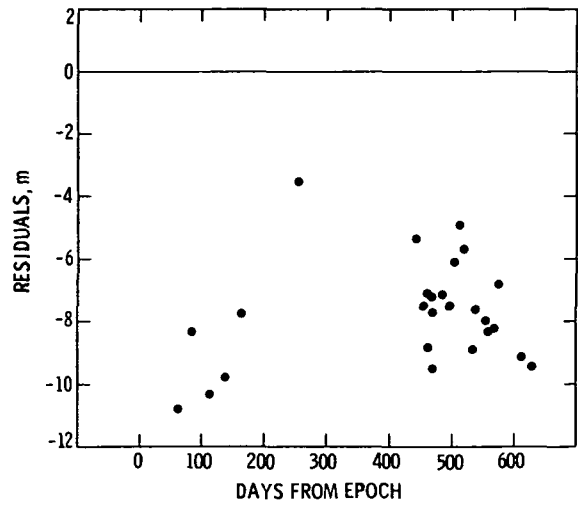


Fig. 14. DDOR residuals passed through, G-A baseline

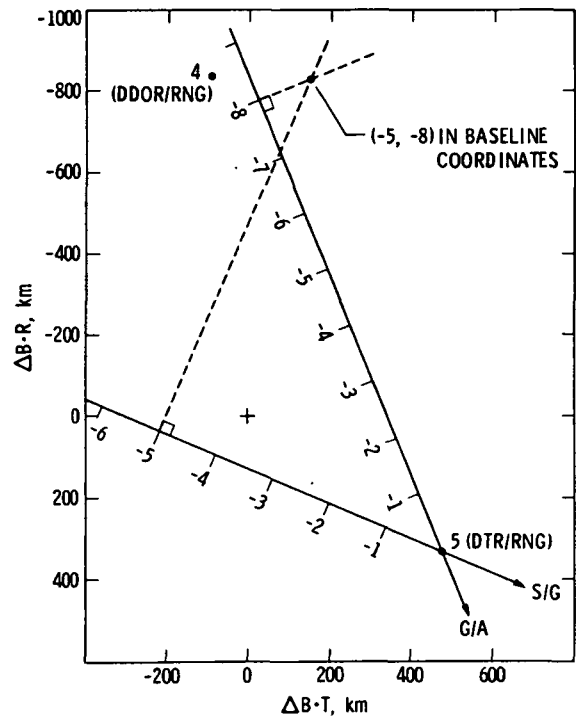


Fig. 15. Baseline residuals resolved into B-plane coordinates

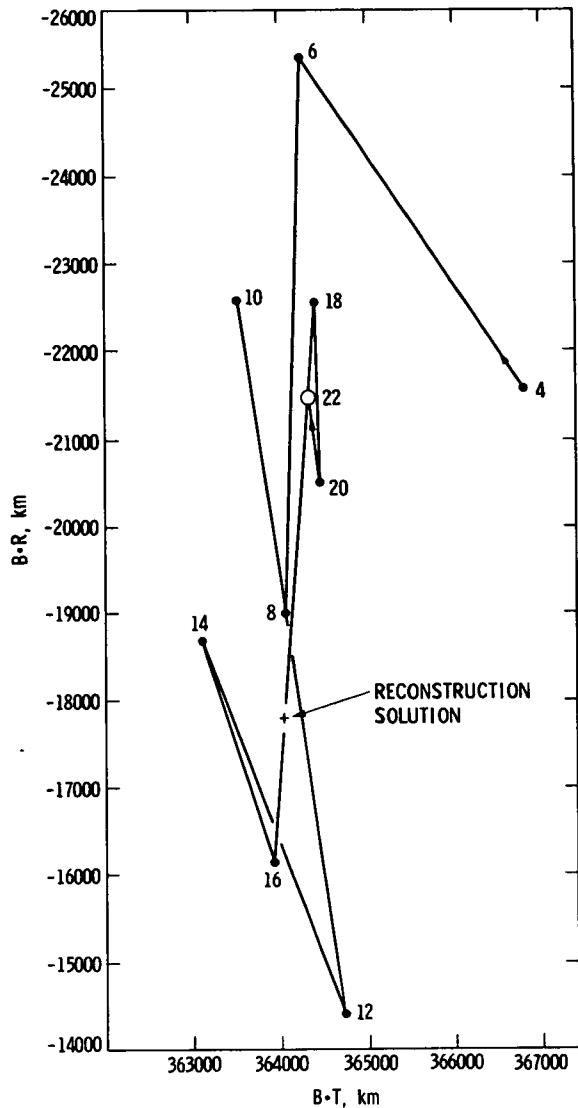


Fig. 16. B-plane history, doppler-range

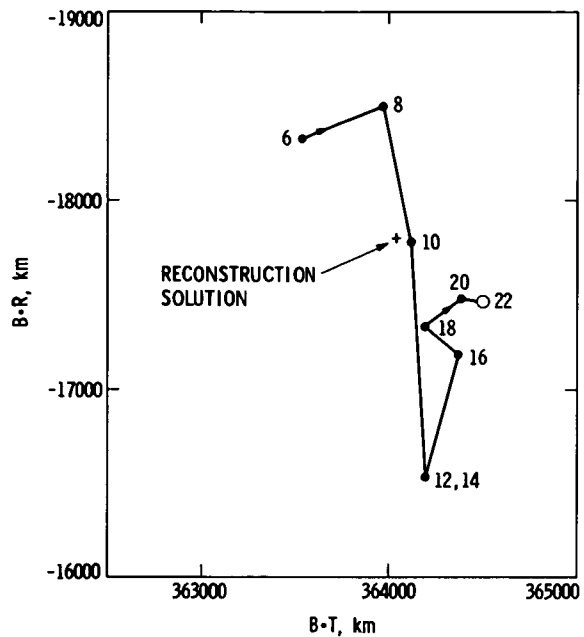


Fig. 17. B-plane history, DTR-range

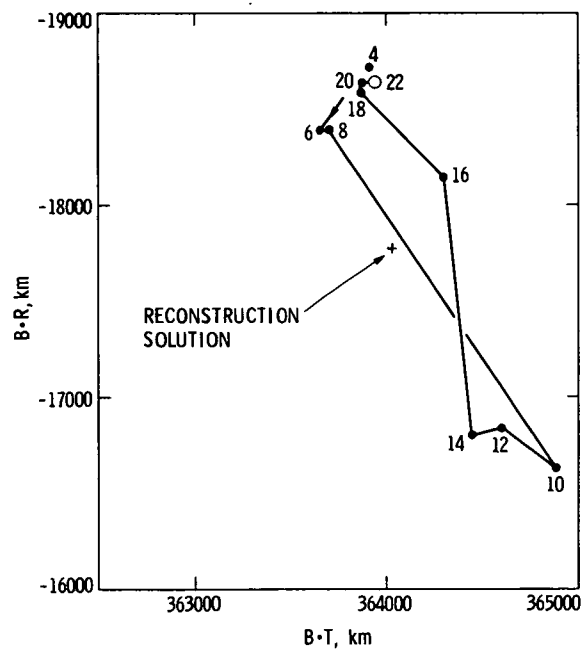


Fig. 18. B-plane history, DDOR-range

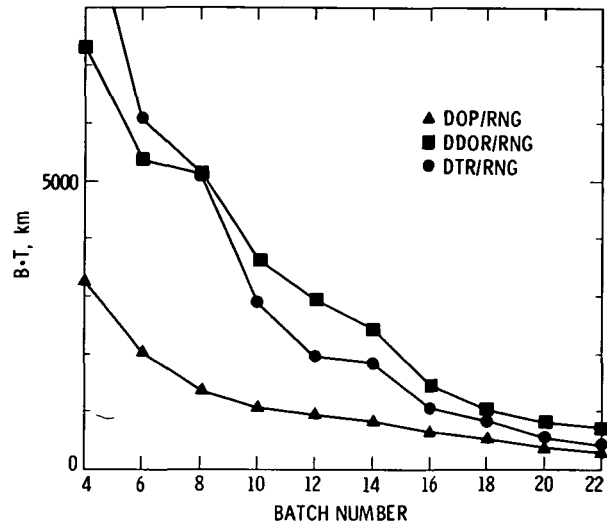


Fig. 19. Formal consider statistics in B.T.

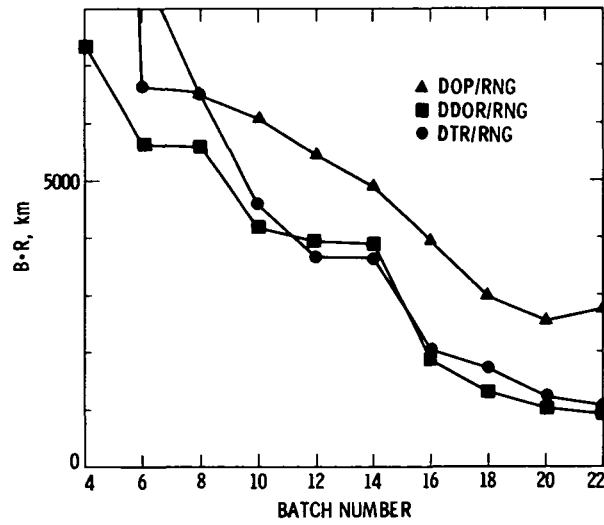


Fig. 20. Formal consider statistics in B.R.

Thermal Background Noise Limitations

S. Gulkis

Atmospheric Sciences Section

Modern detection systems are increasingly limited in sensitivity by the background thermal photons which enter the receiving system. This paper derives expressions for the fluctuations of detected thermal radiation. Incoherent and heterodyne detection processes are considered. The paper is intended to be tutorial in style. Many good references to the subject of photon detection statistics are given.

I. Introduction

An important consideration in evaluating and designing sensitive receiving systems for astronomy, deep space communications, and other related activities (such as the search for extraterrestrial intelligence), in which the goal is to detect the presence of a weak signal in the presence of noise, is the evaluation of the noise. In general, noise is due to the combined presence of both the signal and various sources of unwanted noise. The unwanted noise may arise in the detector itself, from the immediate surroundings of the detector (i.e., emission from the telescope), or from the (background) emission which enters the telescope and is intercepted by the detector. Background emission may originate from the atmosphere, from nearby objects, or from the cosmic background itself.

When the detection device is a square-law detector, the noise manifests itself as fluctuations in the output voltage (or current) from the detector $V(t)$, where

$$V(t) = rP(t) \quad (1)$$

In this expression $P(t)$ is the instantaneous power incident on the detector, and r is a constant of proportionality.

A measure of the fluctuations in $V(t)$ about its mean is the variance defined by

$$\begin{aligned} \text{var} [V(t)] &= \lim_{T \rightarrow \infty} \frac{1}{T} \int_{-T/2}^{+T/2} (V(t) - \bar{V})^2 dt \\ &= r^2 \lim_{T \rightarrow \infty} \frac{1}{T} \int_{-T/2}^{+T/2} (P(t) - \bar{P})^2 dt \quad (2) \end{aligned}$$

This parameter is frequently encountered in estimating the signal-to-noise ratio of a system. In general, a calculation of the variance requires a knowledge of both the signal and noise, as well as the frequency response of the system.

Frequently, there is a desire to know the variance when $P(t)$ is due to a finite band of thermal radiation at temperature T .

In particular, this result is useful when the dominating source of noise is bandlimited thermal radiation whose power greatly exceeds the signal power. This situation is commonly referred to as the background limited noise condition. Numerous approximations of the background limited noise appear in the literature, especially in the thermal limit, where $h\nu/kT \ll 1$ and in the quantum limit where $h\nu/kT \gg 1$. However, the more general expressions which describe thermal radiation over the entire range of $h\nu/kT$ are not as readily available. In this note, I derive some useful expressions related to the detection of thermal radiation and discuss some of the results. The purpose of the paper was primarily to acquaint the author with the trends of background limited noise. It is printed here in the anticipation that others may find the discussion useful. Many important points related to the detection process and signal/noise ratios are not covered in this note. In particular, I omitted all discussions of the type of detector involved in the detector process. The reader is referred to the Bibliography for additional discussions.

II. Derivations

A. Photons as Independent Particles

We assume initially that the radiation field incident on the detector is a stream of statistically independent photons. For this situation, each photon produces a power

$$p(t) = h\nu \delta(t - t_0) \quad (3)$$

and an energy given by

$$E = \int_{-\infty}^{+\infty} p(t) dt = h\nu \quad (4)$$

Equation (3) is not strictly correct since photons are bosons and consequently do not occupy available energy states independently. In particular, the statistics of arrival times of photons at a detector indicate that photons are "bunched". Nevertheless, we will continue with this assumption and apply a correction for the bunching later on. The justification for this approach is threefold: (1) it is relatively straightforward; (2) it introduces the terms in the results in a clear manner; and (3) the analysis leads to the quantum or particle-like noise term.

Since the total power received by the detector is a linear superposition of the sum of all the photons reaching the detector during the interval $(0, \theta)$, we can write for the total power received by the detector when K photons arrive

$$P_K = \sum_{k=1}^K h\nu \delta(t - t_k) \quad (5)$$

where t_k is the arrival time of the k photon. These arrival times are random and unknown.

Series such as that given by Eq. (5) can be evaluated using Campbell's theorem, which is discussed in detail by Rice (Ref. 1). Campbell's theorem states that (1) the average value of $P(t)$ (averaged over both time and over all values of k) is given by

$$\overline{P(t)} = R \int_{-\infty}^{+\infty} p(t) dt \quad (6)$$

and (2) the variance is given by

$$\text{var } [P(t)] = \Delta P^2 = R \int_{-\infty}^{+\infty} p^2(t) dt \quad (7)$$

where R is the average number of photon arrivals per second. The principal quantity of interest in this note is the variance, for this quantity is related to the precision of physical measurements.

To evaluate the variance, we need to evaluate both R and the integral

$$\int_{-\infty}^{+\infty} p^2(t) dt$$

R can be calculated directly from Eq. (6), using Eq. (4) and Planck's radiation law to calculate the average power. Planck's law gives for the radiance of a blackbody radiator at temperature T and frequency ν

$$B = \frac{2 h\nu^3}{c^2} \frac{1}{e^{h\nu/kT} - 1} \quad (8)$$

where

B = radiance, $\text{W m}^{-2} \text{Hz}^{-1} \text{rad}^{-2}$

h = Planck's constant ($= 6.63 \times 10^{-34}$ joule sec)

ν = frequency, Hz

c = velocity of light, ($= 3 \times 10^8$ m/sec $^{-1}$)

k = Boltzmann's constant, ($= 1.38 \times 10^{-23}$ joule K^{-1})

T = temperature, K

Thus a blackbody source of emission at temperature T produces a power given by

$$P = A\Omega B d\nu \quad (9)$$

where Ω is the solid angle subtended by the source, A is the effective collecting area of the detector (telescope), and $d\nu$ is the bandwidth of the received radiation. Thus we have for R

$$R = \frac{A\Omega B}{h\nu} = 2A\Omega \left(\frac{\nu}{c}\right)^2 \frac{d\nu}{e^{h\nu/kT} - 1} \quad (10)$$

To evaluate the integral in Eq. (7), we use Parseval's theorem to rewrite it as

$$\Delta P^2 = 2R \int_0^\infty |S(f)|^2 df \quad (11)$$

where $S(f)$ is the Fourier transform of $p(t)$. Hence we have

$$|S(f)| = \int_{-\infty}^{+\infty} p(t) e^{-2\pi ift} dt = h\nu \quad (12)$$

The variance or mean square value of the power fluctuation is derived by combining Eqs. (11) and (12) to yield

$$\Delta P^2 = 2R(h\nu)^2 \int df \quad (13)$$

If there is a postdetection filter in the system which passes a range of frequencies Δf , then the power content of the fluctuating power is given by

$$\Delta P^2 = 2R(h\nu)^2 \Delta f \quad (14)$$

Substituting for R in Eq. (14), we obtain

$$\Delta P^2 = 4A\Omega \left(\frac{\nu}{c}\right)^2 \frac{1}{e^{h\nu/kT} - 1} (h\nu)^2 d\nu \Delta f \quad (15)$$

It is of interest to note that the familiar shot noise equation can be derived from Eq. (14) by substituting $E = h\nu$ for the photon energy and $P = Rh\nu$ for the average power delivered to the detector. This result is a consequence of the fact that shot noise is related to the statistics of independent particles (our initial assumption), which obey Poisson statistics. Thus we have

$$\Delta P = (2EP\Delta f)^{1/2} \quad (16)$$

B. Photons as Bosons

We now consider the problem of the nonindependence of the photons. In a Bose-Einstein system composed of weakly interacting photons at thermal equilibrium, the average number of photons in a given energy state (the occupancy) is given by (Ref. 2)

$$\bar{n} = \frac{1}{e^{h\nu/kT} - 1} \quad (17)$$

and the mean square fluctuations are given by

$$(n - \bar{n})^2 = \bar{n}(\bar{n} + 1) \quad (18)$$

An analysis which takes into account the Bose-Einstein statistics leads to a variance given by (Refs. 3, 4)

$$\Delta P^2 = 4\Omega A \left(\frac{\nu}{c}\right)^2 (h\nu)^2 n(n+1) d\nu \Delta f \quad (19)$$

Comparing this expression with Eq. (15) reveals that the fluctuations are higher by $(1+n)$. The independent photon calculations are corrected for Bose-Einstein statistics by multiplying by the factor $(n+1)$. The term $(n+1)$ is known as the Bose factor. This factor is a monotonically decreasing function of $h\nu/kT$, approaching unity for large values of $h\nu/kT$. Photons behave like individual particles in this spectral region. In the Rayleigh-Jeans limit ($kT \gg h\nu$), the fluctuations are larger than those of independent particles. This increased noise power is due to the wavelike nature of photons. It results from each mode in the field beating with itself to produce a mean square power fluctuation. In the Rayleigh-Jeans limit, the variance becomes

$$\Delta P^2 = 4\Omega A \left(\frac{\nu}{c}\right)^2 (kT)^2 d\nu \Delta f \quad (20)$$

We obtain the classical low-frequency approximation

$$\Delta P = P_0 \sqrt{\frac{2}{d\nu\tau}} \quad (21)$$

by taking

$$\Omega A \left(\frac{\nu}{c}\right)^2 = 1$$

and by defining $P = kT d\nu$ and $\Delta f = 1/2t$.

C. Noise Equivalent Power

A standard measure of sensitivity, used in the optical and infrared spectral regions, is the noise equivalent power (NEP),

defined as the incident signal power required to produce a detector signal equal to the rms noise power in a 1-Hz post-detection bandwidth. We have from Eq. (19)

$$NEP = \left[4\Omega A \left(\frac{\nu}{c}\right)^2 (h\nu)^2 n(n+1) d\nu \right]^{1/2} \quad (22)$$

The units of NEP are watts/ $\sqrt{\text{Hz}}$, although occasionally authors incorrectly drop the $\sqrt{\text{Hz}}$ term. The reference bandwidth $d\nu$, field of view Ω , and detector area A should be specified with each NEP.

The NEP reduces to the following expression in the thermal limit

$$NEP = 2kT \sqrt{\Omega A \left(\frac{\nu}{c}\right)^2 d\nu} \quad (23)$$

D. Heterodyne Detection

We consider here a square law mixer as defined by Eq. (1). For a heterodyne receiver, $P(t)$ is given by (e.g., Blaney, Ref. 5)

$$P(t) = [(2P_L)^{1/2} \cos \omega_L t + (2P_B)^{1/2} \cos(\omega_B t - \phi)]^2 \quad (24)$$

where P_L is the local oscillator power (single polarization), P_B is the signal power, and ϕ is the phase difference between the local oscillator and the signal. As in our previous discussion, we assume that P_B arises from the radiation from a thermal source inside the antenna pattern. Hence we are interested in the noise fluctuations due to coherently detected thermal radiation.

The resultant form of $P(t)$ on dropping high-frequency terms is

$$P(t) \propto P_L + P_B + 2\sqrt{P_L P_B} \cos[(\omega_L - \omega_B) - \phi] \quad (25)$$

The first two terms create a dc current in the mixer while the last term produces the IF current. The variance of $P(t)$ includes the sum of the variances of the local oscillator power, the background power, and the cross product of the local oscillator voltage and the background voltage. The resultant noise power has the form

$$\Delta P^2 \propto h\nu P_L d\nu + h\nu P_L A \Omega \left(\frac{\nu}{c}\right)^2 \bar{n} d\nu + (NEP)^2 \Delta f \quad (26)$$

Two important points to note about this equation are the following. The variance due to the local oscillator power is due

only to the random arrival times of the photons. Poisson statistics apply since the phase of the local oscillator power is fixed. The second point is that the local oscillator power is a multiplicative factor in the first two terms but not the third. Since the "signal" in a heterodyne system is multiplied by the local oscillator power, the local oscillator power may be increased to the point where the background power term is negligible. For this condition we have the following

$$\Delta P^2 \propto P_L h\nu d\nu + P_L h\nu A \Omega \left(\frac{\nu}{c}\right)^2 \bar{n} d\nu \quad (27)$$

III. Discussion

The principal results derived above for the rms noise power which results from the detection of blackbody radiation are as follows:

Incoherent detection (rms power)

$$\Delta P = 2h\nu \sqrt{\bar{n}(\bar{n}+1)} \sqrt{\Omega A \left(\frac{\nu}{c}\right)^2 d\nu \Delta f} \quad (28)$$

Heterodyne detection (spectral power)

$$\Delta P \propto h\nu \left[1 + A \Omega \left(\frac{\nu}{c}\right)^2 \bar{n} \right] d\nu \quad (29)$$

These equations are frequently interpreted in terms of either the NEP or in terms of an equivalent temperature. The equivalent temperature representation of the incoherent detection process follows from taking the input and output bandwidths to be equal and the beam filling factor to be unity. It follows that Eqs. (28) and (29) can then be written as

$$\Delta P = 2h\nu \sqrt{\bar{n}(\bar{n}+1)} d\nu \quad (30)$$

$$\Delta P \propto h\nu (\bar{n}+1) d\nu \quad (31)$$

Noting that these equations are now in the form of a spectral density times a bandwidth, the equivalent temperature is defined as follows:

$$T_E = \frac{2h\nu}{k} \sqrt{\bar{n}(\bar{n}+1)} \quad (32)$$

$$T_E = \frac{h\nu}{k} (\bar{n}+1) \quad (33)$$

Figures 1 and 2 show equivalent temperatures T_E for incoherent and heterodyne detectors. We note from these figures

that in the thermal limit the equivalent temperature equals the source temperature for both the incoherent and linear amplifier cases. However, in the quantum limit, the linear amplifier noise increases like $h\nu$, whereas the incoherent noise power decreases. Thus, incoherent noise power is much less than the

noise power following a heterodyne detector if the frequency is sufficiently high and the background emission low. In the radio spectral region, the 2.7 K cosmic background radiation provides a natural noise source and there is no disadvantage of using a heterodyne detector (or a linear amplifier).

Acknowledgments

I would like to thank R. Beer, R. W. Boyd, C. Stelzried, P. Swanson, and R. Menzies for their very helpful comments and for leading me to a number of useful references.

References

1. Rice, S. O., "Mathematical Analysis of Random Noise," *Bell System Tech. J.*, Vol. 23, July 1944, Vol. 24, Jan. 1945.
2. Tolman, R. C., *The Principles of Statistical Mechanics*, Oxford University Press, 1938.
3. Boyd, R. W., "Photon Bunching and the Photon-Noise-Limited Performance of Infrared Detectors," *Infrared Phys.*, Vol. 22, pp. 157-162, 1982.
4. Kingston, R. H., *Detection of Optical and Infrared Radiation*, Springer-Verlag, 1978.
5. Blaney, T. G., "Signal-To-Noise Ratio and Other Characteristics of Heterodyne Radiation Receivers," *Space Science Reviews*, Vol. 17, pp. 691-701, 1975.

Bibliography

- Alkemade, C. Th. J., Bolwijn, P. T., and van der Veer, J. H. C., "Single-Beam Measurements of Bose-Einstein Fluctuations in a Natural Gaussian Radiation Field," *Physics Letters*, Vol. 22, No. 1, pp. 70-72, 1966.
- Brown, R. H., and Twiss, R. Q., "Correlation Between Photons in Two Coherent Beams of Light," *Nature*, Vol. 177, No. 4497, pp. 27-29, 1956.
- Elbaum, M., and Teich, M. C., "Heterodyne Detection of Random Gaussian Signals in the Optical and Infrared," *Optics Communications*, Vol. 27, No. 2, pp. 257-261, 1978.
- Heffner, H., "The Fundamental Noise Limits of Linear Amplifiers," *Proc. of the IRE*, Vol. 50, pp. 1604-1608, 1962.
- Hodara, H., "Statistics of Thermal and Laser Radiation," *Proc. IEEE*, Vol. 53, pp. 696-704, 1965.
- Jacobs, S. F., and Sargent, M., III., "Photon Noise Limited D^* for Low Temperature Backgrounds and Long Wavelengths," *Infrared Physics*, Vol. 10, pp. 233-235, 1950.
- Jakeman, E., Oliver, C. J., and Pike, E. R., "Optical Homodyne Detection," *Advances in Physics*, Vol. 24, pp. 349-405, 1975.

- Kattke, G. W., and Van Der Ziel, A., "Verification of Einstein's Formula for Fluctuations in Thermal Equilibrium," *Physica*, Vol. 49, pp. 461-464, 1970.
- Keyes, R. J. (Editor), *Optical and Infrared Detectors*, Springer-Verlag, 1977.
- Kruse, P. W., McGlauchlin, L. D., and McQuistan, R. B., *Elements of Infrared Technology*, Wiley, New York, 1962.
- Mandel, L., and Wolf, E., "Coherence Properties of Optical Fields," *Rev. of Mod. Physics*, Vol. 37, No. 2, pp. 231-287, 1965.
- Oliver, B. M., "Thermal and Quantum Noise," *Proc. IEEE*, Vol. 53, No. 5, pp. 436-454, 1965.
- Pierce, J. R., and Posner, E. C., *Introduction to Communication Science and Systems*, Plenum Press, 1980.
- van Vliet, K. M., and Zijlstra, R. J. J., "On the Interaction of a Black-body Radiation Field with a Photoconductor," *Physica*, 89A, pp. 353-362, 1977.
- van Vliet, K. M., "Noise Limitations in Solid State Photoconductors," *Applied Optics*, Vol. 6, No. 7, pp. 1145-1169, 1967.
- van Vliet, K. M., "Noise in Semiconductors and Photoconductors," *Proc. IRE*, Vol. 46, pp. 1004-1018, 1958.
- van Vliet, K. M., "Photon Fluctuations and Their Interactions with Solids," *Physica*, 83B, pp. 52-69, 1976.

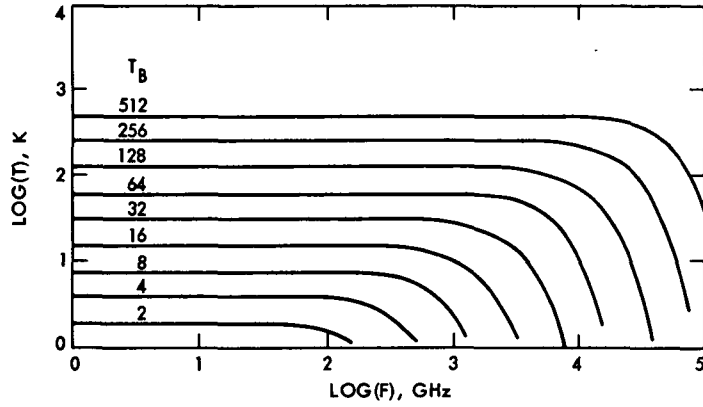


Fig. 1. Equivalent temperatures of incoherent detected thermal noise for a number of different background temperatures for 2 to 512 K

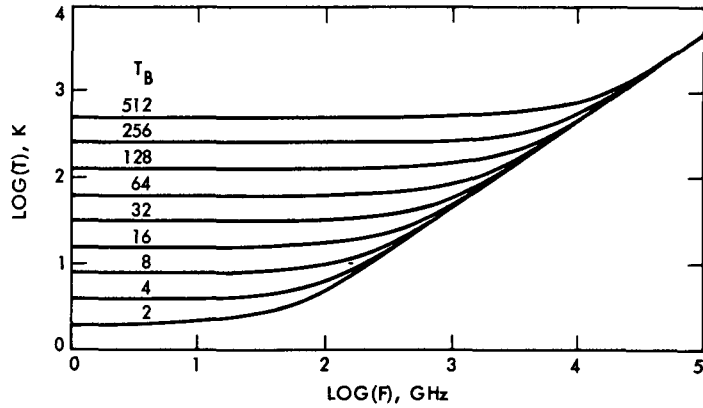


Fig. 2. Equivalent temperatures of heterodyne detected thermal noise for a number of different background temperatures from 2 to 512 K

Dg

K_A-Band Weather-Dependent System Performance Estimates for Goldstone

R. C. Clauss

TDA Technology Development

M. M. Franco and S. D. Slobin

Radio Frequency and Microwave Subsystems Section

A K_A-band atmospheric noise temperature and attenuation statistical model is developed for Goldstone, based on water vapor radiometer measurements at 31.4 GHz made during winter and spring 1981. An equivalent X-band model is derived from these measurements, and the two sets of data are compared to determine the possible advantages of developing DSN telecommunications links at 32 GHz. For a nominal elevation angle of 30 degrees and identical antennas, it is found that a K_A-band system at Goldstone will show a 5 to 10 dB signal-to-noise ratio advantage over an X-band system more than 99 percent of the time.

I. Introduction

Previous studies (Refs. 1 and 2) have shown the advantages and feasibility of developing a DSN communications link at K_A-band (32 GHz). Existing communications frequencies are at S-band (2.3 GHz) and X-band (8.5 GHz), and operation in these bands has proven to be spectacularly successful as can be seen, for example, by the number and quality of pictures taken by the two Voyager spacecraft at Jupiter and Saturn. A description of the Voyager Telecommunications System is given in Ref. 3. As future spacecraft send back data from farther and farther into space, methods will have to be developed to receive their progressively weaker signals.

The signal-to-noise ratio on the ground in a telecommunications link (for a 1-Hz bandwidth) may be defined by the equation (Ref. 3):

$$SNR = \frac{P_T A_T A_R f^2}{c^2 R^2 L_a k T_s L_s} \quad (1)$$

where

P_T = spacecraft transmitted power, W

A_T = spacecraft antenna effective area, m²

A_R = ground receiving antenna effective area, m²

f = frequency, Hz

c = velocity of light, 3 × 10⁸ m/sec

R = distance from antenna to spacecraft, m

L_a = atmospheric loss factor, ratio > 1.0

k = Boltzmann's constant, 1.38×10^{-23} joules/K

T_s = system equivalent noise temperature, K

L_s = all other attenuation mechanisms other than the atmosphere, ratio > 1.0

As the maximization of SNR is a goal of any telecommunications system, all factors in Eq. (1) are constantly being examined in an attempt to increase those in the numerator and decrease those in the denominator. Clearly it is desirable to increase spacecraft transmitter power and antenna area (to increase gain) and to increase ground antenna size so as to intercept more of this larger and more concentrated signal. Not so obvious is the interaction among the factors f^2 , L , and T_s , all of which are related to frequency. As frequency increases, so do the losses due to the atmosphere (in general) and so does the system noise temperature. The one-to-one correspondence between attenuation and noise temperature is given by the relationship (Ref. 4).

$$T_a = T_p (1 - 1/L) \quad (2)$$

where

T_a = atmospheric noise temperature (one component of system noise temperature), K

T_p = equivalent physical temperature of the attenuating atmosphere, K

L = atmospheric loss factor, $10^{A(\text{dB})/10}$, ratio > 1.0

$A(\text{dB})$ = attenuation of the atmosphere, dB

Further discussions of atmospheric noise temperature concepts and the statistics of actual Goldstone X-band measurements are given in Refs. 5-7.

An attempt to develop a 32-GHz noise temperature model by extrapolating 8.5-GHz statistics will lead to large errors due to accuracy uncertainties at the lower frequency. Cloud and rain effects scale by frequency squared over the microwave frequency range, and, coincidentally, water vapor effects at 8.5 and 32 GHz also have a nearly f^2 relationship. As $f^2 = 14.2$ for these two frequencies, uncertainties of 1 K at X-band model to 14 K uncertainties at K_A -band. Thus for comparison of X and K_A -band systems, K_A -band measurements (which can be made with accuracies comparable to X-band) can be used to derive an accurate X-band model.

II. Calculation of the Models

A two-channel water vapor radiometer (WVR) was used at Goldstone (DSS 13) to measure the increase in sky brightness

(noise) temperature caused by tropospheric effects at 31.4 GHz. The second WVR channel operated at 20.6 GHz. These measurements were carried out during February through April 1982 and appear to be typical of the "rainy" period of the year in the desert. The average total yearly rain in the Mojave Desert is about 3.5 inches, compared with 20 inches in Madrid and 26 inches in Canberra, the locations of the other two DSN 64-m antennas.

For the purposes of this report, it will be assumed that the 31.4-GHz measurements accurately reflect measurements which would have been made at 32 GHz. In addition to the 1500 hours of measured noise temperature data, humidity data from one year's radiosonde runs at Edwards Air Force Base (also a California desert location) were used to generate yearly statistics of water vapor noise temperature effects. The measured K_A -band data were judiciously expanded (tripled) to create a fictitious six-month-long "winter," to ensure a worst-case analysis. It was assumed that the highest noise temperatures due to water vapor (radiosonde measurements) occurred in the summer and fall and were independent of the rain events. Both the water vapor data and K_A -band data were thus merged to create a year model of noise temperature statistics for a Goldstone atmosphere and a 30-degree radiometer elevation angle. The cumulative distribution for this model is given in line 1 of Table 1. (Cumulative distribution is the percent time a measurement is less than or equal to a particular value.)

Table 1 shows the complete series of calculations carried out to develop K_A - and X-band noise temperature, attenuation, and SNR models. Line 2 gives the K_A -band model developed from Goldstone noise temperature measurements and radiosonde data. The value 9.84 K is the oxygen-only baseline as given in Ref. 7; the Goldstone measurements were made relative to the clear, dry baseline. Line 3 gives the "wet" contribution of water vapor, clouds, and rain (line 2 minus oxygen). Clouds and rain have a frequency-squared relationship, and for the frequencies considered, so does water vapor. The X-band "wet" contribution (line 4) can be obtained by dividing line 3 by 14.2 ($f^2 = (32/8.5)^2 = 14.2$). The total X-band contribution (line 5) is obtained by adding X-band oxygen (3.54 K, Ref. 7) to line 4. Using Eq. (2) and a mean atmospheric physical temperature of 10°C (283.16 K), it is found that 0.1 dB loss results in a 6.45 K noise temperature contribution. Applying this rule-of-thumb factor to lines 2 and 5 yields K_A - and X-band atmospheric attenuations at 30-degree elevation (lines 6 and 7).

Table 2 presents the noise temperature values which will be appropriate for 1985-era Deep Space Network receiving systems. Values in this table are added to lines 2 and 5 to obtain total K_A - and X-band system noise temperatures

(lines 8 and 9). These system noise temperature cumulative distributions are shown in Fig. 1. The attenuation above the clear, dry baseline (lines 10 and 11) is obtained by dividing the "wet" contributions (lines 3 and 4) by 6.45 K/0.1 dB.

For a given system, the SNR degradation from baseline conditions caused by increased atmospheric noise temperature and attenuation is given by

$$\Delta SNR = 10 \log_{10} [T_{system}/T_{base}] + \Delta dB \quad (3)$$

where

T_{system} = system noise temperature, K (lines 8, 9)

T_{base} = baseline system noise temperature, K (lines 8, 9 at 0%).

ΔdB = attenuation above clear, dry baseline, dB (lines 10, 11)

The ΔSNR results are shown in lines 12 and 13. For receiving systems described in Table 2, and with antennas of the same gain, it can be seen that a K_A -band system shows much inferior SNR performance than does an X-band system. Line 14 shows a direct SNR degradation comparison of K_A - and X-band systems as given by

$$\Delta SNR (K/X) = -10 \log_{10} \frac{T_{system, K}}{T_{system, X}} - (A_K - A_X) \quad (4)$$

where

T_{system} = lines 8, 9

A_K = line 6

A_X = line 7

Even under clear, dry conditions (0%), the K_A -band system appears to be inferior to an X-band system due to higher attenuation and noise temperature (all other things being equal). Then from where does the advantage of K_A -band over X-band come? It is the f^2 factor in Eq. (1). For transmitting antennas of equal size and receiving antennas of equal size with "perfect" surfaces, the net advantage of operating at higher frequencies increases as f^2 (or 11.51 dB for 32 and 8.5 GHz). When this 11.51 dB is factored into the equation for SNR, it can be seen (line 15) that for adverse weather conditions that are exceeded only 0.5% of the time (cumulative distribution = 99.5%) the K_A -band system still retains a 5-dB advantage over X-band. For more benign weather conditions this advantage increases. Figure 2 shows the distribution of K_A -band SNR advantage relative to X-band for Goldstone and a 30-deg elevation angle. This curve is read, for example, "90-percent of the time the K_A -band SNR advantage over X-band exceeds 8.20 dB, up to a maximum of 10.62 dB."

III. Conclusion

It is seen from the models developed that a K_A -band system retains a substantial SNR advantage (at least 5 dB) over an X-band system more than 99 percent of the time at Goldstone. This, of course, depends on equal antenna and transmitter performance at the two frequencies. Even if the hybrid K_A -band model is somewhat in error, the X-band model is derived from it and both will be "wrong" in the same way. From the analysis presented here, it can be seen that for Goldstone, at least, operations at K_A -band will not be limited by the troposphere. For the overseas DSN locations, where the weather is far more severe, the advantage will not be so large for such a large percentage of the time. Atmospheric noise temperature measurements at both K_A - and X-band must be made at the overseas sites to develop models and system performance estimates there also.

References

1. Potter, P. D., "64-Meter Antenna Operation at K_A -Band," *TDA Progress Report 42-57*, pp. 65-70, Jet Propulsion Laboratory, Pasadena, Calif., June 15, 1980.
2. Potter, P. D., "Use of K_A -Band for Radio Metric Determinations," *TDA Progress Report 42-58*, pp. 59-66, Jet Propulsion Laboratory, Pasadena, Calif., Aug. 15, 1980.
3. Edelson, R. E., et al., "Voyager Telecommunications: The Broadcast from Jupiter", *Science*, Vol. 204, pp. 913-921, June 1, 1979.
4. Slobin, S. D., "Microwave Noise Temperature and Attenuation of Clouds at Frequencies Below 50 GHz," JPL Publication 81-46, Jet Propulsion Laboratory, Pasadena, Calif., July 1, 1981.
5. Slobin, S. D., et al., "X-Band Atmospheric Noise Temperature Statistics at Goldstone, DSS 13, 1975-1976," *DSN Progress Report 42-38*, pp. 70-76, Jet Propulsion Laboratory, Pasadena, Calif., Apr. 15, 1977.
6. Slobin, S. D., et al., "X-Band Atmospheric Noise Temperature Data and Statistics at Goldstone, DSS 13, 1977-1978," *DSN Progress Report 42-52*, pp. 108-116, Jet Propulsion Laboratory, Pasadena, Calif., Aug. 15, 1979.
7. Slobin, S. D., et al., "X-Band Atmospheric Noise Temperature Statistics at Goldstone, DSS 13, 1979 and 1980, and Clear Air Noise Temperature Models for Goldstone," *TDA Progress Report 42-64*, pp. 161-167, Aug. 15, 1981.

ORIGINAL PAGE IS
OF POOR QUALITY

Table 1. K_A -and X-band atmospheric models for Goldstone (30-deg elevation angle)

1. Cumulative distribution (% time)	0	50	80	90	95	98	99	99.5
2. K_A -band noise temperature model, K	9.84	19	25	29	35	43	53	69
3. K_A -band water vapor, cloud, rain contribution, K	0	9.16	15.16	19.16	25.16	33.16	43.16	59.16
4. Water vapor, clouds, rain, modelled to X-band, K	0	0.65	1.07	1.35	1.77	2.34	3.04	4.17
5. X-band total noise temperature, K	3.54	4.19	4.61	4.89	5.31	5.88	6.58	7.71
6. K_A -band attenuation, dB	0.15	0.29	0.39	0.45	0.54	0.67	0.82	1.07
7. X-band attenuation, dB	0.05	0.06	0.07	0.076	0.082	0.09	0.10	0.12
8. K_A -band system noise temperature, K	25.84	35	41	45	51	59	69	85
9. X-band system noise temperature, K	21.54	22.19	22.61	22.89	23.31	23.88	24.58	25.71
10. K_A -band attenuation above baseline, dB	0	0.14	0.24	0.30	0.39	0.51	0.67	0.92
11. X-band attenuation above baseline, dB	0	0.01	0.02	0.026	0.032	0.04	0.05	0.07
12. Δ SNR, K_A -band, dB	0	1.46	2.24	2.71	3.34	4.10	4.94	6.09
13. Δ SNR, X-band, dB	0	0.14	0.23	0.29	0.37	0.49	0.62	0.84
14. K_A -band link SNR relative to X-band, dB	-0.89	-2.21	-2.90	-3.31	-3.86	-4.51	-5.20	-6.14
15. Net K_A -band link SNR advantage relative to X-band (11.51 dB + line 14)	10.62	9.30	8.61	8.20	7.65	7.00	6.31	5.37

Table 2. 1985-era DSN receiving system noise temperatures (30-deg elevation angle)

Contributor	K_A -band	X-band
Maser and plumbing, K	7.3	8.9
Cosmic background, K	2.2	2.6
Ground radiation, K	6.5	6.5
Total	16.0	18.0

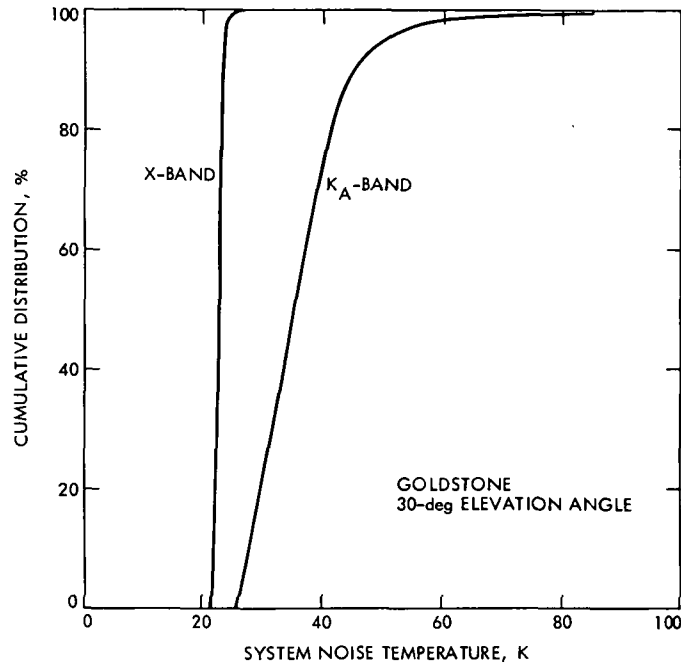


Fig. 1. Cumulative distribution of X- and KA-band system noise temperature for Goldstone, 30-deg elevation angle (see Table 1, Lines 8 and 9)

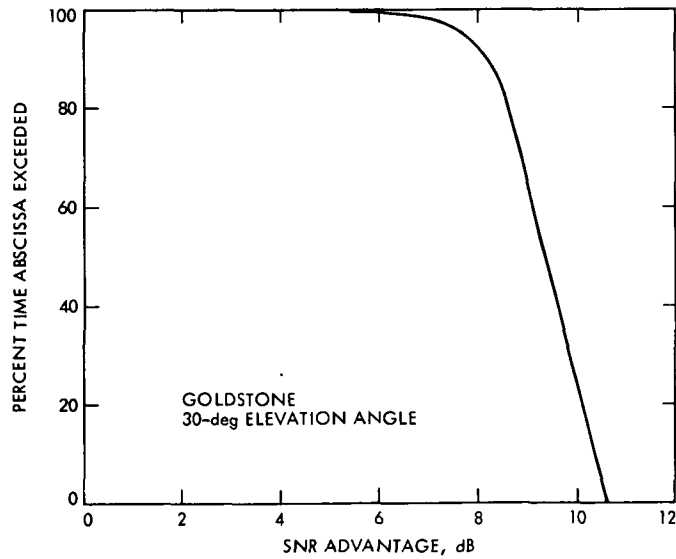


Fig. 2. Distribution of KA-band SNR advantage relative to X-band for Goldstone, 30-deg elevation angle (see Table 1, Line 15, and text)

Dg

N83 14332

2000 100000
20000 1000000

X-Band Noise Temperature Effects of Rain on DSN Antenna Feedhorns

S. D. Slobin and M. M. Franco

Radio Frequency and Microwave Subsystems Section

R. C. Clauss

TDA Technology Development

Simulated rain tests were carried out to determine the noise temperature contribution of liquid water adhering to the aperture cover material on both a standard DSN X-band feedhorn and on an S/X-band common aperture feedhorn. It was found that for the particular common aperture feedhorn tested, system noise temperature increases were much greater when the plastic horn cover material was old and weathered than when it was new. The age and condition of the aperture cover material is believed to be a major factor in the amount of degradation experienced by a telecommunications system during rain events.

I. Introduction

At microwave frequencies above about 5 GHz, rain is considered to be the major contributor to large signal-to-noise ratio (SNR) degradations in telecommunications systems. In most temperate locales, rain falls a total of about 5 to 7% of the time (as measured by minute-sized sample periods). This amounts to 400 to 600 hours per year (Ref. 1). For a location whose average total yearly rainfall is 500 mm (Pasadena, Calif.) this corresponds to a mean rain rate of about 1 mm/hr, or a very light rain. Link degradation comes from both spacecraft signal attenuation and increased system noise temperature due to emission from the liquid water particles themselves. As an example, at X-band, 30-deg elevation angle, a rain rate of 5 mm/hour (a moderate rain) will give an attenuation of 0.4 dB, a system noise temperature increase of 25 K, and a

3-dB SNR degradation for a 30 K baseline system noise temperature. The same rain at 32 GHz will give 9-dB attenuation, 220 K noise temperature increase, and an 18-dB SNR degradation. Fortunately, 5 mm/hour rain is exceeded only 0.2% of the year (18 hours) at Canberra, the rainiest of the DSN tracking antenna locations. Again, fortunately, using the Canberra example, fully half the total yearly rainfall (approximately 580 mm) is deposited at a rate less than about 3 mm/hour (a rate exceeded only 0.5% of the year, 45 hours). For X-band, the *atmospheric* effects of rain are expected to be small more than 99% of the time.

It has been found, however, during tracking of spacecraft that significant telecommunications link degradation occurs during periods of even light rain. This degradation can last as

long as an entire pass (approximately eight hours) as has been observed during a Voyager 1 Jupiter near-encounter pass over DSS 43 (Canberra) in 1979. The rain rate during this pass was measured by an on-site rain gauge to be quite low (approximately 1 mm/hour) but continuous for the entire day. All antenna components were continually wet and this condition contributed to significant and continuous link degradation.

The antenna components which were wetted, in particular, were the plastic sheet covering the antenna feedhorn and the metallic surfaces of the antenna reflector system, the paraboloid, hyperboloid, and reflex feed elements. The "attachment" of rain to these various surfaces is of two types: "wetting" and "non-wetting." As a common example of a "wetted" surface, one may consider a common schoolroom blackboard that has been washed off in order to remove chalk dust. The surface character changes as the water fills the microscopic pores and scratches of the board. The board becomes covered with a thin sheet of liquid water. After a short while, the water evaporates, leaving a dry, non-shiny surface. A "non-wetted" surface is one such as a newly waxed automobile hood, which when rained upon becomes covered with beads or drops of water ranging in size from 1 mm diameter to as much as 25 mm diameter, approximately. It was found that the wetted surface causes larger noise temperature effects than does the non-wetted surface. This noise temperature increase can cause serious problems during low signal level tracking periods, for example, Voyager at Uranus and Neptune. It has thus become necessary to ascertain the effects of rain on antenna components and to propose methods of overcoming the resulting degradation.

A previous study at the DSN Madrid tracking station (Ref. 2) has shown a remarkable agreement between experimental and theoretical results of noise temperature measurements of sheets of water held in a container over the aperture of both S-band and X-band horns. Significant levels of noise temperature (100 K at X-band) and attenuation were measured for water layers as thin as 0.1 mm. Those tests did not involve wetting of the feedhorn cover; the results presented in this report are obtained from wetting of actual DSN antenna feedhorns.

II. Experiment Description

An experiment was devised to test the effects of simulated rain on the X-band feedhorns used on the DSN antennas. A standard X-band feedhorn, an S/X-band common aperture feedhorn, and an ambient load were connected to a maser as shown in Fig. 1. The system noise temperature (T_{op}) for each horn path was calculated by comparing the power level with that from the ambient load path. A Y-factor measurement technique is used in which

$$\begin{aligned}
 Y \text{ (ratio)} &= \frac{\text{power from ambient load}}{\text{power from horn}} \\
 &= \frac{T_{op, \text{ ambient load}}}{T_{op, \text{ horn}}} \\
 &= \frac{T_{\text{ambient}} + T_{\text{maser}}}{T_{op, \text{ horn}}}
 \end{aligned} \tag{1}$$

where

$$\begin{aligned}
 T_{op} &= \text{system operating noise temperature, K} \\
 T_{\text{ambient}} &= \text{ambient load physical temperature, K} \\
 T_{\text{maser}} &= \text{maser noise temperature, K}
 \end{aligned}$$

The maser noise temperature is assumed to be 5 K for the purposes of these calculations. The actual determination of T_{op} by Eq. (1) is insensitive to the value of T_{maser} . T_{op} includes the cosmic background noise temperature (2.7 K), the atmosphere (2.5 K, clear sky), horn and waveguide (approximately 11 K in this test), and maser (approximately 5 K). The maser noise temperature itself can be determined from a separate test in which a calibrated waveguide horn is attached directly to the maser. Power levels are recorded looking at both the clear sky and an aperture load. A Y-factor is determined:

$$\begin{aligned}
 Y &= \frac{\text{power level on aperture load}}{\text{power level on clear sky}} \\
 &= \frac{T_{op, \text{ load}}}{T_{op, \text{ clear sky}}} \\
 &= \frac{T_{\text{maser}} + T_p}{T_{\text{maser}} + T_{\text{cosmic}} + T_{\text{atm}} + T_{\text{horn}}}
 \end{aligned} \tag{2}$$

where

$$\begin{aligned}
 T_{\text{maser}} &= \text{maser noise temperature to be determined} \\
 T_{\text{cosmic}} &= \text{cosmic background noise temperature (2.7 K)} \\
 T_p &= \text{physical temperature of aperture load and horn} \\
 T_{\text{atm}} &= \text{atmospheric noise temperature (2.5 K)} \\
 T_{\text{horn}} &= \text{noise temperature of calibrated horn (1.5 K)}
 \end{aligned}$$

The maser noise temperature is then found from

$$T_{maser} = \frac{T_p - Y(T_{cosmic} + T_{atm} + T_{horn})}{Y - 1} \quad (3)$$

The system operating noise temperature (T_{op}) when looking at the large S/X horn is determined from Eq. (1) for a specific example using the following input values.

$$T_{ambient} = 290.2 \text{ K } (17^\circ\text{C})$$

$$T_{maser} = 5.0 \text{ K}$$

$$Y = 14.09 \text{ (11.49 dB)}$$

Then,

$$T_{op, S/X} = 20.95 \text{ K.}$$

This value is typical of the clear sky noise temperature and includes approximately 9 K contributed by 127 cm of waveguide, orthomode transducer, waveguide bend, and curved waveguide switch port.

The method of carrying out the rain tests was to measure the degradation of each horn relative to the other horn, which then serves to eliminate the effect of small changes in the atmospheric noise temperature contribution.

A plastic spray bottle with a positive displacement (0.8 cm^3) pump was filled with distilled water and used to provide the "rain" for these tests. Both horns were pointed vertically (toward the zenith), which, however, is not a normal tracking position. This position allowed a maximum of water to remain on the horn, although there was no pooling of liquid in the center of the aperture cover, due to the domed shape caused by internal waveguide and horn pressurization. A normal average tracking elevation angle might be 45 deg, in which case some water is expected to run off the horn in worst-case conditions. The spray bottle delivered 0.8 cm^3 per spray, generally in a large number of very tiny drops. Upon striking a surface, many of these drops would coalesce to form 3-mm to 10-mm-size drops on the surface, depending on whether the surface was wetting or non-wetting.

The first test series was carried out on the large S/X feedhorn with weathered Kapton (manufactured by Du Pont) aperture cover material. This material was approximately four years old at the time of the tests and had been exposed every day to sunlight, rain, and blowing dust and sand (2 years at

Goldstone and 2 years at JPL). Water was sprayed on the Kapton first on the center and then at increasing distances from the center to create as uniform a coverage as possible.

After a given number of sprays, the water droplets on the Kapton were smeared by hand. Then an additional 250 cm^3 (approximately) of water was poured all over the horn cover. This amount of water caused runoff and represented a maximum water retention case for vertical pointing. It is expected that more nominal pointing angles (45-deg elevation) would not retain as much water. Power levels were measured at all points in the experiment. These tests were repeated on new shiny Kapton material placed over and touching the old material. Clean, dry, new Kapton did not measurably increase the noise temperature of the system. Table 1 gives the results of these tests. It is seen that the weathered Kapton material exhibits much higher noise temperature effects than does the new material.

The film thickness of 100 sprays (80 cm^3) of water smeared evenly on an area 116.8 cm in diameter is 0.074 mm ; 312 cm^3 ; of water make a film thickness of 0.29 mm . Smearing water on a shiny surface does not distribute it evenly but merely causes it to coalesce into larger drops or areas of water.

In addition to tests on the large S/X common aperture horn, the small (18.4-cm-diameter) standard DSN feedhorn was tested in a similar manner. The aperture material was Kapton, in shiny, good condition. Table 2 presents results of the small horn tests. Five sprays (4 cm^3) on the small horn deposited a substantial amount of water (the horn was very wet); the noise temperature increase when smeared was moderate (37 K). The ratio of horn areas is about 40 to 1; thus 4 cm^3 on the small horn is equivalent to about 160 cm^3 on the large horn. The effects of water on Teflon (Du Pont) material was measured on the small horn. A piece of Teflon sheet (0.13 mm thick, $30 \times 70 \text{ cm}$) was placed over the horn. The clean dry Teflon did not measurably increase the noise temperature of the system. System performance is substantially improved by the use of Teflon as opposed to the new shiny Kapton material for small amounts of water that would be equivalent to conditions experienced during light rainfall.

Another test compared the large and small horns when equal water densities were applied to the aperture covers. The diameter of the large horn is 116.8 cm, and of the small horn is 18.4 cm. The area ratio is 40.3. Numerous single-spray measurements were made on the small horn. Each single-spray covered most of the aperture of the small horn with water drops. Forty-spray measurements were made on the large horn with both the weathered aperture material and the new Kapton material. Table 3 presents the results of these

tests. These results are more or less consistent with the results shown in Table 1 for the large horn. The one-spray value in Table 2 for the small horn is about 70% higher than for this test. This may be due to a difference in water particle distribution in the two cases. The fact that the large horn/new Kapton increase of 3.74 K (Table 3) is double that of the small horn/new Kapton value (1.80 K), for the same water particle density, may be attributable to the fact that the phase center of the large horn is located 171.5 cm from the aperture, whereas the phase center of the small horn is only 3.6 cm from the aperture. Perhaps differences in aperture electric field strength create the measured difference.

III. Noise Temperature of S/X Common Aperture Feedhorn

The noise temperature contribution of the S/X common aperture feedhorn was determined by comparing the system noise temperature of this horn with that of a standard X-band reference horn (not the DSN X-band horn). This reference horn was carefully calibrated by the National Bureau of Standards and was found to contribute a noise temperature of 1.5 K. Using the DSN horn as a baseline, the S/X and reference horns were alternately connected to the same waveguide switch port and common waveguide run.

The results indicate that the S/X common aperture horn (with 12.7-cm round aluminum waveguide/rotary joint, 10.2 cm quarter-wave polarizer, and 0.13-mm-thick Kapton) is 1.14 K hotter than the NBS reference horn with 0.025 mm Kapton.

IV. Conclusion

The series of tests described here indicates the seriousness of the noise temperature effects due to water on the aperture covers of DSN feedhorns. Noise temperature increases in excess of 30 K begin to degrade the telecommunications link; increases of 100 K or more generally result in loss of spacecraft signal.

It has been shown that weathered Kapton aperture cover material exhibits greater rain-induced degradation than does new, unweathered material. New Teflon exhibits less degradation than new Kapton for small amounts of water. The aging and weathering properties of Teflon are not presently known. A careful review of data taken during these preliminary tests shows that additional work is needed to determine methods of reducing the rain-induced degradation using passive means. These tests indicate that large improvements in spacecraft communications can be made in the DSN during periods of rain.

References

1. Potter, P. D., et al., "A Study of Weather-Dependent Data Links for Deep Space Applications," Technical Report 32-1392, Jet Propulsion Laboratory, Pasadena, Calif., Oct. 15, 1969.
2. Urech, J. M., "Preliminary Report on DSN System Performance Under Local Weather Effects," *DSN Progress Report 42-52*, Jet Propulsion Laboratory Pasadena, Calif., Aug. 15, 1979.

ORIGINAL PAGE IS
OF POOR QUALITY

Table 1. Results of simulated rain tests on S/X common aperture feedhorn with old and new Kapton aperture cover material

Test	X-band noise temperature increase, K	
	Old Kapton	New Kapton
1. Clean, dry	0.00	0.00
2. One spray in center (0.8 cc)	1.31	0.33
3. 2 sprays total	2.07	0.75
4. 3 sprays total	3.55	0.89
5. 4 sprays total	5.00	1.10
6. 5 sprays total	6.98	1.52
7. 6 sprays total	7.67	1.81
8. 7 sprays total	8.76	1.95
9. 8 sprays total	9.68	2.17
10. 9 sprays total	10.20	2.75
11. 10 sprays total, 38 cm square	11.04	3.49
12. Smearred by hand, 46 cm square	12.22	4.26
1. Clean, dry	0.00	0.00
2. 30 sprays total (24 cm ³)	25.78	4.34
3. 30 sprays total smearred 90 cm diameter	28.16	4.96
1. Clean, dry	0.00	0.00
2. 100 sprays total (80 cm ³)	54.20	-
3. 100 sprays total smearred (0.074 mm thick)	43.93	9.59
4. Water poured on	141.16 K (312 cm ³ total, 0.29 mm thick)	112.81 K (397 cm ³ total, 0.37 mm thick)
	188.11 K (910 cm ³ total, 0.85 mm thick)	

ORIGINAL PAGE IS
OF POOR QUALITY

Table 2. Results of simulated rain tests on standard DSN feedhorn (18.4 cm diameter) with and without Teflon sheet on top of Kapton aperture material

Test	X-band noise temperature increase, K	
	Horn with Teflon	Horn without Teflon
1. Clean, dry	0	0
2. 1 spray total (0.8 cm ³)	0.43	3.04
3. 2 sprays total	3.35	6.73
4. 3 sprays total	9.59	8.49
5. 4 sprays total	7.33	13.17
6. 5 sprays total	11.39	14.50
7. 5 sprays smeared	—	36.73

Table 3. Equal drop-density comparison of large and small feedhorn noise temperature increase

	X-band noise temperature increase, K
Small horn New shiny Kapton 1 spray average	1.80
Large horn Weathered Kapton aperture material 40 sprays	35.09
Large horn New shiny Kapton 40 sprays	3.74

ORIGINAL PAGE IS
OF POOR QUALITY

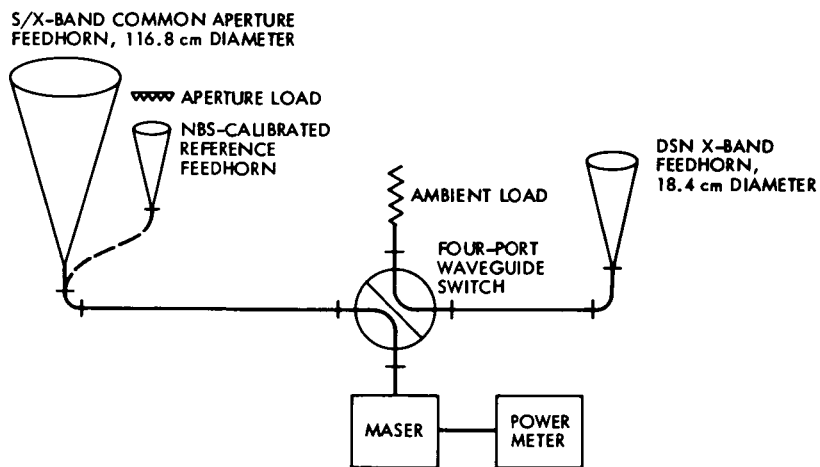


Fig. 1. Experimental setup for testing rain effects on X-band feedhorns

Viterbi Decoder Node Synchronization Losses in the Reed-Solomon/Viterbi Concatenated Channel

L. J. Deutsch

Communications Systems Research Section

R. L. Miller

Information Systems Engineering Section

The Viterbi decoders currently used by the Deep Space Network (DSN) employ an algorithm for maintaining node synchronization that significantly degrades at bit signal-to-noise ratios (SNRs) of below 2.0 dB. In a recent report by the authors, it was shown that the telemetry receiving system, which uses a convolutionally encoded downlink, will suffer losses of 0.85 dB and 1.25 dB respectively at Voyager 2 Uranus and Neptune encounters. This report extends the results of that study to a concatenated (255, 223) Reed-Solomon/(7, 1/2) convolutionally coded channel, by developing a new radio loss model for the concatenated channel. It is shown here that losses due to improper node synchronization of 0.57 dB at Uranus and 1.0 dB at Neptune can be expected if concatenated coding is used along with an array of one 64-meter and three 34-meter antennas.

I. Introduction

All planned NASA and European Space Agency (ESA) deep space missions will have the capability of using a concatenated Reed-Solomon/convolutional coding scheme for downlink telemetry (Ref. 1). Voyager 2 also has this capability on board, and its encounter with Uranus in 1986 will be the first use of this scheme by a space flight project. A simplified block diagram of a concatenated coded downlink system is shown in Fig. 1.

Although the specific details of the codes may differ among the various missions, the basic code parameters, and hence the overall system performances, are identical. The convolutional inner code is a $k = 7$, rate $1/2$ code. The Reed-Solomon

outer code is a (255, 223) code with 8-bit symbols. The differences in the codes for specific missions involve different orderings and inversions in the convolutional code's connection vectors and different finite field representations and generating polynomials for the Reed-Solomon code. The baseline performance of this coding scene in the presence of space loss and receiver thermal noise was determined in Ref. 2. It is the purpose of this report to model two additional losses. These are noisy carrier referencing (or "radio loss") and imperfect Viterbi decoder node synchronization. These losses were treated for the convolutional-only channel in Ref. 3.

Noisy carrier referencing is a degradation caused by the effects of noise on the carrier tracking loop in the receiver

(Ref. 4). The noise causes the phase-locked loop to incorrectly estimate the phase of the incoming signal, which results in a nonoptimal signal demodulation. The traditional radio loss models do not apply in the case of concatenated coding, since carrier phase tracking errors vary slowly compared to the decision times in the Viterbi decoder but quickly compared to the decision times in the Reed-Solomon decoder. Thus it was necessary to develop a new model in Section II herein called the mixed-rate model.

The node synchronization loss is a degradation caused by the Viterbi decoder. The encoder for the (7, 1/2) convolutional code outputs a pair of channel symbols for each input bit. Conversely, the decoder must parse the received symbol stream correctly to synchronize the symbols into pairs. When the Viterbi decoder parses the data incorrectly, it is said to be out of node synchronization. The current DSN Viterbi decoders use an internal algorithm for maintaining node synchronization that fails below a certain channel SNR. This critical SNR value is called the node synchronization threshold. Hardware tests (Ref. 5) and mathematical modeling (Ref. 3) have demonstrated that the node synchronization threshold of the Maximum-Likelihood Convolutional Decoders (the DSN's Viterbi decoders, or MCDs) is about 2.0 dB.

The modeling described in Sections II and III of this report predicts that losses to the concatenated coding system due to poor node synchronization will amount to 0.57 dB at Voyager 2 Uranus encounter and 1.0 dB at Neptune encounter. These results assume that a perfect carrier array consisting of one 64-meter antenna and three 34-meter antennas is used for telemetry reception.

II. The Mixed-Rate Model

This section describes the model used to calculate the effects of noisy carrier referencing on concatenated coded telemetry. Traditionally, there have been two basic models used for radio loss calculations for coded data: the "high-rate model" and the "low-rate model." The high-rate model assumes that the length of time needed by the decoder for decisions is so small that the phase estimate in the carrier tracking loop is constant. The decoded bit error rate performance is therefore given by the average of the bit error rates caused by the different possible phase errors. This is reflected in the equation

$$p_{bit}(x) = \int_{-\pi}^{\pi} f(x \cos^2 \phi) p(\phi) d\phi. \quad (1)$$

In equation (1), x is the bit SNR incident upon the receiving antenna. The effect of a phase error ϕ is a degradation of

$\cos^2 \phi$ in SNR. The quantity $p(\phi)$ is the phase error density function and $f(x)$ is the decoder's bit error rate as a function of SNR in the case of perfect carrier tracking.

The low-rate model, on the other hand, assumes that the phase errors change so much faster than the time it takes to decode one bit that an average SNR can be used. This leads to the equation

$$p_{bit}(x) = f \left[x \int_{-\pi}^{\pi} \cos^2 \phi p(\phi) d\phi \right] \quad (2)$$

For data rates and carrier loop bandwidths that are typical of Voyager planetary encounters, carrier phase errors remain relatively constant for 600 data bit times (Ref. 3). Since the memory length of the Viterbi decoders is only 64 bits, the high-rate model applies to the convolutional-only channel. Each Reed-Solomon word, however, is 2040 bits in length. In addition, interleaving can further delay the decoding time, so that the low-rate model applies to a Reed-Solomon-only channel. Unfortunately, neither model applies well to the concatenated channel.

The mixed-rate model resolves this dilemma by applying the high-rate model to the inner convolutional code and the low-rate model to the outer Reed-Solomon code. First, Eq. (1) is used to calculate the Viterbi-decoded bit error probability of the inner convolutional channel. The value x is taken to be E_v/N_0 , the bit SNR of the inner convolutional channel. The function $f(x)$ is taken to be the ideal (no radio loss) performance of the Viterbi decoder. The phase error density $p(\phi)$ is derived in Ref. 5 to be

$$p(\phi) = \frac{\exp(\cos \phi)}{2\pi I_0(\rho)}$$

where ρ is the loop SNR of the carrier tracking loop, and I_0 is the zero order modified Bessel function.

The average Reed-Solomon symbol error rate (the probability of one or more errors occurring in a string of eight consecutive bits) π is estimated to be $2.5 p_{bit}$, where p_{bit} is the bit error rate of the inner convolutional channel. Figure 2 shows the ratio π/p_{bit} for various channel and carrier loop SNRs. A ratio of 2.5 is about average for SNRs in the 2-3 dB range of E_v/N_0 , where most of the mass of the integral in (1) occurs. The overall concatenated bit error rate is then calculated assuming that the inner channel bit error rate p_{bit} and the symbol error rate π vary quickly with respect to a Reed-Solomon decoder decision time. The mixed-rate model yields a concatenated bit error rate of

$$p_{RS} = \frac{p_{bit}}{\pi} \sum_{i=17}^{255} \binom{255}{i} \left(\frac{i}{255}\right) \pi^i (1-\pi)^{255-i} \quad (3)$$

The bit SNR of the concatenated channel is taken to be

$$E_b/N_0 = (E_v/N_0) 255/223$$

due to the additional overhead of the Reed-Solomon code.

In the case of infinite carrier loop SNR, i.e., no radio loss, $p_{bit} = f(E_v/N_0)$. Figure 3 shows p_{RS} as a function of E_b/N_0 for this case with the assumption that π/p_{bit} is 2, 2.5 or 3. The total difference between the performances predicted by these hypotheses at the bit error rate of 10 is less than 0.17 dB. This implies that the assumption that this ratio is a constant will not seriously affect the relative performance estimates made by using the mixed-rate model.

III. Node Synchronization Model

The model of Viterbi decoder node synchronization losses used in this study is described in Ref. 3. It is assumed that for values of E_v/N_0 above the node synchronization threshold the Viterbi decoder performs normally and in perfect synchronization. For SNRs below the threshold, the decoder's internal synchronization algorithm always believes that the decoder is out of node synchronization. The result of this condition is that the decoder continually oscillates between correct and incorrect node synchronization and produces an essentially random output.

In order to introduce the above information into the mixed-rate model of Section II, it is only necessary to choose a suitable Viterbi decoder performance function $f(x)$. The function $f(x)$ for x larger than the node synchronization threshold is taken to be the ideal performance function as exhibited in Ref. 6. For values of x below the threshold, $f(x)$ is assumed to be equal to 1/2, a value which represents a random decoder output.

IV. Numerical Results

The performance of the concatenated channel with radio losses and node synchronization losses was computed using the mixed-rate model of Section II together with the Viterbi decoder performance function in Section III. Performance curves were generated for carrier loop SNRs of between 10 and 20 dB and for node synchronization thresholds of between 0.0 and 2.5 dB. Some of the results are plotted in Fig. 4. The predicted performance of the concatenated chan-

nel with a node synchronization threshold of 2.0 dB and carrier tracking loop SNRs of 11, 12, and 13.5 dB is shown along with some actual hardware test data generated in the Telecommunication Development Laboratory (TDL) (Ref. 5). The close agreement between the actual data and the predicted performance corroborates the mixed-rate model.

Graphs of Reed-Solomon decoded bit error rate performance for node synchronization thresholds of 0.0 and 2.0 dB appear in Figs. 5 and 6 respectively for various loop SNRs. These were used to generate the radio loss curves shown in Fig. 7. Radio loss is defined to be the additional energy per bit (in dB) needed to achieve some predetermined bit error rate in a system with imperfect carrier tracking compared to a system with ideal carrier tracking. In this case, the ideal system is taken to be one in which the node synchronization threshold of the Viterbi decoder is equal to 0 (or minus infinity dBs). The performance of this ideal system is therefore given by the mixed-rate model with $f(x)$ equal to the ideal performance function of Ref. 6. The fixed bit error rate is 10^{-5} , the concatenated bit error rate needed for transmission of compressed imaging data.

The difference between the two curves in Fig. 7 represents the incremental SNR loss due to poor node synchronization performance. Data from design control tables predict that for Voyager 2 Uranus encounter at a modulation index of 76° and 90% weather, a 64-meter antenna would have an associated loop SNR of about 13.2 dB. A four-element array consisting of one 64-meter antenna and three 34-meter antennas would have a combined loop SNR of 15.4 dB, provided a combined carrier referencing scheme (Refs. 6, 7) is used. The associated node synchronization losses for the concatenated channel would be 0.89 dB for the 64-meter antenna alone and 0.57 dB for the array. The arrayed loss would be slightly worse if baseband-only combining were used. For Neptune encounter with a 74° modulation index, the loop SNR of the 64-meter antenna would be 10.8 dB while that of the array would be about 13.6 dB. These correspond to node synchronization losses of 1.25 dB and 1.0 dB respectively.

The losses for the concatenated channel due to poor node synchronization performance are plotted as a function of node synchronization threshold in Fig. 8 for various carrier tracking loop SNRs. These represent the additional degradations over the carrier phase tracking losses. The performance points for the 64-meter antenna and the four-element array for Voyager 2 Uranus and Neptune encounters are included in the figure. It is evident from the figure that there is much to be gained by improving the performance of the Viterbi decoder's node synchronization algorithm.

V. Conclusions

If one compares the node synchronization losses for the concatenated channel (Fig. 8) with those for the convolutional-only channel (Ref. 3), it is clear that the concatenated channel is more sensitive to this type of degradation. The difference becomes more pronounced at higher carrier tracking loop SNRs, becoming about a 0.1-dB difference at a loop SNR of 15 dB and a node synchronization threshold of 2.0 dB. This is not a significant additional loss. The conclusion that must be drawn is that poor node synchronization by itself does not degrade the concatenated channel much more than it does the convolutional-only channel.

There are other related factors, however, that may greatly increase the effects of poor node synchronization on the con-

catenated link. When the Viterbi decoder decides that it is out of synchronization, it might add or delete a channel symbol from the data stream. This could result in a loss of codeword synchronization (or frame synchronization) in the Reed-Solomon decoder. If frame synchronization is lost, it is likely that several Reed-Solomon frames might be lost before resynchronization occurs. This could mean that thousands of bits would be only Viterbi decoded. The model described in this report does not consider the effects of frame synchronization losses.

Other sources of degradation that should be considered are imperfect subcarrier tracking and demodulation and imperfect symbol tracking. These effects are currently under investigation and will be the subject of a subsequent report.

References

1. Stephens, R. R., and Pellet, M. F., "Joint NASA/ESA Telemetry Channel Coding Guideline: Issue 1," NASA/ESA Working Group (NEWG) Publication, Jan. 1982.
2. Miller, R. L., Deutsch, L. J., and Butman, S. A., "Performance of Concatenated Codes for Deep Space Missions," *TDA Progress Report 42-63*, Jet Propulsion Laboratory, Pasadena, Calif., June 15, 1981.
3. Deutsch, L. J., and Miller, R. L., "The Effects of Viterbi Decoder Node Synchronization Losses on the Telemetry Receiving System," *TDA Progress Report 42-68*, Jet Propulsion Laboratory, Pasadena, Calif., Apr. 15, 1982.
4. Lindsey, W. C., and Simon, M. K., *Telecommunications Systems Engineering*, Prentice Hall, Inc., N. J., 1973.
5. Liu, K. Y., and Lee, J. J., "An Experimental Study of the Concatenated Reed-Solomon/Viterbi Channel Coding System and Its Impact on Space Communications," Publication 81-58, Jet Propulsion Laboratory, Pasadena, Calif., Aug. 15, 1981.
6. Divsalar, D. D., and Yuen, J. H., "Improved Carrier Tracking Performance with Coupled Phase-Locked Loops," *TDA Progress Report 42-66*, Jet Propulsion Laboratory, Pasadena, Calif., Dec. 15, 1981.
7. Deutsch, L. J., Lipes, R. G., and Miller, R. L., "Virtual Center Arraying," *TDA Progress Report 42-65*, Jet Propulsion Laboratory, Pasadena, Calif. Oct. 15, 1981.

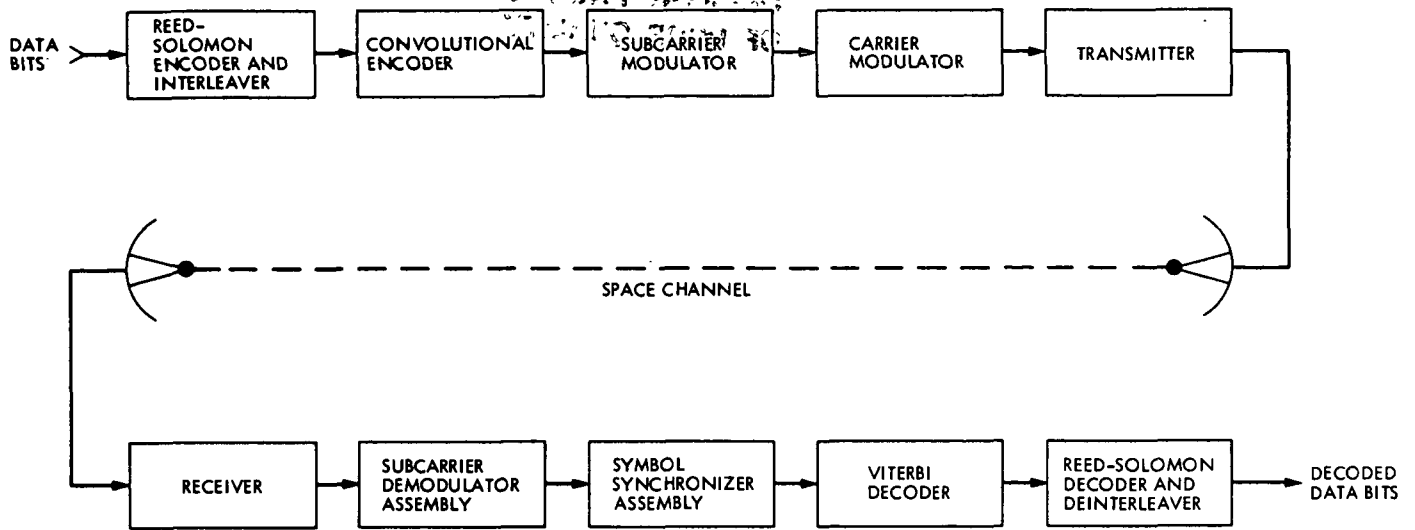


Fig. 1. Concatenated coding system block diagram

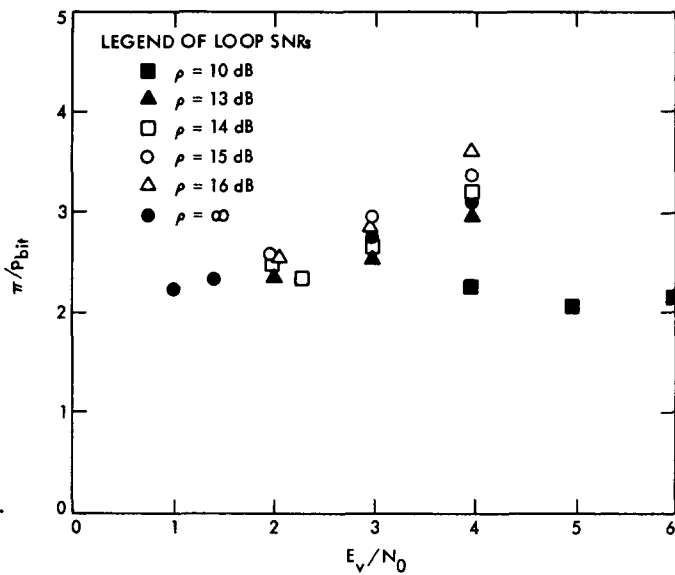


Fig. 2. The relationship between Viterbi decoder bit error rate ρ and Reed-Solomon symbol error rate π

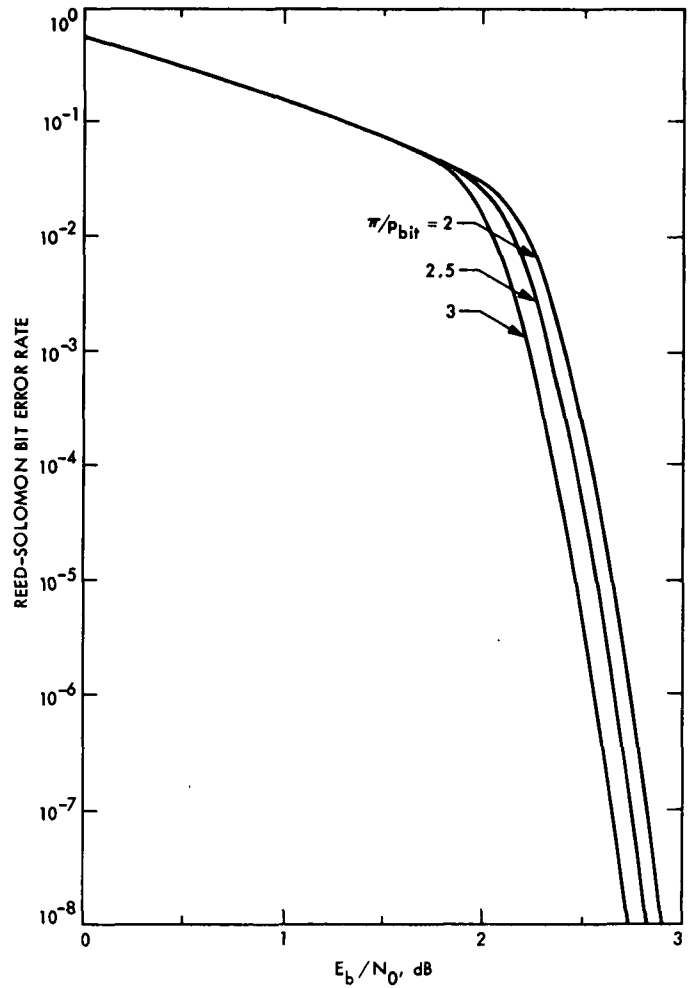


Fig. 3. Concatenated performance assuming that π/p_{bit} is a constant

ORIGINAL PAGE IS
OF POOR QUALITY

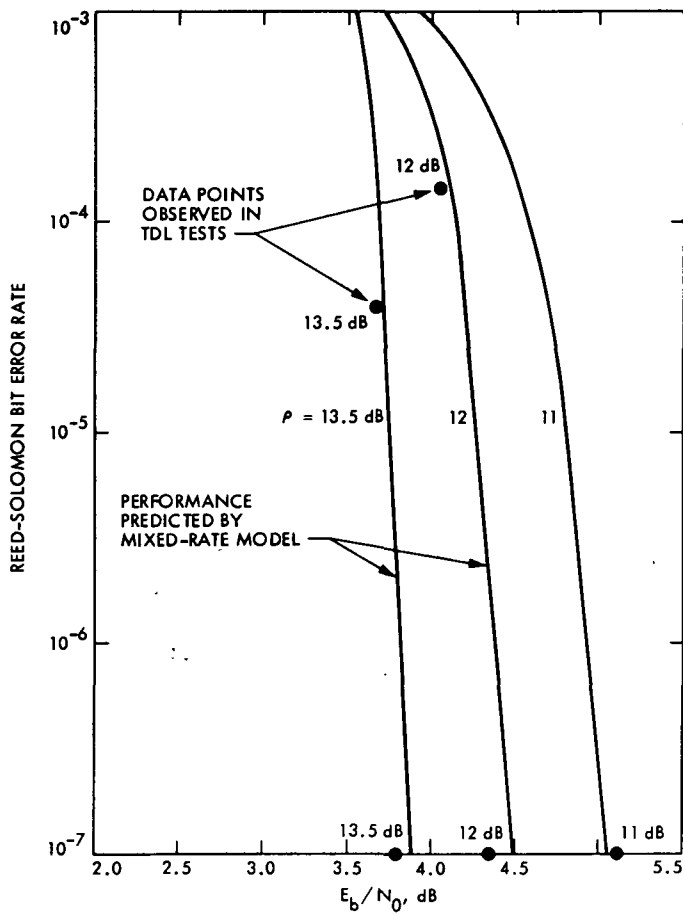


Fig. 4. A comparison of the mixed-rate model with node synchronization losses to hardware test data

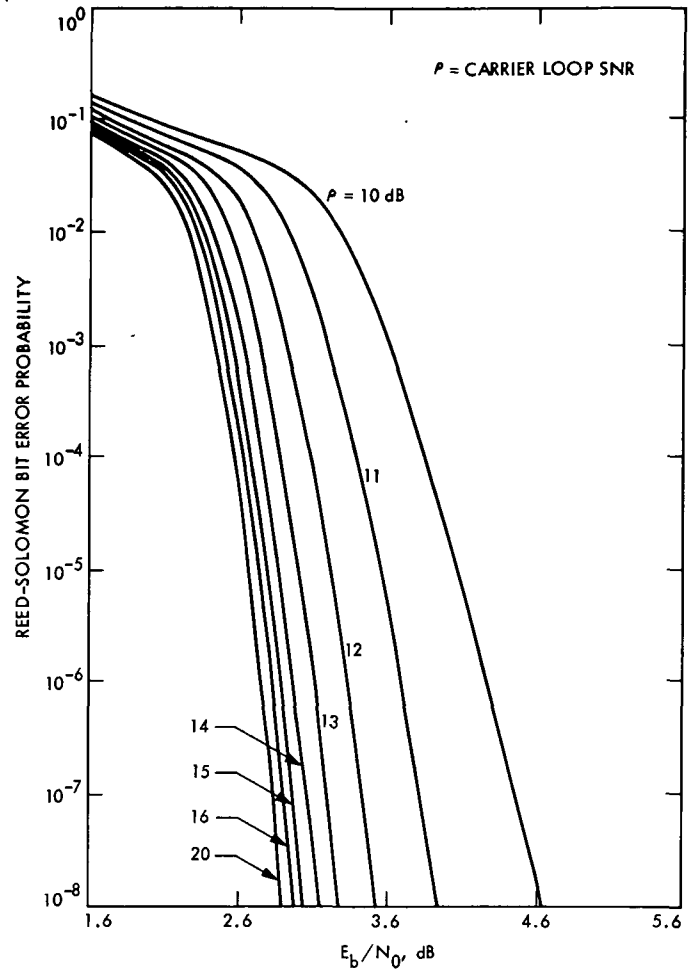


Fig. 5. Performance of the concatenated channel: node synchronization threshold = 0.0 dB

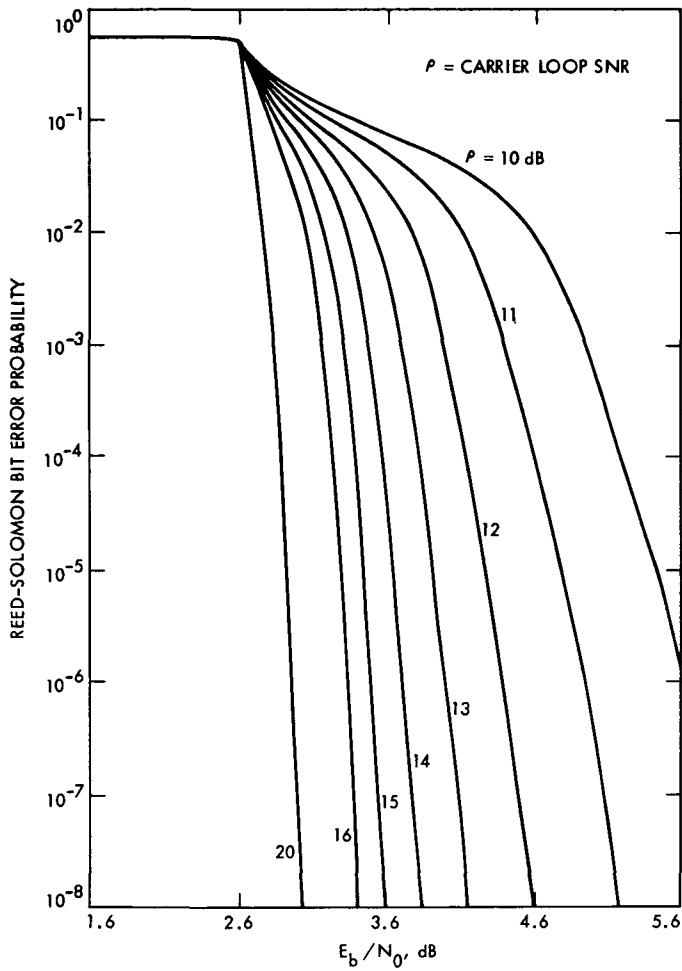


Fig. 6. Performance of the concatenated channel: node synchronization threshold = 2.0 dB

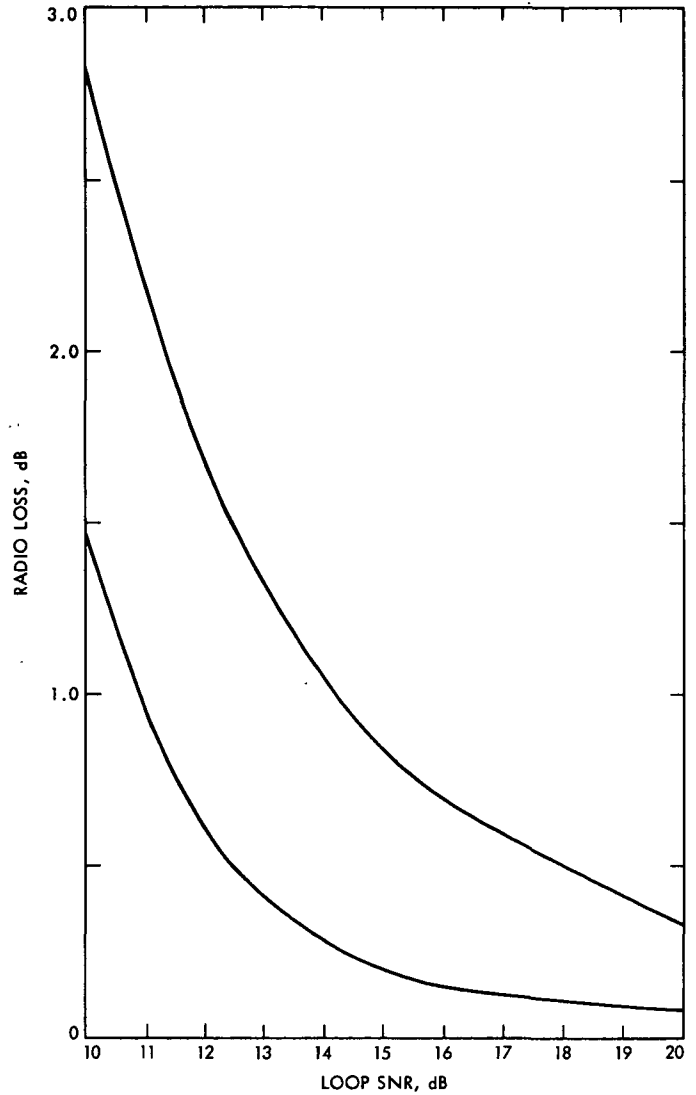


Fig. 7. Radio loss for the concatenated channel at $\text{BER} = 10^{-5}$ and node synchronization thresholds of 0.0 and 2.0 dB

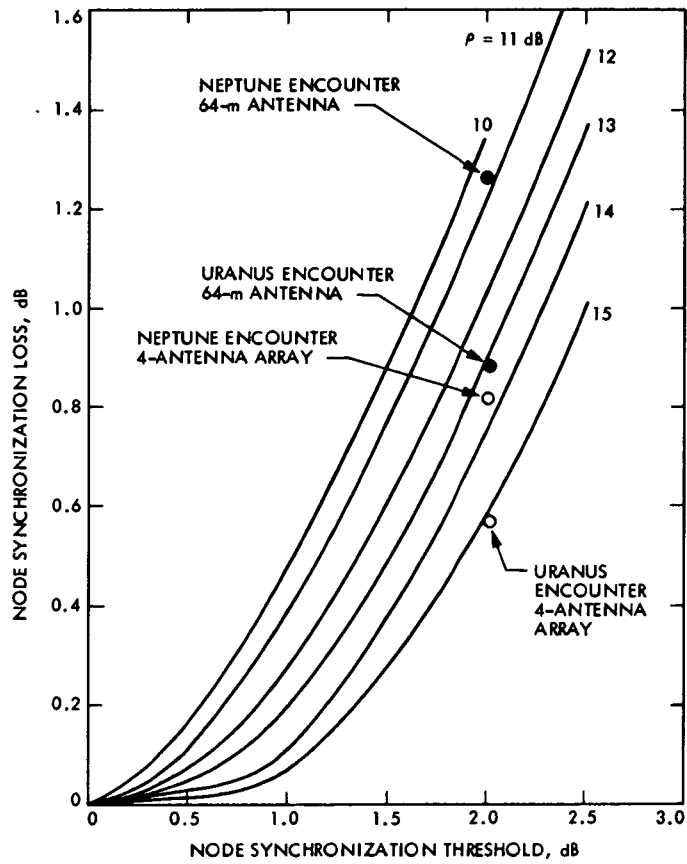


Fig. 8. Node synchronization losses for the concatenated channel at various carrier tracking loop SNRs ρ

Performance of Concatenated Reed-Solomon/Viterbi Channel Coding

D. Divsalar and J. H. Yuen
Communications Systems Research Section

This paper briefly reviews the concatenated Reed-Solomon (RS)/Viterbi coding system. Then the performance of the system is analyzed and results are derived with a new simple approach. We present a functional model for the input RS symbol error probability π . Based on this new functional model, we compute the performance of a concatenated system in terms of RS word error probability, output RS symbol error probability, bit error probability due to decoding failure, and bit error probability due to decoding error. Finally we analyze the effects of the noisy carrier reference and the slow fading on the system performance.

I. Introduction

The Voyager 2 spacecraft, which was launched in 1977 and has encountered Jupiter and Saturn systems in 1979 and 1981 respectively, will fly by Uranus in 1986 and Neptune in 1989. Voyager delivered 115.2 kbps at Jupiter (5 AU from earth), and 44.4 kbps at Saturn (10 AU from earth), both with 5×10^{-3} bit error probability. In order to enhance Voyager's communications capability, NASA's Jet Propulsion Laboratory is expected to exercise a planned option by switching on its Reed-Solomon (RS) encoder on the Voyager spacecraft. This results in a RS/Viterbi concatenated coded communication link to increase the achievable data rate. Reed-Solomon decoders will be installed in NASA's Deep Space Network (DSN) ground stations in time for the 1986 Uranus encounter.

The concatenated RS/Viterbi channel coding and its performance has been considered in the past; for example, see Refs. 1-5. This paper gives a brief review of this topic and shows the derivation of the results with a new simple approach that will be useful to system design engineers.

In concatenated RS/Viterbi channel coding, the key parameter for evaluating the performances of the system is the input RS symbol error probability π . Based on previous simulation and measurement results, we give a simple functional model for RS decoder input symbol error probability π . Using this model, we evaluate the RS word error probability, output RS symbol error probability and bit error probability. Finally we consider the effects of phase jitter and slow fading channels:

C-2

namely, the effects of Rayleigh, Rician, and log-normal fading channels on the performance of this concatenated RS/Viterbi channel. We use the outer code RS (255, 223), convolutional rate 1/2 and constraint length 7 code to illustrate these results.

II. System Model

The block diagram of the concatenated coding system is given in Fig. 1. The Reed-Solomon/Viterbi concatenated code consists of a Reed-Solomon (RS) outer code and a convolutional inner code which is Viterbi decoded.

The binary input data sequence is divided into J bit sequences to form symbols over a $M = 2^J$ -ary alphabet; i.e., there are M possible RS symbols. The RS coder then encodes the symbols such that any combination of t or fewer symbol errors per RS word ($2^J - 1$ symbols per word) can be corrected. A very simple block diagram of an RS block coder is shown in Fig. 2. All coding and decoding operations involve RS symbols, not individual bits. Here $K = M - 1 - 2t$ information symbols (or $J[M - 1 - 2t]$ information bits) from some data source enter the RS coder to the left. The result of coding operations is a *codeword* of length $N = 2^J - 1 = M - 1$ symbols, of which the first $K = M - 1 - 2t$ are the same symbols as those entering to the left. This makes the code *systematic*. The remainder of the codeword is filled in with $2t$ parity symbols; $t = (N - K)/2$ represents the number of correctable RS symbol errors in an RS codeword. That is, if t or less RS symbols are in error in any way, the decoder will be capable of correcting them. An RS symbol is in error if any of the J bits making up the symbol are in error. The minimum distance of RS code is $2t + 1$ symbols.

The interleaving buffers are required because the inner Viterbi decoder errors tend to occur in bursts, which occasionally are as long as several constraint lengths. Without interleaving, Viterbi decoder burst error events would tend to occur within one RS codeword. Thus over a period of time there would be a tendency for some codewords to have "too many" errors to be corrected. The performance of the RS decoder is severely degraded by highly correlated errors among several successive symbols. The purpose of interleaving and de-interleaving is to make the RS symbol errors, at the input of the RS decoder, independent of each other and disperse the RS symbol errors, in other words, to break the burst errors out of the Viterbi decoder among several code words.

The level of interleaving I corresponds to the number of RS code words involved in the interleaving and de-interleaving operation. Interleaving and de-interleaving operations over a Viterbi channel can be explained simply by considering two $I \times 2^J - 1$ matrices, one at the input of the channel and one at

the output. For interleaving, put the code words with length $2^J - 1$ in rows 1, 2, \dots , I of the matrix, then transmit the symbols of columns 1, 2, \dots , $2^J - 1$ through the channel. For de-interleaving, do the reverse operation. For the RS code (255, 223), simulation results (Ref. 3) have shown that the interleaving level of $I = 16$ is sufficient to make the RS symbol errors independent of each other for the ($K = 7$, $r = 1/2$) Viterbi channel. Thus we can assume henceforth that the combination of interleaving, convolutional code, additive white Gaussian noise (AWGN) channel, Viterbi decoder and de-interleaving creates an equivalent M -ary discrete memoryless channel (DMC) with transition error probability π , shown in Fig. 3.

III. A Functional Model for the RS Decoder Input Symbol Error Probability

Based on simulation results of Linkabit for π given in Ref. 3 and then using a least-squares curve fit, we proposed a simple model for π as

$$\pi\left(\frac{E_b}{N_0}\right) = \begin{cases} \exp\left(\beta_0 - \beta_1 \frac{E_b}{N_0}\right); & \frac{E_b}{N_0} \geq T^* \\ 1 - \frac{1}{M}; & \frac{E_b}{N_0} \leq T^* \end{cases} \quad (1)$$

where $\beta_0 = 4.9551$, $\beta_1 = 5.2275$, $T^* = \max(\beta_0/\beta_1, T)$, T is Viterbi decoder node synchronization threshold (for $E_b/N_0 < T$ Viterbi decoder produces random output), and E_b/N_0 is the bit SNR of the Viterbi channel (inner code). For perfect node synchronization $T^* = \beta_0/\beta_1$. Figure 4 shows the baseline symbol error probability π for the (255, 223) RS code vs E_b/N_0 of the Viterbi channel (inner code), using (1).

IV. Error Events in RS Decoding

Consider an (N, K) Reed-Solomon code. We know that t -error correcting RS code can decode a code word correctly if the number of symbol errors are t or less where $t = (N - K)/2$. Consider the space of all received vectors y of length N and spheres of radius t around code words in this N -dimensional vector space, as is shown in Fig. 5. These spheres do not overlap because the minimum distance between codewords is $2t + 1$. Since we have a linear code, without loss of generality, we assume the all zero codeword x_0 is sent. In decoding the RS code words, depending on what region in the observation space of Fig. 5 the received vector y falls, three disjoint events may occur. The first event occurs if there are t or less input RS

symbol errors in a received codeword. This occurs if the received vector \mathbf{y} falls in the double-shaded sphere around \mathbf{x}_0 , $\mathbf{y} \in S_C$. In this case the decoder successfully corrects the errors, decodes \mathbf{x}_0 as the codeword and outputs the correct information block $\hat{\mathbf{u}}_0 = \mathbf{u}_0$. Then, the "correct decoding" event occurs. The second event happens if there are more than t input RS symbol errors in a received codeword and the corrupted codeword is not within a distance of t symbols to any other codeword. In other words, \mathbf{y} does not fall in any sphere of radius t around the codewords, $\mathbf{y} \in S_F$. In this case the RS decoder fails to decode and we say that a "decoding failure" event occurs. Here, the decoder just outputs the first $N - 2t$ undecoded Viterbi channel symbols (input RS symbols) that may contain symbol errors. The third event happens if there are more than t input RS symbol errors in a received codeword and the corrupted codeword is within a distance of t symbols to some other codeword than the correct codeword \mathbf{x}_0 . This happens if \mathbf{y} falls in any one of the single-shaded spheres, $\mathbf{y} \in S_I$. Here the decoder decodes incorrectly and outputs an incorrect information block. Then, a "decoding error" event occurs.

V. Error Performance Analysis

In this section we derive expressions for RS codeword, RS symbol, RS bit, and RS information block error probabilities.

A. RS Codeword Error Probability

Denote the word error probability for an (N, K) RS code by $P_w(N, t)$. An RS codeword is in error when there are more than t channel symbol errors in a received codeword \mathbf{y} ; i.e., $\mathbf{y} \in \{S_F \cup S_I\}$. Therefore, we should consider all combinations of k channel symbol errors within the N symbols, for all $k > t$. Thus

$$P_w(N, t) = \sum_{k=t+1}^N \binom{N}{k} \pi^k (1 - \pi)^{N-k} \quad (2)$$

where π is the RS decoder input symbol error probability leaving the Viterbi decoder (groups of J bits).

B. RS Symbol Error Probability

Denote the RS symbol error probability by P_S . This error may result when the received codeword is either $\mathbf{y} \in S_F$ or $\mathbf{y} \in S_I$. Denote the RS symbol error probabilities when $\mathbf{y} \in S_F$ and $\mathbf{y} \in S_I$ by $P_{S,F}$ and $P_{S,I}$, respectively. Since these events are disjoint, we have

$$P_S = P_{S,F} + P_{S,I} \quad (3)$$

1. **Derivation of $P_{S,F}$.** Recall that when the RS decoder fails to decode, $\mathbf{y} \in S_F$, the decoder simply outputs the first $M - 1 - 2t$ Viterbi channel symbols as the "decoded" information block \mathbf{u}_0 . Hence the output RS symbol error pattern is exactly the same as the first $M - 1 - 2t$ undecoded input symbols to the RS decoder. An output RS symbol at position say k , $k = 1, 2, \dots, M - 1 - 2t$ is in error, when the input RS symbol at the same position k is in error and there are at least t input RS symbol errors in the remaining $N - 1$ symbols of received codeword (i.e., other than the position k). The probability of the input RS symbol at position k being in error is π . The probability that there will be t or more input RS symbol errors in the remaining positions, i.e., the $N - 1$ places of the received codeword, is

$$P_w(N - 1, t - 1) = \sum_{m=t}^{N-1} \binom{N-1}{m} \pi^m (1 - \pi)^{N-m-1} \quad (4)$$

Thus

$$P_{S,F} = \pi \cdot P_w(N - 1, t - 1) \quad (5)$$

2. **Derivation of $P_{S,I}$.** As we have seen, a decoding error occurs if the received codeword \mathbf{y} belongs to one of the spheres in S_I . Consider a particular codeword \mathbf{x}_n which has exactly n particular nonzero symbols. This codeword has a distance n from the all zero codeword \mathbf{x}_0 and hence has weight n . Let

$$W_1, W_2, W_3, \dots, W_n$$

be n independent identically distributed (iid) random variables corresponding to the n nonzero symbols of \mathbf{x}_n , and

$$Z_1, Z_2, Z_3, \dots, Z_{N-n}$$

be $N - n$ iid random variables corresponding to the $N - n$ zero symbols of \mathbf{x}_n . Each of these random variables W_i , $i = 1, 2, \dots, n$, and Z_j , $j = 1, 2, \dots, N - n$, can be either 0 or 1. Let us compute the probability that \mathbf{x}_0 is sent and the decoder decodes it as \mathbf{x}_n , i.e., the decoder has made an incorrect decision. Denote this probability by $Pr\{\mathbf{x}_0 \rightarrow \mathbf{x}_n\}$. This event occurs if \mathbf{y} falls in a sphere with radius t around the codeword \mathbf{x}_n . The probability that a zero symbol is sent and a nonzero symbol of a particular value is received is $\pi/(M - 1)$. But the probability that a zero symbol is sent and a nonzero symbol of any value is received is π , since there are $M - 1$ nonzero symbols. For computation convenience, without loss of generality, we can assume the first n symbols in \mathbf{x}_n are the nonzero symbols. Now let $\mathbf{y} = (y_1 \dots, y_N)$ and $\mathbf{x}_n = (x_{1,n}, x_{2,n}, \dots, x_{N,n})$, and define

$$W_i = \begin{cases} 0; & y_i = x_{i,n} \\ 1; & y_i \neq x_{i,n} \end{cases} \quad i = 1, 2, \dots, n \quad (6)$$

where

$$\Pr\{W=i\} = \binom{n}{i} \left(1 - \frac{\pi}{M-1}\right)^i \left(\frac{\pi}{M-1}\right)^{n-i} \quad (12)$$

then given x_0 is sent

$$\Pr\{W_i = 0\} = \frac{\pi}{M-1} \quad (7)$$

$$\Pr\{W_i = 1\} = 1 - \frac{\pi}{M-1}$$

and

$$\Pr\{Z=j\} = \binom{N-n}{j} \pi^j (1-\pi)^{N-n-j} \quad (13)$$

Similarly, if we define

$$Z_i = \begin{cases} 0; & y_{n+i} = x_{n+i,n} \\ 1; & y_{n+i} \neq x_{n+i,n} \end{cases} \quad i = 1, 2, \dots, N-n \quad (8)$$

Therefore

$$\Pr\{x_0 \rightarrow x_n\} = \sum_{i=0}^t \sum_{j=0}^{\min(t-i, N-n)} \Pr\{W=i\} \Pr\{Z=j\} \quad (14)$$

This is an exact analytic result. An upper bound using the Chernhoff bound technique (Ref. 6) is derived in Appendix A. This gives a simpler expression than the exact result in (14).

then given x_0 is sent

$$\Pr\{Z_i = 0\} = 1 - \pi \quad (9)$$

$$\Pr\{Z_i = 1\} = \pi$$

Let $q(n)$ denote the number of codewords of distance n from x_0 ; then the symbol error probability $P_{S,I}$ due to decoding error is

$$P_{S,I} = \sum_{n=2t+1}^N \frac{n}{N} q(n) \Pr\{x_0 \rightarrow x_n\} \quad (15)$$

Let

$$W = \sum_{i=1}^n W_i \quad \text{and} \quad Z = \sum_{i=1}^{N-n} Z_i$$

RS code is a maximum distance separable (MDS) code. Therefore we have (Ref. 7)

Then denoting the weight between two vectors by $\omega(\cdot, \cdot)$ we have

$$q(n) = (M-1) \binom{N}{n} \sum_{m=0}^{n-2t-1} \binom{n-1}{m} (-1)^m M^{n-2t-m-1} \quad (16)$$

$$\begin{aligned} \Pr\{x_0 \rightarrow x_n\} &= \Pr\{\omega(x_n, y) \leq t | x_0\} \\ &= \Pr\{W+Z \leq t\} \end{aligned} \quad (10)$$

C. RS Bit Error Probability

But

Denote the RS bit error probability by $P_b(RS)$. This bit error is either due to decoding failure or decoding error. Denote the RS bit error probability when $y \in S_F$ and $y \in S_I$ by $P_{b,F}(RS)$ and $P_{b,I}(RS)$, respectively. Since these events are disjoint, we have

$$\begin{aligned} \Pr\{W+Z \leq t\} &= \sum_{i=0}^t \Pr\{W=i\} \Pr\{Z \leq t-i\} \\ &= \sum_{i=0}^t \Pr\{W=i\} \sum_{j=0}^{\min(t-i, N-n)} \Pr\{Z=j\} \end{aligned} \quad (11)$$

$$P_b(RS) = P_{b,F}(RS) + P_{b,I}(RS) \quad (17)$$

1. Derivation of $P_{b,F}(RS)$. Recall that when the RS decoder fails to decode, it outputs the first $M-1-2t$ input RS symbols as "decoded" information block u_0 . A bit at

position say m , $m = 1, 2, \dots, J$ within the RS output symbol at position say k ; $k = 1, 2, \dots, M - 1 - 2t$ of a codeword is in error if the bit at position m within the input RS symbol at position k of an undecoded codeword is in error and there are t or more RS symbol errors in the received codeword out of the Viterbi decoder in other positions than position k . But the probability that a bit would be in error in an undecoded RS codeword is the bit error rate of the Viterbi decoder denoted by P_b (Viterbi). The probability that there are t or more RS symbol errors in an undecoded codeword in positions other than position k is given by (4). Thus the RS bit error rate $P_{b,F}(RS)$ is

$$P_{b,F}(RS) = P_b(\text{Viterbi}) \cdot P_w(N-1, t-1) \quad (18)$$

2. Derivation of $P_{b,I}(RS)$. We have derived the symbol error probability $P_{S,I}$ in (15). Now the bit error probability $P_{b,I}$ is

$$P_{b,I}(RS) = \frac{M}{2(M-1)} P_{S,I} \quad (19)$$

Based on our functional model for π , $P_{b,I}(RS)$ is shown in Fig. 6 for (255, 223) RS code using (19) with (14) and (15). In Fig. 7 we have shown $P_{b,F}(RS)$, $P_{S,F}$ and P_w for concatenated coding with (255, 223) RS code and (7, 1/2) convolutional code vs the E_b/N_0 of the concatenated channel. For $E_b/N_0 < 2\text{dB}$, $P_w(N-1, t-1) \cong 1$; hence (18) becomes $P_{b,F}(RS) = P_b(\text{Viterbi})$. Note that the code rate of the RS code is

$$RS \text{ code rate} = (N-2t)/N \quad (20)$$

As is seen from Figs. 6 and 7

$$P_{S,I} \ll P_{S,F}$$

and

$$P_{b,I}(RS) \ll P_{b,F}(RS) \quad (21)$$

Therefore

$$P_S \cong P_{S,F}$$

and

$$P_b(RS) \cong P_{b,F}(RS) \quad (22)$$

At this point, since the probability of a decoding error event is very small, it can be ignored for further computations.

Using this fact, we determine the RS of information block error probability.

D. RS Information Block Error Probability

Note that if a codeword is in error it is not necessary that the corresponding information block be in error. This error probability is important for source coding (data compression). Denote the information block error probability by $P_I(N, t)$. Ignoring the probability of decoding error event to find $P_I(N, t)$, we should subtract the probability of all possible patterns of symbol error that happen only in the parity check symbols, from P_w . This implies there is no error in the information block. Thus we have

$$P_I(N, t) = P_w(N, t) - \sum_{k=t+1}^{2t} \binom{2t}{k} \pi^k (1-\pi)^{N-k} \quad (23)$$

Obviously, in the practical range of error probability the last term can be ignored and we can say approximately

$$P_I(N, t) \cong P_w(N, t) \quad (24)$$

VI. Effects of Phase Jitter

If the data rate is sufficiently large with respect to the PLL loop bandwidth so that the phase error does not vary significantly during the Viterbi decoder error bursts, then the phase error can be assumed to be constant during one RS symbol. In addition, since we have $I = 16$ level of interleaving, the phase errors affect the RS input symbols approximately independently. Noting the approach we have taken for the derivations of P_w , P_S and $P_b(RS)$, we have

$$P_w = E\{P_w(\phi_1, \phi_2, \dots, \phi_N)\} = \sum_{k=t+1}^N \binom{N}{k} \overline{\pi(\phi)}^k [1 - \overline{\pi(\phi)}]^{N-k} \quad (25)$$

and

$$P_b(RS) = \overline{P_b(\text{Viterbi}|\phi)} \sum_{k=t}^{N-1} \binom{N-1}{k} \overline{\pi(\phi)}^k [1 - \overline{\pi(\phi)}]^{N-k-1} \quad (26)$$

where

$$\overline{\pi(\phi)} = \int_{-\pi}^{\pi} \pi \left(\frac{E_b}{N_0} \cos^2 \phi \right) p(\phi) d\phi \quad (27)$$

and $p(\phi)$ is the probability density function of phase jitter given by (Ref. 8)

$$p(\phi) = \frac{\exp(\rho \cos \phi)}{2\pi I_0(\rho)}; \quad -\pi \leq \phi \leq \pi \quad (28)$$

where ρ is the SNR in the tracking loop bandwidth and $\pi(\phi)$ is given by (1), replacing E_b/N_0 with $(E_b/N_0) \cos^2 \phi$. Figure 8 shows $\pi(\phi)$ for various loop SNR ρ . The effect of a noisy carrier reference on Reed-Solomon Viterbi bit error rate performance, given by (26), is shown in Fig. 9. Note that in (26) $\overline{P_b}(\text{Viterbi}|\phi)$ can be computed from

$$\overline{P_b}(\text{Viterbi}|\phi) = \int_{-\pi}^{\pi} f\left(\frac{E_b}{N_0} \cos^2 \phi\right) p(\phi) d\phi \quad (29)$$

where

$$f(x) = \begin{cases} \exp(\alpha_0 - \alpha_1 x); & x \geq T \\ \frac{1}{2}; & x < T \end{cases} \quad (30)$$

and

$$\alpha_0 = 4.4514 \quad \alpha_1 = 5.7230.$$

T is the Viterbi decoder node synchronization threshold, where

$$T \geq \frac{\ln 2 + \alpha_0}{\alpha_1}$$

and with equality for perfect node synchronization. In this paper we have assumed perfect node synchronization. The effect of node sync on RS decoding can be found using (25) through (30) with the model for π given in (1); results are illustrated in Fig. 9. Further detail is given in Ref. 9.

For the effect of a noisy carrier reference on RS/Viterbi, we also recommend Ref. 5 to the interested reader.

VII. Effects of Slow Fading on the RS/Viterbi Decoder Performance

Usually the RF telemetry signal can be expressed as

$$S(t) = \sqrt{2} A \sin [\omega_c t + m(t)] \quad (31)$$

where $m(t)$ contains the telemetry information which can be a subcarrier, biphasic modulated with a binary data stream. Now if this signal is passed through a fading channel, at the output we have

$$r(t) = \sqrt{2} a(t) \sin [\omega_c t + m(t) + \phi(t)] + n(t) \quad (32)$$

where $a(t)$ is random amplitude process and $\theta(t)$ is random phase process. If $a(t)$ and $\theta(t)$ change slowly with time, and the spectral bandwidths of $a(t)$ and $\theta(t)$ are narrow with respect to average loop bandwidth of PLL at the receiver, then $\theta(t)$, together with the carrier phase, can be tracked by PLL.

Here we consider a slow varying fading channel with perfect tracking. Depending on the channel, we can have Rayleigh, Rician, or log-normal channels. Consider first the Rician channel, since it is Rayleigh with an added specular component. If we pass transmitted signal (31) through a Rician channel we get

$$r(t) = \sqrt{2} A \sin [\omega_c t + m(t)] + \sqrt{2} n_c(t) \cos [\omega_c t + m(t)] + \sqrt{2} n_s(t) \sin [\omega_c t + m(t)] + n(t) \quad (33)$$

where n_c and n_s are zero mean Gaussian random processes each with variance σ^2 . Then the received signal amplitude $a(t)$ has the Rician probability density function

$$p(a) = \frac{a}{\sigma^2} \exp\left\{-\frac{a^2 + A^2}{2\sigma^2}\right\} I_0\left(\frac{aA}{\sigma^2}\right) \quad a \geq 0 \quad (34)$$

Define

$$\gamma^2 \triangleq \frac{A^2}{2\sigma^2} \quad (35)$$

as the ratio of the specular power to the fading power. Suppose the received power is P where

$$P = A^2 + 2\sigma^2 \quad (36)$$

Let's normalize $a(t)$ as

$$y(t) = \frac{a(t)}{\sqrt{P}} \quad (37)$$

Then

$$p(y) = 2y(1 + \gamma^2) \exp\{-(1 + \gamma^2)y^2 - \gamma^2\} \\ I_0 \left[2y \sqrt{\gamma^2(1 + \gamma^2)} \right] \quad y \geq 0 \quad (38)$$

with

$$\overline{y^2} = 1 \quad (39)$$

For the Rayleigh channel we don't have specular components, which means $A = 0$ or $\gamma^2 = 0$. Then pdf for y is

$$p(y) = 2y \exp(-y^2) \quad y \geq 0 \quad (40)$$

Figure 10 shows $p(y)$ given in (38) and (40). For Log-normal channels the received signal amplitude is of the form

$$a(t) = A e^{\chi(t)} \quad (41)$$

where $\chi(t)$ is Gaussian random process with variance σ_x^2 . Pdf of normalized $a(t)$ is

$$p(y) = \frac{1}{y \sqrt{2\pi} \sigma_x} \exp\{-(\ln y + \sigma_x^2)^2 / 2\sigma_x^2\} \quad y > 0 \quad (42)$$

Therefore in all cases we can assume the received signal is

$$r(t) = \sqrt{2P} y \cos[\omega_c t + m(t) + \theta(t)] + n(t) \quad (43)$$

where pdf of y is given by (38), (40) or (42).

If the signal amplitude changes very slowly in comparison to the bit rate, y will remain constant over a large number of bits. On the other hand, 16 levels of interleaving makes y affect RS symbols independently. Therefore, we have

$$\pi = \overline{\pi(y)} = \int_0^\infty \pi\left(\frac{E_b}{N_0} y^2\right) p(y) dy \quad (44)$$

and

$$P_b(\text{Viterbi}) = \overline{P_b(\text{Viterbi}|y^2)} = \int_0^\infty f\left(\frac{E_b}{N_0} y^2\right) p(y) dy \quad (45)$$

Using these averages in (2), (5), and (18) we can get performance of concatenated coded system in the presence of a slow fading channel. The corresponding performance curves are shown in Figs. 11 and 12.

VIII. Combined Effect of Phase Jitter and Slow Fading

With a similar argument as before, we can find the combined effect of phase jitter and slow fading by finding the average of π and P_b (Viterbi) over the phase error ϕ and amplitude fading factor y as

$$\pi = \overline{\pi(y, \phi)} = \int_0^\infty \int_{-\pi}^\pi \pi\left(\frac{E_b}{N_0} y^2 \cos^2 \phi\right) p(\phi|y) d\phi dy \quad (46)$$

where (for details of effects of a fading channel on PLL see Ref. 10).

$$p(\phi|y) = \frac{e^{\rho(y^2) \cos \phi}}{2\pi I_0(\rho(y^2))} \quad (47)$$

$$\rho(y^2) = \frac{y^2 P_c}{N_0 B_L (y^2) \Gamma(y^2)} \quad (48)$$

and similarly

$$P_b(\text{Viterbi}) = \int_0^\infty \int_{-\pi}^\pi f\left(\frac{E_b}{N_0} y^2 \cos^2 \phi\right) p(\phi|y) p(y) d\phi dy \quad (49)$$

Using these in our performance formulas, we get the desired results.

IX. Conclusion

Key parameters for characterizing the performance of concatenated Reed-Solomon/Viterbi coding have been considered. Simple derivations of close form expressions for a number of error probabilities are presented; these include RS codeword, RS information block, RS symbol, and RS bit error probabilities. A functional model for the RS decoder input symbol error probability is found which enables us to carry out numerical computations of the above-mentioned error probabilities. In addition, the effects of noisy carrier reference and slow fading on the RS/Viterbi decoding performance are determined.

References

1. Forney, G. D., *Concatenated Codes*, MIT Press, Cambridge, Mass., 1967.
2. Rice, R. F., *Channel Coding and Data Compression System Considerations for Efficient Communication of Planetary Imaging Data*, Technical Memorandum 33-695, Jet Propulsion Laboratory, Pasadena, Calif., 1974.
3. Odenwalder, J. P., "Concatenated Reed-Solomon/Viterbi Channel Coding for Advanced Planetary Missions: Analysis, Simulations, and Tests," submitted to JPL by Linkabit Corp., San Diego, Calif., Contract No. 953866, 1974.
4. Miller, R. L., Deutsch, L. J., and Butman, S. A., *On the Error Statistics of Viterbi Decoding and the Performance of Concatenated Codes*, Publication 81-9, Jet Propulsion Laboratory, Pasadena, Calif., Sept. 1981.
5. Liu, K. Y., *The Effects of Receiver Tracking Phase Error on the Performance of the Concatenated Reed-Solomon/Viterbi Channel Coding System*, Publication 81-62, Jet Propulsion Laboratory, Pasadena, Calif., Sept. 1, 1981.
6. Viterbi, A. J., and Omura, J. K., *Principles of Digital Communication and Coding*, McGraw-Hill, N.Y., 1979.
7. MacWilliams, F. J., and Sloane, N. J. A., *The Theory of Error-Correcting Codes*, Elsevier/North Holland, N.Y., 1977.
8. Lindsey, W. C., and Simon, M. K., *Telecommunication Systems Engineering*, Prentice Hall, N.Y., 1972.
9. Divsalar, D., "The Effects of Node Synchronization of Viterbi Decoder on Concatenated Reed-Solomon/Viterbi Channel Coding," (to appear in the next issue of the *TDA Progress Report*).
10. Weber, W. J., III, "Performance of Phase-Locked Loops in the Presence of Fading Communication Channels," Vol. 24, *IEEE Trans. Comm.*, pp. 487-499, May 1976.

ORIGINAL PAGE IS
OF POOR QUALITY

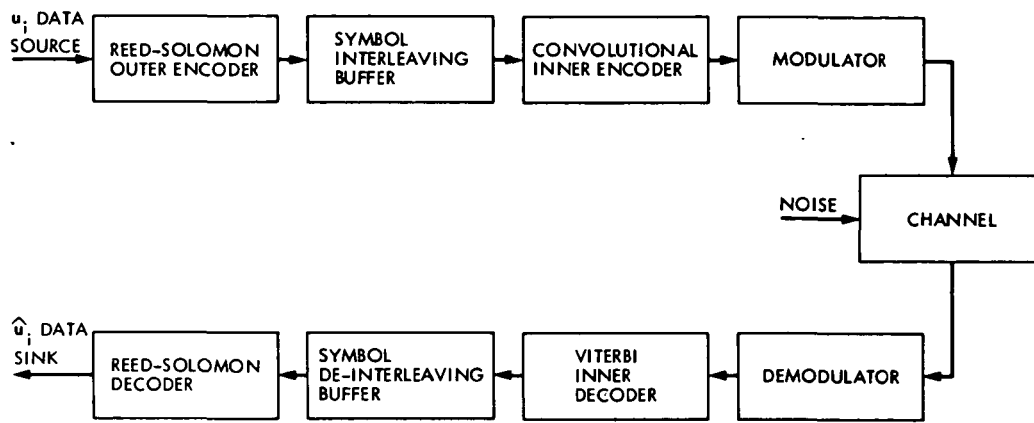


Fig. 1. Concatenated Reed-Solomon/Viterbi coding system diagram

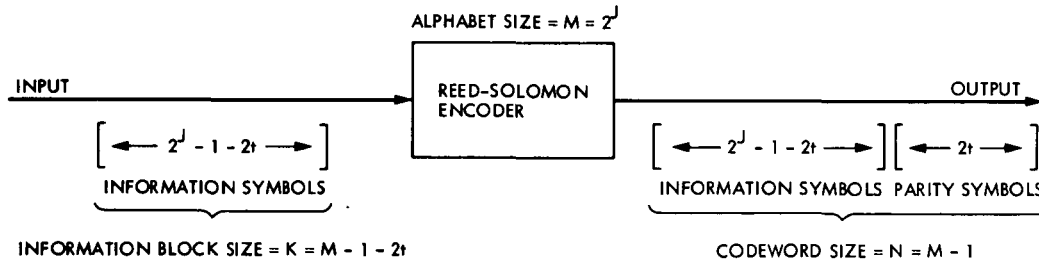


Fig. 2. Basic Reed-Solomon code structure

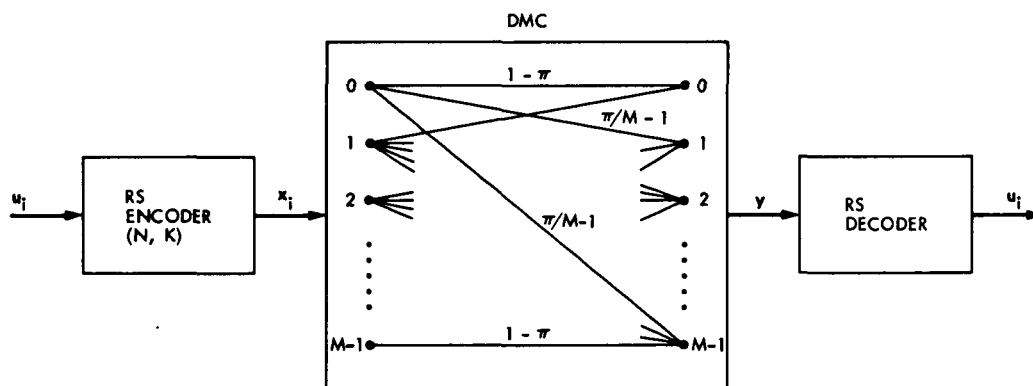


Fig. 3. Equivalent M -ary discrete memoryless channel (DMC) of Fig. 1

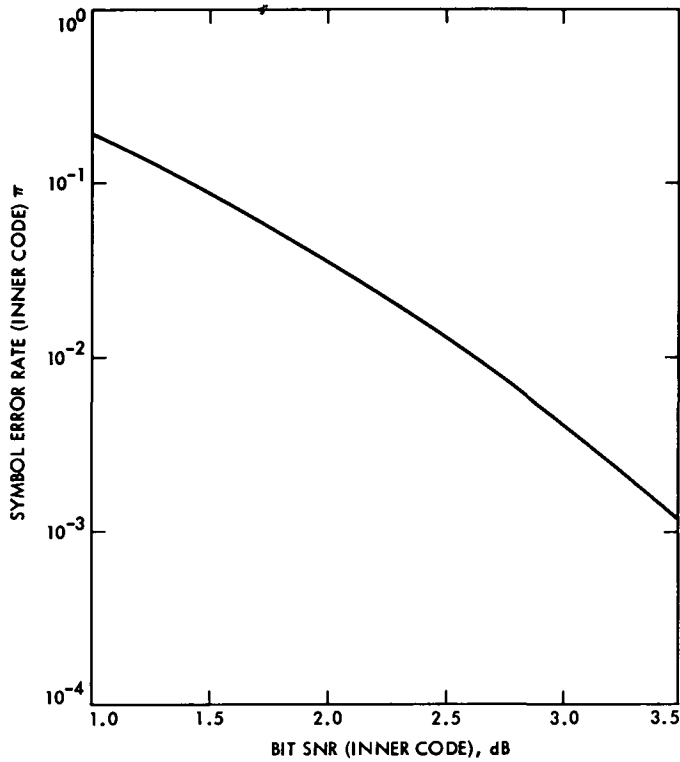


Fig. 4. Symbol error probability π computed from Eq. (1)

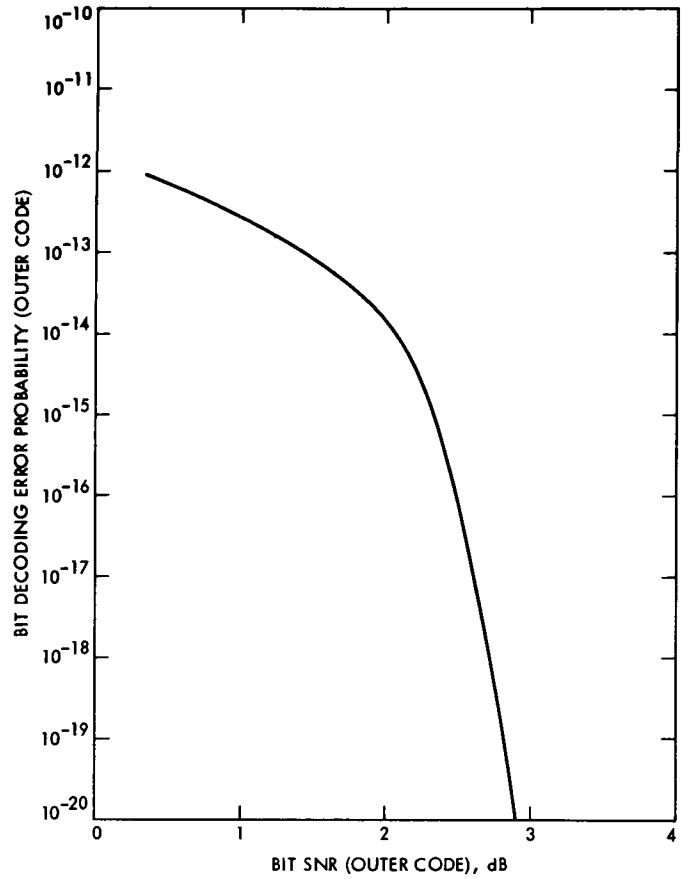


Fig. 6. $P_{b,i}(RS)$ vs bit SNR for (255,223) RS outer code and ($K=7$, $r=1/2$) convolutional inner code

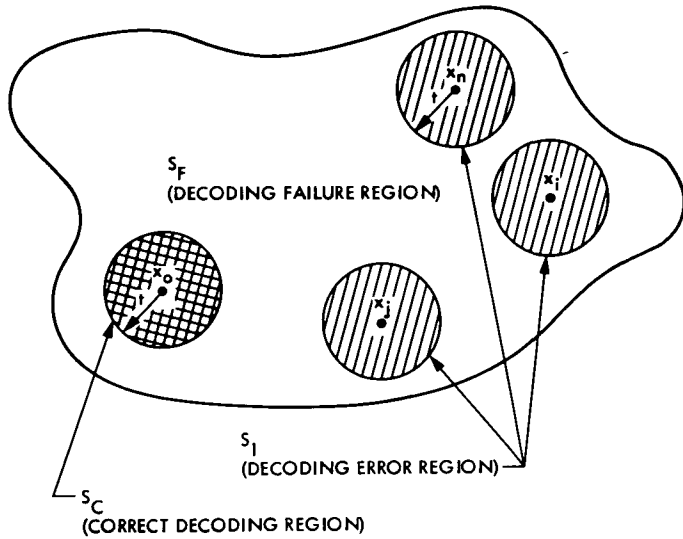


Fig. 5. Received codeword space of all vectors y with length N

ORIGINAL PAGE IS
OF POOR QUALITY

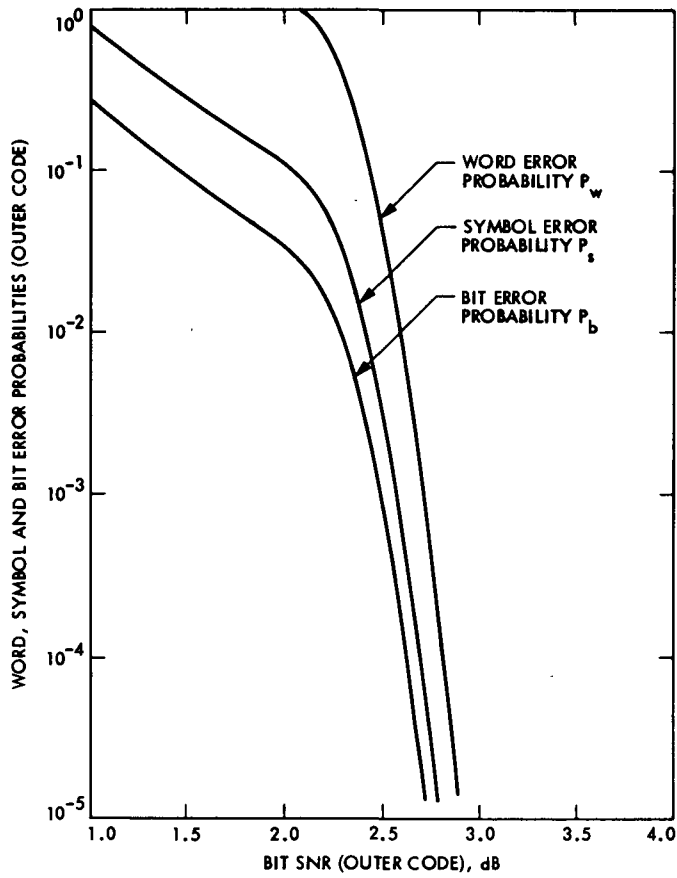


Fig. 7. $P_{b,F}(RS)$, $P_{s,F}$ and P_w performance curves

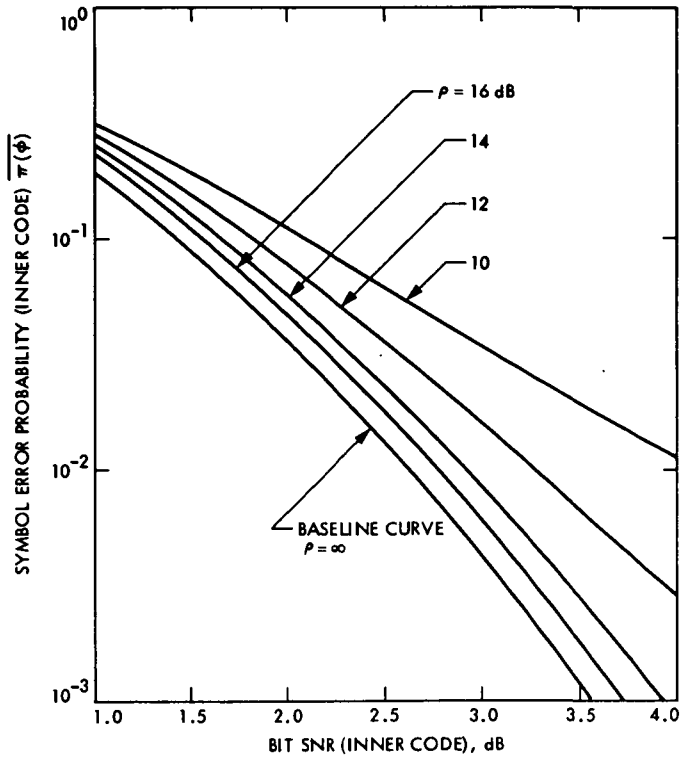


Fig. 8. Effects of noisy carrier reference on symbol error probability π

ORIGINAL PAGE IS
OF POOR QUALITY

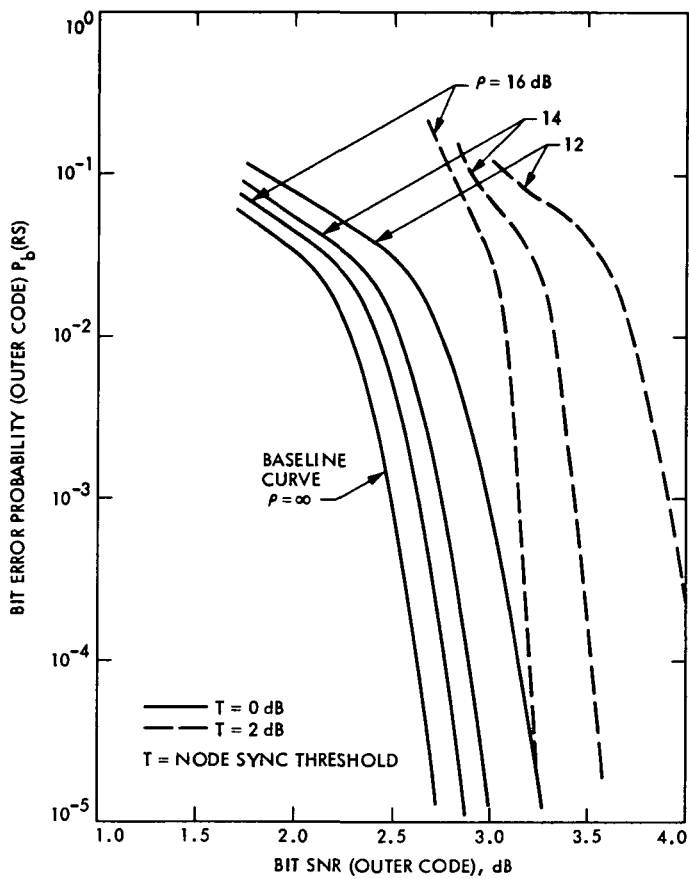


Fig. 9. Effects of noisy carrier reference on concatenated RS/Viterbi bit error rate P_b (RS)

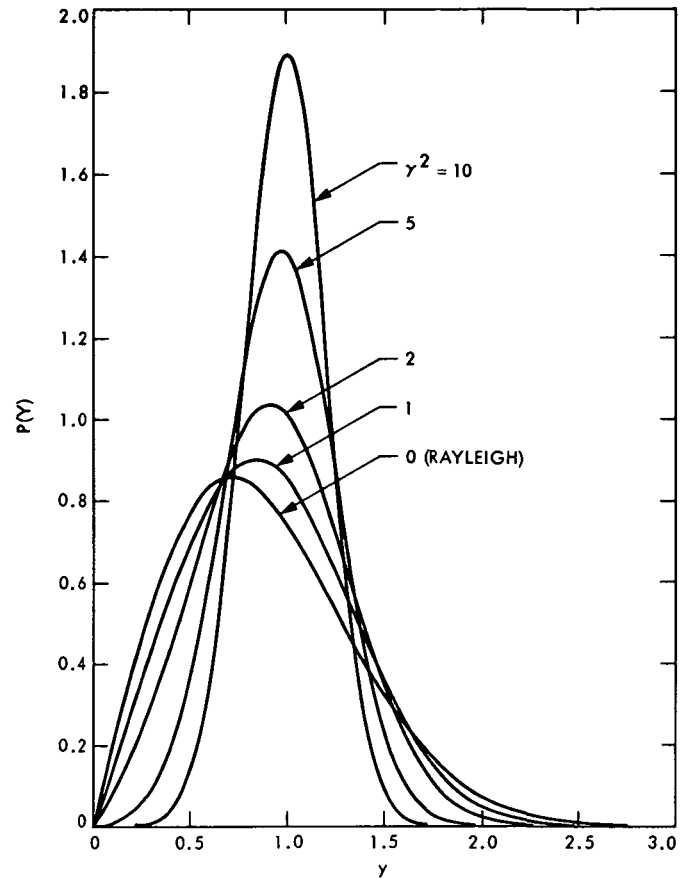


Fig. 10. Rician ($\gamma^2 > 0$) and Rayleigh ($\gamma^2 = 0$) probability density functions

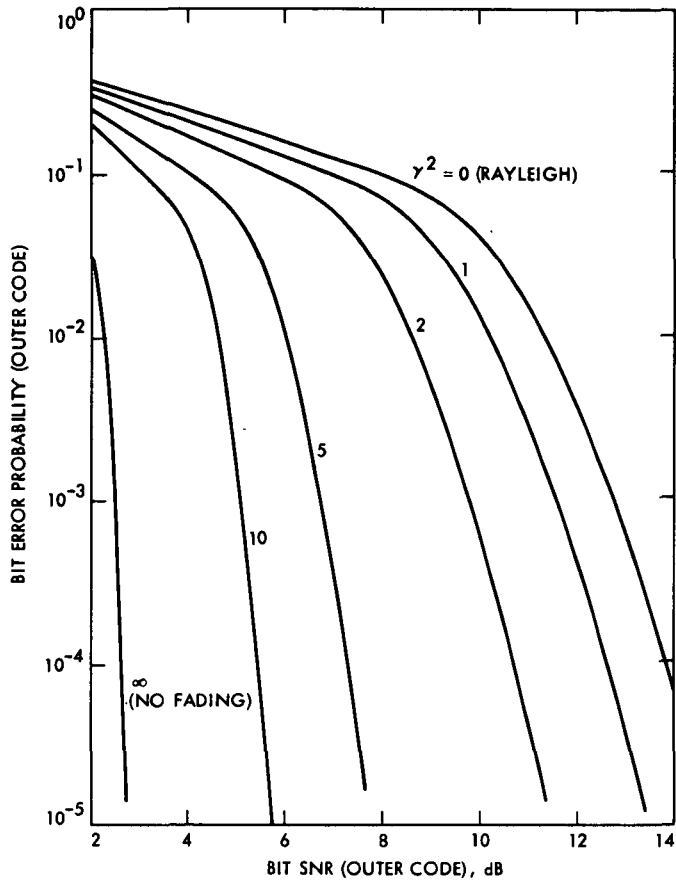


Fig. 11. $P_b(RS)$ vs bit SNR for Rician ($\gamma^2 > 0$) and Rayleigh ($\gamma^2 = 0$) fading channels

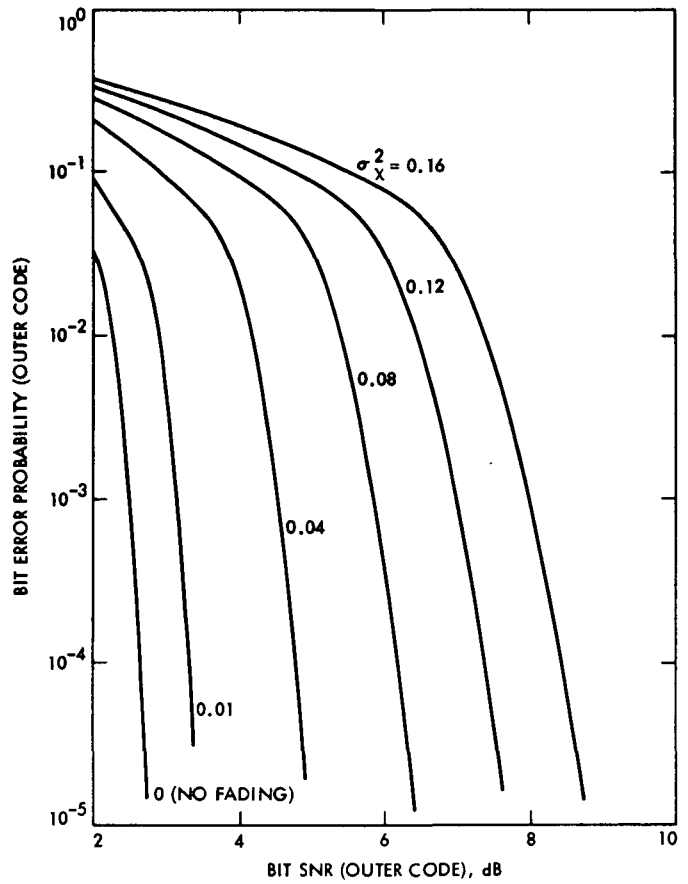


Fig. 12. $P_b(RS)$ vs bit SNR for log-normal fading channels

Appendix

Chernoff Bound on $Pr \{x_0 \rightarrow x_n\}$

Here we would like to find a simple upperbound on $P_r(x_0 \rightarrow x_n)$ using the Chernoff bound technique. Note for $\lambda > 0$ we have

$$\begin{aligned} Pr\{x_0 \rightarrow x_n\} &= Pr\{W + Z \leq t\} = Pr\{t - W - Z \geq 0\} \leq \{e^{\lambda(t-W-Z)}\} \\ &= e^{\lambda t} E\{e^{-\lambda W}\} E\{e^{-\lambda Z}\} \end{aligned} \quad (A-1)$$

But

$$E\{e^{-\lambda W}\} = E\left\{e^{-\lambda \sum_{i=1}^n w_i}\right\} = \prod_{i=1}^n E\{e^{-\lambda w_i}\} = \left[\frac{\pi}{m-1} - \left(1 - \frac{\pi}{m-1}\right)e^{-\lambda}\right]^n \quad (A-2)$$

Similarly

$$E\{e^{-\lambda Z}\} = E\left\{e^{-\lambda \sum_{i=1}^{N-n} z_i}\right\} = [(1 - \pi) + \pi e^{-\lambda}]^{N-n} \quad (A-3)$$

Therefore,

$$Pr\{x_0 \rightarrow x_n\} \leq \min_{\lambda > 0} e^{\lambda t} \left[\frac{\pi}{m-1} + \left(1 - \frac{\pi}{m-1}\right)e^{-\lambda}\right]^n [(1 - \pi) + \pi e^{-\lambda}]^{N-n} \quad (A-4)$$

Electronic Simulation of a Barometric Pressure Sensor for the Meteorological Monitor Assembly

C. N. Guiar and L. W. Duff
DSN Engineering Section

This article presents an analysis of the electronic simulation of barometric pressure used to self-test the counter electronics of the digital barometer. The barometer is part of the Meteorological Monitor Assembly that supports navigation in deep space communication. The theory of operation of the digital barometer, the design details, and the verification procedure used with the barometric pressure simulator are presented.

I. Introduction

The Meteorological Monitor Assembly (MMA) is one of the subsystems in the Deep Space Network's technical facility which provide the meteorological information necessary for calibrating radiometric data in support of navigational requirements for various deep space communication projects. The assembly as shown in Fig. 1 includes equipment required for the measurement, data processing, and handling of the following major types of data:

- (1) Barometric pressure.
- (2) Rainfall/water precipitation rate.
- (3) Dewpoint temperature of ambient air.
- (4) Azimuth and elevation angles of the large, 64-m antenna.
- (5) Faraday rotation.
- (6) Polarization angle.
- (7) Ground level solar radiation.
- (8) Dry bulb temperature of ambient air.

In supporting field operators, a need evolved for verification of the operation of the barometric pressure instrumentation (digital barometer) using self-test electronics. The barometric pressure simulator was developed for this purpose and is presented by the block diagram in Fig. 2. This article reports on the design details and verification procedures incorporated in the barometric pressure simulator development.

II. Barometer Functional Description

Schematic diagrams of the Bell & Howell digital barometer (P/N 4-461-004) are shown in Figs. 3 and 4. The digital barometer basically consists of a digital pressure transducer and a front panel light-emitting diode (LED) display. The barometric pressure to be measured is received at the rear panel connector, where it is applied to the input of the transducer. The transducer converts the pressure into a frequency which varies linearly with pressure. This signal is fed into a presettable counter where it is converted to a digital data signal. The digital output signal is applied to the rear panel connector as a parallel binary coded decimal (BCD) output, and also to the front panel LED assembly, which produces a five-digit display.

A precision dual-capacitor pressure-sensing element generates two variable frequencies, one varying directly and the other varying inversely with the pressure applied to the input fitting. The mixer accepts these two frequencies as input and provides an output signal which has a frequency that is the difference between the two input frequencies and varies linearly with pressure change. The purpose of processing the signal in this manner is to provide a more stable and accurate frequency input for the counter electronics. The frequency signal is fed to a digital counter that is programmed to sample the output frequency of the sensing element. The time period of the sample count can be varied by setting the span-adjust switches which will provide a readout in the desired units.

The digital barometer is currently equipped with a capability to self-test the display. When the test switch on the front panel is momentarily pressed to the ON position, all segments of the digital display are lit, producing a display of 88888. Any LED failure in the display will thus be revealed. This was the only self-test feature available with this type of barometer.

In the event that any counter circuit in the group U1-U5 as shown in Fig. 4 fails (e.g., bit malfunction), there is no self-contained means of determining this failure. The counter circuits can be tested by providing a known frequency f_0 to the counter inputs, producing a BCD output that should correspond with f_0 . Therefore, if the BCD output does not correspond properly to the input frequency, it can be assumed that the counter electronics within the barometer have malfunctioned.

III. Barometric Pressure Simulator

The barometric pressure simulator provides known frequencies to the inputs of counters U1-U5 (Fig. 4) to determine if they are counting correctly. Frequency-generating circuitry and delay, latch, and flag electronics as shown in Fig. 5 comprise the barometric pressure simulator. Details of these electronics are given in the remainder of this section.

A. Frequency and Barometric Pressure Relationship

In determining the factor by which the circuit scales simulated barometric pressure according to frequency, a frequency generator was connected directly to the input of the barometer counter electronics (U13) in parallel with a frequency counter measuring system as shown in Fig. 6. Several barometric pressure readings were taken for various frequency values. The resulting test data given in Table 1 indicate that a change in frequency of approximately 7.4 kHz produced a 1.0 mbar¹ change in barometric pressure. The linear frequency-

pressure relationship can be assumed to take the form:

$$f = mp + b \quad (1)$$

where f is the frequency in kHz, p is the pressure in mbars, m is the slope in kHz/mbar, and b is the ordinate intercept in kHz. If frequency is zero, the pressure is zero; therefore, b is zero. The average slope, determined using the data in Table 1, is 7.4 ± 0.5 kHz/mbar.

A resolution of 12 bits was chosen to provide a suitable range of frequencies for use in barometric pressure simulation. The 12-bit word, transferred through the latching network from the HP9821A calculator, is used as the input for three cascaded, synchronous, 4-bit counters as shown in Fig. 5. The least significant bit output (LSB) provides the necessary frequency and is determined by:

$$f_{LSB} = \frac{\text{clock frequency}}{(16 - b_1)(16 - b_2)(16 - b_3)} \quad (2)$$

where b_1 is the input bit value for first counter, b_2 is the input bit value for second counter, and b_3 is the input bit value for third counter.

The value 16, used in the denominator, corresponds to the number of increments from binary 0000 to 1111.

A 6-MHz crystal-controlled oscillator provides a constant, stable clock signal for control of the digital electronics. The actual frequency used for barometric pressure simulation (f_0) is generated by subtracting the LSB frequency from the clock frequency. Table 2 shows a few examples for various 12-bit inputs and their corresponding simulated barometric pressure.

B. Handshake

A simplified block diagram of the HP11202A I/O interface is shown in Fig. 7. The interface provides 8-bit data exchange between the HP9821A calculator and the barometric pressure simulator. Data bits D0-D5 are used for data information and D6 and D7 for control.

Data is transferred in a "half-duplex" mode, meaning data can be either input or output, but not both at the same time. All data and control lines are compatible with standard TTL levels.

When the calculator is given a WRITE command a Select Code Signal is output. The Select Code Signal is used to address the correct device. The status of the Service Interrupt line (SIO) is then checked by the calculator. If a low signal is detected on the SIO line the interface is not busy, allowing data to be held low on the chosen calculator output lines

¹ One millibar (mbar) is equal to 0.0147 psi or 0.101 kPa.

(D00-D07). The Calculator Status Line (S03) signal then sets the I/O line low to indicate that an output operation has been initiated. Next, the Control Enable Line (CEO) and SELECT code signals are output. The CEO signal provides the correct timing for interface operations. If the Select Code Signal addresses the correct device, data is ready to be transferred to the output lines. The device control line ($\overline{\text{CTL}}$) is transmitted to the barometric pressure simulator 5 μsec later, indicating data has been transferred to the output lines (D0-D7). All data will be held on these lines until the barometric pressure simulator returns the Device Ready ($\overline{\text{FLG}}$) signal, indicating data have been accepted.

C. Latch and Delay

The six data bits (D0-D5) are connected to three 4-bit bistable latches. These latches are used as temporary storage for binary information between HP9821A calculator and frequency generating electronics. Since 12 data bits are needed in the frequency-generating circuitry, data transfer takes place in two segments. The first segment involves sending six bits through one-half of the latch electronics, with the second transfer sending six more data bits through the remaining half.

Data bits D6 and D7 are used for the interchange of data and control of the transfer of data through the latching electronics and into the barometer. Timing between control commands and data inputs is very important if latching is to take place in the correct sequence. Once a FLG signal is returned

to the calculator at the end of each WRITE command, all data on the calculator output lines is cleared. Delay circuitry is provided which allows the control commands to reach the latching network only when data information (D0-D5) is present.

D. Verification of Simulator Operation

The final function of the barometric pressure simulator provides a means for data verification. Since a known frequency is provided, the BCD output of the barometer can be checked by transferring this data back to the HP9821A calculator for comparison. If the calculated frequency does not agree with the BCD output frequency by approximately ± 0.5 mbar, it can be assumed that the counter electronics of the barometer have malfunctioned and correction measures should be applied.

IV. Summary

The barometric pressure simulator provides a method for self-testing the counter electronics of the Bell & Howell digital barometer using electronic simulation of barometric pressure. A prototype model of the simulator has been built and tested and will soon be integrated into the digital barometer for placement in the MMA, thus supporting field operators in the area of barometric data verification. Operating instructions, theory of operation, and associated software for the barometric pressure simulator will be published in an operation and maintenance manual.

ORIGINAL PAGE IS
OF POOR QUALITY

Table 1. Test data for determination of scale factor for pressure vs frequency

Barometer reading, mbars	Frequency reading, MHz	$\frac{\Delta \text{ Pressure,}}{\Delta \text{ Frequency}}$ kHz/mbar
606.8	4.509	
596.8	4.435	7.4
506.0	3.763	7.44
406.7	3.031	7.38
306.7	2.292	7.38
206.9	1.556	7.35

Average = 7.4 kHz/mbar

Table 2. Sample 12-bit inputs and their corresponding simulated barometric pressure

12-bit input	(1)	(2)	(3)
0111 1001 1111	95.24	797.9	795.4
0111 1010 1111	111.1	795.8	793.3
0111 1000 1111	83.3	799.5	797.5
0111 0000 1111	41.7	805.2	802.7
0100 1001 1111	71.4	801.2	798.7
0101 1111 1111	545.4	737.1	734.6
0111 1111 1111	666.7	720.7	718.2

(1) Frequency at LSB = $\frac{6 \text{ MHz}}{(16 - b_1)(16 - b_2)(16 - b_3)}$

(2) Simulated barometric pressure = $P' = \frac{6 \text{ MHz} - f_{LSB}}{7.4 \text{ kHz/mbar}}$

(3) Corrected barometric pressure = $(P' - 2.5) \text{ mbars}$

ORIGINAL PAGE IS
OF POOR QUALITY

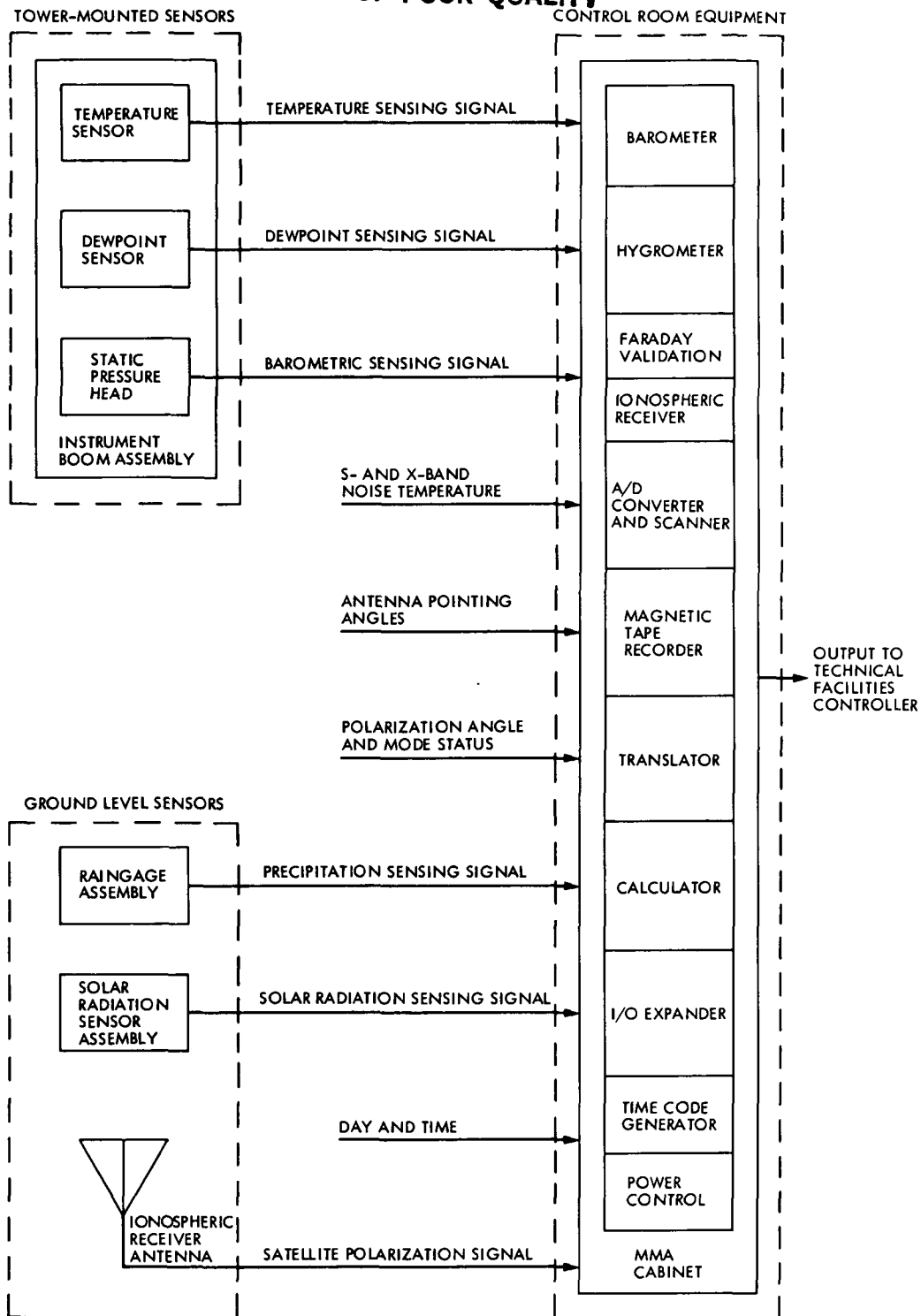


Fig. 1. Overall block diagram of MMA

ORIGINAL PAGE IS
OF POOR QUALITY

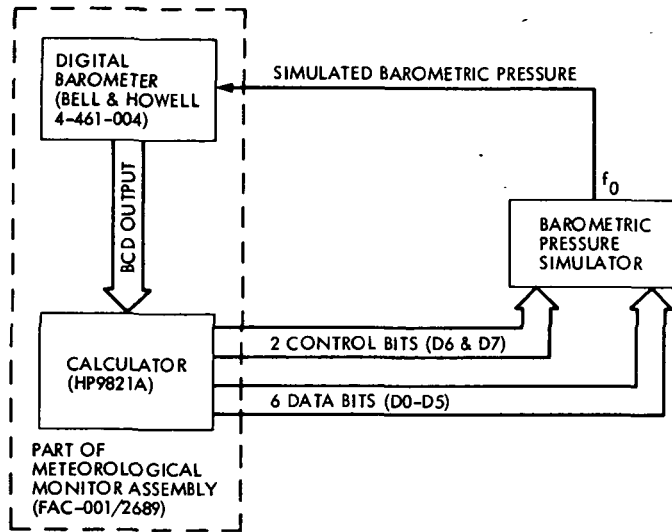


Fig. 2. Barometric self-test electronics block diagram

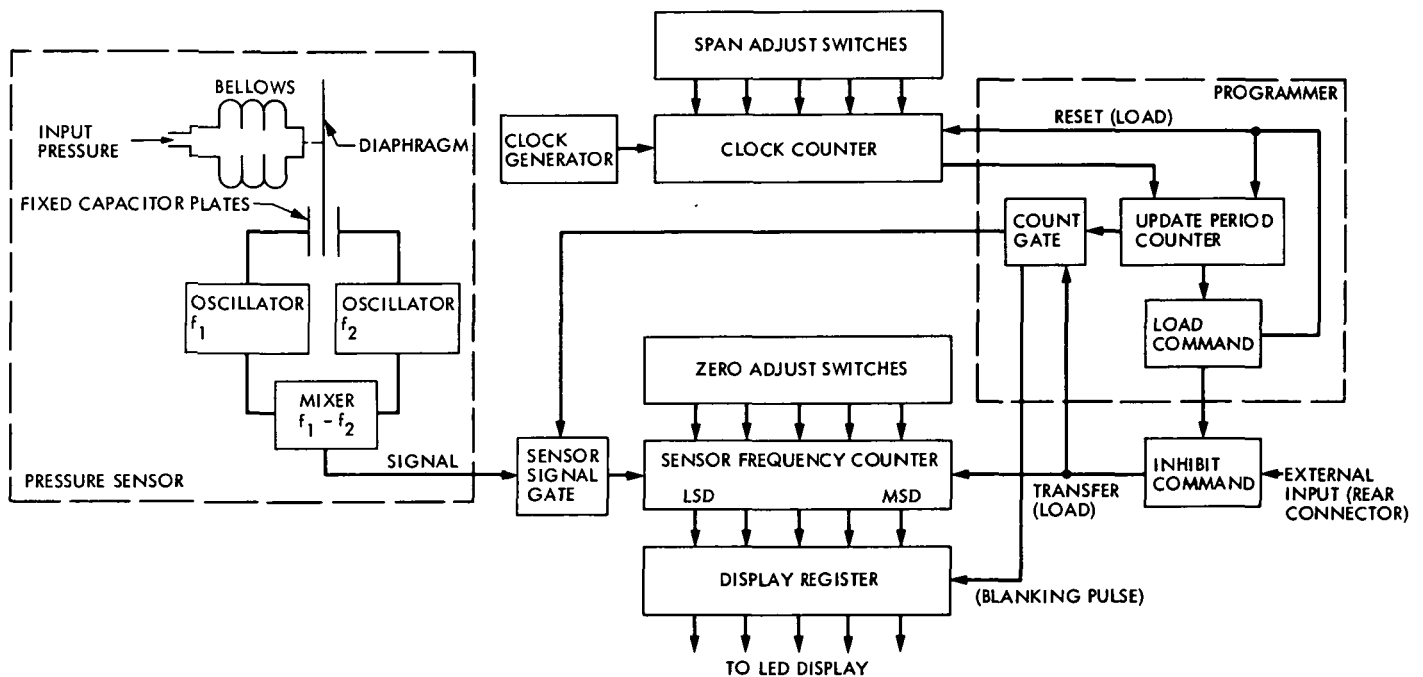


Fig. 3. Functional block diagram for Bell & Howell digital barometer (P/N 4-461-004)

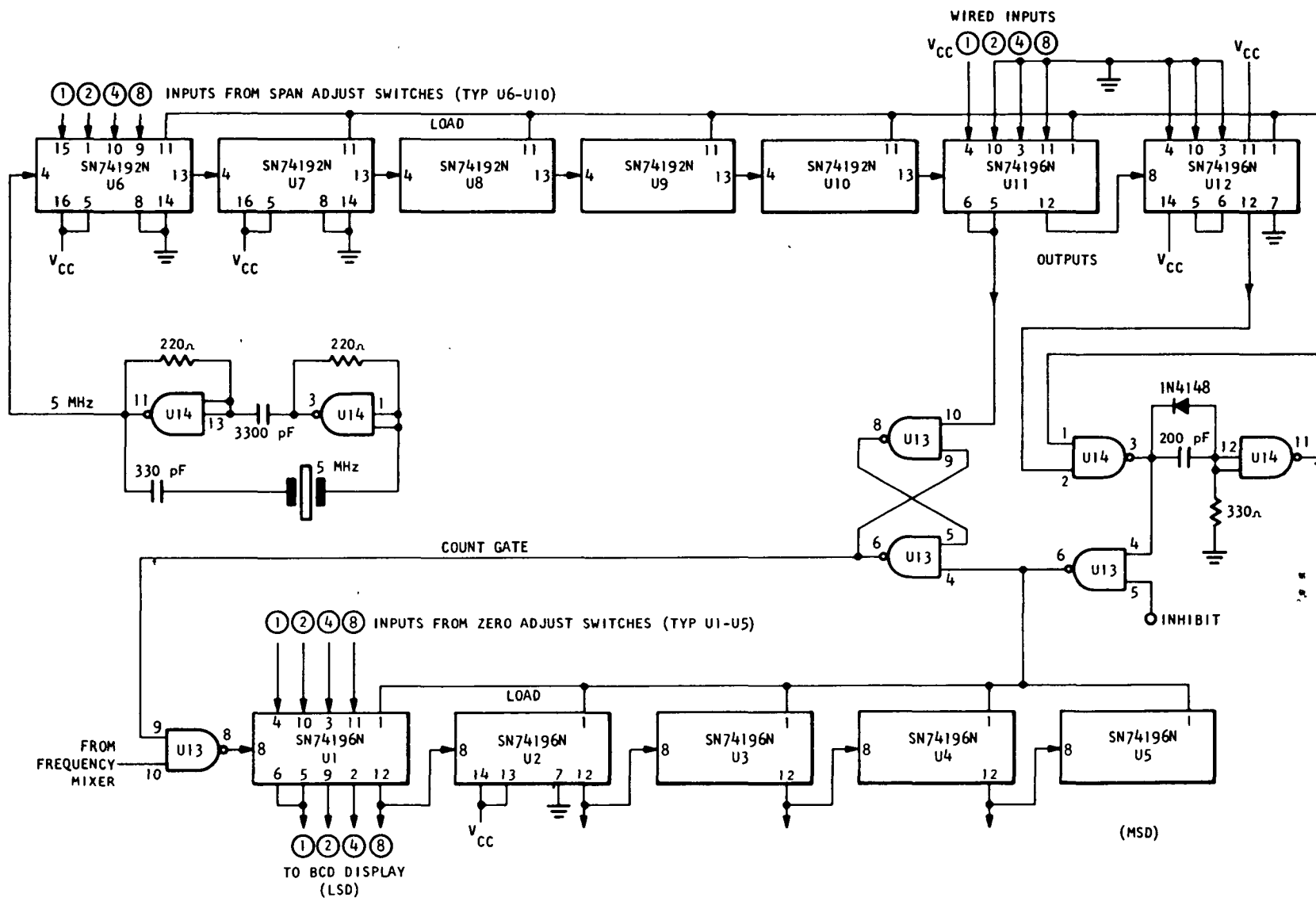


Fig. 4. Simplified schematic diagram of digital electronics for Bell & Howell digital barometer (P/N 4-461-004)

ORIGINAL PAGE IS
OF POOR QUALITY

REF ID: A61170
 DATE: 11/09/70

ORIGINAL PAGE IS
 OF POOR QUALITY

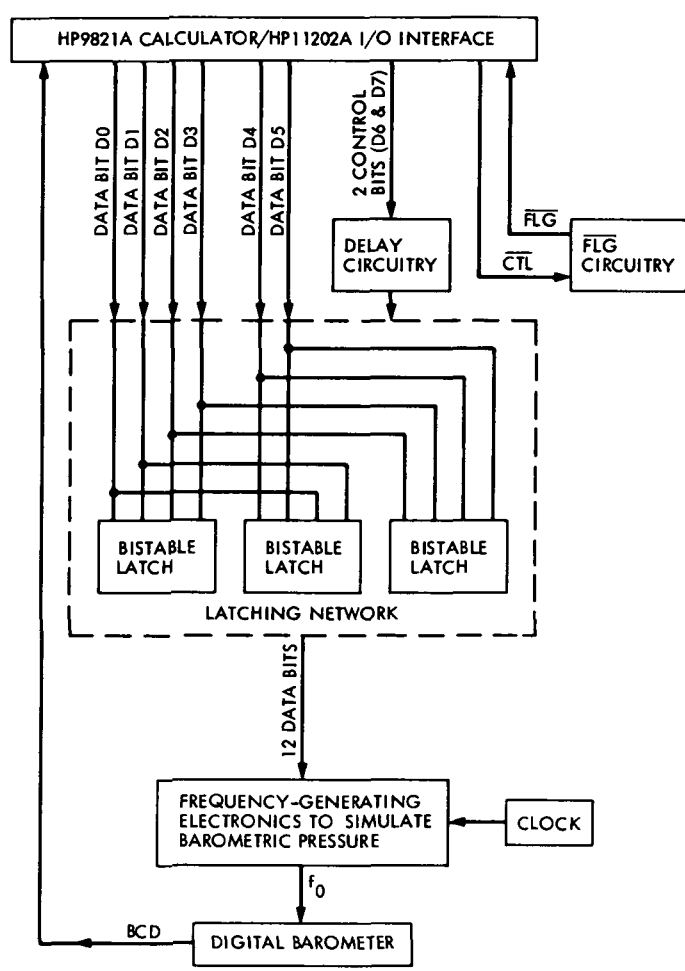


Fig. 5. Block diagram for barometric pressure simulator

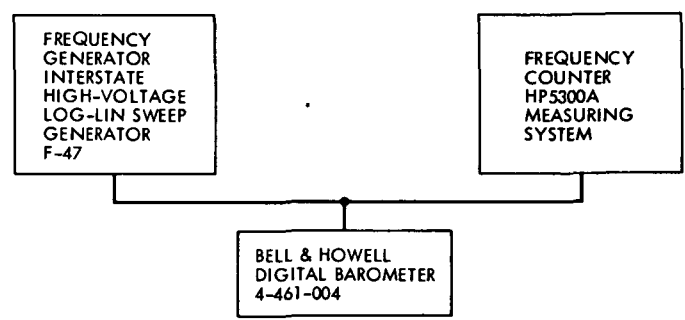


Fig. 6. Test setup for frequency vs simulated barometric pressure scale factor determination

ORIGINAL PAGE IS
OF POOR QUALITY

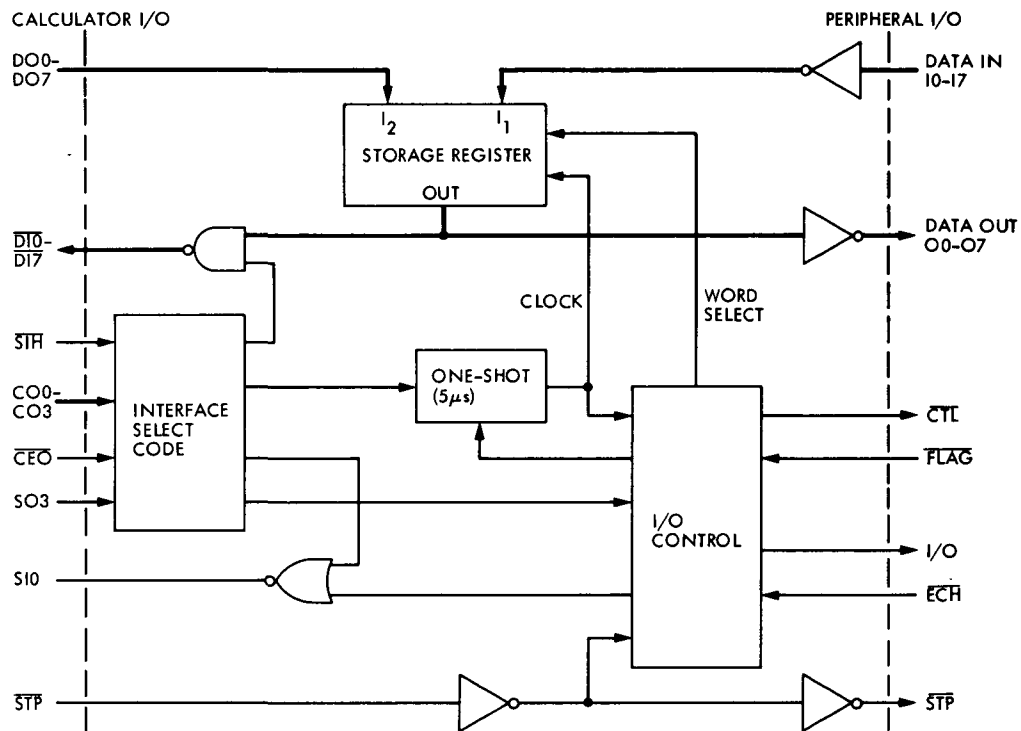


Fig. 7. Simplified block diagram of the HP11202A I/O Interface

The Fabrication and Surface Tolerance Measurements of the JPL Clear Aperture Microwave Antenna

J. Carpenter, S. Rocci, and C. T. Chian
DSN Engineering Section

Present ground station microwave antennas of the Deep Space Network are of the symmetric dual reflector (cassegrainian) type. An investigation is being made of alternative high-performance offset antenna designs which have a clear aperture (no reflector or structure blockage) with shaped reflector surfaces. A 1.5-m, 32-GHz clear aperture model was built for experimental studies. This article describes the unique processes of fabrication, surface measurement and alignment.

I. Introduction

Present microwave antennas in the NASA-owned Deep Space Network (DSN) are of the dual-reflector (cassegrainian) type. Recently an investigation has been made of alternative ground station antenna designs to increase the performance and enable efficient operation at 32 GHz. Significant advances in the synthesis microwave, analysis and performance optimization of several designs have been completed since 1978 (Ref. 1). Parallel studies on structural designs of antennas with symmetrical and asymmetrical reflectors were undertaken. The clear aperture (sometimes called offset) antenna design with dual-shaped reflectors emerged as a superior design. A 1.5-m clear aperture antenna model with shaped-reflector surfaces was selected as a proof-of-design for experimental verification. The predicted superior performance has a potential 2 to 3 dB increase in the gain to noise temperature ratio (G/T). This proof-of-design antenna was to be carefully tested at JPL both for mechanical stability and for the high-performance electrical (microwave) characteristics. The antenna synthesis and

analysis has predicted a high aperture efficiency of 86%. It was necessary to obtain a highly accurate surface finish with minimum surface and alignment tolerance to permit accurate estimates of the electrical (microwave) loss at 32 GHz at the 0.5% level for surface error to wavelength ratio. This accuracy requirement corresponds to a mechanical setting accuracy at the 0.04-mm (0.0015-inch) level.

II. Surface Tolerances

The geometry specifications and the design details were developed in house to meet the needs of the high performance sought. The subreflector and feedhorn as shown in Figs. 1 and 2 were to be adjustable in X, Y, and Z axes plus a rotation for further mechanical alignment and microwave testing. The goal for the main reflector and subreflector surface tolerance was to be equal to 0.18 mm (0.007 in.) or better. The alignment error must be equal to 0.5 mm (0.020 in.) or better for optimum performance.

III. Fabrication Steps

After the documentation was completed a search was initiated to locate a vendor with the unique capability to machine the shaped surface of the reflectors to the specified tolerance. Among 20 firms contacted, Tempe Precision Aircraft Co. of Tempe, Arizona, was selected in June 1981, with a contract completion date of Feb. 1, 1982. The details of the computer coordinates for machining the reflectors were developed in house as described in the appendix. Details of the fabrication of the major components are as follows:

A. Main Reflector

This is designed to be 1.5 m in diameter. A 1524 × 1828.8 × 260-mm (5 ft × 6 ft × 10 in.) aluminum billet was blanked ground and mounted on a three-axis, numerically controlled horizontal milling machine as shown in Fig. 3. The excess material was removed to form a unique "parabolic" shape. Since the machine was not large enough to machine the entire surface, the main reflector was rotated in 90 deg increments for machining. Each quadrant was machined in three steps. The first step was rough cut to remove excess material to within 2.8 mm (0.110 in.) of the finished surface. The second step was a cut to remove material to within 0.25 mm (0.010 in.) as shown in Fig. 4. The third cut produced a finished machined surface. The surface was spot-checked after each machining operation to verify the computer program results. After the surface was machined and the perimeter trimmed to the final envelope size, the reflector was removed and hand-finished to remove the tool marks. The main reflector surface was measured at 727 points at Tempe Precision Aircraft Co. as shown in Fig. 5 and verified at JPL machine shop as shown in Fig. 6. The root mean square (rms) error obtained from the two machines was 0.114 mm (0.0045 in.) as outlined in Table 1.

B. Subreflector

The subreflector, which is 0.4 m in diameter, was machined utilizing the same methods and equipment above. An rms error of 0.114 mm (0.0045 in.) was obtained. The X-, Y-, and Z-axis adjustments were obtained utilizing three micrometer translation units with 50 mm travel.

IV. Field Alignment and Installation

The complete assembly was optically and mechanically aligned as shown in Fig. 7 utilizing an optical level (Wild, N-3), a theodolite (Wild T-2), two master precision levels, a series of inside micrometers and a precision fabricated template to maintain the theoretical geometry and to obtain the optimum signal reception. The three subassemblies were aligned within 0.25 mm (0.010 in.), verified and inspected as shown in Fig. 8. The assembly was transported to the test range and installed on an azimuth-elevation positioner located on the roof of the test building and the alignment was rechecked.

V. Results of Surface Measurements

An attempt was made to compute the rms value of the surface distortions in the Z-axis normal to the reflector surface. The surface distortions were measured in a local coordinate system and the reflector surface has a final shape close to a paraboloid. A FORTRAN computer program CAA-RMS, described in the appendix, was developed to transform the local coordinates into a global coordinate system. An rms best fitting program (half-path length error) was used to calculate the rms value of the reflector surface distortion. The rms values of the surface distortion of the main reflector e_1 , were found to be 0.094 mm (0.0037 in.) without best fitting, and 0.0285 mm (0.001123 in.) with best fitting. The surface deviation of the subreflector e_2 (without best fitting), was found to be comparable 0.114 mm (0.0045 in.).

Since comparable machining techniques were used throughout, it is estimated that the fitted rms of the subreflector is approximately 0.028 mm (0.0011 in.). The net effective rms of both reflectors together, with best fitting, is thus approximately $\sqrt{e_1^2 + e_2^2}$ or 0.040 mm (0.0015 in.). This yields 0.5% for the ratio of surface error to wavelength at the 32-GHz microwave frequency, from the Ruze equation, and a gain limit frequency near 600 GHz. The 1.5-m clear aperture antenna model is currently undergoing electrical microwave tests that will be the subject of future TDA reports.

Acknowledgment

The authors acknowledge the technical and administrative assistance given by C. L. Thornton (420), F. W. Stoller (355), E. Laumann (350), D. A. Bathker (333), A. Cha (333), R. Levy (355), and F. Lansing (355) during the various execution steps of this work. The support given by the Design and Mechanical Section (356), Quality Assurance Section (511), and Fabrication Section (664) is also acknowledged.

Reference

1. Cha, A., "Design of a 1.5-m, 32-GHz, Clear Aperture Antenna," *TDA Progress Report 42-66*, Jet Propulsion Laboratory, Pasadena, Calif., Dec. 1981, pp. 87-93.

ORIGINAL PAGE IS
OF POOR QUALITY

Table 1. Results of surface measurements

Surface deviation, mm (in.)		
	Not best-fit	Best-fit
Main reflector	0.112 (0.0044)	0.028 (0.0011)
Sub-reflector	0.114 (0.0045)	0.028 ≅ (0.0011)
RSS	0.160 (0.0063)	0.038 ≅ (0.0015)

Half pathlength error, 0.0381 mm (0.0015 in.); surface tolerance loss
≅ 0.5% of wavelength (32 GHz); gain limit frequency ≅ 600 GHz.

ORIGINAL PAGE IS
OF POOR QUALITY

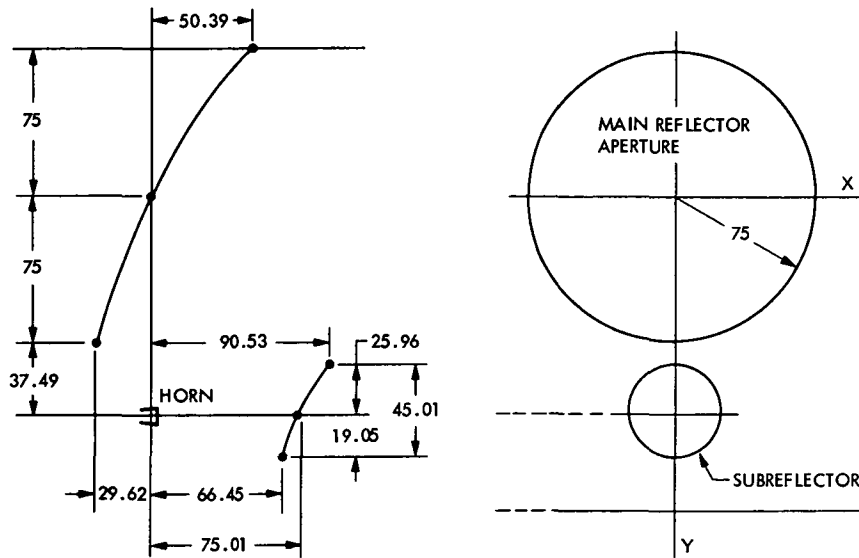


Fig. 1. Geometry of offset clear aperture dual reflector (in cm)

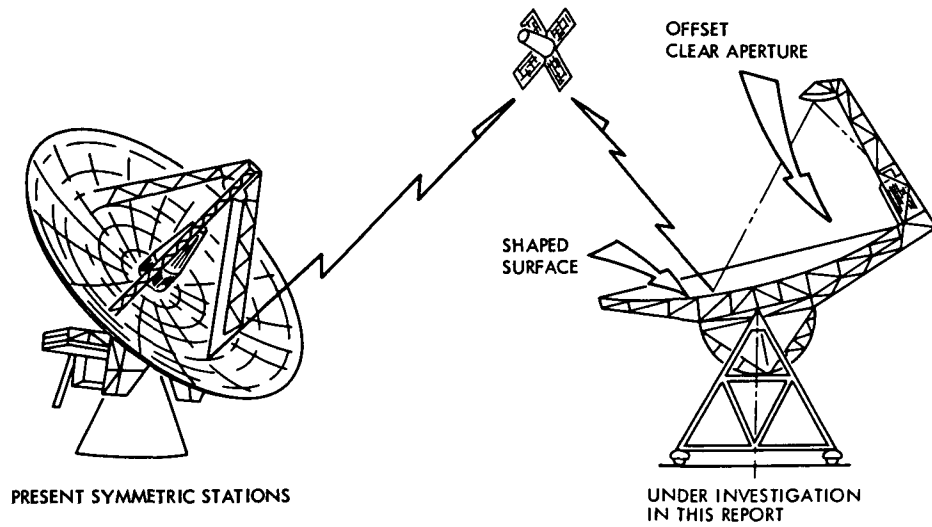


Fig. 2. Alternative reflector configurations for very low noise and high-gain ground stations

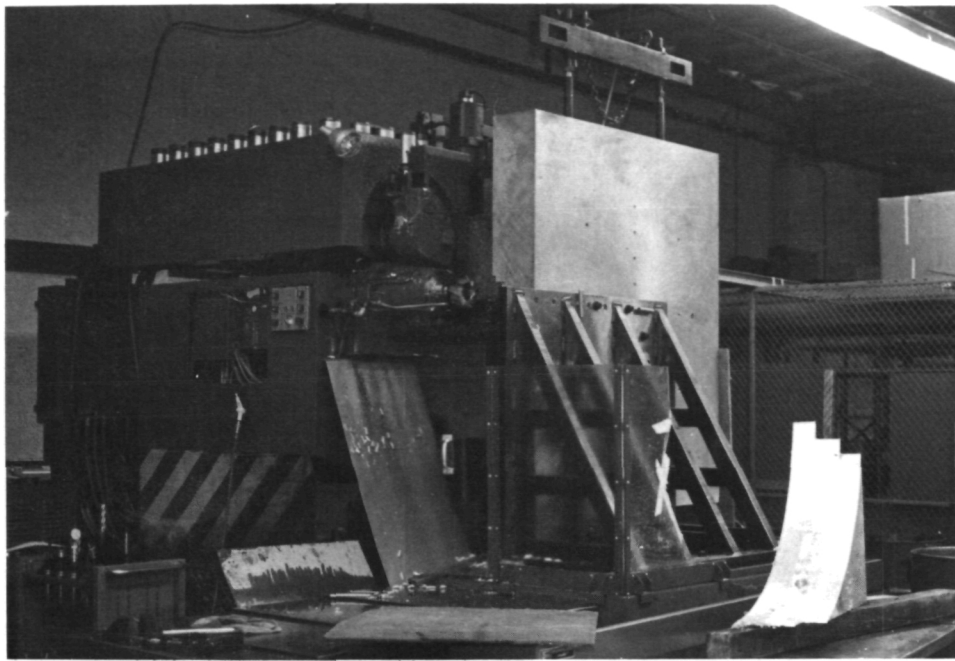


Fig. 3. Milling machine and tooling showing billet

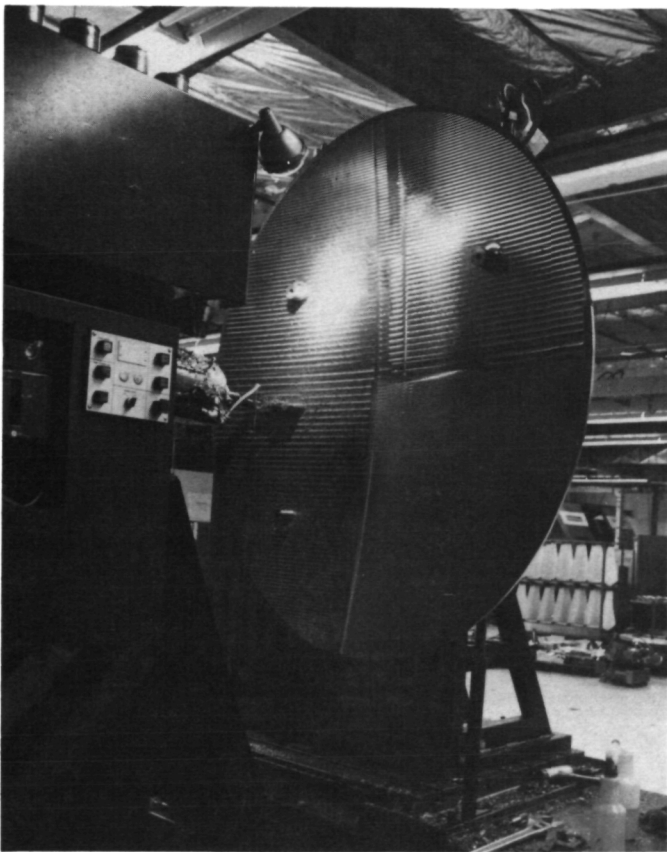


Fig. 4. First rough cut and one quadrant of second cut of main reflector

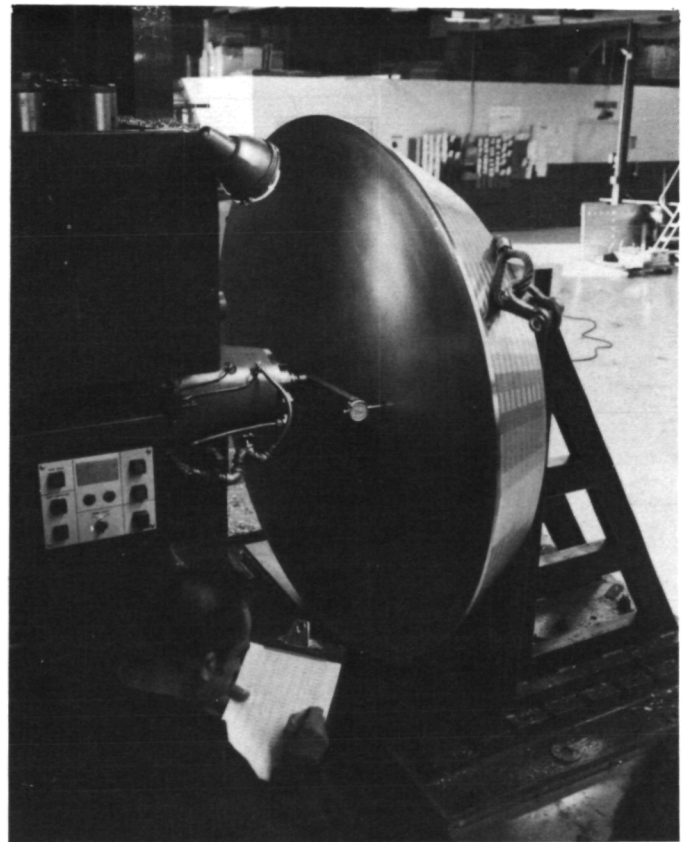


Fig. 5. Checking the rms of the completed reflector at Tempe Precision

**ORIGINAL PAGE
BLACK AND WHITE PHOTOGRAPH**

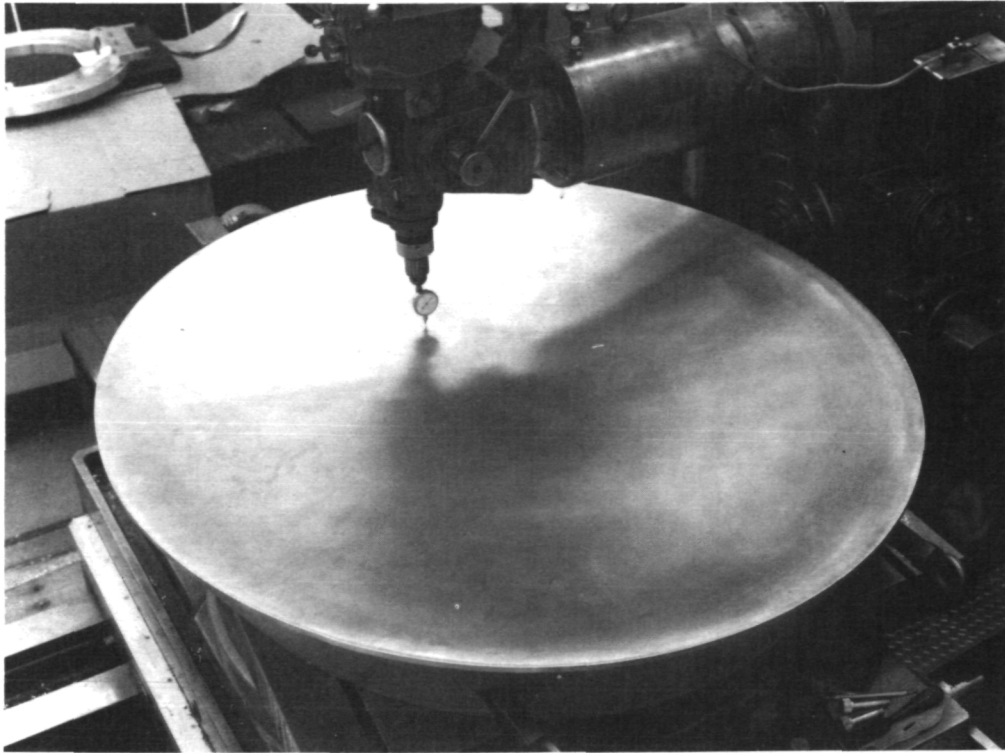


Fig. 6. Checking the rms of the reflector at JPL machine shop

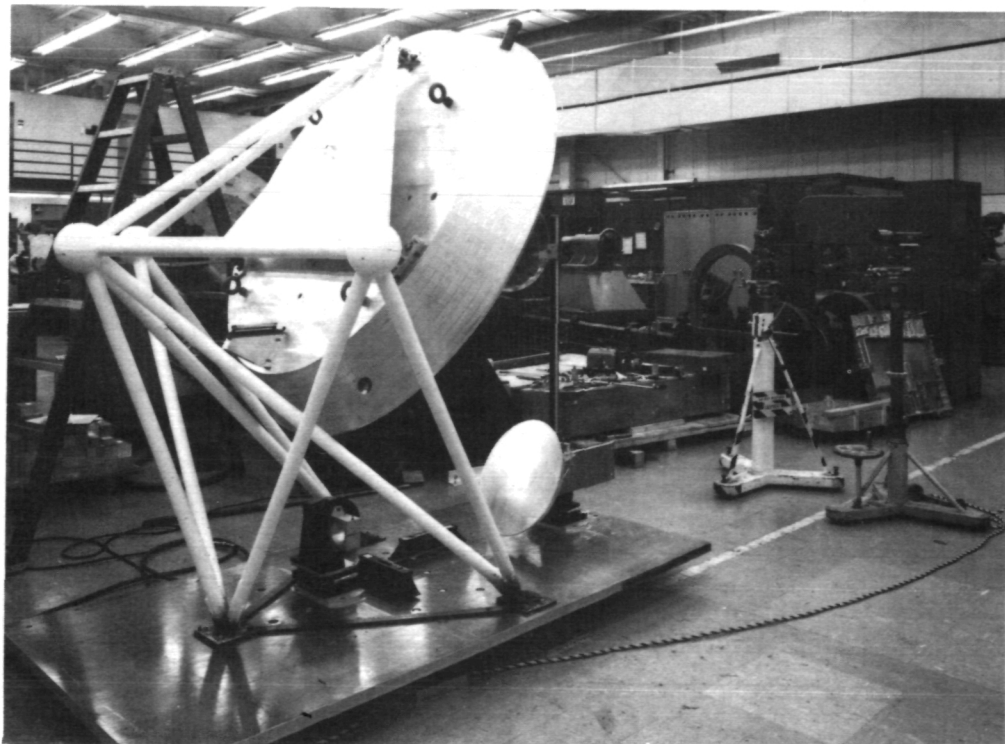


Fig. 7. Alignment equipment for the clear aperture antenna

ORIGINAL PAGE
BLACK AND WHITE PHOTOGRAPH

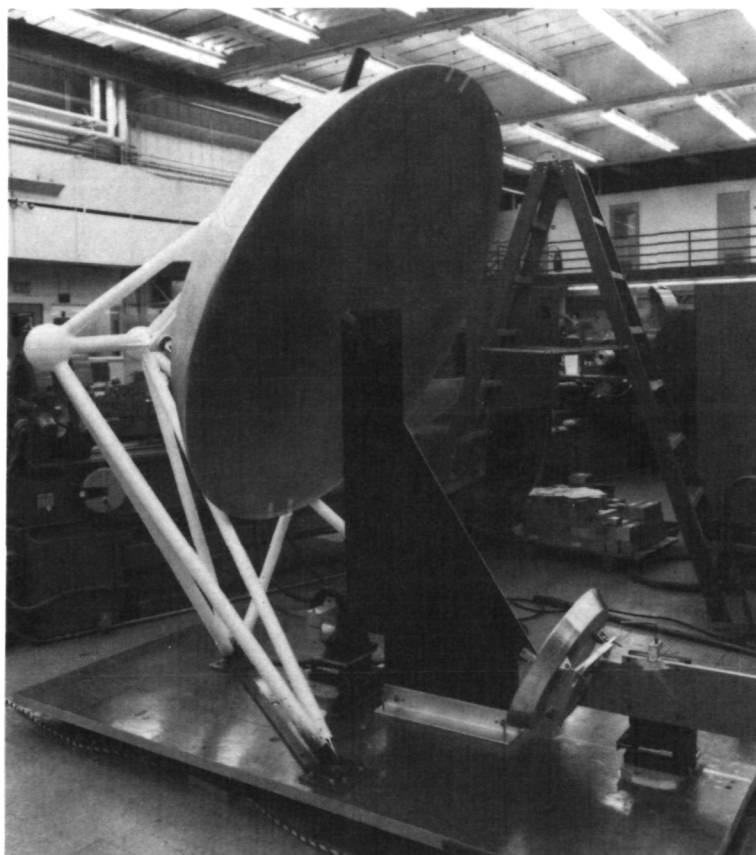


Fig. 8. Axis alignment of the clear aperture antenna

Appendix

Details of Computer Program CAA-RMS

The computer program CAA-RMS, written in FORTRAN, was developed to transform the measured surface distortions from a local-coordinate system into a global-coordinate system as shown in Fig. A-1. The output of this program as shown in Fig. A-2 is used as input to the JPL RMS-BEST-FITTING PROGRAM to calculate the best fitting rms value of the reflector surface distortion.

I. Surface Geometry Equations

The paraboloid is defined by

$$Z = \frac{X^2 + Y^2}{4F} = \frac{R^2}{4F} \quad (\text{A-1})$$

where F = focal length

The slope is defined by

$$\frac{\Delta Z}{\Delta R} = \frac{R}{2F} = \frac{\sqrt{X^2 + Y^2}}{2F} \quad (\text{A-2})$$

The normal vector at any point on the paraboloid is

$$N = (N_1, N_2, N_3) = \left(-\frac{2X}{C_1}, -\frac{2Y}{C_1}, \frac{4F}{C_1} \right) \quad (\text{A-3})$$

where

$$C_1 = \sqrt{4X^2 + 4Y^2 + 16F^2}$$

The coordinate transformation from the local coordinate (x_1, y_1, z_1) to the global coordinate (X, Y, Z):

$$\left. \begin{aligned} X &= x_1 \\ Y &= Y_{off} + y_1 \cos \theta - z_1 \sin \theta \\ Z &= Z_{off} + y_1 \sin \theta + z_1 \cos \theta \end{aligned} \right\} \quad (\text{A-4})$$

The measured distortion vector ΔZ has components U, V, W :

$$\left. \begin{aligned} U &= 0 \\ V &= \Delta Z \cdot \sin \theta \\ W &= \Delta Z \cdot \cos \theta \end{aligned} \right\} \quad (\text{A-5})$$

The projection of the distortion vector on the normal has components:

$$\left. \begin{aligned} P_1 &= C_2 \cdot N_1 \\ P_2 &= C_2 \cdot N_2 \\ P_3 &= C_2 \cdot N_3 \end{aligned} \right\} \quad (\text{A-6})$$

where

$$C_2 = U \cdot N_1 + V \cdot N_2 + W \cdot N_3$$

The length of the projected vector

$$PL = \sqrt{P_1^2 + P_2^2 + P_3^2} \quad (\text{A-7})$$

When the normal is projected in dZ direction:

$$|dZ| = \frac{PL}{\cos(\text{SLOPE})} = \frac{PL}{\cos\left(\sqrt{\frac{X^2 + Y^2}{2F}}\right)} \quad (\text{A-8})$$

A listing of the program is given in Fig. A-3.

II. Sample Calculation

A. Input

Focal length of fitting paraboloid, $F = 1342.39$ mm (52.85 in.)

Offset of local coordinate system:

$$X_{off} = 0$$

$$Y_{off} = 1434.08 \text{ mm (56.46 in.)}$$

1. 2. 3. 4. 5. 6. 7. 8. 9. 10. 11. 12. 13. 14. 15. 16. 17. 18. 19. 20. 21. 22. 23. 24. 25. 26. 27. 28. 29. 30. 31. 32. 33. 34. 35. 36. 37. 38. 39. 40. 41. 42. 43. 44. 45. 46. 47. 48. 49. 50. 51. 52. 53. 54. 55. 56. 57. 58. 59. 60. 61. 62. 63. 64. 65. 66. 67. 68. 69. 70. 71. 72. 73. 74. 75. 76. 77. 78. 79. 80. 81. 82. 83. 84. 85. 86. 87. 88. 89. 90. 91. 92. 93. 94. 95. 96. 97. 98. 99. 100.

$$Z_{off} = 383.03 \text{ mm (15.08 in.)}$$

Angle between local and global systems:

$$\theta = 28.073 \text{ deg}$$

The surface distortions, ΔZ , measured in local coordinates, are read in (a total of 400)

B. Output

RMS values of the surface distortion:

0.094 mm (0.0037 in.) (without fitting)

0.0331 mm (0.001303 in.) (with best fitting)

The printout of this example is shown in Fig. A-4.

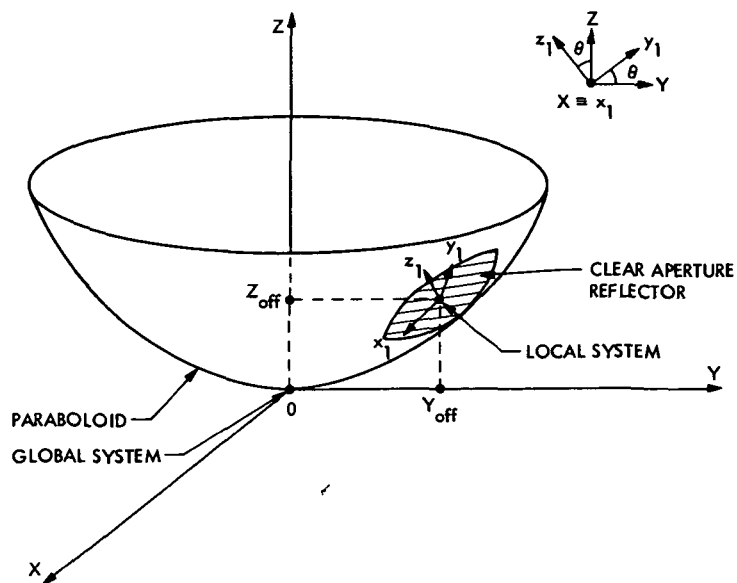


Fig. A-1. Local and global coordinates

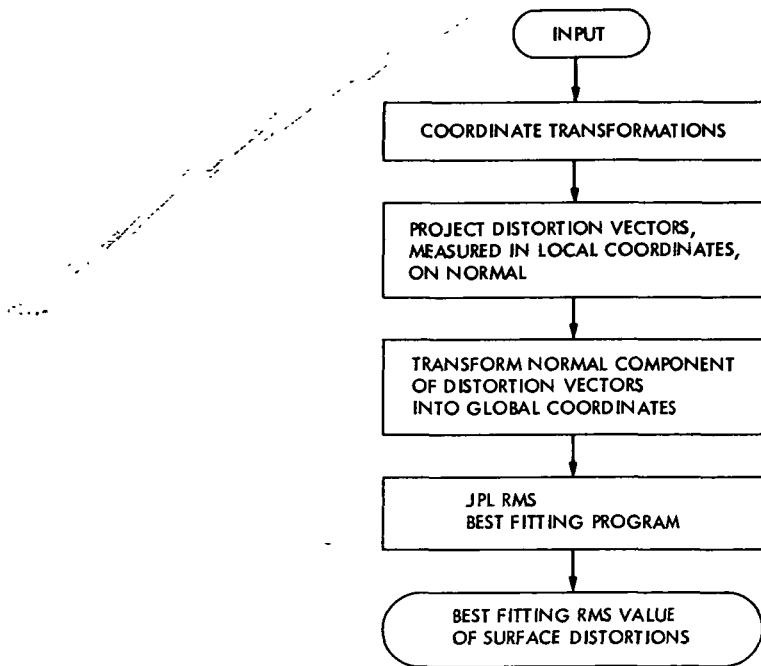


Fig. A-2. Flow chart of rms computer steps

```

08336*MKK(1).CAA-RMS
1 C PROGRAM COMPUTES THE DELTA Z ERRORS OF CLEAR APERTURE REFLECTOR
2 C WHICH HAS A SHAPED SURFACE CLOSE TO A PARABOLOID
3 C THE OUTPUT FITS THE RMS BEST FITTING PROGRAM SO THAT A BEST
4 C THE SURFACE WAS ACTUALLY MEASURED IN A LOCAL COORDINATE SYSTEM
5 C ABOUT ITS X AXIS 28.073 DEGREES
6 C OFFSET IN Y 56.46 INCHES FROM THE PARABOLOIDS' SYSTEM
7 C OFFSET IN Z 15.08 INCHES FROM THE PARABOLOIDS' SYSTEM
8 C
9 C CONSTANTS
10 C
11 REAL N1,N2,N3
12 AREA= 1.0
13 F= 52.05          @ FOCAL LENGTH OF FITTING PARABOLOID
14 YOFF= 56.46      @ Y OFFSET OF LOCAL COORDS SYSTEM
15 ZOFF= 15.08      @ Z OFFSET OF LOCAL COORDS SYSTEM
16 XROT= 28.073+ 0.01745329252
17 NP= 0
18 DIMENSION ID(400), X1(400), Y1(400), Z1(400), ZERR(400)
19 PRINT 4000
20 4000 FORMAT (' ID X Y Z ZZ ZERR V
21 $ W C2 P1 P2 P3 PL TANG DZ')
22 PRINT 4100
23 4100 FORMAT (' C1 N1 N2 N3 '///)
24 $
25 C
26 C READ IN DATA
27 C
28 DO 50 I=1,400
29 READ 1000, ID(I), X1(I), Y1(I), Z1(I), ZERR(I)
30 1000 FORMAT ('
31 IF (ID(I).EQ.0) GO TO 51
32 NP=NP+ 1
33 X= X1(I)
34 Y= YOFF + Y1(I)* COS(XROT)- Z1(I)*SIN(XROT)
35 ZZ= ZOFF + Z1(I)*COS(XROT) + Y1(I)* SIN(XROT)
36 Z= (X*X+ Y*Y)/(4.*F)
37 C N1,N2,N3 = COMPONENTS OF THE NORMAL TO PARABOLOID
38 C1= SQRT(4.*X*X+ 4.*Y*Y+ 16.*F*F)
39 N1= -2.*X/C1
40 N2= -2.*Y/C1
41 N3= 4.*F/C1
42 C U,V,W = COMPONENTS OF THE DISTORSION VECTOR
43 U= 0.
44 V= -ZERR(I)* SIN(XROT)
45 W= ZERR(I)* COS(XROT)
46 C PROJECT DISTORTION VECTOR ON NORMAL
47 C2= U* N1+ V* N2+ W*N3
48 P1= C2* N1
49 P2= C2* N2
50 P3= C2* N3
51 PL= SJRT(P1*P1+ P2*P2+ P3*P3)
52 C SLOPE OR TANGENT ANGLE TO PARABOLOID
53 SLOPE= SQRT(X*X+ Y*Y)/(2.*F)
54 SLOPE= ATAN(SLOPE)
55 DZ= PL/ COS(SLOPE)
56 TANG= SLOPE* 57.2957795131
57 C
58 PRINT 2000, ID(I), X, Y, Z, ZZ, ZERR(I), V, W, C2, P1, P2, P3, PL,
59 $ TANG, DZ
60 PRINT 2100, C1, N1, N2, N3
61 2100 FORMAT ('69X,F9.2,3F8.4)
62 2000 FORMAT ('5,F9.4,F7.4,3F8.4,F9.4)
63 WRITE (10,3000) X,Y,DZ,AREA, ID(I)
64 3000 FORMAT ('2F10.3,30X,F10.4,F10.2,110)
65 50 CONTINUE
66 51 CONTINUE
67 PRINT 5000, NP
68 5000 FORMAT ('1H0,***** - ',I5,' - POINTS PROCESSED')
69 STOP
70 END

```

APKT.S MKK.CAA/LOCAL-DATA

Fig. A-3. CAA-RMS program listing

ORIGINAL PAGE IS
OF POOR QUALITY

```
CLEAR OPERATURE - A                                ORIGIN Y OFFSET =
PUNCH = 0  OPTION = 0  RSTFIT = 0  SPLOSS = 0  NO OF POINTS = 135
FOCAL LENGTH = 1.34239-M ( 52.850-IN)
CNST1 = .00000  CNST2 = .00000  CNST3 = .00000
YOFF = .000  ZOFF = .000  XROT = .000
      INPUT DISTORTIONS OBTAINED ANALYTICALLY - OPTION 0
      NORMAL ANALYSIS FOR INPUT DATA
MINIMIZATION OF RMS WITH RESPECT TO THE DESIGN PARABOLOID
RMS OF 1/2 LAMBDA WEIGHTED BY AREAS = .09-MM      ( .0037-IN)
MINIMIZATION OF RMS WITH RESPECT TO FOCAL LENGTH CHANGE
RMS OF 1/2 LAMBDA WEIGHTED BY AREAS = .03-MM      ( .001303-IN)
NEW FOCAL LENGTH      = 1.34304-M ( 52.876-IN)
DEVIATION OF THE MEAN - 1/2 LAMBDA = -.00007762-MM
X COORDINATE OF VERTEX = -.204-CM      ( -.080-IN)
Y COORDINATE OF VERTEX = .486-CM      ( .191-IN)
Z COORDINATE OF VERTEX = .042-CM      ( .017-IN)
ROTATION ABOUT X AXIS = .001452-RADIANS
ROTATION ABOUT Y AXIS = .000577-RADIANS
ENGLISH UNITS USED FOR MEASUREMENTS AND CALCULATIONS
PLOTING CONTROL CARD DATA - MG = 0  NV = -1  .0000
BRKPT PRINTS
```

Fig. A-4. Sample results of CAA-RMS program

Direct Comparison of Viking 2.3-GHz Signal Phase Fluctuation and Columnar Electron Density Between 2 and 160 Solar Radii

A. L. Berman
TDA Mission Support Office

J. A. Wackley
TDA Engineering Office

W. H. Hietzke
TRW Corporation

The relationship between solar wind induced signal phase fluctuation and solar wind columnar electron density has been the subject of intensive analysis during the last two decades. In this article, a sizeable volume of 2.3-GHz signal phase fluctuation and columnar electron density measurements separately and concurrently inferred from Viking spacecraft signals are compared as a function of solar geometry. These data demonstrate that signal phase fluctuation and columnar electron density are proportional over a very wide span of solar elongation angle.

A radially dependent electron density model which provides a good fit to the columnar electron density measurements and, when appropriately scaled, to the signal phase fluctuation measurements, is given as $N_e(r) = 2.21 \times 10^8 r^{-6} + 1.55 \times 10^6 r^{-2.3}$, where r = heliocentric distance in solar radii and $N_e(r)$ = electron density in cm^{-3} . This model is also in good agreement with K-coronameter observations at 2 solar radii ($2r_0$), with pulsar time delay measurements at $10r_0$, and with spacecraft in situ electron density measurements at 1 AU.

I. Introduction

During the last two decades, solar wind electron density and density fluctuation have been extensively investigated and analyzed via a wide variety of direct and indirect techniques. Although a number of studies have been performed using in situ spacecraft measurements at approximately 1 AU (e.g., Refs. 1-3), the very interesting regions close to the Sun were

and continue to be inaccessible to spacecraft in situ measurements, and hence can only be probed indirectly via effects on observed signals which pass through or originate in these near-Sun regions.

In the early to mid 1960s, solar wind electron density fluctuation experiments focused on measurement of the

angular broadening of compact natural radio sources and subsequent modeling of this parameter as a function of solar elongation angle (Refs. 4-6). In the latter 1960s the emphasis shifted to measurement of signal intensity fluctuation in the form of the "scintillation index m " of natural radio sources (Refs. 7-11). Later studies (Refs. 12-16) emphasized the determination of the solar elongation angle (or radial) dependence of the scintillation index. More recently obtained monochromatic source spacecraft signal scintillation measurements are given in Ref. 17. Very recently, near-Sun spacecraft monochromatic signal spectral broadening has been studied (Refs. 18-20).

In the early attempts to formulate a theoretical basis for natural source intensity scintillation, it was necessary to consider signal phase fluctuation induced by electron density fluctuation. Studies which investigated the geometric dependence of signal phase fluctuation include Refs. 7, 9, 10, 14, and 21. It is, of course, not possible to directly measure phase fluctuation for noncoherent natural radio sources, as is easily done with coherent (e.g., spacecraft) signals. Additionally, the scintillation index of fluctuations from natural sources saturates of the more interesting small solar elongation angles as a result of the finite source size, whereas the monochromatic signal phase fluctuation is not subject to such an effect in this region. During the period (late 1960s, early 1970s) when the study of natural source intensity scintillation was widespread, extremely valuable (monochromatic) near-Sun spacecraft phase fluctuation data was routinely being acquired by the National Aeronautics and Space Administration (NASA)/Jet Propulsion Laboratory (JPL) Deep Space Network for other purposes (primarily tracking system performance monitoring), but was not utilized in the investigation of solar wind density fluctuation.

The first usages of single-frequency spacecraft data to probe the solar corona and solar wind consisted of a spectral broadening experiment with Mariner IV (Ref. 22), range experiments with Mariner 6 and Mariner 7 (Ref. 23), and a Mariner 6 and Mariner 7 experiment utilizing a group-phase technique (Ref. 24). However, the first investigation of solar wind density turbulence which utilized single-frequency spacecraft signal phase fluctuation was an analysis of the 1975 solar conjunction data of the Helios 1, Pioneer 10, and Pioneer 11 spacecraft (Refs. 25, 26). Results of this and subsequent investigations (Refs. 27-30) strongly suggested that signal phase fluctuation is radially proportional to columnar electron density.

This paper presents a direct comparison of concurrent spacecraft signal phase fluctuation and columnar electron density measurements obtained during the 1976 Viking solar conjunction. The data argue in favor of radial proportionality

between signal phase fluctuation and columnar electron density.

II. Data

The data presented in this paper were generated during July through December 1976. During this period the two Viking Orbiter spacecraft underwent solar conjunction with a minimum Sun-Earth-Spacecraft angle of approximately 0.25 deg reached on November 26, 1976. The daily rate of change of the Sun-Earth-Spacecraft angle was approximately 0.3 deg, with the Sun-Earth-Spacecraft angle at the beginning of July being 47 deg, and 10 deg at end of December. During this entire conjunction period, the NASA-JPL Deep Space Network (DSN) maintained essentially continuous coherent communications links with both spacecraft. The ground-transmitted ("uplink") wavelength to the spacecraft was 13 cm (2.1 GHz, S-band). While the spacecraft-transmitted ("downlink") wavelengths were 13 and 3.6 cm (8.4 GHz, X-band).

During these tracking periods the DSN generates frequent measurements of doppler data (accumulated doppler phase) and less frequent measurements of spacecraft range (signal time delay). The doppler frequency referred to here is that frequency component arising from the relative motion of the spacecraft with respect to the ground antenna. These data are used for both navigation (except at small solar offset distances) and radio science (primarily at small solar offset distances). The doppler data are generated by comparing a very precise (5×10^{-14} stability over a day) ground reference frequency to the received frequency. This received frequency is simply the (ground) transmitted carrier frequency (S-band only, 2.1 GHz) which has been received, coherently multiplied (by 240/221 at S-band, 880/221 at X-band), and retransmitted by the spacecraft.

In the course of generating these data, the DSN automatically calculated low-frequency ($\sim 10^{-3}$ Hz) S-band phase fluctuation information for purposes of system performance monitoring. In the algorithm used during this time period, a fixed number (usually 15) of doppler frequency samples (usually 60-second averages) were first differenced with the predicted doppler frequency which is generated by the navigational orbit determination process. A rms doppler frequency fluctuation ("noise") was then computed after fitting with a least squares linear curve fit to remove any possible trajectory (i.e., low-frequency) errors.

A numerical simulation of the computational algorithm used (Ref. 31) provides an approximate relationship between

rms doppler phase fluctuation ϕ and rms doppler frequency fluctuation σ_d :

$$\phi(\tau) \approx 1.67 \tau \cdot \sigma_d(\tau)$$

where

τ = doppler averaging time.

Typically, a DSN ground station generates frequent doppler measurements over a daily period of approximately 4 to 8 hours, referred to as a "tracking pass." The doppler noise data discussed in this paper have been computed in Hz as described previously in this section, and then averaged over a tracking pass to produce a single composite value ("pass average") for each daily tracking period. These Viking doppler noise data have already been extensively analyzed (Refs. 27, 28) and a more detailed explanation of the method of computation appears in Ref. 31.

The DSN generates precision (1.7 m) range (time delay) data via the modulation of a sequential binary coded signal onto the same carrier frequency described previously. At the spacecraft the range code is demodulated, and the carrier signal is coherently multiplied and remodulated with the range code and retransmitted by the spacecraft to the receiving station. The received S- and X-band range codes are compared to a reference range code which has been modulated with the extracted doppler frequency. The spacecraft range is extracted from this comparison. Appropriately multiplying and differencing the S- and X-band measurements immediately results in a direct measurement of columnar electron density (Ref. 32). Beneficially, all nonfrequency dependent effects are differenced out in this process.

The range data are dual-frequency (S-band minus X-band) range delay in nanoseconds. For each tracking pass, anywhere from 1 to as many as 100 individual range measurements were available; a composite range delay was constructed by averaging the highest and lowest value from each tracking pass. Since the *maximum* variation in range delay measurements per tracking pass was typically between 2 and 20%, it is considered that the procedure was more than adequate to secure a reasonable daily composite range delay value.

III. The Data Model

Figure 1 provides the correlation between the concurrent range delay and doppler noise pass average data; as is seen, an empirically selected proportionality constant of 5×10^4 Hz s^{-1} provides a very good fit to the data. Figure 2 presents both range delay and doppler noise vs day of year, while Fig. 3

presents the same data vs signal path offset distance (in solar radii). In both Figs. 2 and 3, the range data have been converted to Hz via the proportionality constant (5×10^4 Hz s^{-1}) shown in Fig. 1.

The model shown in Figs. 2 and 3 represents the signal path integration of an electron density model $N_e(r) = 2.21 \times 10^8 r^{-6} + 1.55 \times 10^6 r^{-2.3}$, where the units are cm^{-3} . The coefficient and the radial exponent (-2.3) of the second term was determined by a least squares curve fit to the phase fluctuation data in Fig. 2 (Refs. 27, 28), while the coefficient of the first term was determined from Viking and Helios phase fluctuation measurements between 2 and 6 solar radii (Fig. 4, from Ref. 30). The radial exponent (-6.0) for the near corona term derives from solar eclipse measurements (Ref. 33). The constant K_2 shown in Figs. 2 and 3 is equal to the speed of light ($cm \text{ sec}^{-1}$) times the columnar content (cm^{-3}) per cm of electron density induced signal delay.

The comparison of range delay to doppler noise for the data acquired from November 28, 1976 to December 5, 1976 (day of year 333 to 340) appears to differ somewhat from the comparison over the remainder of the period and hence (this range data) has been marked with a different symbol in the figures. Possible explanations for this difference are (1) a region of enhanced fluctuation-to-density ratio, or less likely (2) systematically erroneous range measurements.

The observations here discussed are columnar quantities; for ease of comparison to other electron density (radial) distribution work, one desires the generating point source electron density distribution. To facilitate the comparison, a closed form approximation of the integral (of the solar wind component of electron density)

$$\int^{R_{s/c}} r^{-(2+\xi)} dR \quad (1)$$

where

R = signal path

$R_{s/c}$ = Earth-spacecraft distance

r = heliocentric signal distance

is desired. Figure 5 details the appropriate geometrical configuration. Equation (1) is rewritten as:

$$(r_e \sin \alpha)^{-(1+\xi)} \int_{\alpha-\pi/2}^{\beta-\pi/2+\alpha} (\cos \omega)^\xi d\omega \quad (2)$$

where α = Sun-Earth-Spacecraft angle, β = Earth-Sun-Spacecraft angle, r_e = Earth-Sun distance, and:

$$\omega = \tan^{-1} (R - r_e \cos \alpha / r_e \sin \alpha) \quad (3)$$

A Macluarin series is utilized to expand $(\cos \omega)$

$$(\cos \omega)^\xi \cong 1 + \frac{\omega^2}{2!} (-\xi) + \frac{\omega^4}{4!} (-1.1 \xi) + \dots \quad (4)$$

After the indicated integration one has:

$$\int^{R_{s/c}} r^{-(2+\xi)} dR = K r_e^{-(1+\xi)} \beta (\sin \alpha)^{-(1+\xi)} F(\alpha, \beta) \quad (5)$$

where

$$F(\alpha, \beta) \cong 1 - 0.05 \left\{ \frac{(\beta - \pi/2 + \alpha)^3 - (\alpha - \pi/2)^3}{\beta} \right\} - 0.00275 \left\{ \frac{(\beta - \pi/2 + \alpha)^5 - (\alpha - \pi/2)^5}{\beta} \right\} \quad (6)$$

In this work, all data fitting (Eq. 5) makes use of the two independent geometrical parameters α and β , which directly relate to the signal path solar offset distance and signal path length, respectively. Much work in determining electron density distribution has customarily relied on usage of only the dominant geometrical parameter α . Significant errors can result in experimentally determining radial dependence via reliance on only one geometrical parameter (Ref. 34).

It is noteworthy that this electron density model is in good agreement with K-coronameter measurements at $2r_0$ (Refs. 35-37), pulsar time delay measurements at $10r_0$ (Refs. 38, 39), and in situ electron density measurements at 1 AU (Ref. 40). The model gives a significantly higher electron density at

$10r_0$ than spacecraft range data from Helios 1 and 2 (Ref. 41) and Mariners 6 and 7 (Ref. 23). Table 1 presents various model determinations at $10r_0$.

IV. Discussion

Since at least the late 1960s, the theoretical relationship between columnar phase fluctuation and columnar electron density has been extensively hypothesized, but definitive concurrent measurements of the two parameters have not (previously) been available to test the various hypotheses. Recent efforts in theoretically analyzing the radial dependence of phase fluctuation (Refs. 19, 42) have produced phase fluctuation models which are proportional to the product of density fluctuation and solar wind (radial) velocity times a factor of $r^{0.5}(\sigma_{n_e}(r)v(r)r^{0.5})$. Under the common assumptions of (1) proportionality between density and density fluctuation, and (2) the conservation of particle flux, such phase fluctuation models are immediately seen to be proportional to $r^{-1.5}$ and hence are independent of the actual radial dependence of electron density.

These theoretically derived phase fluctuation models of Woo and Callahan are not compatible with the concurrent measurements of Viking doppler noise (phase fluctuation) and range (time delay) as presented in this article. In particular, the $r^{-1.5}$ models fail in the near-corona region, where the electron density radial dependence changes from $r^{-2.3}$ to r^{-6} . This can be seen in the near-corona region of Fig. 3 and in Fig. 4, where the phase fluctuation data are well fit by a model of functional form r^{-5} ($\propto \int r^{-6} dR$). Clearly, a model of the form $r^{-1.5}$ could not reasonably fit these data.

In way of possible explanation of this incompatibility, it is to be noted that analyses performed much earlier and which employed geometrical optics (Refs. 11, 14, and 21) predicted this now observed radial proportionality between signal phase fluctuation and columnar electron density, under the very reasonable assumption of a linear transverse fluctuation scale ($L_t = Kr$), as would directly be expected from a radially outflowing solar wind (Ref. 21).

Acknowledgment

The authors wish to thank D. L. Cain and P. S. Callahan, of the Jet Propulsion Laboratory, for their review of this paper, and the many excellent comments and suggestions which they provided. The authors are particularly indebted to Professor G. L. Tyler, of Stanford University, for his comprehensive review of and assistance provided to this article.

References

1. Intriligator, D. S., and Wolfe, J. H., "Preliminary Power Spectra of the Interplanetary Plasma," *Astrophys. J. Let.*, Vol. 162, L187, 1970.
2. Goldstein, B., and Sisco, G. L., "Spectra and Cross Spectra of Solar Wind Parameters from Mariner 5," *Solar Wind*, NASA SP-308, p. 506, 1972.
3. Unti, T., Neugebauer, M., and Goldstein, B. E., "Direct Measurements of Solar Wind Fluctuations Between 0.0048 and 13.3 Hz," *Astrophys. J.*, Vol. 180, p. 591, 1973.
4. Slee, O. B., "Observations of the Solar Corona Out to 100 Solar Radii," *Mon. Not. R. Astr. Soc.*, Vol. 123, p. 16, 1961.
5. Slee, O. B., "The Outer Solar Corona During the Declining Portion of The Solar Activity Cycle," *Planet. Space Sci.*, Vol. 14, p. 255, 1966.
6. Okoye, S. E., and Hewish, A., "Irregularities of Plasma Density in the Solar Neighborhood," *Mon. Not. R. Astr. Soc.*, Vol. 137, p. 18, 1967.
7. Cohen, M. H., Gundermann, E. J., Hardibeck, H. E., and Sharp, L. E., "Interplanetary Scintillations II. Observations," *Astrophys. J.*, Vol. 147, No. 2, p. 449, 1967.
8. Cohen, M. H., and Gundermann, E. J., "Interplanetary Scintillations IV. Observations Near the Sun," *Astrophys. J.*, Vol. 155, No. 2, p. 645, 1969.
9. Salpeter, E. E., "Interplanetary Scintillations. I. Theory," *Astrophys. J.*, Vol. 147, No. 2, p. 433, 1967.
10. Cronyn, W. M., "The Analysis of Radio Scattering and Space Probe Observations of Small Structure in The Interplanetary Medium," *Astrophys. J.*, Vol. 161, No. 2, p. 755, 1970.
11. Jokipii, J. R., and Hollweg, J. V., "Interplanetary Scintillations and the Structure of Solar Wind Fluctuations," *Astrophys. J.*, Vol. 160, No. 2, p. 745, 1970.
12. Hewish, A., and Symonds, M. D., "Radio Investigation of the Solar Plasma," *Planet. Space Sci.*, Vol. 17, p. 313, 1969.
13. Hewish, A., "Observations of the Solar Plasma Using Radio Scattering and Scintillation Methods," *Solar Wind*, NASA SP-308, p. 477, 1972.
14. Little, L. T., "Small Scale Plasma Irregularities in the Interplanetary Medium," *Astron. & Astrophys.*, Vol. 10, p. 301, 1971.
15. Readhead, A. C. S., "Interplanetary Scintillation of Radio Sources at Metre Wavelengths - II," *Mon. Not. Astr. Soc.*, Vol. 155, p. 185, 1971.
16. Rickett, B. J., "Power Spectrum of Density Irregularities in the Solar Wind Plasma," *J. Geophys. Res.*, Vol. 78, No. 10, 1543, 1973.
17. Chang, H., "Analysis of Dual Frequency Observations of Interplanetary Scintillation Taken by the Pioneer 9 Spacecraft," Ph. D. Thesis, Stanford University, Stanford, Calif. 1976.
18. Rockwell, R. S., "An Empirical Spectral Bandwidth Model for Superior Conjunction," *DSN Progress Report 42-43*, Jet Propulsion Laboratory, Pasadena, Calif., p. 216, Feb. 15, 1978.
19. Woo, R., "Radial Dependence of Solar Wind Properties Deduced from Helios 1/2 and Pioneer 10/11 Radio Scattering Observations," *Astrophys. J.*, Vol. 219, p. 727, 1978.

20. Woo, R., and Armstrong, J. W., "Spacecraft Radio Scattering Observations of Electron Density Fluctuations in the Solar Wind," *J. Geophys. Res.*, Vol. 84 No. A12, p. 7288, 1979.
21. Hollweg, J. V., "A Statistical Ray Analysis of the Scattering of Radio Waves by the Solar Corona," *Astronom. J.*, Vol. 73, No. 10, p. 927, 1968.
22. Goldstein, R. M., *The Superior Conjunction of Mariner IV*, Technical Report 32-1092, Jet Propulsion Laboratory, Pasadena, Calif., 1967.
23. Muhleman, D. O., Esposito, P. B., and Anderson, J. D., "The Electron Density Profile of the Outer Corona and the Interplanetary Medium from Mariner 6 and Mariner 7 Time Delay Measurements," *Astrophys. J.*, Vol. 211, p. 943, 1977.
24. Callahan, P. S., "Columnar Content Measurements of the Solar-Wind Turbulence Near the Sun," *Astrophys. J.*, Vol. 199, p. 227, 1975.
25. Berman, A. L., and Rockwell, S. T., "Analysis and Prediction of Doppler Noise During Solar Conjunctions," *DSN Progress Report 42-30*, p. 231, Jet Propulsion Laboratory, Pasadena, Calif., Dec. 15, 1975.
26. Berman, A. L., and Wackley, J. A., "Doppler Noise Considered as a Function of the Signal Path Integration of Electron Density," *DSN Progress Report 42-33*, p. 159, June 15, 1976.
27. Berman, A. L., and Wackley, J. A., "Viking S-Band Doppler RMS Phase Fluctuations Used To Calibrate the Mean 1976 Equatorial Corona," *DSN Progress Report 42-38*, p. 152, Apr. 15, 1977.
28. Berman, A. L., Wackley, J. A., Rockwell, S. T., and Kwan, M., "Viking Doppler Noise Used To Determine the Radial Dependence of Electron Density in the Extended Corona," *DSN Progress Report 42-38*, p. 167, Apr. 15, 1977.
29. Berman, A. L., "Electron Density in the Extended Corona - Two Views," *DSN Progress Report 42-41*, p. 135, Jet Propulsion Laboratory, Pasadena, Calif., Oct. 15, 1977.
30. Berman, A. L., "Electron Density and Doppler RMS Phase Fluctuation in the Inner Corona," *DSN Progress Report 42-44*, p. 172, Jet Propulsion Laboratory, Pasadena, Calif., Apr. 15, 1978.
31. Berman, A. L., "Phase Fluctuation Spectra: New Radio Science Information To Become Available in the DSN Tracking System Mark III-77," *DSN Progress Report 42-40*, p. 134, Jet Propulsion Laboratory, Pasadena, Calif., Aug. 15, 1977.
32. Koehler, R. L., "Radio Propagation Measurements of Pulsed Plasma Streams from the Sun Using Pioneer Spacecraft," *J. Geophys. Res.*, Vol. 78, No. 15, p. 4883, 1968.
33. Anderson, J. D., Esposito, P. B., Martin W., and Thornton, C. L., "Experimental Test of General Relativity Using Time-Delay Data from Mariner 6 and Mariner 7," *Astrophys. J.*, Vol. 200, p. 221, 1975.
34. Berman, A. L., "Precise Extraction of Geometrical Dependence from Solar Wind Columnar Turbulence Measurements," *DSN Progress Report 42-50*, p. 110, Jet Propulsion Laboratory, Pasadena, Calif., Apr. 15, 1979.
35. Hansen, R. T., Garcia, C. J., Hansen, S. F., and Loomis, H. C., "Brightness Variations of the White Light Corona During the Years 1964-1967," *Sol. Phys.*, Vol. 7, 1969.

36. Saito, K., "A Non-Spherical, Axisymmetric Model of the Solar K Corona of the Minimum Type," *Ann. Tokyo Astron. Observ.*, No. 2, Vol. XII, 1970.
37. Saito, K., Poland, A. I., and Munro, R. H., "A Study of the Background Corona Near Solar Minimum," *Sol. Phys.*, Vol. 55, 1977.
38. Counselman, III., C. C., and Rankin, J. M., "Density of the Solar Corona from Occultations of NP0532," *Astrophys. J.*, Vol. 175, 1972.
39. Weisberg, J. M., Rankin, J. M., Payne, R. R., and Counselman III., C. C., "Further Changes in the Distribution of Density and Radio Scattering in the Solar Corona," *Astrophys. J.*, Vol. 209, p. 252, 1976.
40. Diodato, L., Moreno, G., Signorini, C., and Ogilvie, K. W., "Long-Term Variations of the Solar Wind Proton Parameters," *J. Geophys. Res.*, Vol. 79, No. 34, p. 5095, 1974.
41. Esposito, P. B., Edenhofer, P., and Lüneburg, E., "Solar Corona Electron Density Distribution," *J. Geophys. Res.*, Vol. 85, No. A7, p. 3414, 1980.
42. Callahan, P. S., "A First Principles Derivation of Doppler Noise Expected from Solar Wind Density Fluctuations," *DSN Progress Report 42-42*, p. 42, Jet Propulsion Laboratory, Pasadena, Calif., Dec. 15, 1977.

ORIGINAL PAGE IS
OF POOR QUALITY

Table 1. Electron density models evaluated at $10r_0$

| Source | $N_e(10r_0),_{-3}$
electrons cm^{-3} | Type of
experiment |
|--------------|--|--------------------------------|
| This article | 8000 | Dual-frequency
range |
| Ref. 41 | 4500 | Helios 1 and 2
S-band range |
| Ref. 23 | 5600 | Mariner 7
S-band range |
| Ref. 39 | 8000 | Pulsar time
delay |
| Ref. 38 | 8400 | Pulsar time
delay |

ORIGINAL PAGE IS
OF POOR QUALITY

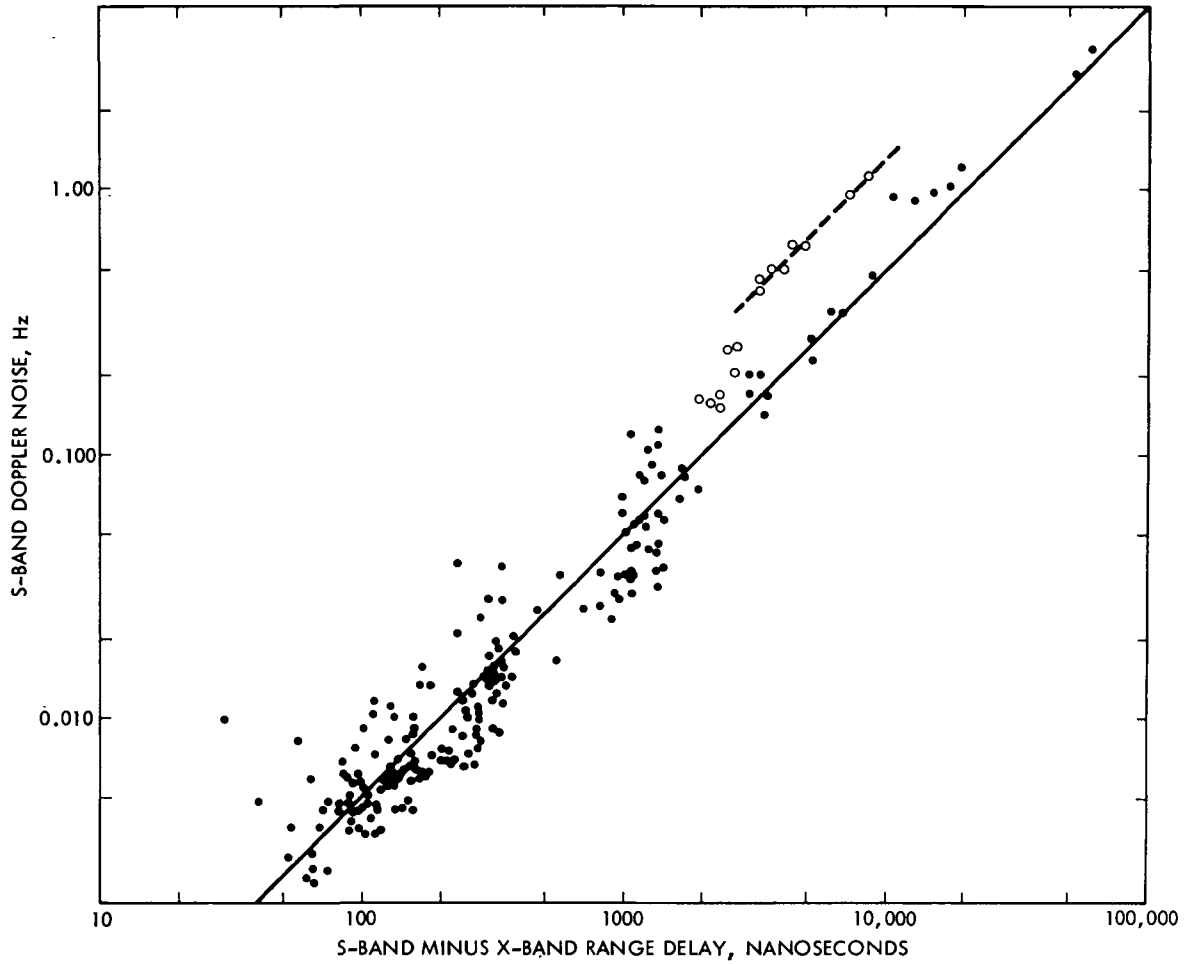


Fig. 1. Correlation between $\sigma_d = 13$ -cm signal phase fluctuation and integrated electron density. The solid data points are from July 2 to November 27, 1976, and December 6 to December 20, 1976, while the hollow points are from November 28, to December 5, 1976. The solid line represents the proportionality constant 5×10^4 Hz/s, while the dashed line represents 1.3×10^5 Hz/s

ORIGINAL PAGE IS
OF POOR QUALITY

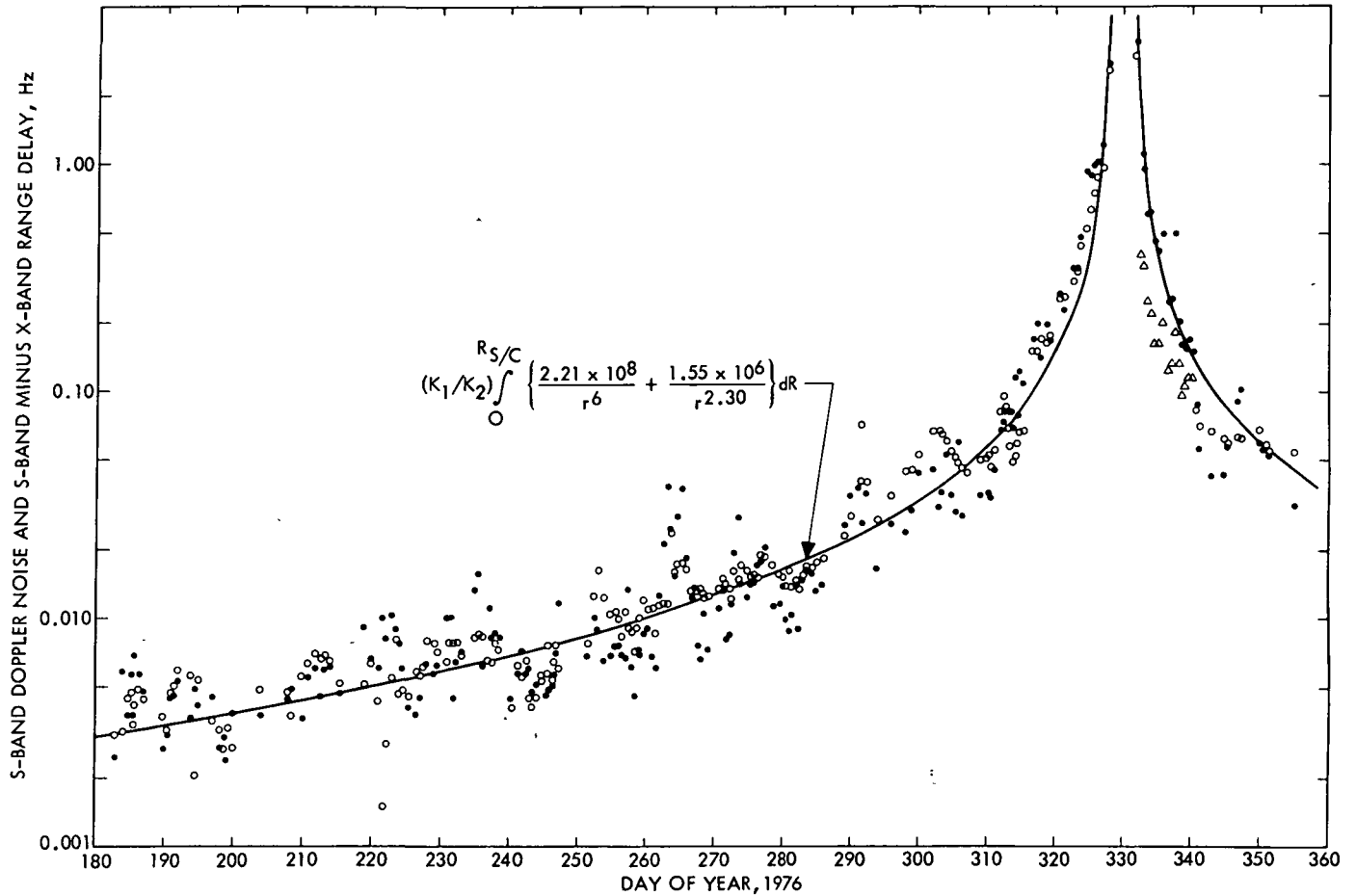


Fig. 2. Signal phase fluctuation and integrated electron density vs day of year, 1976. The solid points are $\sigma_d = 13$ -cm Doppler noise in Hz, while hollow points are dual-frequency range in nanoseconds multiplied by the proportionality constant $K_1 = 5 \times 10^4$ Hz/s. Hollow circles are data from July 2 to November 27, 1976, and December 6 to December 20, 1976, while hollow triangles are data from November 28 to December 5, 1976. The constant $K_2 = 3.93 \times 10^{21} \text{ cm}^{-2} \text{ s}^{-1}$ is the number of columnar electrons per second of dual-frequency range delay

ORIGINAL PAGE IS
OF POOR QUALITY

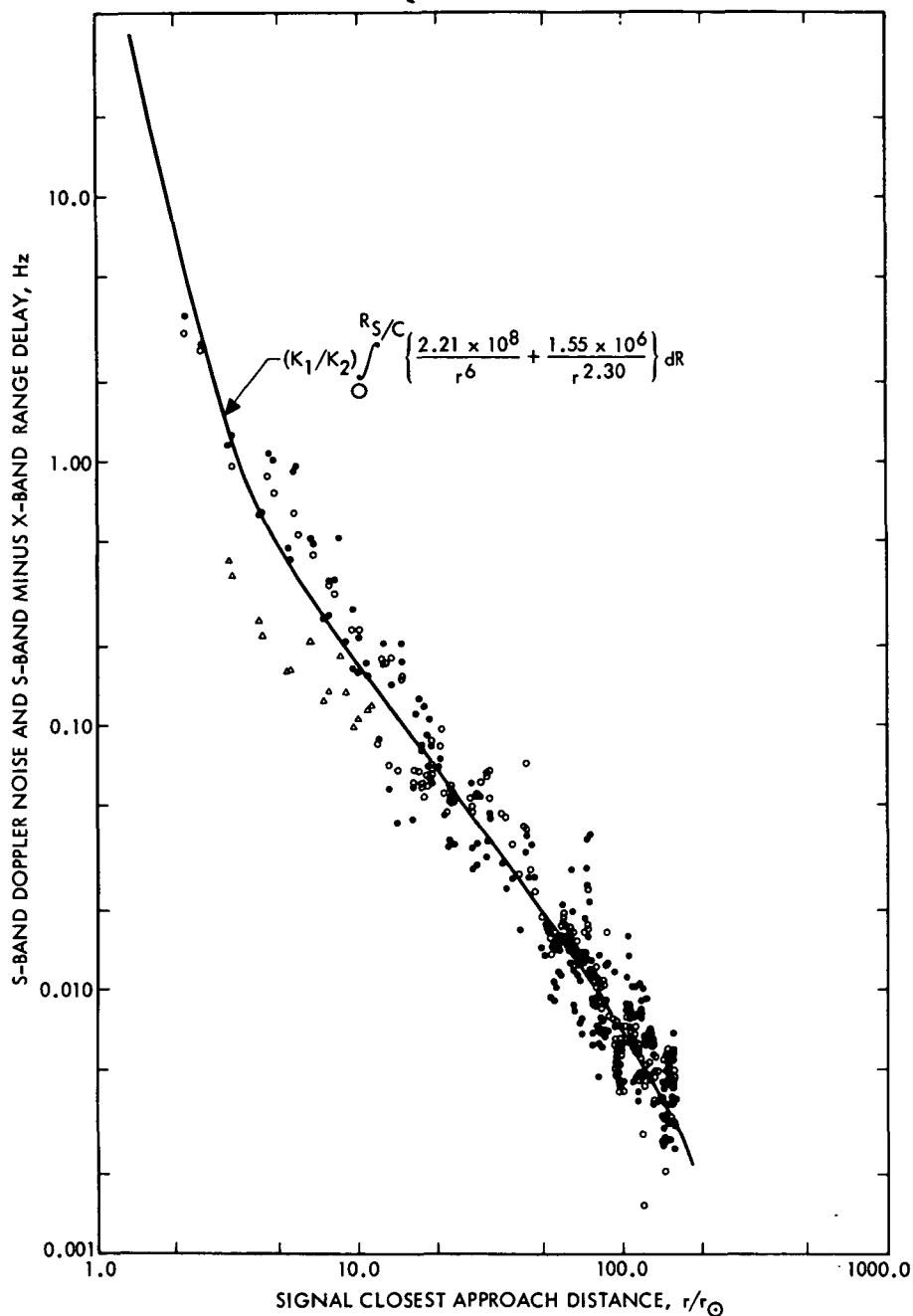


Fig. 3. Signal phase fluctuation and integrated electron density vs solar offset distance. The solid points are $\sigma_d = 13$ -cm Doppler noise in Hz, while the hollow points are dual-frequency range in nanoseconds multiplied by the proportionality constant $K_1 = 5 \times 10^4$ Hz/s. Hollow circles are data from July 2 to November 27, 1976, and December 6 to December 20, 1976, while hollow triangles are data from November 28 to December 5, 1976. The constant $K_2 = 3.93 \times 10^{21} \text{ cm}^{-2} \text{ s}^{-1}$ is the number of columnar electrons per second of dual-frequency range delay

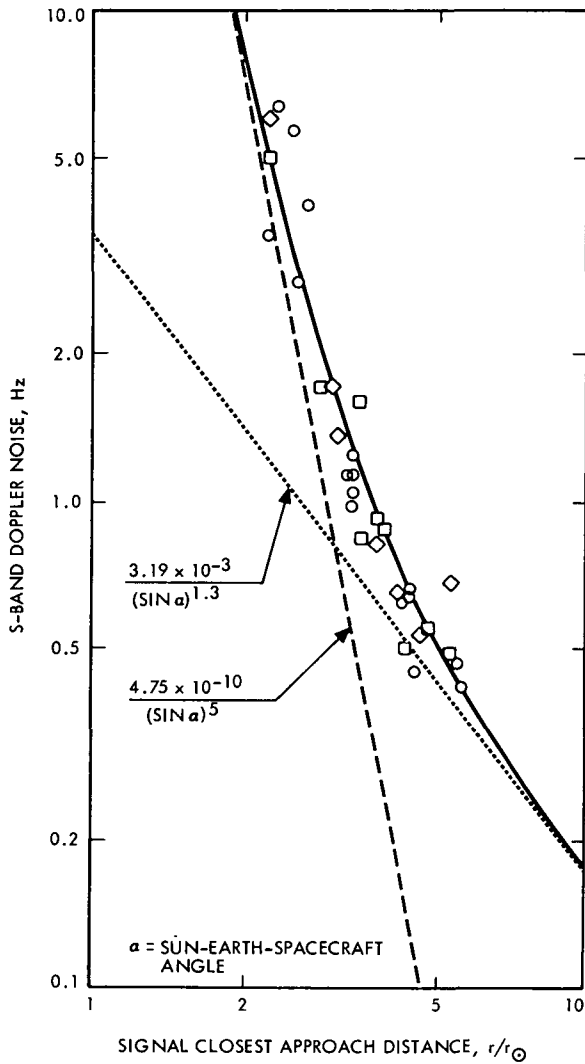


Fig. 4. Signal phase fluctuation in the inner corona. Circles are data from the Viking 1976 solar conjunction, diamonds are data from the Helios 2 1976 solar conjunction, and squares are data from the Helios 1 1975 solar conjunction

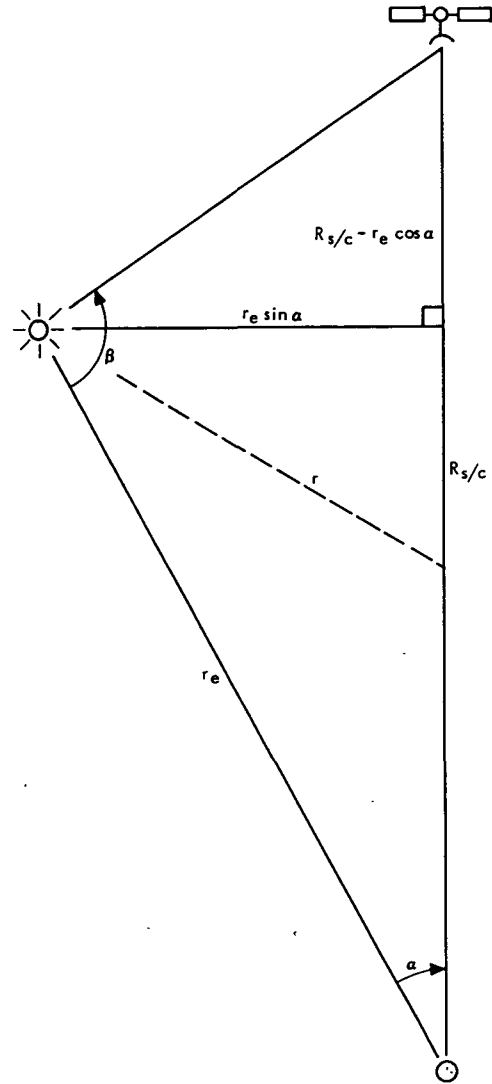


Fig. 5. Sun-Earth-Spacecraft geometrical configuration. r = heliocentric distance to signal path, r_e = Earth-Sun distance, $R_{s/c}$ = Earth-Spacecraft distance, α = Sun-Earth-Spacecraft angle, and β = Earth-Sun-Spacecraft angle

Deep Space Communications Complex Command Subsystem Mark IVA

W. G. Stinnett
DSN Data Systems Section

The Deep Space Communications Complex Command Subsystem will require major changes for the Mark IVA era. A description of the subsystem and its assemblies is contained in this article.

I. Introduction

The requirements for the Mark IVA Deep Space Network will result in major changes to the Deep Space Communications Complex Command Subsystem (DCD). While the basic functions of the subsystem remain the same, the subsystem will undergo major changes to satisfy the Mark IVA requirements. The changes are driven by basically two new requirements: (1) add new flight projects to the existing mission set, and (2) reduce Deep Space Communications Complex (DSCC) operations costs.

The addition of new missions to the existing mission set will require the implementation of a new Block II Command Modulator Assembly (CMA). The existing Block I CMA was first installed in the DSN for the Mariner 71 mission to Mars, and has successfully supported the Deep Space Missions since that time. However, the Block I CMA cannot support the data rates and/or waveforms required by some of the missions in the new mission set.

One of the major goals of the Mark IVA DSN is to reduce operating costs at the Deep Space Communications Complex. For this reason, the Mark IVA plan is to centralize all possible equipment at Goldstone, Spain, and Australia into a Signal

Processing Center (SPC). Furthermore, the equipment is to be remotely controllable from a central location within the SPC. The concepts of centralized equipment and remotely controlled equipment is to be accomplished as part of the Mark IVA DSN implementation. This in turn is to reduce the total number of maintenance and operations personnel at the DSCC. The effect of these concepts on the DSCC Command Subsystem will require (1) a new Command Switch Assembly (CSA) to permit any CMA to interface with any exciter at the SPC, and (2) hardware and software modifications to the Command Processor Assembly to support remote control capability.

II. Mark IVA DSCC Command Subsystem Description

The Command Subsystem (DCD) is an element of the Deep Space Network (DSN) Command System. The subsystem consists of hardware and software assemblies for data processing, command-waveform generation, and switching such that command information can be transmitted to the planetary and highly elliptical earth orbiter spacecraft supported by the DSN.

The subsystem will consist of three assemblies:

- (1) Command Processor Assembly (CPA).
- (2) Command Modulator Assembly (CMA).
- (3) Command Switch Assembly (CSA).

The CPA will serve as the data processing assembly for the subsystem. The CMA will generate the command composite waveform for transmission to the spacecraft. The CSA will provide switching capability to the appropriate antenna at the Deep Space Communications Complex (DSCC). The subsystem will serve as the link in the total end-to-end command system and will accept and store command data from the missions operations centers, modulate the data on the command subcarrier, and route the signal to the appropriate antenna for radiation to the spacecraft. Figure 1 shows the subsystem as the link in the end-to-end command system. Figure 2 shows the allocation of the subsystem functions to the assemblies.

As part of the reconfiguration of the DSN for the Mark IVA era, all subsystem equipment shall be located at the DSCC Signal Processing Center (SPC). Figure 3 provides a block diagram of the subsystem equipment at the SPC. As shown in Fig. 3, four CPA-CMA links will exist at the SPC at the Goldstone, Spain, and Australia complexes. Each link will have the capability to operate independently of any of the other CPA-CMA links. For operational considerations, the design provides for three links to be configured and actively commanding, while the fourth link is to serve as backup. Also shown in Fig. 3 are two links, one active link and one backup at CTA-21 and one link at MIL-71.

III. Assembly Description

A. Command Processor Assembly

The CPA will consist of a minicomputer and special interface hardware. Figure 4 provides a block diagram of the minicomputer and the special hardware.

1. **Minicomputer.** The heart of the CPA will be the Mod-comp II/25, a general-purpose 16-bit digital minicomputer, which will have the following characteristics:

- (1) 64K core memory module.
- (2) Four-port memory logic.
- (3) Power fail-safe option.
- (4) Executive feature option.
- (5) Priority interrupt levels.
- (6) Console I/O device controller.

- (7) Paper-tape reader controller.
- (8) Dual-asynchronous communications interface (2 each)
- (9) Six digital input channels (16 bits per channel)

2. **Interface hardware.** The CPA will interface with special hardware required for command waveform generation, inter-subsystem communication, timing, and external signal interrupts. These interfaces include:

- (1) IEEE-488 interface with the Local Area Network (LAN).
- (2) IEEE-488 interface with the CMA.
- (3) A special frequency and timing interface assembly which receives timing signals and periodic interrupts into the subsystem.

B. Command Modulator Assembly

The CMA consists of a microcomputer and special-purpose hardware (Fig. 5). Each CMA will be connected to a specific CPA (nonswitchable). The output of the CMA is then switchable to any exciter by use of the CSA.

1. **Microcomputer.** The CMA will use a single-board microcomputer with an SBC 340 memory expansion module. Included in this configuration will be the following:

- (1) An 8086 microprocessor.
- (2) 32K bytes of RAM.
- (3) 32K bytes of ROM.
- (4) 24 lines of parallel interface to CMA special-purpose circuits.
- (5) RS-232C maintenance port.

The CMA microprocessor will receive command and control data from the CPA. These data will be used by the microprocessor to configure the CMA special-purpose hardware for generating the command composite waveform for radiation to the spacecraft. The microprocessor will also monitor the status of CMA special-purpose hardware to ensure correct operation.

2. **Special-purpose hardware.** The CMA special-purpose hardware provides the multiple-mission signal generation capability for supporting the planetary and high-earth orbiter missions. The missions to be supported require various uplink acquisition sequences, different modulation methods, etc. The CMA special-purpose hardware provides this required multiple-mission capability and includes the following:

- (1) Subcarrier and data clock synthesizers. The synthesizers are controlled by the CMA microprocessor to

output the required frequencies for the subcarrier and data rate.

- (2) Digital function generators that convert the subcarrier and data clock synthesizer outputs to digital waveforms. These function generators are also capable of synthesizing and scaling sine and square waveforms and resolving the phase of the subcarrier waveform.
- (3) A modulator that accepts the digital function generator outputs and creates the required modulated subcarrier. The modulator selectively creates coherent binary phase shift keyed (CBPSK) modulation with or without data rate amplitude modulation, continuous phase frequency shift keyed (CPFSK) modulation with or without data rate amplitude modulation, or direct data modulation. In addition, the CBPSK data modulator may be Manchester encoded, as required.
- (4) Digital-to-analog circuitry that converts the digitally modulated subcarrier streams into an analog signal, adjusts the amplitude of the signal, and outputs the signal to the exciter.
- (5) Verification and confirmation circuitry that ensures correct operation of the CMA signal-generation hardware and confirms that the correct signal has been modulated onto the carrier by the exciter.

C. Command Switch Assembly (CSA)

The CSA provides the switching interface between the multiple CMAs and exciters at the SPC. The switch is remotely controllable by the Complex Monitor and Control (CMC) operator via the CPA. Figure 6 provides a block diagram of the CSA.

IV. Software and Firmware Description

A. Command Processor Assembly Software

The software used by the subsystem will reside on the CPA's disk storage unit. The disk will be divided into three areas: the CPA operating system and application software files, disk-resident command files, and a temporary command data log area.

The operational program will basically consist of two types of tasks: tasks activated and operating under external interrupt control, and tasks initiated and executed under program control. Each task will bear an assigned priority and will be supported by a standard operating system. Program operation,

because of its interrupt-dependent, real-time nature, may be characterized as time-multiplexed or time-shared processing.

Within the program, data areas and files will be maintained in support of the command processing functions. These data structures will be either static or dynamic in nature. That is, information will either be inserted when the program is assembled, resulting in an invariant data structure, or information will be dynamically stored or altered in specified program areas during program operation. Data structures which are embodied in the program include:

- (1) Mission-dependent data tables.
- (2) Canned program messages.
- (3) Text keywords.
- (4) GCF communication codes.
- (5) DSS internal communication codes.
- (6) Configuration/standards and limits tables.
- (7) Command stacks and queues.
- (8) Command files.
- (9) CRT display files.

B. Command Modulator Assembly Firmware

The firmware used by the subsystem will reside on ROM within the microcomputer. The firmware will be divided into three areas: test and diagnostic routines for the computer and preliminary initialization routines, executive routines, and application routines.

The test and diagnostic routines are executed when power is applied or a software reset is invoked.

The real-time, interrupt-driven nature of the CMA will be addressed through the use of the real-time, multi-tasking executive routines. The executive response to hardware interrupts and software calls and schedules the appropriate application routines.

The application routines control and monitor the operation of the CMA special-purpose hardware and interface with the CPA to receive control and command data.

V. Mark IVA Command Subsystem Implementation

The implementation of the assemblies of the Mark IVA Command Subsystem is in process and in varying stages of completeness.

The Block II CMA prototype is in the final stage of check-out. A fabrication contract is in place for production of the units to be installed in the DSN. The Block II CMA will be the subject of a subsequent article in which detailed design and performance will be discussed.

The CSA prototype is being manufactured. After the prototype is tested, the production units will be built for installation in the network.

The CMA firmware has been coded and is being tested concurrently with the prototype CMA hardware. This firmware will be integrated into the subsystem (interfacing with the CPA and production CMA hardware) at the Verification and Test Facility (VTF) in 1983.

The CPA software is being defined (new interfaces) and will be integrated into the subsystem and the command system at the VTF in 1983.

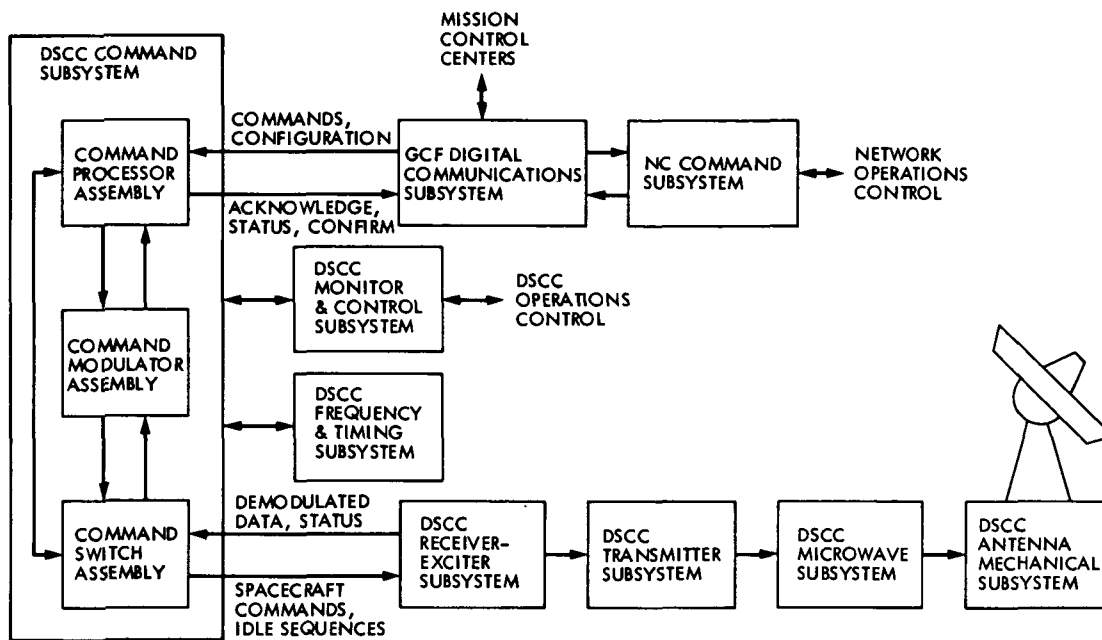


Fig. 1. DSCC Command Subsystem within DSN Command System

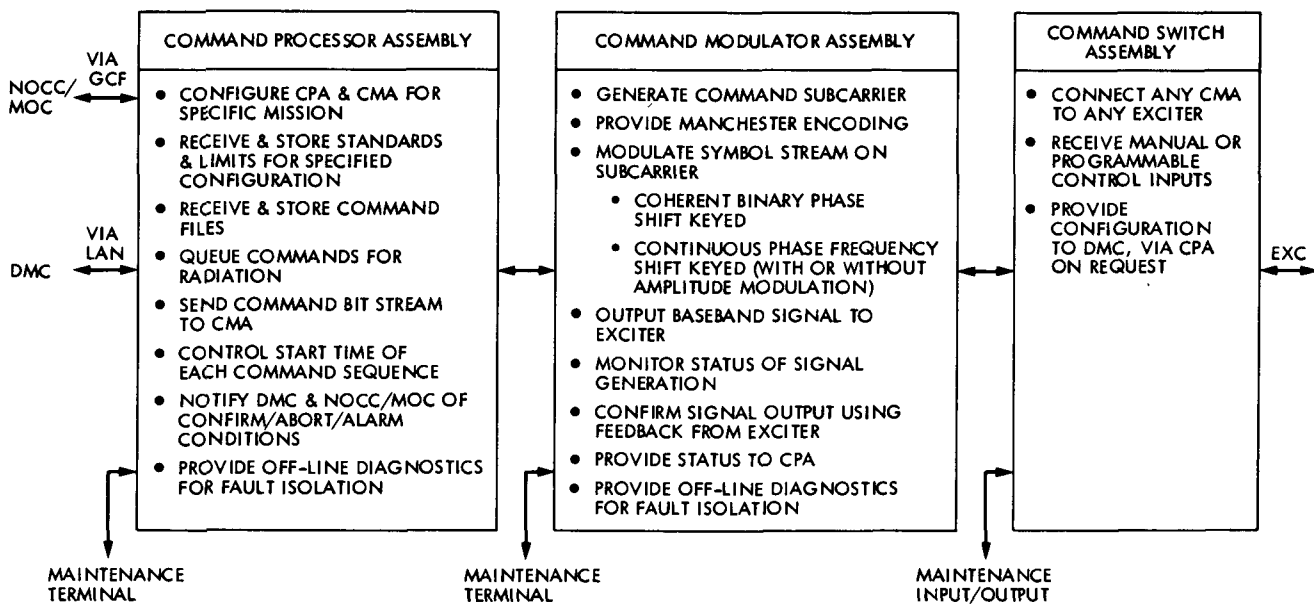
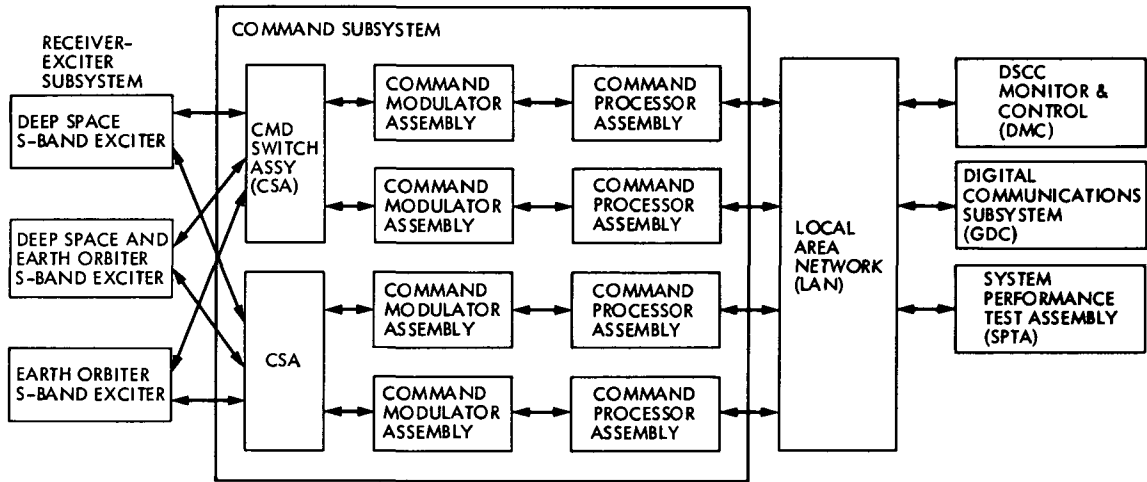
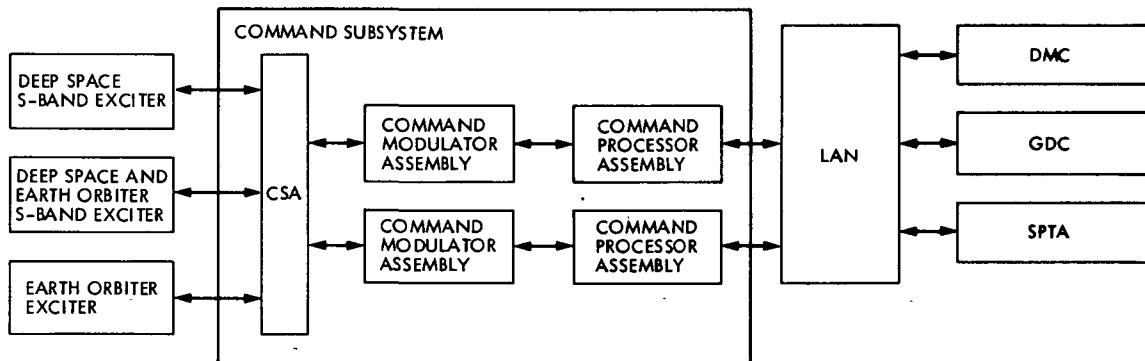


Fig. 2. Allocation of functions to assemblies

GOLDSTONE, SPAIN, AUSTRALIA



COMPATIBILITY TEST AREA (CTA-21)



MERRITT ISLAND (MIL-71)

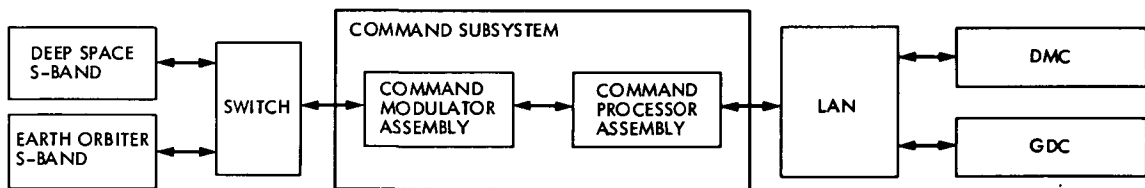


Fig. 3. Command Subsystem configurations

ORIGINAL PAGE IS
OF POOR QUALITY

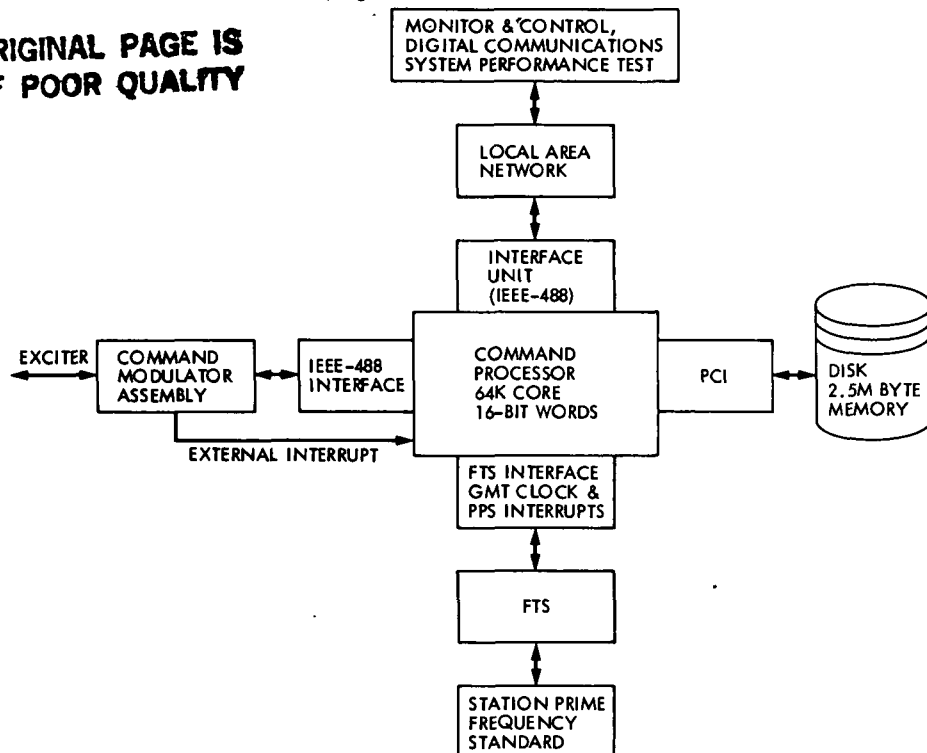


Fig. 4. CPA and associated equipment, functional block diagram

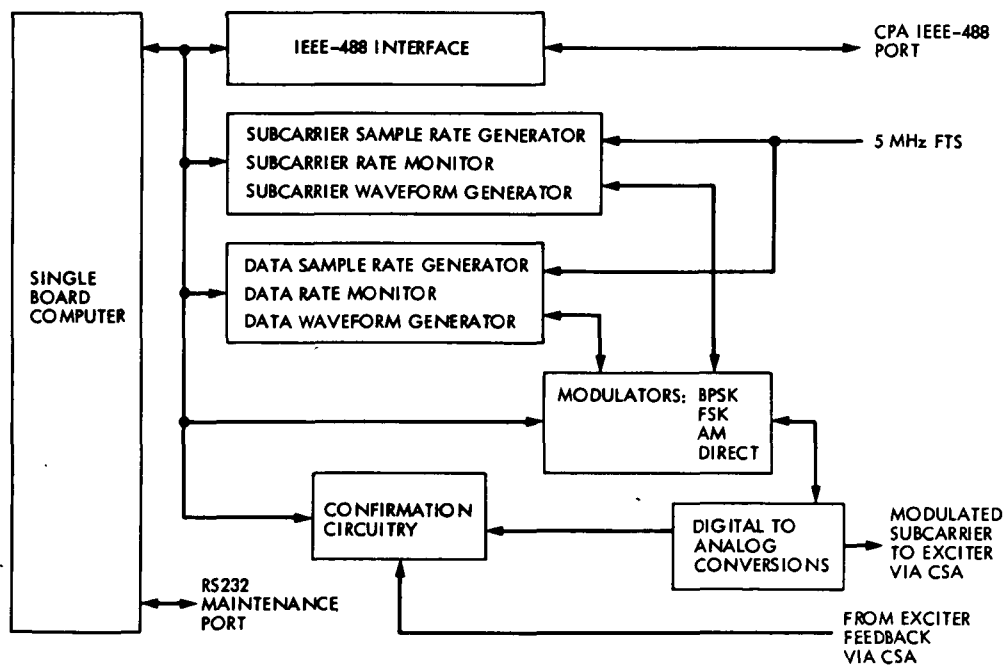


Fig. 5. Command modulator assembly, functional block diagram

ORIGINAL PAGE IS
OF POOR QUALITY

SI 2041 JAMIDIR
YTJAUQ 5009 2,

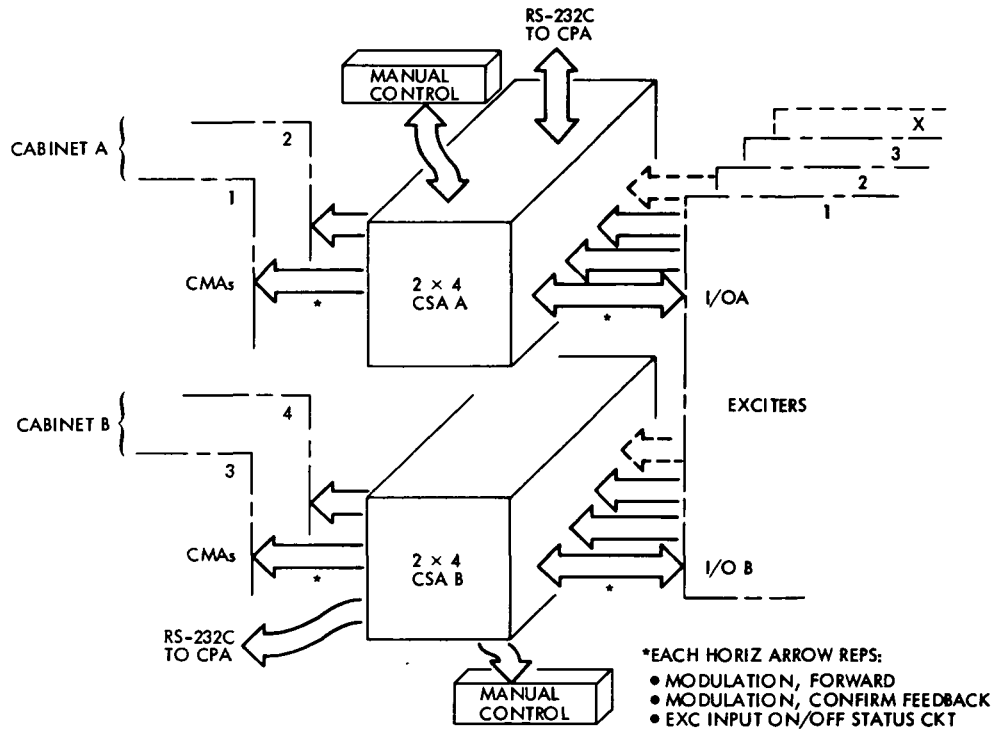


Fig. 6. Command switch assembly, functional block diagram

A Compact Presentation of DSN Array Telemetry Performance

C. A. Greenhall

Communications Systems Research Section

The telemetry performance of an arrayed receiver system, including radio losses, is often given by a family of curves giving bit error rate vs bit SNR, with tracking loop SNR at one receiver held constant along each curve. This study shows how to process this information into a more compact, useful format in which the minimal total signal power and optimal carrier suppression, for a given fixed bit error rate, are plotted vs data rate. Examples for baseband-only combining are given. When appropriate dimensionless variables are used for plotting, receiver arrays with different numbers of antennas and different threshold tracking loop bandwidths look much alike, and a universal curve for optimal carrier suppression emerges.

I. Introduction

In an internal memorandum, J. W. Layland wrote:

The task of comparing the performance of the Arrayed Deep Space Network with and without combined carrier references (CCR) seems to be needlessly complex. While the analysis machinery which has been built for us is capable of precisely describing the link performance under a plethora of conditions, interpretation of those results in terms useful for deciding whether to deploy the CCR or not is difficult, and potentially even ambiguous. There are too many "free" variables which seem to be available - even though physical constraints will interrelate many of them. Our task is somewhat analogous to driving a car with a separate steering wheel for each front wheel.

sum of the bit signal-to-noise ratios at all the array elements, with ρ_{L1} , the tracking loop SNR at the strongest array element, held constant (Refs. 1 and 2 and Fig. 1). We need such a plot (a family of six curves in this instance) for each channel code, each DSN antenna array, each signal combining method, and each choice of threshold tracking loop bandwidth $w_{L0} = 2b_{L0}$. (It is assumed that all receivers in the array use the same w_{L0} .)

This presentation is more convenient for the person generating the plots than for the person who has to interpret them. To reduce the volume of results, one can settle on a fixed telemetry performance, $P_E = 0.005$, for example, and use each waterfall curve set to generate one "radio loss" curve:

$$E_b/N_0 - (E_b/N_0)_\infty \text{ vs } \rho_{L1},$$

For example, the telemetry performance of a DSN receiver array can be represented by a family of "waterfall" curves giving bit error rate P_E as a function of array total E_b/N_0 , the

where E_b/N_0 is the array total bit SNR needed to attain P_E for the given ρ_{L1} , and $(E_b/N_0)_\infty$ is the SNR needed to attain P_E for $\rho_{L1} = +\infty$, i.e., perfect phase tracking (Ref. 1).

In the memorandum quoted above, Layland suggested another presentation format, in which one plots total power threshold as a function of data rate, again for a fixed P_E . Further, for each data rate, one uses the optimal modulation angle θ , i.e., the θ that requires the least total power. This eliminates θ as a free parameter and tells how to design the signal.

In the present paper, this idea is applied to a set of results for baseband-only combining. As Layland suggests, we hold to a bit error rate of 0.005. It turns out that a judicious choice of dimensionless variables allows us to use a "universal" curve for the optimal θ (or carrier suppression $\cos^2\theta$) as a function of data rate. Further, when regarded from this point of view, all the arrays look the same within 0.5 dB. In other words, we have a nearly universal curve for total power-to-noise ratio vs data rate. The differences among the arrays can then be seen by plotting E_b/N_0 vs data rate.

II. A Sample of Results

The source data come from internal memoranda of D. Hansen and D. Divsalar, and from unpublished results of L. Deutsch. Let us list the conditions:

- (1) (7, 1/2) convolutional code, maximum likelihood decoding.
- (2) One-way radio losses only.
- (3) High-rate bit error probability model.
- (4) Baseband-only combining with weights optimal for perfect phase tracking.
- (5) $w_{L0} = 10$ Hz or 30 Hz, the same for all receivers in the array.
- (6) Antenna array combinations (diameters in meters): 64, 64-34, 64-34-34, 64-34-34-34. We assume that gain-to-noise ratio is proportional to area.

For each array and w_{L0} there is a set of six waterfall curves giving P_E vs E_b/N_0 for $\rho_{L1} = 10, 11, 12, 13.5, 15,$ and 40 dB. Figure 1 is the plot for the four-element array and $w_{L0} = 10$ Hz.

Setting a telemetry performance threshold of $P_E = 0.005$, we compute optimal modulation angle and minimal total power-to-noise ratio. Results are plotted in Figs. 2-4.

The dimensionless variables used for plotting are listed below. In the plots, the term X (dB) always means $10 \log_{10} X$.

- (1) R_d/w_{L0} = normalized data rate, where R_d = data rate.
- (2) $\cos^2\theta$ = carrier suppression.

- (3) $P_T/(N_0 w_{L0})$ = normalized array total power-to-noise ratio, where P_T/N_0 is the sum of the P_T/N_0 values of the receivers in the array (P_T = carrier power + data power, N_0 = 1-sided noise spectral density).
- (4) E_b/N_0 = array total bit SNR, the sum of the E_b/N_0 values of the receivers in the array (E_b = data energy per bit).

Figure 2 is a "universal" curve giving optimal carrier suppression vs *normalized* data rate. The modulation angle is truncated at 80 deg. Actually, the several arrays yield distinct curves, which all agree within about 1 dB. Since the optimization problem is smooth, a deviation from optimal carrier suppression causes only a second-order increase in the total power needed to maintain the required performance. This is why one curve will do for all the array- w_{L0} combinations.

Figure 3 shows the array total P_T/N_0 needed to achieve $P_E = 0.005$. Total power has been minimized by the proper choice of carrier suppression (Fig. 2). Although this curve is again billed as universal, it is actually about 0.5 dB thick in the vertical direction. Thus it is intended only as a long-range snapshot. We shall soon tell how to compute values with greater accuracy.

For each array, Fig. 4 shows the array total E_b/N_0 needed to achieve $P_E = 0.005$. Since E_b/N_0 varies much less than P_T/N_0 , we can now easily distinguish the different arrays. Still, the curves all fit within a 0.5-dB band. Having these E_b/N_0 curves, one can compute P_T/N_0 more accurately than before by the formula

$$\frac{P_T}{N_0 w_{L0}} = \frac{1}{1 - \cos^2 \theta} \frac{E_b}{N_0} \frac{R_d}{w_{L0}} \quad (1)$$

where $\cos^2\theta$ is read from Fig. 2 and E_b/N_0 from Fig. 4.

III. Remarks and Cautions

These results, though incomplete and inaccurate, are adequate for a pilot study. The E_b/N_0 curves are probably good within ± 0.1 dB. The author's source data consist of meager sets of numbers read from photocopied computer-generated graphs. Although both the Hansen-Divsalar and the Deutsch graphs were processed, we show only the Hansen-Divsalar results because Deutsch's basic Viterbi decoding error curve (used in the high-rate model) is slightly different, and his graphs are harder to read accurately. Thus, for each array there

is only one w_{L0} . The Deutsch results indicate that the E_b/N_0 curves for $w_{L0} = 10$ Hz lie perhaps 0.1 dB above the corresponding curves for $w_{L0} = 30$ Hz. This, of course, does not mean that narrowing the loop bandwidth makes telemetry worse; recall that data rate is normalized by w_{L0} . Thus for a given array, if we were to plot the 10 Hz and 30 Hz E_b/N_0 values against unnormalized data rate, the 10-Hz curve would lie to the left of the 30-Hz curve, and therefore below it.

Notice, too, that the E_b/N_0 curve for any multiple-antenna array lies above the curve for one antenna. This is because we are, in effect, comparing the array to a single large fictitious antenna with the same total area. The array is worse because the tracking loop of the fictitious receiver gets more carrier power than any of the loops of the array receivers. To compare a 64-m station to the 4-element array on the basis of E_b/N_0 at the 64-m station, one can simply move the 4-element curve down by $1 + 3(34)^2/64^2 = 2.66$ dB.

A particular point on any of these curves is valid only if ρ_{L1} , the loop SNR at the strongest array element, is at least 10 dB. The left-hand endpoint of each E_b/N_0 curve shows the R_d/w_{L0} value beyond which this condition fails. For the array

in question, the "universal" carrier suppression and total power curves must not be used to the left of this value.

IV. Conclusions

Layland's suggestion for presenting array telemetry performance appears to work well when applied to a set of results for baseband-only combining. Each set of waterfall curves is distilled into one curve of E_b/N_0 vs normalized data rate R_d/w_{L0} , with P_E kept constant and modulation angle optimized. By plotting array total E_b/N_0 and using w_{L0} as a normalizing factor, we absorb the gross differences among the different antenna arrays and receiver bandwidths, thus leaving a set of curves that differ by at most 0.5 dB. Further, there emerge approximate universal curves for optimal carrier suppression and minimal array total $P_T/(N_0 w_{L0})$ vs R_d/w_{L0} .

Although this work is merely a small pilot study, the method may be useful for comparing a variety of situations, including various carrier combining methods and channel codes. If this is the case, then the method could also be used for handbook specification of the arrayed DSN. The carrier suppression curve (Fig. 2) may be convenient for mission design.

References

1. Divsalar, D., Hansen, D., and Yuen, J., "The Effect of Noisy Carrier Reference on Telemetry with Baseband Arraying," *TDA Progress Report 42-63*, pp. 128-135, Jet Propulsion Laboratory, Pasadena, Calif., June 15, 1981.
2. Deutsch, L., Miller, R., and Butman, S., "New Results on Antenna Arraying: Part I," *TDA Progress Report 42-62*, pp. 105-111, Jet Propulsion Laboratory, Pasadena, Calif., Apr. 15, 1981.
3. Tausworthe, R., "Limiters in Phase-Locked Loops: A Correction to Previous Theory," *Space Programs Summary 37-54*, Vol. 3, pp. 201-204, Jet Propulsion Laboratory, Pasadena, Calif., 1968.
4. Springett, J., and Simon, M., "An analysis of the phase coherent-incoherent output of the bandpass limiter," *IEEE Trans. Comm. Tech.*, Vol. COM-19, pp. 42-49, 1971.
5. Henrici, P., *Elements of Numerical Analysis*, Wiley, New York, 1964.
6. Brodlie, K., "A review of methods for curve and function drawing," in *Mathematical Methods in Computer Graphics and Design*, K. Brodlie, ed., pp. 33-37, Academic Press, London, 1980.

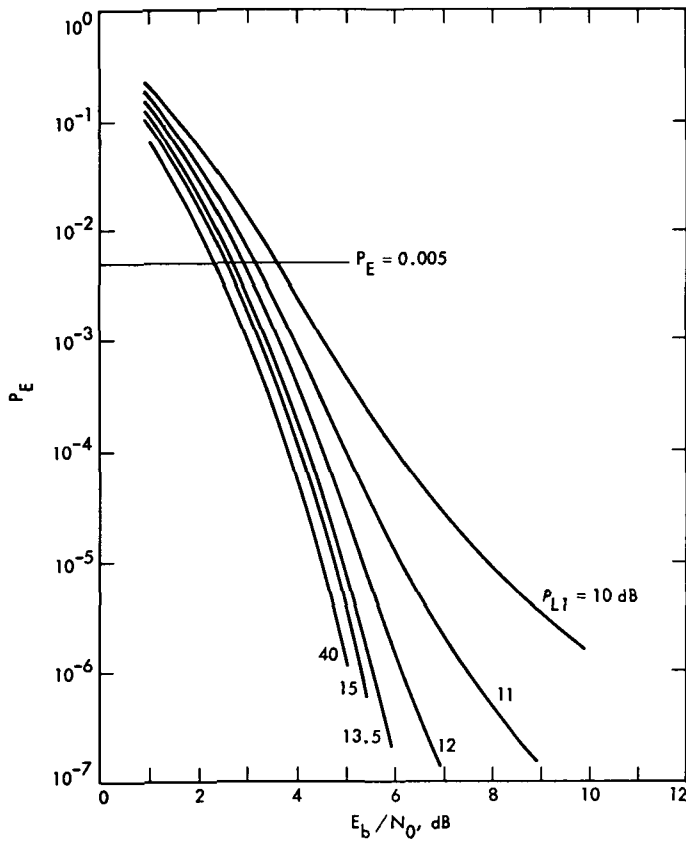


Fig. 1. A family of waterfall curves giving bit error rate P_E vs array total E_b/N_0 , with ρ_{L1} = tracking loop SNR at the largest antenna. Conditions: (7, 1/2) code, one-way radio losses, baseband-only combining, 10-Hz tracking loops, four-element array: 64-34-34-34 m (after Hansen)

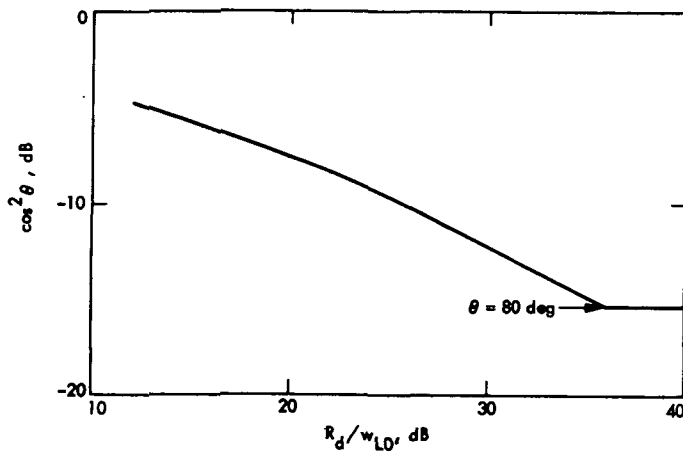


Fig. 2. An approximate universal curve for optimal carrier suppression vs data rate normalized by threshold loop bandwidth. Conditions: (7, 1/2) code, one-way radio losses, one to four DSN stations, baseband-only combining, $P_E = 0.005$. The modulation angle θ is truncated at 80 deg

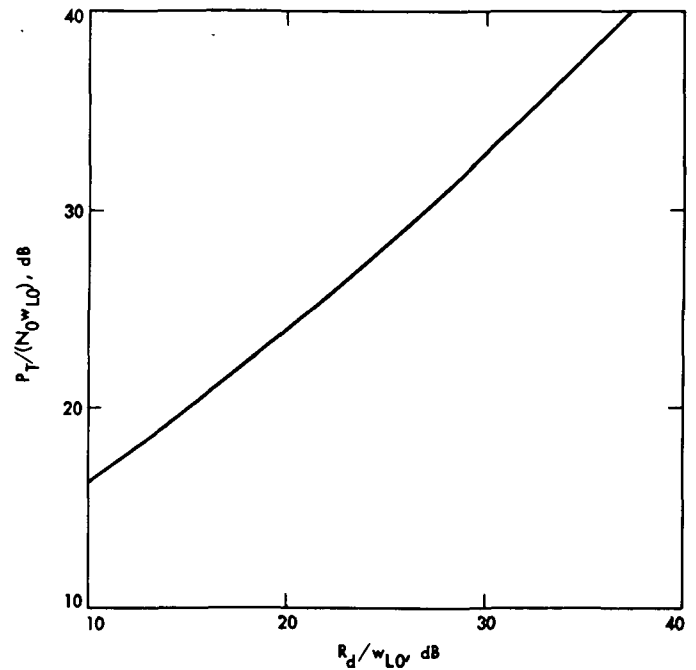


Fig. 3. An approximate universal curve giving normalized array total power-to-noise ratio vs normalized data rate, for an error rate $P_E = 0.005$. Carrier suppressions from Fig. 2 are used. This curve actually consists of several curves differing by at most 0.5 dB. Conditions: same as Fig. 2

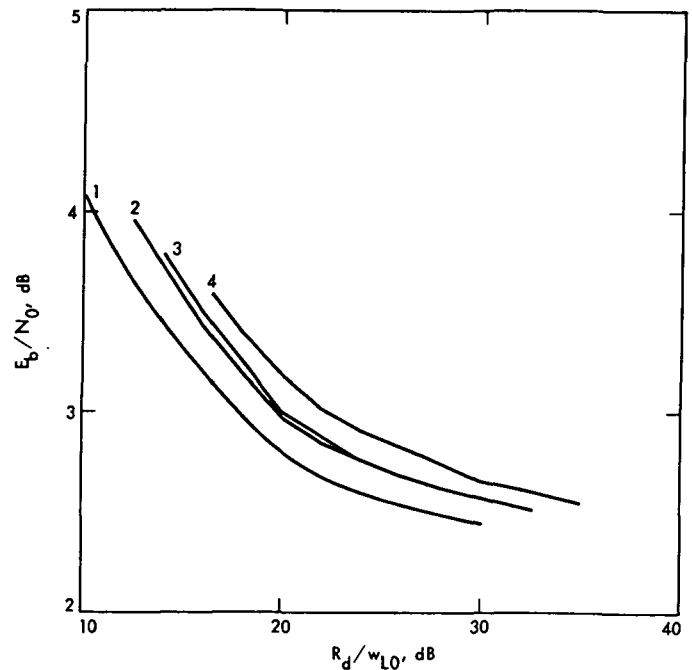


Fig. 4. Array total E_b/N_0 needed to achieve an error rate $P_E = 0.005$, with carrier suppression from Fig. 2. Arrays: (1) One antenna, $w_{L0} = 30$ Hz; (2) 64 m - 34 m, 10 Hz; (3) 64-34-34 m, 10 Hz; (4) 64-34-34-34 m, 10 Hz. Conditions: same as Fig. 2

Appendix

Processing Details

I. Tracking Loop Formulas

We are given a set of waterfall curves, giving P_E vs array total E_b/N_0 with ρ_{L1} fixed at 10, 11, 12, 13.5, 15, and 40 dB. Since loop SNR ρ_L is a nonlinear function of carrier margin m , a more well-behaved quantity, we first convert the ρ_L values to the equivalent m values. Recall that the DSN definition of m is

$$m = \frac{P_c}{N_0 w_{L0}}$$

where P_c = carrier power.

For the reader's convenience, here is a set of formulas relating ρ_L to m for the DSN carrier tracking loops.

w_H = 2-sided IF predetection bandwidth

$$\rho_{H0} = \frac{2w_{L0}}{w_H} \quad (A-1)$$

= threshold predetection SNR

Define

$$\phi(x) = e^{-x} [I_0(x) + I_1(x)] \quad (A-2)$$

Then

$$\alpha_0 = \frac{1}{2} \sqrt{\pi \rho_{H0}} \phi\left(\frac{1}{2} \rho_{H0}\right) \quad (A-3)$$

= threshold limiter suppression factor

$$\rho_H = m \rho_{H0} \quad (A-4)$$

= predetection SNR

$$\alpha = \frac{1}{2} \sqrt{\pi \rho_H} \phi\left(\frac{1}{2} \rho_H\right) \quad (A-5)$$

= limiter suppression factor

$$r = 2\alpha/\alpha_0 \quad (A-6)$$

$$w_L = \frac{r+1}{3} w_{L0} \quad (A-7)$$

= two-sided loop noise bandwidth

$$\Gamma = \frac{1 + \rho_H}{0.862 + \rho_H} \quad (A-8)$$

= limiter performance factor

This is a rough approximation due to Tausworthe (Ref. 3). For more accuracy, one should use a formula of Springett and Simon (Ref. 4):

$$\Gamma = \frac{1 - \exp(-\rho_H)}{\alpha^2(1 + 0.0975 \exp(-0.2146 \rho_H))} \quad (A-9)$$

Then we have

$$\rho_L = \frac{2m w_{L0}}{w_L \Gamma} = m \frac{6}{(r+1) \Gamma} \quad (A-10)$$

This gives loop SNR in the form $\rho_L = m \psi(m; \rho_{H0})$. To obtain m from ρ_L , one can iterate the formula $m = \rho_L / \psi(m; \rho_{H0})$ from some initial guess for m . The iteration, which is convergent because ψ is a slowly varying function, can be accelerated by Steffensen's method (Ref. 5).

II. Optimal Carrier Suppression

Having converted each ρ_{L1} to m_1 = carrier margin at the strongest array element, we multiply m_1 by array total antenna area/area of largest antenna to obtain total carrier margin m . We draw a horizontal line across the set of waterfall curves at the desired P_E (5×10^{-3} in this study). The intersections of this line with the waterfall curves give several points $[m_{dB}, (E_b/N_0)_{dB}]$, through which we interpolate a smooth function

$$(E_b/N_0)_{dB} = g(m_{dB}) \quad (A-11)$$

by means of cubic splines or a similar method. (The author used a local cubic method of Butland and Brodlie, Ref. 6.)

Then we can also write

$$\frac{E_b}{N_0} = f(m) = 10^{g(m_{dB})/10} \quad (A-12)$$

Define the dimensionless variables

$$p = \frac{P_T}{N_0 w_{L0}}$$

$$r = R_d/w_{L0}$$

where P_T/N_0 is the array total. Then we have the fundamental equation

$$p = m + rf(m) \quad (\text{A-13})$$

This just says total power = carrier power + data power, and data power is set for the desired P_E . Now, given r (i.e., data rate), we ask for the minimal p (i.e., total power) that gives the desired P_E . To get it we just set $dp/dm = 0$:

$$0 = 1 + rf'(m)$$

$$f'(m) = -1/r \quad (\text{A-14})$$

If we solve Eq. (A-14) for m , then we can get p from Eq. (A-13). The optimal carrier suppression is m/p .

There are two tricks for simplifying this procedure. First, there is no need to solve Eq. (A-14) for m in terms of r . Indeed, if we use m as independent variable instead of r , then Eqs. (A-14) and (A-13) give r , p , and m/p as functions of m ; we then plot p , E_b/N_0 , and m/p vs r . If the modulation angle θ ($m/p = \cos^2 \theta$) comes out greater than 80 deg, then set

$$p = m \sec^2 (80 \text{ deg})$$

and solve for r from Eq. (A-13).

The second trick comes from using Eq. (A-11) directly. By Eq. (A-12),

$$g'(m_{dB}) = mf'(m)/f(m) \quad (\text{A-15})$$

which, combined with Eqs. (A-13) and (A-14), gives

$$\frac{rf(m)}{m} = \frac{1}{g'(m_{dB})}$$

$$\frac{p}{m} = 1 - \frac{1}{g'(m_{dB})} \quad (\text{A-16})$$

Since $p/m = \sec^2 \theta$, we have

$$\tan^2 \theta = -1/g'(m_{dB}) \quad (\text{A-17})$$

We use Eq. (A-17) to determine θ , reduce it to 80 deg if necessary, and compute p and r as before. It is curious that optimal modulation angle can be so easily extracted from the slope of g .

III. Adjusting for the Universal Carrier Suppression Curve

Carrying out all of the above for several array configurations, we may find that the curves of optimal $\cos^2 \theta$ vs r almost fall on top of each other, within 1 dB, say. We can then replace these curves by one universal curve. If, however, we combine a universal θ with an E_b/N_0 from above, then Eq. (1), which in our present notation reads

$$p = \frac{r E_b/N_0}{\sin^2 \theta} \quad (\text{A-18})$$

gives a wrong answer for p .

For the user's sake, it is necessary to apply a small fudge factor to E_b/N_0 . As we mentioned, a small deviation of θ from the optimum hardly changes p , since p has been minimized as a function of θ . Given r , we have exact and universal values of $\cos^2 \theta$, and an exact value of E_b/N_0 . An adjusted value of E_b/N_0 is obtained from Eq. (A-18) by pretending that adjusted $p = \text{exact } p$:

$$\frac{(E_b/N_0)_{adj}}{\sin^2 \theta_{univ}} = \frac{(E_b/N_0)_{exact}}{\sin^2 \theta_{exact}}$$

These adjusted values were used for Fig. 4.

As a check, we can derive a new value of p from

$$(E_b/N_0)_{adj} = f(p_{new} \cos^2 \theta_{univ})$$

The new p might be about 0.01 dB greater than the old p derived from inserting either $(E_b/N_0, \theta)$ pair into Eq. (A-18).

Deep Space Network Utilization for Flight Projects, Calendar Year 1981

C. L. Adkins and E. K. Goto
Control Center Operations

This article reports on the utilization of the Deep Space Network during calendar year 1981 in support of all flight projects.

I. Introduction

The Deep Space Network (DSN) Operations Scheduling Group, assigned to the Control Center Operations (CCO) Section, has the responsibility not only to schedule the allocation of network activities on a day-to-day basis, but also to forecast future network requirements and maintain accountability of how time is utilized throughout the network.

In order to accomplish these activities, various publications are generated by the DSN Scheduling Group (Ref. 1). Of these publications, the DSN Forecast (Ref. 2) and the Station Utilization Report, became the basis for the raw data utilized to develop this synopsis of flight project support for calendar year 1981. In addition, information is provided to show the number of real-time scheduling changes generated by each flight project. A real-time schedule change is a change to the original weekly published DSN 7-day operations schedule. Only changes that affected flight project support have been included.

II. Publications

A. DSN Forecast

The DSN Forecast provides a quarterly listing of:

- (1) All project testing or tracking support required from the DSN. These requirements are based on each project's Support Instrumentation Requirements Document (SIRD) and Network Support Plan (NSP).
- (2) Each project's required support by antenna size and longitude. Each unit of tracking requirement in the DSN Forecast represents 12 hours and is shown in 4-week increments.
- (3) One year of history comparing project requirements vs actual support provided, and three years of project requirements in the future.

B. Station Utilization Report

The Station Utilization Report (SUR) published weekly provides:

- (1) A breakdown of time accountability for each Deep Space Station (DSS) within the DSN, based upon its current station operating hours.
- (2) A breakdown of all activities supported by work code category as authorized by the National Aeronautics and Space Administration's Office of Space Tracking and Data Systems.

III. Objective

The objective of this report is to show a correlation of flight project requirements and actual time received during calendar year 1981.

It must be noted that this report is only looking at one work code category utilized within the DSN. Currently there are three major work code categories with a total of 23 subcategories. These major work code categories and titles are listed below along with the number of associated subcategories.

- (1) Work code category one, "DSN User Support," includes Spacecraft Tracking, Project/DSN Testing, Radio Astronomy, and Advanced Systems. There are a total of 11 subcategories.
- (2) Work code category two, "Facility Support," includes Maintenance, Training, Engineering Support and Minor Modifications. There are a total of nine subcategories.
- (3) Work code category three, "Other Activities," includes Major Modifications, Host Country Radio Science, and Miscellaneous. There are a total of three subcategories.

IV. Data Synopsis

A. Total Hours by Individual Flight Project

Table 1 shows the total hours requested and total hours received by individual flight projects. The percentages reflect how the total requirement for each individual flight project was satisfied. Actual hours received include pre/post calibration times.

B. Total Hours of All Flight Projects

The same hours were utilized for Table 2. However, the percentages were based on total hours for all flight projects for both requested hours and actual hours. The far-right-

hand column denotes the total number of hours from acquisition of signal (AOS) to loss of signal (LOS) for each flight project.

C. Flight Project Percentage Distribution

Figure 1 represents a quick-look view by flight project and distribution of the percentage of hours in work code category IAI.

D. Flight Project Hours, Schedule Changes and Major Milestones

Figure 2 represents a quick-look correlation of flight project hours, changes to the weekly published DSN 7-day operations schedule and major milestones relative to calendar year 1981. The data are presented in 13 blocks, with each block containing four weeks of data.

V. Summary

During calendar year 1981, the Deep Space Network expended 63% of its total capability in support of work code category IAI, "Flight Project Support." The prime flight projects supported were Pioneer 10, Pioneer 11, Pioneer-Venus, Viking, Helios 1, Voyager 1 and Voyager 2. In addition, Pioneer 6, Pioneer 7, Pioneer 8 and Pioneer 9 were provided support on a best efforts basis.

Many factors influence the total number of hours provided for flight project support. Some of the major factors in 1981 are listed below:

- (1) The fluctuation of mutual viewperiods between all spacecraft which became critical from September through December 1981.

- (2) Extended station downtimes

DSS 14 2 Jan.-15 Jan. 1981

DSS 42 12 Jan.-2 Jan. 1981

DSS 12 4 Feb.-22 Mar. 1981

DSS 14 5 Oct.-25 Nov. 1981

- (3) Termination of Helios 2 on 8 Jan. 1981.

- (4) Voyager 2 Saturn Encounter on 27 Aug. 1981.

- (5) Termination of the 26-meter subnet (DSSs 11, 44, and 62) on 1 Dec. 1981.

References

1. Durham, R., "DSN Scheduling System," *TDA Progress Report 42-62*, pp. 132-141, Jet Propulsion Laboratory, Pasadena, Calif., Apr. 15, 1981.
2. Enari, D. M., and Holritz, C. A., "Network Loading Visibility for Management," *DSN Progress Report 42-31*, pp. 128-131, Jet Propulsion Laboratory, Pasadena, Calif., Feb. 15, 1976.

Table 1. Total hours received by individual flight project

| Project | Requested hours | Actual hours | % of $\frac{\text{actual hours}}{\text{requested hours}}$ |
|---------------|-----------------|--------------|---|
| Pioneer 6 | 0 | 184.5 | — |
| Pioneer 7 | 0 | 163.1 | — |
| Pioneer 8 | 0 | 58.7 | — |
| Pioneer 9 | 0 | 541.7 | — |
| Pioneer 10 | 8,748 | 5,551.8 | 63.5 |
| Pioneer 11 | 9,078 | 6,042.8 | 66.6 |
| Pioneer-Venus | 12,852 | 9,773.3 | 76.0 |
| Viking | 606 | 132.3 | 21.8 |
| Voyager | 25,650 | 20,786.0 | 81.0 |
| Helios | 4,872 | 4,745.7 | 97.4 |

"Actual hours" includes pre- and postcalibration time.

Table 2. Total hours of all flight projects

| Project | Requested hours | Percent of total requested hours | Actual hours | Percent of total actual hours | Spacecraft hours |
|---------------|-----------------|----------------------------------|--------------|-------------------------------|------------------|
| Pioneer 6 | 0 | — | 184.5 | 0.4 | 139.5 |
| Pioneer 7 | 0 | — | 163.1 | 0.3 | 113.7 |
| Pioneer 8 | 0 | — | 58.7 | 0.1 | 47.5 |
| Pioneer 9 | 0 | — | 541.7 | 1.1 | 428.8 |
| Pioneer 10 | 8,748 | 14.1 | 5,551.8 | 11.5 | 4,689.4 |
| Pioneer 11 | 9,078 | 14.7 | 6,042.8 | 12.5 | 5,109.0 |
| Pioneer-Venus | 12,852 | 20.8 | 9,773.3 | 20.3 | 8,277.1 |
| Viking | 606 | 1.0 | 132.3 | 0.3 | 74.3 |
| Voyager | 25,650 | 41.5 | 20,786.0 | 43.4 | 16,516.5 |
| Helios | 4,872 | 7.9 | 4,745.7 | 10.0 | 3,784.3 |

"Actual hours" includes pre- and postcalibration time.

2001 2001

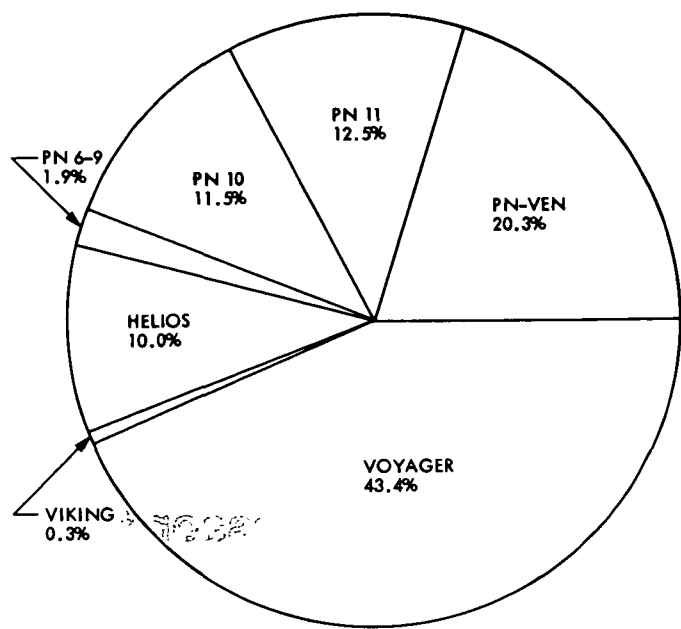


Fig. 1. Flight project percentage distribution

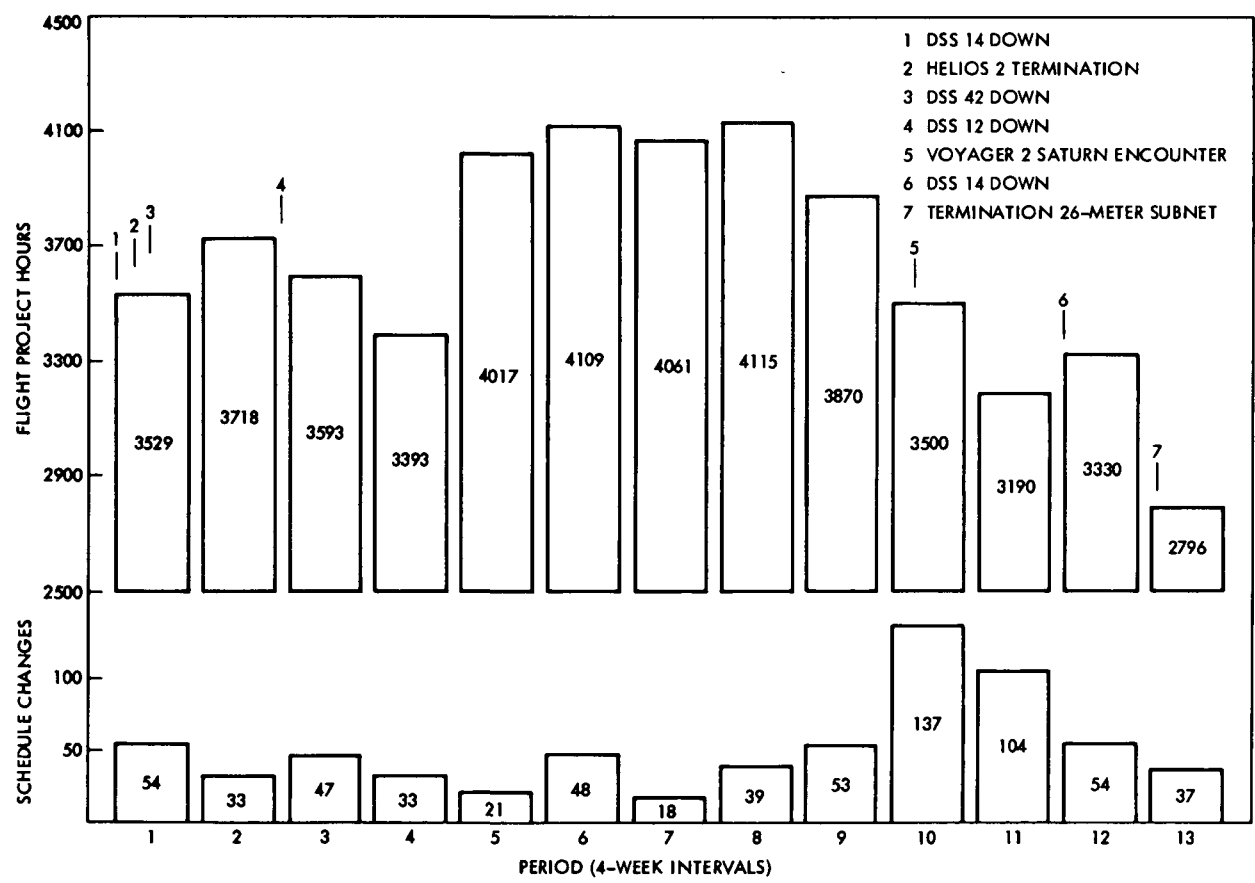


Fig. 2. Flight project hours, schedule changes, and major milestones

Mark IVA Microprocessor Support

A. L. Burford

Operations Sustaining Engineering Section

This report discusses the requirements and plans for the maintenance support of microprocessor-based controllers in the Deep Space Network Mark IVA System. Additional new interfaces and 16-bit processors have introduced problems not present in the Mark III System. This report also points out the need for continuous training of maintenance personnel to maintain a level of expertise consistent with the sophistication of the required tools.

I. Introduction

The Mark IVA System makes extensive use of microprocessor-based controllers. Much of the equipment is in areas remote to the complex control room environment and difficult to access, e.g., high places on antennas (see Figs. 1 and 2). These subsystem controllers will require lightweight, highly portable test equipment for maintenance. Easily accessible controllers within the complex control room may be tested with more sophisticated analyzers. This equipment will be resident in a rollaround maintenance cart, thus providing greater flexibility and in-depth testing.

While technological advances have increased data throughput, these same advances have introduced new maintenance problems, namely, poor visibility into the system. Test equipment, such as data analyzers and in-circuit emulators, will be available to help solve these problems.

II. Maintenance Philosophy

The Mark III microprocessor controllers implemented in the Deep Space Network were not compatible with existing

automatic test equipment. This and other factors forced a maintenance practice that often resulted in diagnosing a problem to the chip level in an operations environment. This approach has been generally successful primarily due to the test equipment supplied and the skill level of the technicians involved.

The availability requirements placed on the Mark IVA System require conformance to the DSN maintenance philosophy which establishes boundaries for various levels of maintenance. Briefly stated, Level 1 is "failure detection"; Level 2 is "failure identification and replacement (to the least replaceable element)"; Level 3 is "off-line repair" (normally depot repair). These boundaries are not to be considered "law"; emergency situations will dictate Level 3 repair at a Level 2 location. Faced with this possibility, capability must be provided in a maintenance and operations environment to perform Level 3 repair.

III. Mark III Support

The backbone of the current microprocessor support for 8-bit processors includes the Micro/Sys DS22 and the Millen-

nium Microsystem Analyzer, Ref. 1. The DS22 uses the CPM operating system and has been used for development of diagnostics for the Mark III System controllers. The DS22 interfaces with the Millennium Microsystem Analyzer (an in-circuit emulator) and the Data I/O System 19 PROM (Programmable Read Only Memory) programmer; in addition, it can be connected to a modem for communication with other computers (Fig. 3). The unit has been used extensively for on-the-job-training of on-site personnel; this has been a valuable contribution. Because of its portability and flexibility, the Millennium analyzer will continue to be used in the Mark IVA era. The DS22 will continue to support the Millennium for diagnostic development.

No field support presently exists for 16-bit processors. The only support for 16-bit processors (the digitally controlled oscillator is the only one in the Mark III System) has been from the Development Engineering Group. This requires returning the boards to engineering for repair in a prototype mockup.

IV. Requirements for Mark IVA Support

With the advent of 16-bit microprocessors in the network it is obvious that additional requirements beyond the capabilities of the DS22 and the Millennium Microsystem Analyzer are needed. Only recently have portable testers for 16-bit microprocessors become available from industry. Various instruments are currently being investigated for their suitability to the Mark IVA requirements for supporting Level 2 and Level 3 maintenance (see Fig. 4). Level 3 requirements include complete software compatibility, with the development system used to develop the controllers, thus eliminating situations that require lengthy workaround solutions. The prominent development system used at JPL is the INTEL Microprocessor Development System. To satisfy future requirements an INTEL Development System and in-circuit emulation for 16-bit processors will be needed at each complex.

V. Test Equipment Requirements

The following paragraphs provide a review of the test equipment requirements for supporting microprocessor maintenance in the Mark IVA System.

- (1) The 8-bit processors are adequately supported by the Millennium Microsystem Analyzer. Several 16-bit instruments are being investigated for support of the INTEL 8086 microprocessor. A major consideration for Level 2 maintenance is portability.

- (2) The requirement for conventional instruments to support time domain analysis, voltage, and continuity measurements still exists. This would include oscilloscopes, counters, meters, etc.
- (3) Logic analyzers will be required for detailed data domain analysis. Bus adapters are being considered for these instruments to preclude the problem of connecting many probes to the unit under test.
- (4) In-circuit emulators will continue to be used because they essentially provide front panel controls for the unit under test. In addition, these instruments are invaluable for providing digital signature analysis.

VI. Digital Interface Testing

A. General-Purpose Interface Bus

In the Mark IVA System all of the recently supplied instrumentation have as an interface the IEEE 488 Bus. A planned tester for this interface is the Racal-Dana GPIB-488 analyzer, which includes the following features: (1) Passive Mode, displays the bus activity in real-time; (2) Trace Mode, captures data for later display and analysis; (3) Single Step Mode, allows bus transactions to be single stepped or stopped.

B. Serial Interface

The standard serial interface used is RS232C. This interface is prevalent wherever serial data is being transferred. An excellent tester for this interface is the "Model 60 EIA interface monitor and breakout panel," manufactured by International Data Sciences, Inc. This device is equipped with switches for breaking any line and jumpers for altering the signal paths. Light emitting diodes are used to display the status of each line.

C. JPL Standard Interface

The JPL standard interface (sometimes called the 15-line interface) was used extensively in the Mark III System and will be used in the Mark IVA. A switch box and LED (light emitting diode) display is used to test this interface. To provide rapid fault isolation on this bus, a more sophisticated tester will be provided as part of the rollaround cart.

D. Local Area Network

The DSN version of Ethernet is the Local Area Network used throughout the Signal Processing Center of the Mark IVA System. Because of the Ethernet bus arbitration and bit rates, the testing of this interface poses special problems. An

Ethernet interface will be provided on the rollaround cart and software supplied to verify local operation.

VII. Analog Interface Testing

Means must be provided to assure the integrity of the analog signal processing associated with the subsystem controllers. In some cases it may be possible to loopback signals between the input and output, thus allowing an internal diagnostic to verify proper operation, or it may be possible to test an internal reference, as in the field interface modules (FIM) (Refs 2 and 3). If proper operation is not verified by this approach, then precision voltage source and measurement instruments must be available.

Pursuant to solving this problem, analog signature analysis will be investigated and a determination made as to its practicality in the Mark IVA environment.

VIII. Software Requirements

Diagnostics are an indispensable aspect of fault finding in a microprocessor-based controller. Capability for developing diagnostics for both 8- and 16-bit processors must be at each complex or depot repair facility.

Once it has been established that the kernel of the controller is operational, various levels of diagnostics may be invoked. These diagnostics will be available as resident in the UUT, as PROM, as DISK and as TAPE.

- (1) Resident diagnostics will be located in the "Unit Under Test" (UUT). These diagnostics should point to the defective "Lowest Replaceable Element" (LRE), such as a module. It is expected that these diagnostics will isolate the fault in the majority of the failures (Ref. 2).
- (2) Nonresident diagnostics are provided as "Programmable Read Only Memory" (PROM) for use either in

the UUT or the in-circuit emulator (ICE). These diagnostics would be used for special testing of a particular logic element or toggling of data at a specific node for oscilloscope observation.

- (3) Diagnostics will be provided on disk for downloading either into the UUT or the in-circuit emulator tester.
- (4) Diagnostics will be provided on tape for use in the Fluke Troubleshooter (in-circuit emulator).

IX. Training

Based on DSN maintenance experience the technicians are required to (1) know the functions of the LSI elements, (2) know the logic of the UUT, (3) be able to operate the equipment to assist in maintenance, and (4) be familiar with the hardware and software documentation.

Technician proficiency (relative to training) will affect the required sparing of LREs. If low skill levels exist (for Level 2 maintenance), more spares will be required because more non-defective boards will end up in the repair cycle (increased board float). This complicates testing in the depot environment because all returned boards must be assumed to be defective. The final result is increased operating costs.

For efficient troubleshooting, a thorough knowledge of the instrumentation used in microprocessor fault finding is absolutely essential. Special courses should be developed to raise the level of expertise in this area.

X. Conclusion

An appropriate maintenance program can be developed to provide rapid fault isolation in the field and repair in the depot of Mark IVA controllers if state-of-the-art analyzers, test equipment and adequate training are provided as outlined in this article.

References

1. Burford, A., "Field Repair of Microprocessor-Based Equipment," *TDA Progress Report 42-69*, Jet Propulsion Laboratory, Pasadena, Calif., June 15, 1982
2. Baher, F., "Field Interface Module for Antenna Control Assembly," *TDA Progress Report 42-69*, Jet Propulsion Laboratory, Pasadena, Calif., June 15, 1982
3. Valtier, H., "Field Interface Module Software Description," *TDA Progress Report 42-69*, Jet Propulsion Laboratory, Pasadena, Calif., June 15, 1982

ORIGINAL PAGE IS
OF POOR QUALITY

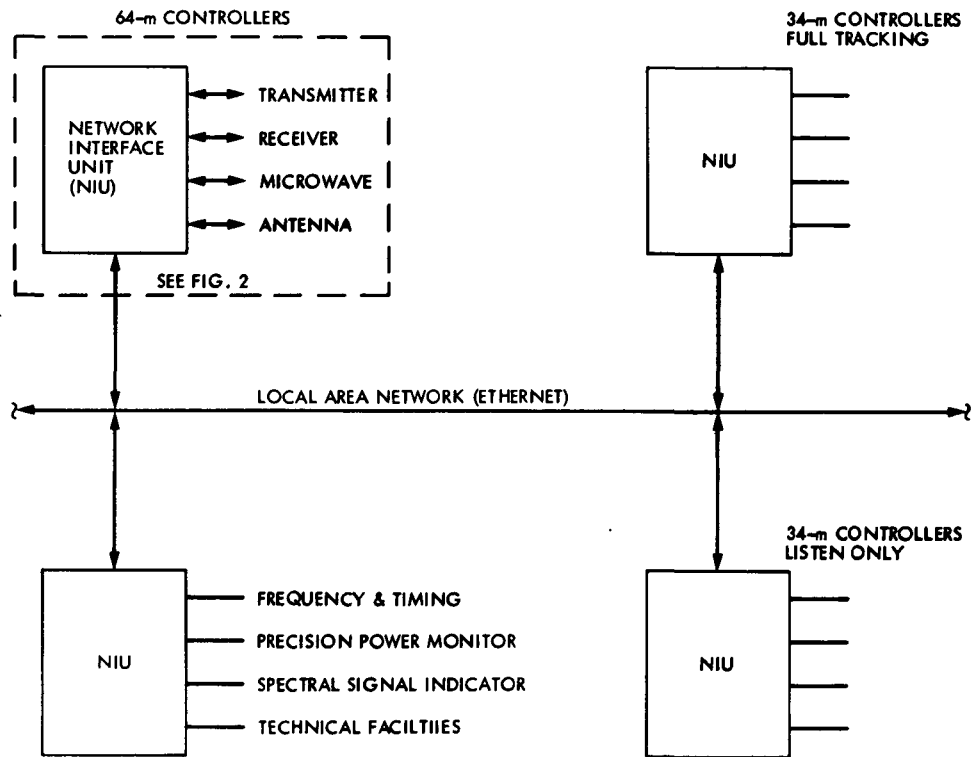


Fig. 1. Mark IVA controller network

ORIGINAL PAGE IS
OF POOR QUALITY

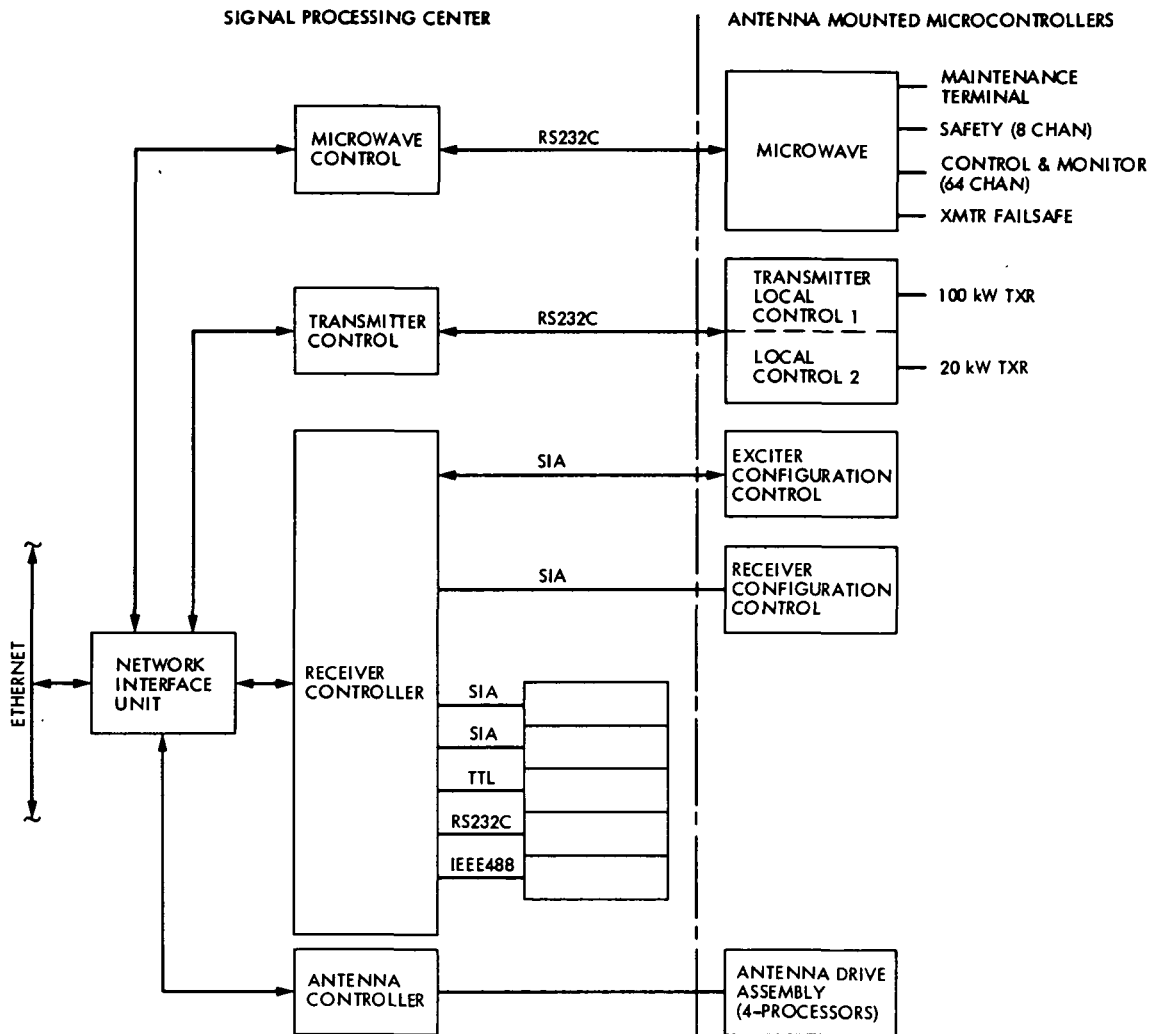


Fig. 2. Microcomputer controller locations

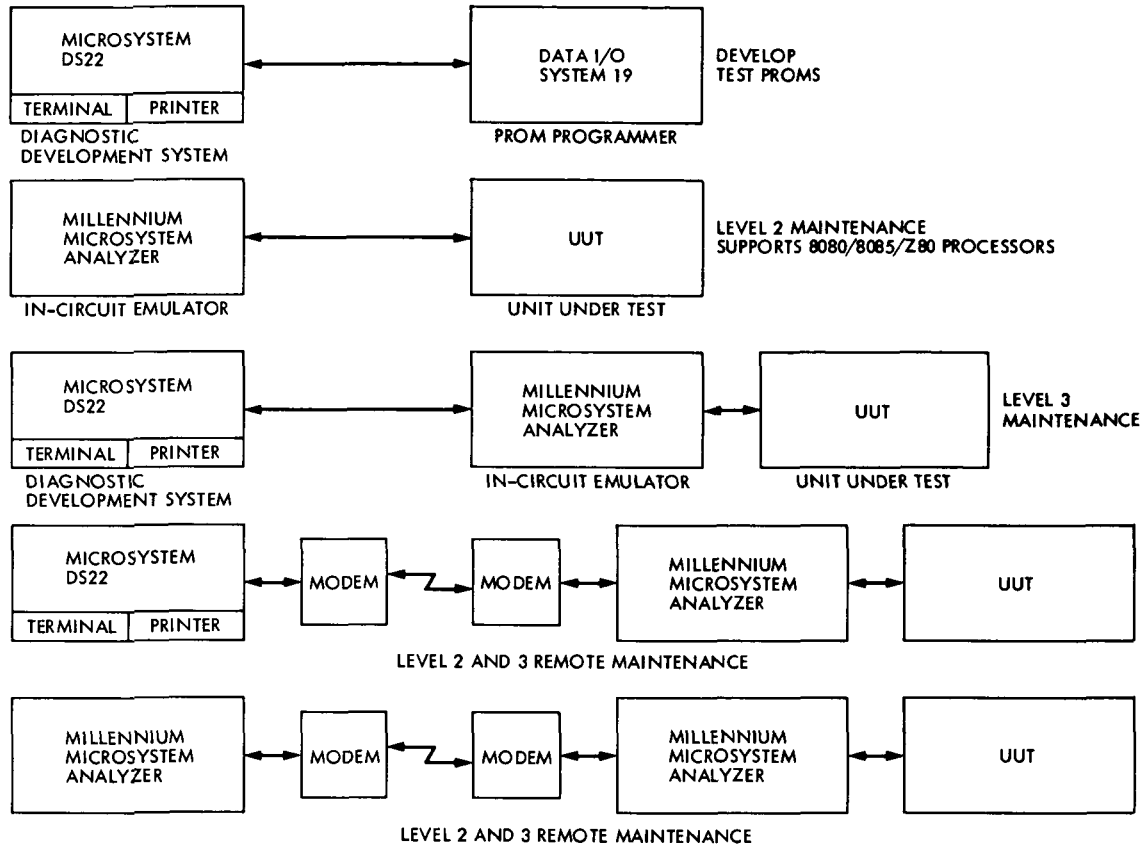


Fig. 3. Mark III 8-bit microprocessor maintenance support equipment

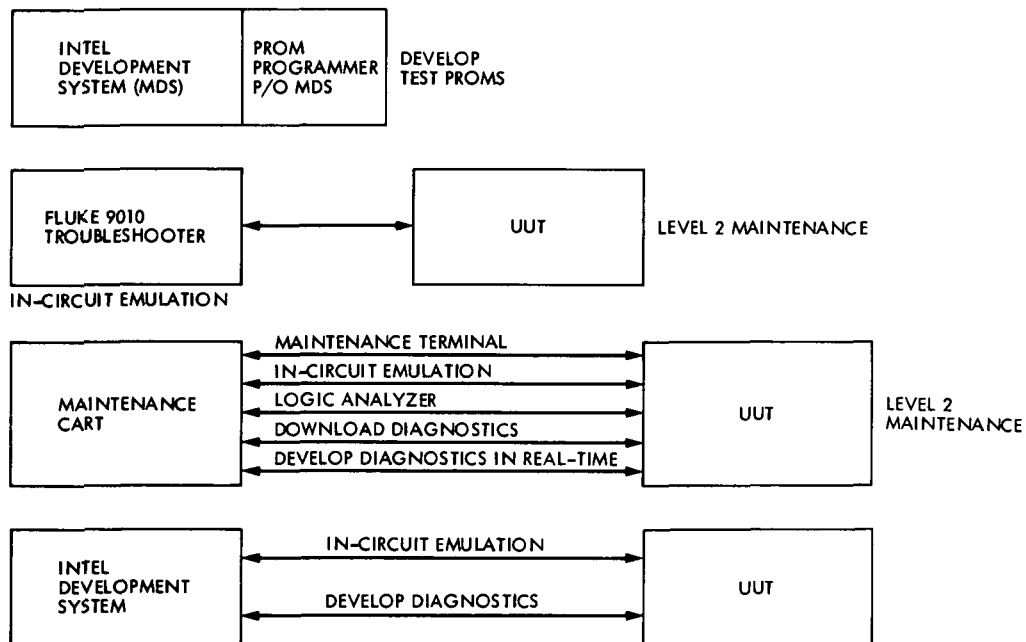


Fig. 4. Mark IVA 16-bit microcomputer maintenance support

A DSN Optimal Spacecraft Scheduling Model

W. A. Webb
Mission Design Section

A computer model is described which uses mixed-integer linear programming to provide optimal DSN spacecraft schedules given a mission set and specified scheduling requirements. A solution technique is proposed which uses Benders' Method and a heuristic starting algorithm.

I. Introduction

The DSN optimal scheduling problem refers to the problem of assigning tracking times to a set of spacecraft over a specified period of time, given the view periods of the spacecraft and a set of restrictive tracking requirements. For a typical DSN tracking situation, this is a complex decision-making problem with many variables and constraints.

A mixed-integer linear mathematical programming model is presented which may serve as a basis for both sophisticated constraint checking and automated optimal scheduling. A solution technique is proposed which uses a combination of Benders' Method and a heuristic algorithm. The proposed Benders' algorithm uses standard linear programming for the continuous variable subproblem and specialized 0,1 integer programming for the discrete variable subproblem. The proposed model will offer great facility for altering or updating the constraint set (tracking requirements) and is amenable to modern interactive computer graphics technology.

A prototype computer model was developed using the mixed-integer linear model and a standard mixed-integer programming subroutine. An experimental study was conducted using this model. The results of this study demonstrated the

need for a decomposition technique such as Benders' Method and development of a specialized heuristic starting algorithm for the 0, 1 integer subproblem.

II. Problem Description

A. Problem Statement

The DSN spacecraft (S/C) scheduling problem is stated as: given the station rise and set times of a number of S/C at each of three locations (Goldstone, Australia, and Spain) and specified tracking requirements and constraints for each S/C, determine a tracking schedule which maximizes the total tracking time over all S/C and stations.

B. 24-Hour and N-Day Scheduling Models

The problem was formulated and explored in two ways:

- (1) Develop an optimization model to determine a 24-hour tracking schedule which reflects tracking requirements.
- (2) Develop an optimization model to determine a detailed N-day tracking schedule which reflects tracking requirements.

The first approach, that of determining a 24-hour schedule, is used to formulate and solve for an optimal tracking schedule using linear programming. The 24-hour tracking schedule model may be used to study the allocation of resources portion of the DSN scheduling problem and to develop a basic facility for the problem.

The second approach, that of determining a N -day schedule is more difficult. The N -day model may be used for determining real-time or actual DSN schedules. The N -day scheduling problem is nonlinear as it includes determining the sequence or order of S/C tracking as well as the linear resource allocation problem.

C. Possible Constraints for the Scheduling Model

In both the 24-hour and N -day models, the objective function chosen is the maximization of the total tracking time over all S/C and all stations. This form is a good candidate for a representation of DSN utilization. Several types of requirements or constraint possibilities were considered and are stated as follows:

- (1) Minimum and maximum tracking pass length.
- (2) Number of tracking passes per scheduling period.
- (3) Minimum and maximum station-to-station overlap of tracking passes.
- (4) Tracking on consecutive days or stations.
- (5) Minimum elevation angle for tracking.
- (6) Station handover or S/C switching time.
- (7) Antenna selection at a station complex.
- (8) S/C tracking time priority.
- (9) Minimum and maximum acquisition of signal (AOS) and loss of signal (LOS) times.
- (10) Pre- and post-calibration periods.
- (11) Station downtime or maintenance periods.

Several of these constraint types were considered in developing the 24-hour model, and all were investigated in developing the N -day model.

III. 24-Hour Spacecraft Scheduling Model

A. Problem Formulation and Definitions

Given a subnet of DSN 64-meter Deep Space Stations at Goldstone, Australia, and Spain, and a view period schedule for n S/C at each station, the problem is to maximize the total

daily tracking time subject to specified constraints for the missions.

For a given set of missions and corresponding daily view period schedule, a tracking schedule is defined as follows: for each view period, a station either does not track the S/C at all or tracks the S/C for a single subinterval of the view period. A station may track only one S/C at a time and each S/C is only tracked by one station at a time. Each tracking period must satisfy the minimum duration parameter δ . Also, in the usual case, weighting constraints on the relative total daily tracking time between missions are imposed. These weighting constraints are specified in the form of either equality or inequality constraints.

For each station, it is assumed that the n tracking periods are either continuous or disjoint subintervals of the cyclic 24-hour day. It is assumed that the n tracking periods occur in the same cyclic order as the rise times of the Goldstone view periods. Although the view periods for a S/C generally overlap stations in the east-west cyclic order of the stations (e.g., Goldstone, Australia, Spain, Goldstone), the view period configuration does not change much from station to station, on a given day, and this choice almost always provides an optimum schedule.

The problem may now be formulated as a linear program whose variables provide the start and end times of the tracking periods for each S/C at each station required to provide maximum tracking time (given the above assumptions). Let the view period of S/C i and station j have rise and set times r_{ij} and s_{ij} . The set times may be shifted by 24 hours so that $0 \leq r_{ij} < 24$, $r_{ij} < s_{ij} < r_{ij} + 24$. The tracking period for S/C i and station j is $(r_{ij} + z_{ij}, s_{ij} - w_{ij})$, where z_{ij} and w_{ij} are the non-negative variables of the linear program. Figure 1 illustrates these variables. Table 1 provides a list of variables and parameters used in the problem formulation.

B. Objective Function

The objective function to be maximized is the total weighted tracking time for n S/C, over stations $j, j = 1, 2, 3$.

Let the view period rise time for S/C i and station j be r_{ij} and the view period set time for S/C i and station j be s_{ij} . The tracking time, T_{ij} , of S/C i at station j is

$$T_{ij} = (s_{ij} - w_{ij}) - (r_{ij} + z_{ij}) \quad (1)$$

and the total tracking time for S/C i over all stations is

$$TT_i = \sum_{j=1}^3 T_{ij} \quad i = 1, 2, \dots, n. \quad (2)$$

The objective function is then formulated as

$$\max \sum_{i=1}^n c_i TT_i \quad (3)$$

or

$$\max \left\{ \sum_{i=1}^n -c_i \left[\sum_{j=1}^3 (w_{ij} + z_{ij}) \right] + c' \right\} \quad (4)$$

C. Constraints

The constraints for the 24-hour linear programming model included the following:

- (1) Minimum tracking period.
- (2) No overlap of tracking periods for a given S/C.
- (3) No overlap of S/C tracking periods for a given station.
- (4) Weighting of S/C tracking time inequality constraints.

As an example of a constraint formulation, the minimum tracking period constraint is presented. The minimum tracking period constraint states that the tracking periods for S/C i at station j have duration $\geq \delta_{ij}$. The constraint is

$$T_{ij} = (s_{ij} - w_{ij}) - (r_{ij} + z_{ij}) \geq \delta_{ij} \quad (5)$$

or

$$z_{ij} + w_{ij} \leq -r_{ij} + s_{ij} - \delta_{ij} \quad (6)$$

$$i = 1, 2, \dots, n$$

$$j = 1, 2, 3.$$

The constraints for the 24-hour linear programming model are described in detail in Ref. 1.

IV. Mixed-Integer Linear Programming N-Day Scheduling Model

A. Continuous Variable Allocation Model

The variables for the linear programming model are the continuous linear programming rise variable z and the set variable w . The 24-hour model is actually an allocation model in that the order of S/C tracking is assumed; in this case all S/C are always tracked at each station in the order of rising over the Goldstone station. Also, the objective function and all of the constraints are linear in the variables, z and w , of the

problem. The allocation problem here is the assignment of specific acquisition of signal (AOS) and loss of signal (LOS) times as determined by the optimal values of z and w in the linear programming solution.

The linear programming allocation problem may be written as

$$\begin{aligned} \min c'x \\ Ax \leq b \\ x \geq 0 \end{aligned} \quad (7)$$

where c is an n -vector of weighting coefficients (c' is the transpose of c), x is an n -vector of the continuous linear programming variables z and w , A is a $m \times n$ matrix of coefficients of the constraint equations, and b is a m -vector of the right-hand side constants of the constraint equations. The problem may be easily converted from a minimization problem to a maximization problem by using the fact that $\max g(x) = -\min -g(x)$. The x -vector is non-negative because negative value of either z or w would mean that tracking begins outside the view period, which is not realistic.

B. N-Day Sequencing Problem

The N -day scheduling problem, where $N > 1$, is actually an allocation problem for each arbitrary 24-hour period and a sequencing (or S/C ordering) problem over the N -days. This is so because in the general case, over any N -day scheduling period, the number of tracking passes for any S/C may be $< N$. Therefore, optimal decisions must be made concerning which days to track which S/C. It is no longer applicable to track all S/C simply in the order of Goldstone rise as for the 24-hour model.

The sequencing or, in this case, the S/C ordering problem is, in general, a nonlinear problem and linear programming is no longer applicable. This is because the ordering possibilities must be modeled using discrete integer variables; i.e., a S/C is either tracked within a particular view period or it is not. Because it is a yes/no decision, the problem may be set up so that the variables take on only 0 or 1 values. These variables are commonly called indicator variables and, for the N -day scheduling problem, indicate whether or not a particular S/C is tracked within each specified view period. So, for a tracking situation with i S/C, j stations, and k days the number of indicator variables required is ijk . As a typical example, for a scheduling problem with 6 S/C, 3 stations and 7 days, 126 integer indicator variables are required. Each set of values of the indicator variables represents a particular S/C order. The number of possible S/C orderings is 2^{ijk} . For the example

given, the number of possible S/C orderings is 2^{126} or 8.5×10^{37} . For each order specified by the indicator variables, a S/C allocation problem must be solved in order to determine its objective function value so that the optimal schedule may be found. Obviously, the N -day optimal scheduling problem is a large-scale optimization problem with potentially severe computational considerations.

C. Formulation of Switching Constraints

The purpose of the switching constraints is to set up the lower and upper bounds on the tracking pass lengths for each possible view period. For a given view period (recall there is one for each S/C, station, and day), let LB denote the lower bound and UB denote the upper bound, and y be the 0,1 indicator variable. The constraints are called switching constraints because the set (LB, UB) goes to $(0,0)$ as the indicator variable steps from 1 to 0. In the latter case the tracking pass is switched out and the S/C is not tracked within this view period. For this particular view period, let T be the tracking pass length where, from the previous section,

$$T = (s - w - r - z) \quad (8)$$

The set of switching constraints for this view period is

$$\begin{aligned} T &\geq 0 \\ T &\leq UB \\ T &\leq LB + (y - 1)M \\ T &\leq yM \\ y &= 0 \text{ or } 1 \end{aligned} \quad (9)$$

where M is an arbitrarily large number. Note that zero always satisfies the upper bound constraint but not the lower bound constraint. Therefore, the lower bound must either be some value $LB > 0$ or included as zero if no lower bound is specified. Also, if no minimum or maximum tracking pass length is specified, $LB = 0$ and $UB = \text{length of the tracking pass } (s - r)$. In this case there are redundant equations in the constraint set.

D. Formulation of Other Constraint Types

The form of the switching constraints is such that it includes both the continuous variables z and w and the discrete 0,1 variable y . It is possible to write all of the constraint types mentioned in terms of these variables. This includes tracking on consecutive days and stations, number of tracking passes required during N days, station and S/C overlap requirements, antenna switching options, and minimum elevation angle requirements. Also, since the equations or inequalities representing these constraints are additively separable, the

formulation of the problem may be divided into two subproblems, one containing only the continuous variables z and w , and the other containing only the discrete 0,1 variables.

E. Formulation of the N -Day Scheduling Model

A math programming problem which contains both continuous and discrete variables is called a mixed-integer program. Since the optimal scheduling problem also has a linear objective function and only linear constraints in the continuous variables, it is a mixed-integer linear programming problem. Mixed-integer linear programming (MILP) problems are a specific category of optimization problems in the field of operations research, and there are several solution techniques available for these problems in the literature. These problems are often of a large-scale nature and are typically computationally difficult.

The form of the constraint set suggests that by rearranging all equations and inequalities, so that the continuous variable and discrete 0,1 variables are separate, the problem may be solved by dealing with the continuous and discrete subproblems separately. The objective function also may be separated into a continuous variable and discrete variable portion. There are several solution procedures which take advantage of a separable structure. These procedures frequently couple two individual solution procedures and iterate between them. In this case, the continuous subproblem may be solved by linear programming and the discrete 0,1 variable subproblem solved by a specialized 0,1 integer programming algorithm.

Let x be an n -vector of z and w continuous variables and y be a p -vector of discrete 0,1 variables; c is an n -vector of weighting coefficients for the continuous variables and \bar{c} is a p -vector of weighting constraints for the 0,1 discrete variables. Rearranging continuous and discrete variables, the problem form is

$$\min c'x + \bar{c}'y$$

$$\text{subject to } Ax + \bar{A}y = b \quad (10)$$

$$x \geq 0, y \in Y$$

where A and \bar{A} are $m \times n$ and $m \times p$ coefficient matrices, respectively, for the constraint set and b is a m -vector of right-hand side constants of the constraint set. Y is the subset of the set of integer variables which contains only the values 0 and 1. Recall that the left-hand subproblem is a continuous-variable linear problem and the right-hand subproblem is a nonlinear problem.

V. Results of Prototype Study

A prototype computer model was developed using the mixed-integer linear programming model presented. A standard mixed-integer subroutine was used to solve typical example DSN scheduling problems. The computer program was designed to be run in an interactive graphics mode. This enables a user to sit at an interactive graphics terminal and conveniently and efficiently make scheduling decisions. The effects of potential changes to the current schedule are quickly presented on the video display.

The prototype study positively demonstrated the feasibility of developing a mathematical model and interactive computer tool to aid in making complex DSN scheduling decisions. The following advantages of such an automated tool were identified:

- (1) Scheduling decisions could be made very efficiently using graphics terminals in an interactive mode:
- (2) Better schedules would result in terms of network utilization or other selected criteria.
- (3) Less effort and time would be required by the schedulers.
- (4) Conflicts could be resolved in a systematic way if desired.
- (5) Clear-cut criteria for conflict resolution choices could be provided.

- (6) Manual scheduling will always be possible and automated decisions may be overridden.

As a result of this study it was also determined that a more powerful solution procedure needed to be developed to solve complex scheduling problems more efficiently. It is out of this need that the proposed development of a solution procedure using Benders' Method and a heuristic starting algorithm evolved. The theoretical basis of Benders' Method and its application to the DSN optimal spacecraft scheduling problem are presented in an appendix.

VI. Further Development

Plans for further development of the optimal spacecraft scheduling model include the following steps:

- (1) Develop a mixed-integer linear programming computer model which uses Benders' Method for solution of the DSN scheduling problem.
- (2) Develop an efficient heuristic starting algorithm to use in the Benders' Model.
- (3) Present test data for the model using actual DSN scheduling examples.
- (4) Provide favorable comparisons, both in efficiency and results, between the research model and the current DSN scheduling procedure.

Reference

1. Webb, W. A., "Scheduling of Tracking Times for Interplanetary Spacecraft on the Deep Space Network," Joint National Meeting of the Institute of Management Sciences and Operations Research Society of America, New York, May 1978.

Bibliography

- Baker, K. R., *Introduction to Sequencing and Scheduling*, John Wiley and Sons, New York, 1974.
- Benders, J. F., "Partitioning Procedures for Solving Mixed Variable Programming Problems," *Numerische Mathematik*, 4, pp. 238-252, 1962.
- Dantzig, G. B., *Linear Programming and Extension*, Princeton University Press, Princeton, N.J., 1963.
- Greenhall, C. A., "TDA Data Management Planning: Construction of Maximal Daily Tracking Schedules," *DSN Progress Report 42-27*, Jet Propulsion Laboratory, Pasadena, Calif., pp. 187-191, 1975.
- Lasden, L. S., *Optimization Theory for Large Systems*, The Macmillan Co., New York, 1970.
- Webb, W. A., "A Proposed Optimal Spacecraft Scheduling Model for the NASA Deep Space Network," Joint National Meeting of the Institute of Management Sciences and Operations Research Society of America, Detroit, Michigan, April 1982.

Table 1. Definition of problem variables and parameters

| | |
|---------------|--|
| r_{ij} | View period rise time for S/C i and station j |
| s_{ij} | View period set time for S/C i and station j |
| z_{ij} | Linear program rise variable for S/C i and station j |
| w_{ij} | Linear program set variable for S/C i and station j |
| T_{ij} | Tracking time for S/C i at station j |
| TT_i | Total tracking time for S/C i over all stations |
| δ_{ij} | Minimum tracking period duration for S/C i and station j |
| c_i | Objective function tracking time weighting for S/C i |

6-27-73 2010.00
VOLUME 0000 20

ORIGINAL PAGE IS
OF POOR QUALITY

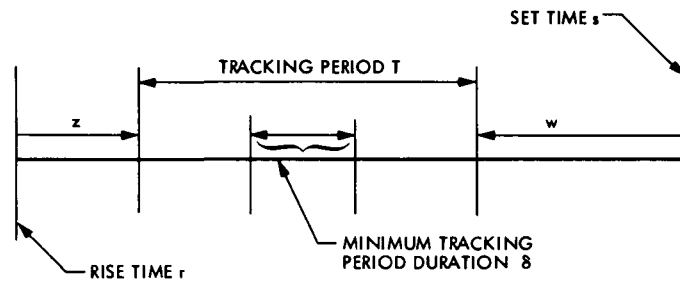


Fig. 1. Tracking period and linear programming variables

Appendix

Solution of the N -Day Scheduling Problem by Benders' Method

The form of the N -day scheduling problem as formulated by a mixed-integer linear programming model lends itself very well to solution by Benders' partitioning algorithm for mixed-variable optimization problems. Benders' Method may be used on mixed-integer programming problems which are separable into the linear and nonlinear (integer) portions. The separable subproblems may then be solved individually to determine their individual optimal solutions and summed to determine the optimum of the original problem. This partitioning procedure takes up less computer storage and allows the usage of specialized techniques for each portion of the problem. For example, linear programming may be used for the linear part of the problem. The method also allows the use of a good initial schedule which may be determined by a heuristic algorithm and, thus, save considerable time in arriving at optimal solution.

I. Theoretical Basis of Benders' Method

Benders' Method may be applied to an optimization problem of the form

$$\left. \begin{array}{l} \min c'x + f(y) \\ \text{subject to } Ax + F(y) = b \\ x \geq 0, y \in Y \end{array} \right\} \text{problem} \quad (\text{A-1})$$

where $\min g(x) = -\max -g(x)$.

For this discussion, the matrix A is $m \times n$, x and c are n -vectors (c' is the transpose of c), y is a p -vector, f is a scalar-valued function of y , F is an m -vector whose components are functions of y , b is an m -vector, and Y an arbitrary subset of E^p . The functions f and F need not be linear; in fact, for the scheduling problem Y is the set of variables in E^q with integral values components. Problem P will be referred to as the primal problem. For the scheduling problem, x is the set of continuous variables which determine the allocation of tracking passes and Y is the vector of integer variables which describe the tracking frequency and order.

Since P is linear in x for fixed values of y , it is natural to attempt to solve it by fixing y , solving a linear program in x , obtaining a "better" y , etc. Of course, only values of y for which there exist x satisfying the resulting linear constraints

may be considered. That is, y must lie in the set

$$\bar{Y} = \{y \in Y \mid \exists x \geq 0 \exists Ax = b - F(y)\} \quad (\text{A-2})$$

$$= \{y \in Y \mid \gamma^j (b - F(y)) \leq 0, j = 1, \dots, K\} \quad (\text{A-3})$$

where γ^j are all (K of these) of the simplex multipliers of Phase I of the simplex method. The simplex method is a two-phase procedure for finding an optimal solution to linear programming problems. Phase I finds an initial basic feasible solution if one exists, or gives the information that one does not (in which case the constraints are inconsistent and the problem has no solution). Phase II uses this solution as a starting point and either finds a minimizing solution or yields the information that the minimum is unbounded (i.e., $-\infty$). So \bar{Y} is the set of all $y \in Y$ such that you get feasible constraints for problem P . A feasible right-hand side does not exist unless that right-hand side makes an obtuse angle with every one of the Phase I simplex multipliers.

Define the function $\sigma(b, y)$ as

$$\left. \begin{array}{l} \sigma(b - F(y)) = \min c'x \\ \text{subject to } Ax = b - F(y) \\ x \geq 0. \end{array} \right\} \quad (\text{A-4})$$

Now if $y \in \bar{Y}$ then $\sigma(b - F(y)) < \infty$, and if $y \in Y \sim \bar{Y}$ (i.e., if y is not feasible), then $\sigma = +\infty$.

(A-5)

Recall from linear programming duality theory that if y is feasible then

$$\min c'x = \max \pi [b - F(y)] \quad (\text{A-6})$$

where π is the set of dual variables corresponding to the primal problem $\min c'x$. Let $\{\pi^1, \dots, \pi^J\}$ be all possible optimal simplex multiplier vectors from Eq. (A-6). Then for $y \in Y$,

$$\sigma [b - F(y)] = \max \pi^i [b - F(y)] \quad (\text{A-7})$$

$$i = 1, \dots, J.$$

**ORIGINAL PAGE IS
OF POOR QUALITY**

Rewrite problem P as

$$\begin{aligned} & \min f(y) + \min c'x \\ & y \in \bar{Y} \text{ subject to } Ax = b - F(y) \\ & x \geq 0. \end{aligned} \quad (\text{A-8})$$

Recall from classical optimization theory that

$$\min_{x,y} f(x,y) = \min_y \min_x f(x,y). \quad (\text{A-9})$$

The form of problem (A-8) now becomes

$$\min \{f(y) + \sigma [b - F(y)]\} \quad (\text{A-10})$$

subject to

$$\begin{aligned} \gamma^j [b - F(y)] &\leq 0 \quad j = 1, \dots, K \\ y &\in Y. \end{aligned}$$

Substituting further from duality theory

$$\begin{aligned} & \min \{f(y) + \max \pi^i [b - F(y)]\} \\ & i = 1, \dots, J \end{aligned} \quad (\text{A-11})$$

subject to

$$\begin{aligned} \gamma^j [b - F(y)] &\leq 0 \quad j = 1, \dots, K \\ y &\in Y. \end{aligned}$$

Recalling that

$$\begin{aligned} \min f(x) &= \min \eta \\ x \in X \quad \eta - f(x) &\geq 0 \\ x &\geq 0, \end{aligned} \quad (\text{A-12})$$

problem (A-11) may be written as

$$\begin{aligned} & \min \eta \\ & \text{subject to} \\ & \eta \geq f(y) + \max \pi^i [b - F(y)] \quad i = 1, \dots, J \\ & 0 \geq \gamma^j [b - F(y)] \quad j = 1, \dots, K \\ & y \in Y \end{aligned} \quad (\text{A-13})$$

or

$$\begin{aligned} & \min \eta \\ & \text{subject to} \\ & \left. \begin{aligned} \eta &\geq f(y) + \pi^i [b - F(y)] \\ 0 &\geq \gamma^j [b - F(y)] \quad i = 1, \dots, J \\ y &\in Y \quad j = 1, \dots, K \end{aligned} \right\} \text{Problem } M. \end{aligned} \quad (\text{A-14})$$

Problem M will be referred to as the master problem and is equivalent to problem P . Problem M includes all of the simplex multipliers of Phases I and II of the simplex method applied to Problem P . In general, it has many constraints. Furthermore, the constraints are not known explicitly because the simplex multipliers π^i and γ^j are not known.

II. Application of Benders' Method to the N -Day Scheduling Problem

The original problem, Problem P , is restated from the previous subsection as

$$\begin{aligned} & \min c'x + F(y) \\ & \text{subject to } Ax + F(y) = b \\ & x \geq 0, y \in Y \end{aligned} \quad \left. \vphantom{\begin{aligned} & \min c'x + F(y) \\ & \text{subject to } Ax + F(y) = b \\ & x \geq 0, y \in Y \end{aligned}} \right\} \text{Problem } P \quad (\text{A-15})$$

This problem may be rewritten in the form of the DSN scheduling problem by introducing slack variables to convert equality constraints to inequality constraints and by using the fact that $\max g(x) = -\min -g(x)$. The x -vector represents the continuous w and z variables which determine the tracking

pass allocations for a given tracking order, and the y variables are the 0,1 switching variables which determine the order and frequency of tracking. Decomposition allows the continuous variable subproblem to be solved by linear programming and the 0,1 integer problem to be solved by specialized 0,1 integer programming algorithms. Solving each of the subproblems separately results in a savings of computer storage required by breaking a large problem into two smaller ones. Time savings in arriving at a solution results from taking advantage of linear programming for the continuous subproblem and a specialized algorithm for the 0,1 integer subproblem. Also, considerable computing time may be saved by making a good choice of the starting schedule to begin the Benders' procedure.

To solve the scheduling problem using Benders' Method, let $y^0 \in \bar{Y}$ be the initial scheduling order (e.g., the scheduling order resulting from the schedule determined by a heuristic algorithm). Solve the primal problem, Problem P , as a function of y^0 where

$$\sigma(b - F(y^0)) \triangleq \min c'x \quad (\text{A-16})$$

subject to

$$Ax = b - F(y^0)$$

$$x \geq 0.$$

This subproblem represents the schedule allocation problem given the sequence specified by order y^0 and may be solved by linear programming. Let x^0 be an optimal solution, and let π^0 be the vector of optimal simplex multipliers.

Let $UB \triangleq f(y) + \sigma(b - F(y))$ be defined as the upper bound on the objective function for the scheduling order specified by y . For the initial schedule y^0 ,

$$UB^0 = f(y^0) + \sigma(b - F(y^0)). \quad (\text{A-17})$$

Now solve the first relaxed master problem,

$$\min \eta$$

$$\text{subject to } \eta \geq f(y) + \pi^0 [b - F(y)]. \quad (\text{A-18})$$

$$y \in Y$$

Recall that a relaxed master problem has fewer constraints than the master problem M . For the N -day scheduling problem this is a 0,1 integer program problem which may be solved by specialized techniques. Let (η^1, y^1) be the solution. Note that

η^1 is a lower bound for P since the objective function is being minimized for more constraints at each iteration and must have an equal or higher value. Define the lower bound on problem P as

$$LB \triangleq \eta$$

where $\eta^1 \leq UB^0$. Now if $LB = UB$ at any iteration, an optimal solution has been found and the algorithm stops. If at any iteration $LB = \eta < UB$, solve the linear program,

$$\sigma [b - F(y')] = \min c'x$$

$$\text{subject to } Ax = b - F(y') \quad (\text{A-19})$$

$$x \geq 0$$

and determine a new x' which represents a new schedule allocation. The algorithm is continued in this manner until $LB = UB$ (or the bounds are sufficiently close to meet some tolerance criteria).

Suppose at some iteration the set of constraints

$$Ax = b - F(y') \quad (\text{A-20})$$

$$x \geq 0$$

is infeasible. In this case, Phase I of the simplex method will generate a γ' so that

$$\gamma' [b - F(y')] > 0. \quad (\text{A-21})$$

A new relaxed master problem is formulated as

$$\min \eta$$

$$\text{subject to } \eta \geq f(y) + \pi^1 [b - F(y)] \quad (\text{A-22})$$

$$0 \geq \gamma' [b - F(y)]$$

$$y \in Y.$$

Let (η^2, y^2) be the optimal solution to this 0,1 integer programming problem. Note that η^2 must be at least as large as η^1 because another constraint has been added.

On the other hand, suppose $y' \in \bar{Y}$ (i.e., is feasible); solve for

$$\begin{aligned} \sigma(b - F(y')) &= \min c'x \\ \text{subject to } Ax &= b - F(y') \\ x &\geq 0 \end{aligned} \quad (\text{A-23})$$

and let x' be an optimal solution. Let π' be an optimal simplex multiplier vector. Set $UB' = \min \{UB^0, f(y') + \sigma [b - F(y')]\}$ so that if the new value is smaller than the previous upper bound then it becomes the new upper bound. Note that while lower-bound values are monotonically increasing at each iteration, the upper bounds are not generally monotonically decreasing.

If at some iteration $LB' = \eta' = UB'$ and an optimal schedule has been found, then the y' vector of 0,1 integers specifies the order of spacecraft tracking throughout the N days and the x' vector specifies the acquisition and loss of signal times for each tracking pass. If $\eta' < UB'$, a new constraint is added to the relaxed master problem, a new y' is determined, and a new iteration is performed.

III. A Heuristic Starting Schedule for the Benders' Model

Recall that the first step in implementing Benders' Method for the N -day scheduling problem is to solve the subproblem

$$\begin{aligned} \sigma(b - F(y^0)) &= \min c'x \\ \text{subject to } Ax &= b - F(y^0) \\ x &> 0 \end{aligned} \quad (\text{A-24})$$

where y^0 is a vector which represents the order of S/C tracking during the scheduling period. This subproblem may generally be solved fairly easily by linear programming, even for large problems. The resulting solution, x , may then be used to determine a new y' , and the iterative process continues.

The vector y^0 is easily determined from the schedule which is determined using a heuristic algorithm. Note that the actual allocation of acquisition and loss of signal times is not of interest here and this fact may play a role in determining the heuristic algorithm. Also, note that the upper bound, UB , which is a function of the y vector,

$$UB = f(y) + \sigma [b - F(y)] , \quad (\text{A-25})$$

is not monotonic since the functions $f(y)$ and $F(y)$ are non-linear. However, a well-designed heuristic algorithm which results in good suboptimal initial scheduling orders, specified by the y^0 vector, may result in a saving of perhaps 80% or more of the computational time normally required for determining optimality starting with an arbitrarily chosen y^0 .

Potential Availability of Diesel Waste Heat at Echo Deep Space Station (DSS 12)

R. D. Hughes
DSN Engineering Section

Energy consumption at the Goldstone Echo Deep Space Station (DSS 12) is predicted and quantified for a future station configuration which will involve implementation of proposed energy conservation modifications. Cogeneration by the utilization of diesel waste-heat to satisfy site heating and cooling requirements of the station is discussed. Scenarios involving expanded use of on-site diesel generators are presented.

I. Introduction

As part of the Deep Space Network (DSN) effort in energy conservation and energy self-sufficiency at ground-based tracking stations, the on-site availability of low-to-medium-temperature waste heat has been viewed as an important cogeneration energy resource that requires additional investigation. At the Echo Deep Space Station, DSS 12, diesel-driven electric generators presently supply all of the site's electrical needs during "on-peak" daily time periods for the purpose of reducing purchased utility electricity costs. "On-peak" time periods are defined by Southern California Edison Company, the utility company, as 1:00 p.m. to 7:00 p.m. summer weekdays and from 5:00 p.m. to 10:00 p.m. on winter weekdays; where summer commences at 12:01 a.m. on May 1, and winter commences at 12:01 on November 1. During these on-peak periods, waste heat generated in the jacket cooling water and exhaust gases presents an energy and cost savings potential if utilized in place of conventional heat sources.

Since the diesel generators are supplying the entire site's load during generator operating periods, they are in a "load-following" mode, and knowledge of an accurate load profile is necessary in order to predict the available quantity and optimum timing of diesel waste heat. Thus, as a first phase of

the study, this report is devoted to the determination of a "projected" energy consumption profile which takes into account proposed energy saving modifications to the Echo facility. Also, since any available waste heat would be used to satisfy some or all of the space heating and cooling requirements of the station, profiles of projected heating and cooling loads have been constructed for future economic analyses.

An attempt is made in this work to quantify the amount of waste heat available for satisfying given heating and cooling loads. The conceptual design details and economic feasibility of the facility systems necessary for waste heat utilization as well as the waste heat potential at other major DSS stations will be discussed in subsequent articles.

II. Projected Energy Consumption Profiles

A major part of the energy conservation effort at the Goldstone Deep Space Communications Complex (GDSCC) has been directed toward the modification of the heating, ventilating, and air-conditioning (HVAC) systems. Due to the ongoing nature of this effort, a baseline energy profile for the Echo site was constructed which represents the existing conditions (Ref. 1). Then a future projection of the energy

requirements was established depicting the new profile after the proposed modifications have been completed.

The station energy requirements were determined by exercising the JPL-computerized model, ECP, which simulates energy consumption in buildings using a description of building construction and occupancy, exterior weather data, and interior mechanical, lighting, HVAC and electrical systems.

The accuracy of this model was verified by comparing the simulation results to actual energy consumption data which were obtained by recording on-site meter readings. This verification process was performed for the Echo buildings and facilities, as reported in Ref. 1, as they existed before any energy conservation modifications were made. Once the ECP model was verified for existing conditions, various modifications were modeled to determine their energy and cost saving potential. The most effective set of modifications for each building based on relevant economic criteria was then proposed for future building modifications.

Some examples of cost-effective modifications are: add zero energy-band "deadband" thermostat control, add outside air economizers, add timeclocks to air handlers, use automatic reset "floating" setpoints, lower inside design temperatures in winter to 68°F, increase inside design conditions in summer to 78°F, reduce outside air infiltration/exfiltration rates by weatherproofing, replace incandescent lighting with fluorescent, balance air flow rates, and replace some evaporative coolers with packaged vapor-compression units.

To construct the projected Echo site energy profile, the ECP-simulated results for the projected building conditions were modeled and summed for only the major energy-consuming buildings. The summed energy profiles were increased by 5% to account for those miscellaneous minor buildings which consume small amounts of energy and were not modeled separately. The total monthly space heating load, space cooling load, electrical energy consumption by cooling and heating equipment, and overall electrical consumption are shown in Tables 1-4, respectively, where they are itemized by building and summed for the entire station. Also, hourly energy consumption rates for two typical days, one in January and one in August, representing extreme winter and summer ambient conditions, are shown in Tables 5-9.

The loads and consumption values for building G-38 have been scaled from those of building G-21 because of recent major changes in the nature of building G-38 usage. Building G-21 was used as an analogous model for G-38 because the consumption profiles, interiors, and occupancy patterns of the two buildings are similar.

The predicted reductions in energy consumption are found significant when compared to the unmodified, existing conditions summarized in Ref. 1. The total Echo station annual electrical consumption will drop from the present value of 4,468 MWh(e) to 3,382 MWh(e) for a savings of 1,086 MWh(e) or about 24% per year. Since the average cost of electricity at GDSCC for FY '81 was about \$0.06/kWh(e) this represents an annual cost savings of about \$65,000. As expected, the category in which the greatest savings occurred was HVAC electrical consumption, which was reduced from 1,226,680 kWh(e)/yr to 371,265 kWh(e)/yr for a reduction of 70%.

Figure 1 shows a comparison of overall electrical consumption profiles on a monthly basis before and after the proposed modifications. Figure 1 also shows the on-peak diesel generated electrical energy profiles as projected after modifications (overall electrical consumption) and when reduced by assuming that the entire cooling and heating electrical load is met by waste heat (non-HVAC electrical consumption). Thus an upper and lower bound are established on the amount of electrical power generated, and accordingly, on the amount of waste heat available.

Figure 2 shows predicted heating and cooling load profiles on a monthly basis. Figure 3 and 4 show the projected overall electrical consumption profiles with generating periods delineated for a typical day in January and August, respectively.

III. Required vs Available Waste Heat

The questions of how much waste heat is actually available and how to most economically utilize the waste heat were approached in two ways: (1) on the basis of average energy consumption for each month and (2) on the basis of hourly energy consumption rates for a typical day in winter and summer. To help answer those questions, the recoverable portion of the waste heat is calculated as presented below:

A. Recoverable Waste Heat

The effective input thermal energy of the fuel consumed by a diesel generator system is distributed into the following sources of output energy for average operating conditions (Ref. 2):

| | |
|---|-----|
| Mechanical work | 30% |
| Recoverable jacket cooling water heat | 27% |
| Recoverable flue gas heat | 15% |
| Cooling-oil heat, nonrecoverable flue gas heat, radiation | 28% |

This energy balance (Ref. 2) assumes that 90% of the jacket coolings water heat is recoverable and 70% of the flue gas heat is recoverable. The flowrate of the exhaust gas heat-exchange fluid must be such that the exhaust gas temperature remains above 160°C (325°F) to avoid water vapor condensation and sulphur-related corrosion of the exhaust system.

Thus approximately 72% of the net fuel energy is recoverable from the diesel generator system. The ratio of electrical energy generated to recoverable jacket water heat to recoverable exhaust heat is:

$$1.0: 0.9: 0.5$$

assuming negligible generator losses.

A block diagram of a typical waste-heat recovery system used to augment a conventional HVAC system is shown in Fig. 5. This represents one possible configuration for such a system; other arrangements are possible.

The preceding energy ratio was applied to the projected energy quantities in Tables 1-9. The amount of waste heat available from the generators is compared to that required to satisfy the heating and cooling loads and is shown in Tables 10-12. It was assumed that there was a 10% loss in the hot fluid supply system (piping, etc.) and a 0.67 coefficient of performance for the absorption refrigeration system. Thus the waste heat required to satisfy the heating load is given as (heating load) ÷ 0.9 and the waste heat required to satisfy the cooling load is (cooling load) ÷ (0.9 × 0.67).

Plots of available vs. required thermal energy profiles are shown in Fig. 6 for monthly quantities and in Figs. 7 and 8 for January and August typical-day hourly profiles respectively.

B. Waste Heat Availability and Utilization

The data shown in Table 10 indicate that on the annual basis the amount of waste heat available (taking an average value between the upper and lower bound) is enough to supply all of the heating load and approximately one-half of the cooling load. Such an evaluation, however, implies the existence of an efficient storage system for both hot and cold thermal fluids. Since a chilled-water system with thermal storage capability has been proposed for the Echo site as an economically feasible HVAC modification, the implementation of a waste heat utilization system which requires thermal storage may be quite feasible.

When waste heat availability is analyzed on a monthly basis, Fig. 6 shows that sufficient waste heat is available to satisfy

the heating load every month, or to satisfy the complete cooling load five months out of the year and part of the cooling load for the remainder of the year. When waste heat availability is analyzed on a daily basis it should be noted that Tables 11 and 12 represent conditions for a "weekday" which differ from "weekend" conditions. Thus, for a typical weekday in January, the available waste heat is nearly equal to the total required for both heating and cooling; for an individual weekday, the relative amount of waste heat availability is greater than on a monthly basis, since the monthly total takes into account weekends when no generation usually occurs.

Finally, on an hourly basis, it can be seen that in August almost all of the waste heat can be used without storage and about half of the cooling load per day can be met with waste heat. On the other hand, for conditions in January, if no thermal storage were available, only about 22% of the waste heat would be utilized.

C. Increase Due to Expanded Generator Operation

The possibility exists (depending on detailed economic analysis results) that it may be financially advantageous to expand the periods of diesel generator operation in order to take better advantage of waste heat recovery equipment. For example, if the hours of diesel generator operation in August were expanded to the period 7:00 a.m. to 10:00 p.m., the net amount of waste heat generated would almost double (about 10,000 kWh per day) and would nearly be enough to satisfy the maximum weekday cooling load. In addition, there exist periods of operating the generators in a "spinning reserve" mode during critical tracking maneuvers. When a critical tracking period occurs, electrical power is switched to diesel generation regardless of the time of day, and enough diesel generators are brought on line so that they are only operating at partial load. In this fashion, one or more generators could be dropped from operation in the event of malfunction and the remaining generators would assume the load, thus utilizing "spinning reserve." This mode of operation occurs 10-20% of the time. If critical periods are assumed to be random in the overlap of "on-peak" periods, then the amount of waste heat available is approximately 10% greater than indicated by the projected profiles.

IV. Summary

It has been shown that sufficient waste heat will be produced at the Echo site to satisfy approximately all of the heating and cooling load in the winter and one-half in the summer. This quantification is based on the assumption that diesel generators are only operating during "on-peak" periods and energy consumption is according to projected conditions.



Also, an efficient thermal storage system would be required to meet these conditions. If expanded diesel operation were implemented, a greater waste heat utility would be realized. A

conceptual design and economic analysis using the results of this report will be necessary in order to determine the technical feasibility of waste heat utilization at the Echo station.

References

1. Guiar, C. N., et al., "Energy Consumption for the Echo Station (DSS 12)," *TDA Progress Report 42-66*, pp. 355-363, Jet Propulsion Laboratory, Pasadena, Calif., Dec. 15, 1981.
2. Caterpillar Tractor Co., "Total Energy Handbook," Aug. 1969.



ORIGINAL PAGE IS
OF POOR QUALITY

Table 1. Monthly heating load at Echo for projected conditions (kWh_e)

| Month | Building | | | | | | | | | Total |
|----------------------|----------|--------|-------|------|--------|--------|---------|-------------------|---------------------|---------|
| | G-21 | G-23 | G-24 | G-26 | G-28 | G-33 | G-34/35 | G-38 ^a | Others ^b | |
| Jan | 1,899 | 8,459 | 1,266 | 105 | 5,916 | 4,366 | 59 | 1,310 | 1,169 | 24,549 |
| Feb | 779 | 6,519 | 281 | — | 4,295 | 1,948 | — | 536 | 718 | 15,076 |
| Mar | 604 | 6,373 | 179 | — | 4,506 | 1,749 | — | 416 | 691 | 14,518 |
| Apr | 524 | 5,505 | — | — | 3,870 | 1,146 | — | 363 | 572 | 11,980 |
| May | — | 5,403 | — | — | — | 240 | — | — | 282 | 5,925 |
| Jun | — | 4,002 | — | — | — | — | — | — | 200 | 4,202 |
| Jul | — | 3,238 | — | — | — | — | — | — | 162 | 3,400 |
| Aug | — | 3,378 | — | — | — | — | — | — | 169 | 3,547 |
| Sept | — | 4,474 | — | — | — | — | — | — | 224 | 4,698 |
| Oct | 217 | 4,603 | — | — | 2,992 | 499 | — | 149 | 419 | 8,799 |
| Nov | 926 | 7,008 | 249 | — | 4,515 | 2,148 | — | 639 | 774 | 16,259 |
| Dec | 2,136 | 8,825 | 1,553 | 144 | 6,308 | 4,987 | 155 | 1,474 | 1,279 | 26,861 |
| Annual total | 7,085 | 67,787 | 3,528 | 249 | 32,402 | 17,003 | 214 | 4,887 | 6,659 | 139,814 |
| Average monthly load | 590 | 5,649 | 294 | 21 | 2,700 | 1,417 | 18 | 407 | 555 | 11,651 |
| Power average, kW | 0.81 | 7.74 | 0.40 | 0.03 | 3.70 | 1.94 | 0.02 | 0.56 | 0.76 | 16.0 |

^aValues scaled from G-21 load.

^bAssumed to be 5% of the total of the buildings listed.



ORIGINAL PAGE IS
OF POOR QUALITY

Table 2. Monthly cooling load at Echo for projected conditions (kWh,)

| Month | Building | | | | | | | | | Total |
|-----------------------|----------|--------|---------|---------|--------|---------|---------|-------------------|---------------------|-----------|
| | G-21 | G-23 | G-24 | G-26 | G-28 | G-33 | G-34/35 | G-38 ^a | Others ^b | |
| Jan | — | 788 | 18,607 | — | — | — | — | — | 970 | 20,365 |
| Feb | — | 1,487 | 16,806 | — | — | — | 376 | — | 933 | 19,602 |
| Mar | — | 1,807 | 18,607 | — | — | 105 | 580 | — | 1,055 | 22,154 |
| Apr | — | 2,283 | 18,385 | 3,920 | — | 2,876 | 6,730 | — | 1,710 | 35,903 |
| May | 1,150 | 883 | 22,513 | 24,158 | 1,702 | 12,710 | 10,499 | 9,570 | 4,159 | 87,344 |
| Jun | 3,519 | 2,753 | 28,128 | 41,594 | 3,470 | 26,591 | 23,616 | 29,292 | 7,938 | 166,701 |
| Jul | 4,592 | 3,892 | 33,134 | 55,095 | 3,882 | 37,832 | 34,404 | 38,219 | 10,553 | 221,603 |
| Aug | 4,500 | 3,643 | 32,948 | 54,919 | 3,481 | 37,304 | 34,024 | 37,450 | 10,414 | 218,692 |
| Sept | 3,210 | 2,032 | 25,913 | 38,570 | 2,546 | 27,776 | 19,570 | 26,718 | 7,317 | 153,652 |
| Oct | 1,709 | 2,799 | 21,050 | 12,007 | — | 6,969 | 13,839 | 14,222 | 3,630 | 76,225 |
| Nov | — | 1,473 | 18,005 | — | — | — | 615 | — | 1,005 | 21,098 |
| Dec | — | 629 | 18,607 | — | — | — | — | — | 962 | 20,198 |
| Annual total | 18,680 | 24,468 | 272,703 | 230,263 | 15,081 | 152,163 | 144,253 | 155,471 | 50,646 | 1,063,728 |
| Average monthly total | 1,557 | 2,039 | 22,725 | 19,189 | 1,257 | 12,680 | 12,021 | 12,956 | 4,221 | 88,644 |
| Power average, kW | 2.13 | 2.79 | 31.13 | 26.29 | 1.72 | 17.37 | 16.47 | 17.75 | 5.78 | 121.43 |

^aValues scaled from G-21 load.

^bAssumed to be 5% of the total of the buildings listed.

ORIGINAL PAGE IS
OF POOR QUALITY

Table 3. Electrical energy consumed by heating and cooling equipment for projected conditions (kWh_e)

| Month | Building | | | | | | | | | Total |
|-----------------------------|----------|--------|--------|--------|------|--------|---------|-------------------|---------------------|---------|
| | G-21 | G-23 | G-24 | G-26 | G-28 | G-33 | G-34/35 | G-38 ^a | Others ^b | |
| Jan | — | 904 | 4,449 | — | — | — | 66 | — | 271 | 5,690 |
| Feb | — | 1,135 | 3,659 | — | — | — | 225 | — | 251 | 5,270 |
| Mar | — | 1,270 | 4,052 | — | — | 247 | 372 | — | 297 | 6,238 |
| Apr | — | 1,433 | 4,134 | 1,638 | — | 910 | 1,858 | — | 499 | 10,472 |
| May | 2,839 | 1,492 | 6,324 | 8,579 | — | 4,827 | 3,038 | 4,700 | 1,590 | 33,389 |
| Jun | 4,456 | 2,108 | 9,336 | 15,120 | — | 10,130 | 6,570 | 10,000 | 2,886 | 60,606 |
| Jul | 4,981 | 2,510 | 11,880 | 20,360 | — | 15,210 | 10,020 | 15,300 | 4,013 | 84,274 |
| Aug | 4,844 | 2,421 | 11,560 | 20,030 | — | 14,290 | 9,639 | 14,300 | 3,854 | 80,938 |
| Sept | 4,183 | 1,888 | 8,056 | 13,580 | — | 8,534 | 5,183 | 8,200 | 2,481 | 52,105 |
| Oct | 1,224 | 1,656 | 5,340 | 4,394 | — | 2,721 | 3,298 | 3,300 | 1,097 | 23,030 |
| Nov | — | 1,166 | 3,540 | — | — | — | 209 | — | 246 | 5,161 |
| Dec | — | 842 | 2,881 | — | — | — | 174 | — | 195 | 4,092 |
| Annual total | 22,527 | 18,825 | 75,211 | 83,701 | | 56,869 | 40,652 | 55,800 | 17,680 | 371,265 |
| Average monthly consumption | 1,877 | 1,569 | 6,268 | 6,875 | | 4,739 | 3,388 | 4,650 | 1,473 | 30,939 |
| Power average kW | 2.57 | 2.15 | 8.59 | 9.55 | | 6.49 | 4.64 | 6.37 | 2.02 | 42.38 |

^aScaled from G-21 values

^bAssumed to be 5% of the total of the buildings listed

ORIGINAL PAGE IS
OF POOR QUALITY

Table 4. Overall electrical consumption at Echo for projected conditions (MWh_e)

| Month | Building | | | | | | | | | Total |
|-----------------------------|----------|------|-------|-------|------|-------|---------|-------------------|---------------------|---------|
| | G-21 | G-23 | G-24 | G-26 | G-28 | G-33 | G-34/35 | G-38 ^a | Others ^b | |
| Jan | 4.4 | 1.9 | 50.9 | 57.8 | 6.1 | 37.5 | 32.9 | 36.4 | 11.4 | 239.3 |
| Feb | 4.1 | 2.1 | 45.4 | 52.4 | 5.7 | 33.5 | 30.1 | 34.1 | 10.4 | 217.8 |
| Mar | 4.4 | 2.3 | 50.2 | 57.8 | 6.1 | 37.9 | 33.6 | 36.3 | 11.4 | 240.0 |
| Apr | 4.3 | 2.4 | 48.4 | 60.3 | 6.0 | 37.4 | 34.4 | 35.9 | 11.5 | 240.6 |
| May | 7.8 | 2.5 | 52.4 | 72.4 | 6.6 | 43.9 | 37.0 | 65.1 | 14.4 | 302.1 |
| Jun | 9.6 | 3.1 | 54.1 | 79.9 | 6.6 | 48.8 | 40.1 | 79.5 | 16.1 | 337.8 |
| Jul | 10.1 | 3.5 | 58.3 | 87.1 | 6.7 | 56.0 | 44.7 | 84.2 | 17.5 | 368.1 |
| Aug | 10.0 | 3.4 | 57.9 | 86.8 | 6.7 | 55.8 | 44.3 | 83.1 | 17.4 | 365.4 |
| Sept | 9.3 | 2.9 | 52.7 | 78.4 | 6.6 | 46.5 | 38.8 | 77.2 | 15.6 | 328.0 |
| Oct | 5.8 | 2.7 | 51.3 | 66.0 | 6.1 | 41.1 | 37.7 | 48.4 | 13.0 | 272.1 |
| Nov | 4.3 | 2.2 | 48.5 | 56.1 | 6.0 | 36.1 | 32.2 | 36.0 | 11.1 | 232.5 |
| Dec | 4.4 | 1.8 | 51.2 | 57.8 | 6.1 | 35.7 | 33.0 | 36.5 | 11.3 | 237.8 |
| Annual total | 78.5 | 30.8 | 621.3 | 812.8 | 75.3 | 510.2 | 438.8 | 652.7 | 161.1 | 3,381.5 |
| Average monthly consumption | 6.5 | 2.6 | 51.8 | 67.7 | 6.3 | 42.5 | 36.6 | 54.4 | 13.4 | 281.8 |
| Power average, kW | 8.9 | 3.6 | 71.0 | 92.7 | 8.6 | 58.2 | 50.1 | 74.5 | 18.4 | 386.0 |

^aValues scaled from G-21

^bAssumed to be 5% of the total of the buildings listed.

**ORIGINAL PAGE IS
OF POOR QUALITY**

Table 5. Echo hourly heating load for a typical day in January for projected conditions (kW_t)

| Hour | Building | | | | | | | | | Total |
|---------------------|----------|-------|------|------|-------|-------|---------|-------------------|---------------------|-------|
| | G-21 | G-23 | G-24 | G-26 | G-28 | G-33 | G-34/35 | G-38 ^a | Others ^b | |
| 1 | — | 18.2 | 3.6 | — | 14.0 | 7.7 | — | — | 2.2 | 45.7 |
| 2 | — | 18.0 | 4.2 | — | 15.3 | 8.0 | — | — | 2.3 | 47.8 |
| 4 | — | 18.1 | 4.8 | — | 16.5 | 8.4 | — | — | 2.4 | 50.2 |
| 6 | — | 18.1 | 4.2 | — | 15.4 | 7.8 | — | — | 2.3 | 47.8 |
| 8 | 22.7 | 17.9 | 3.1 | 1.6 | 12.7 | 9.2 | — | 15.7 | 4.1 | 87.0 |
| 10 | 20.2 | 16.4 | — | — | 6.7 | 4.6 | — | 1.8 | 2.5 | 52.2 |
| 12 | — | 15.6 | — | — | 2.6 | 0.6 | — | — | 0.9 | 19.7 |
| 14 | — | 15.6 | — | — | — | — | — | — | 0.8 | 16.4 |
| 16 | — | 16.1 | — | — | — | — | — | — | 0.8 | 16.9 |
| 18 | 15.8 | 17.4 | — | — | 2.9 | 2.9 | — | 10.9 | 2.5 | 52.4 |
| 20 | — | 18.5 | — | — | 5.0 | 5.0 | — | — | 1.4 | 29.9 |
| 22 | — | 18.5 | 1.1 | — | 6.2 | 6.2 | — | — | 1.6 | 33.6 |
| 24 | — | 18.3 | 2.9 | — | 7.2 | 7.2 | — | — | 1.8 | 37.4 |
| Daily total | 117.4 | 416.9 | 41.3 | 3.2 | 187.8 | 120.3 | — | 56.8 | 47.2 | 990.9 |
| Average hourly load | 4.9 | 17.4 | 1.7 | 0.1 | 7.8 | 5.0 | — | 2.4 | 2.0 | 41.3 |

^aScaled from G-21 values.

^bAssumed to be 5% of the total of the buildings listed.

Table 6. Echo hourly cooling load for a typical day in January for projected conditions (kW_t)

| Hour | Building | | | | | | | | | Total |
|---------------------|----------|------|-------|------|------|------|---------|-------------------|---------------------|-------|
| | G-21 | G-23 | G-24 | G-26 | G-28 | G-33 | G-34/35 | G-38 ^a | Others ^b | |
| 1 | — | 1.1 | 25.0 | — | — | — | — | — | 1.3 | 27.4 |
| 2 | — | 1.1 | 25.0 | — | — | — | — | — | 1.3 | 27.4 |
| 4 | — | 1.1 | 25.0 | — | — | — | — | — | 1.3 | 27.4 |
| 6 | — | 1.1 | 25.0 | — | — | — | — | — | 1.3 | 27.4 |
| 8 | — | 1.1 | 25.0 | — | — | — | — | — | 1.3 | 27.4 |
| 10 | — | 1.8 | 25.0 | — | — | — | — | — | 1.3 | 28.1 |
| 12 | — | 2.1 | 25.0 | — | — | — | — | — | 1.4 | 28.5 |
| 14 | — | 2.1 | 25.0 | — | — | — | — | — | 1.4 | 28.5 |
| 16 | — | 1.8 | 25.0 | — | — | — | — | — | 1.3 | 28.1 |
| 18 | — | 1.1 | 25.0 | — | — | — | — | — | 1.3 | 27.4 |
| 20 | — | 0.7 | 25.0 | — | — | — | — | — | 1.3 | 27.0 |
| 22 | — | 0.7 | 25.0 | — | — | — | — | — | 1.3 | 27.0 |
| 24 | — | 1.1 | 25.0 | — | — | — | — | — | 1.3 | 27.4 |
| Daily total | — | 31.6 | 600.0 | — | — | — | — | — | 31.6 | 663.2 |
| Average hourly load | — | 1.3 | 25.0 | — | — | — | — | — | 1.3 | 27.6 |

^aScaled from G-21 values.

^bAssumed to be 5% of the total of the buildings listed.

**ORIGINAL PAGE IS
OF POOR QUALITY**

Table 7. Echo hourly electrical consumption for a typical day in January for projected conditions (kW_e)

| Hour | Building | | | | | | | | | Total |
|---------------------|----------|------|---------|---------|-------|---------|---------|-------------------|---------------------|---------|
| | G-21 | G-23 | G-24 | G-26 | G-28 | G-33 | G-34/35 | G-38 ^a | Others ^b | |
| 1 | 1.7 | 3.6 | 71.8 | 73.6 | 5.0 | 40.5 | 42.9 | 14.1 | 12.7 | 265.9 |
| 2 | 1.7 | 3.6 | 72.4 | 73.6 | 5.0 | 40.5 | 43.4 | 14.1 | 12.7 | 267.0 |
| 4 | 1.7 | 3.5 | 72.9 | 73.6 | 5.0 | 40.5 | 43.4 | 14.1 | 12.7 | 267.4 |
| 6 | 1.7 | 3.5 | 72.3 | 74.7 | 5.0 | 40.5 | 43.4 | 14.1 | 12.8 | 268.0 |
| 8 | 9.3 | 3.4 | 69.9 | 89.2 | 5.0 | 73.4 | 50.7 | 77.4 | 18.9 | 397.2 |
| 10 | 16.5 | 3.8 | 56.1 | 89.0 | 24.1 | 76.2 | 50.7 | 137.3 | 23.1 | 485.8 |
| 12 | 16.3 | 4.1 | 65.8 | 89.0 | 24.1 | 78.2 | 50.7 | 135.6 | 23.2 | 487.0 |
| 14 | 16.3 | 4.2 | 66.1 | 89.0 | 24.1 | 75.8 | 40.7 | 135.6 | 22.6 | 474.4 |
| 16 | 16.3 | 4.1 | 66.0 | 89.0 | 5.0 | 73.1 | 40.7 | 135.6 | 21.5 | 451.3 |
| 18 | 9.3 | 3.8 | 65.5 | 72.6 | 5.0 | 40.5 | 44.4 | 77.4 | 15.9 | 334.4 |
| 20 | 1.7 | 3.6 | 65.8 | 73.6 | 5.0 | 40.5 | 42.9 | 14.1 | 12.4 | 259.6 |
| 22 | 1.7 | 3.6 | 69.0 | 73.6 | 5.0 | 40.5 | 42.9 | 14.1 | 12.5 | 262.9 |
| 24 | 1.7 | 3.6 | 71.0 | 73.6 | 5.0 | 40.5 | 42.9 | 14.1 | 12.6 | 265.0 |
| Daily total | 188.4 | 89.6 | 1,626.4 | 1,921.0 | 234.6 | 1,320.4 | 1,073.6 | 1,567.0 | 401.9 | 8,422.9 |
| Average hourly load | 7.9 | 3.7 | 67.8 | 80.0 | 9.8 | 55.0 | 44.7 | 65.3 | 16.7 | 351.0 |

^aScaled from G-21 values.

^bAssumed to be 5% of the total of the buildings listed.

Table 8. Echo hourly cooling load for a typical day in August for projected conditions (kW_t)

| Hour | Building | | | | | | | | | Total |
|---------------------|----------|-------|---------|---------|-------|---------|---------|-------------------|---------------------|---------|
| | G-21 | G-23 | G-24 | G-26 | G-28 | G-33 | G-34/35 | G-38 ^a | Others ^b | |
| 1 | — | 6.0 | 42.9 | 43.2 | — | 31.3 | 45 | — | 8.4 | 176.8 |
| 2 | — | 5.6 | 36.9 | 35.9 | — | 29.5 | 39.7 | — | 7.4 | 155.0 |
| 4 | — | 4.9 | 30.9 | 16.9 | — | 26.4 | 33.8 | — | 5.6 | 118.5 |
| 6 | — | 4.6 | 27.4 | 5.6 | — | 24.6 | 28.5 | — | 4.5 | 95.2 |
| 8 | — | 4.9 | 26.0 | 41.5 | — | 42.9 | 32.3 | — | 7.4 | 155.0 |
| 10 | 15.5 | 6.3 | 45.7 | 82.3 | 2.8 | 71.7 | 51.7 | 128.7 | 20.2 | 424.9 |
| 12 | 24.3 | 7.7 | 51.0 | 87.2 | 3.9 | 87.9 | 55.9 | 201.8 | 26.0 | 545.7 |
| 14 | 27.8 | 8.4 | 54.1 | 90.7 | 12.0 | 95.3 | 55.6 | 231.0 | 28.7 | 603.6 |
| 16 | 27.4 | 9.8 | 55.6 | 92.5 | 12.3 | 98.4 | 57.3 | 228.2 | 29.1 | 610.6 |
| 18 | 17.2 | 9.1 | 55.6 | 71.4 | 13.0 | 54.1 | 53.4 | 143.5 | 20.9 | 438.2 |
| 20 | — | 8.1 | 53.1 | 70.3 | 10.5 | 49.6 | 51.7 | — | 12.2 | 255.5 |
| 22 | — | 7.0 | 49.6 | 67.5 | 5.3 | 40.4 | 48.5 | — | 10.9 | 229.2 |
| 24 | — | 6.3 | 45.4 | 65.4 | — | 33.1 | 46.1 | — | 9.8 | 206.1 |
| Daily total | 224.4 | 165.1 | 1,060.1 | 1,432.2 | 119.6 | 1,306.0 | 1,107.9 | 1,866.4 | 364.0 | 7,645.7 |
| Average hourly load | 9.4 | 6.9 | 44.2 | 59.7 | 5.0 | 54.4 | 46.2 | 77.8 | 15.2 | 318.6 |

^aScaled from G-21 values.

^bAssumed to be 5% of the total of the buildings listed.

ORIGINAL PAGE IS
OF POOR QUALITY

Table 9. Echo hourly electrical consumption for a typical day in August for modified conditions (kW)

| Hour | Building | | | | | | | | | Total |
|---------------------|----------|-------|---------|---------|-------|---------|---------|-------------------|---------------------|----------|
| | G-21 | G-23 | G-24 | G-26 | G-28 | G-33 | G-34/35 | G-38 ^a | Others ^b | |
| 1 | 1.7 | 6.3 | 77.0 | 97.2 | 5.0 | 57.9 | 54.9 | 14.1 | 15.7 | 329.8 |
| 2 | 1.7 | 6.1 | 75.3 | 96.1 | 5.0 | 57.2 | 57.5 | 14.1 | 15.7 | 328.7 |
| 4 | 1.7 | 5.9 | 73.6 | 93.5 | 5.0 | 56.4 | 55.2 | 14.1 | 15.3 | 320.7 |
| 6 | 1.7 | 5.7 | 69.7 | 92.7 | 5.0 | 55.8 | 53.1 | 14.1 | 14.9 | 312.7 |
| 8 | 9.1 | 5.6 | 68.4 | 112.9 | 5.0 | 91.2 | 61.6 | 75.7 | 21.5 | 451.0 |
| 10 | 39.7 | 6.4 | 76.8 | 125.3 | 25.6 | 107.6 | 66.5 | 330.0 | 38.9 | 816.8 |
| 12 | 43.5 | 7.1 | 79.6 | 128.9 | 25.6 | 115.7 | 70.5 | 361.9 | 41.6 | 874.4 |
| 14 | 45.3 | 7.5 | 83.5 | 131.3 | 25.6 | 116.9 | 61.1 | 376.9 | 42.4 | 890.5 |
| 16 | 45.8 | 7.9 | 84.3 | 132.4 | 6.5 | 115.7 | 62.6 | 381.1 | 41.8 | 878.1 |
| 18 | 36.4 | 7.7 | 84.3 | 111.6 | 6.5 | 65.3 | 58.3 | 302.8 | 33.6 | 706.5 |
| 20 | 1.7 | 7.4 | 81.5 | 111.1 | 6.5 | 63.5 | 60.5 | 14.1 | 17.3 | 363.6 |
| 22 | 1.7 | 6.8 | 79.5 | 108.2 | 6.5 | 60.4 | 57.6 | 14.1 | 16.7 | 351.5 |
| 24 | 1.7 | 6.4 | 77.7 | 106.1 | 5.0 | 58.4 | 55.5 | 14.1 | 16.2 | 341.1 |
| Daily total | 460.0 | 160.9 | 1,867.7 | 2,691.3 | 255.6 | 1,927.7 | 1,439.4 | 3,826.0 | 631.3 | 13,259.9 |
| Average hourly load | 19.2 | 6.7 | 77.8 | 112.1 | 10.7 | 80.3 | 60.0 | 159.4 | 26.3 | 552.5 |

^aScaled from G-21 values.

^bAssumed to be 5% of the total of the buildings listed.

Table 10. Echo site monthly total energy profiles for modified conditions (MWh_e or MWh_t)

| Month | Heating load | W-H required for heating ^a | Cooling load | W-H required for heating ^b | Total W-H required | Generated electrical energy | Reduced generation ^c | W-H generated ^d | Reduced W-H generated ^d |
|------------------|--------------|---------------------------------------|--------------|---------------------------------------|--------------------|-----------------------------|---------------------------------|----------------------------|------------------------------------|
| Jan | 24.5 | 27.2 | 20.4 | 33.8 | 61.0 | 29.7 | 28.9 | 41.6 | 40.5 |
| Feb | 15.1 | 16.8 | 19.6 | 32.5 | 49.3 | 27.0 | 26.3 | 37.8 | 36.8 |
| Mar | 14.5 | 16.1 | 22.2 | 36.8 | 52.9 | 29.8 | 29.0 | 41.7 | 40.6 |
| Apr | 12.0 | 13.3 | 35.9 | 59.5 | 72.8 | 29.9 | 29.1 | 41.9 | 40.7 |
| May ^e | 5.9 | 6.6 | 87.3 | 144.8 | 151.4 | 81.4 | 63.3 | 114.0 | 88.6 |
| Jun | 4.2 | 4.7 | 166.7 | 276.5 | 281.2 | 91.0 | 70.8 | 127.4 | 99.1 |
| Jul | 3.4 | 3.8 | 221.6 | 367.5 | 371.3 | 99.1 | 77.2 | 138.7 | 108.1 |
| Aug | 3.5 | 3.9 | 218.7 | 362.7 | 366.6 | 98.4 | 76.6 | 137.8 | 107.2 |
| Sept | 4.7 | 5.2 | 153.7 | 254.9 | 260.1 | 88.3 | 68.8 | 123.6 | 96.3 |
| Oct | 8.8 | 9.8 | 76.2 | 126.4 | 136.2 | 73.3 | 57.0 | 102.6 | 79.8 |
| Nov | 16.3 | 18.1 | 21.1 | 35.0 | 53.1 | 28.9 | 28.1 | 40.5 | 39.3 |
| Dec | 26.9 | 29.9 | 20.2 | 33.5 | 63.4 | 29.5 | 28.7 | 41.3 | 40.2 |
| Annual total | | 155 | | 1,764 | 1,919 | | | 989 | 817 |

^aW-H ⇒ waste-heat; 90% efficiency assumed (piping loss).

^bAssumed coefficient of performance = 0.67 and piping losses = 10%.

^cHeating and cooling electrical consumption is subtracted to provide a lower bound on W-H available.

^dBoth jacket and flue gas heat recovery taken into account: W-H generated = 1.4 × electrical energy generated.

^eMay 1 through Oct 31 is "summer"; on-peak is 1:00 p.m. to 7:00 p.m. in "summer" and 5:00 p.m. to 10:00 p.m. in "winter."

ORIGINAL PAGE IS
OF POOR QUALITY

Table 11. Echo site hourly total energy profiles for a typical day in January for modified conditions (kW_e or kW_t)

| Hour | Heating load | W-H required for heating ^a | Cooling load | W-H required for heating ^b | Total W-H required | Generated electrical power | Reduced generation ^c | W-H generated ^d | Reduced W-H generated ^d |
|-------------------------|--------------|---------------------------------------|--------------|---------------------------------------|--------------------|----------------------------|---------------------------------|----------------------------|------------------------------------|
| 1 | 45.7 | 50.8 | 27.4 | 45.4 | 96.2 | — | — | — | — |
| 2 | 47.8 | 53.1 | 27.4 | 45.4 | 98.5 | — | — | — | — |
| 4 | 50.2 | 55.8 | 27.4 | 45.4 | 101.2 | — | — | — | — |
| 6 | 47.8 | 53.1 | 27.4 | 45.4 | 98.5 | — | — | — | — |
| 8 | 87.0 | 96.7 | 27.4 | 45.4 | 142.1 | — | — | — | — |
| 10 | 52.2 | 58.0 | 28.1 | 46.6 | 104.6 | — | — | — | — |
| 12 | 19.7 | 21.8 | 28.5 | 47.3 | 69.2 | — | — | — | — |
| 14 | 16.4 | 18.2 | 28.5 | 47.3 | 65.5 | — | — | — | — |
| 16 | 16.9 | 18.8 | 28.1 | 46.6 | 65.4 | — | — | — | — |
| 18 ^e | 52.4 | 58.2 | 27.4 | 45.4 | 103.6 | 334.4 | 326.4 | 468.2 | 457.0 |
| 19 | 41.2 | 45.8 | 27.2 | 45.1 | 90.9 | 297.0 | 289.0 | 415.8 | 404.6 |
| 20 | 29.9 | 33.2 | 27.0 | 44.8 | 78.0 | 259.6 | 251.6 | 363.4 | 352.2 |
| 21 | 31.8 | 35.3 | 27.0 | 44.8 | 80.1 | 261.3 | 253.3 | 365.8 | 354.6 |
| 22 | 33.6 | 37.3 | 27.0 | 44.8 | 82.1 | 262.9 | 254.3 | 368.1 | 356.0 |
| 24 | 37.4 | 41.6 | 27.4 | 45.4 | 87.0 | — | — | — | — |
| Net energy per day, kWh | | | | | | 1,415 | 1,375 | 1,981 | 1,925 |

^aW-H ⇒ waste-heat; 90% efficiency assumed (piping losses).

^bAssumed coefficient of performance = 0.67 and piping losses = 10%.

^cHeating and cooling electrical consumption is subtracted to provide a lower bound on W-H available.

^dBoth jacket and flue gas heat recovery taken into account: W-H generated = 1.4 × electrical energy generated.

^e“On-peak” period is 5:00 p.m. to 10:00 p.m.

ORIGINAL PAGE IS
OF POOR QUALITY

Table 12. Echo site hourly total energy profiles for a typical day in August for modified conditions (kW_e or kW_t)

| Hour | Heating load | W-H required for heating ^a | Cooling load | W-H required for cooling | Total W-H required | Generated electrical power | Reduced generation ^b | W-H generated ^c | Reduced W-H generated ^c |
|-------------------------|--------------|---------------------------------------|--------------|--------------------------|--------------------|----------------------------|---------------------------------|----------------------------|------------------------------------|
| 1 | - | - | 176.8 | 293.2 | 293.2 | - | - | - | - |
| 2 | - | - | 155.0 | 257.0 | 257.0 | - | - | - | - |
| 4 | - | - | 118.5 | 196.5 | 196.5 | - | - | - | - |
| 6 | - | - | 95.2 | 157.9 | 157.9 | - | - | - | - |
| 8 | - | - | 155.0 | 256.0 | 257.0 | - | - | - | - |
| 10 | - | - | 424.9 | 704.6 | 704.6 | - | - | - | - |
| 12 | - | - | 545.7 | 905.0 | 905.0 | - | - | - | - |
| 14 ^d | - | - | 603.6 | 1,001.0 | 1,001.0 | 890.5 | 693.2 | 1,246.7 | 970.5 |
| 15 | - | - | 607.1 | 1,006.8 | 1,006.8 | 882.5 | 687.0 | 1,235.5 | 961.8 |
| 16 | - | - | 610.6 | 1,012.6 | 1,012.6 | 878.1 | 683.6 | 1,229.3 | 957.0 |
| 17 | - | - | 524.4 | 869.7 | 869.7 | 792.3 | 616.8 | 1,109.2 | 863.5 |
| 18 | - | - | 438.2 | 726.7 | 726.7 | 706.5 | 550.0 | 989.1 | 770.0 |
| 19 | - | - | 346.9 | 575.3 | 575.3 | 535.1 | 416.6 | 749.1 | 583.2 |
| 20 | - | - | 255.5 | 423.7 | 423.7 | - | - | - | - |
| 22 | - | - | 229.2 | 380.1 | 380.1 | - | - | - | - |
| 24 | - | - | 206.1 | 341.8 | 341.8 | - | - | - | - |
| Net energy per day, kWh | | | | | | 4,685 | 3,647 | 6,559 | 5,106 |

^aW-H ⇒ waste-heat; assumed coefficient of performance = 0.67 and piping losses = 10%.

^bHeating and cooling electrical consumption is subtracted to provide a lower bound on W-H available.

^cBoth jacket and flue gas heat recovery taken into account: W-H generated = 1.4 × electrical energy generated.

^d"On-peak" period is 1:00 p.m. to 7:00 p.m.

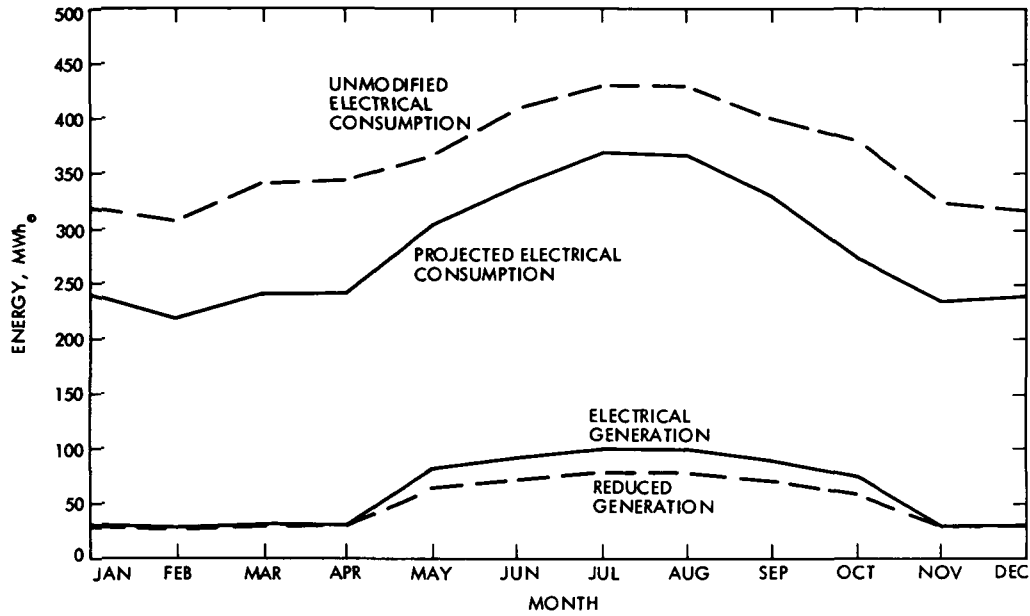


Fig. 1. Overall electrical consumption and generation at Echo site

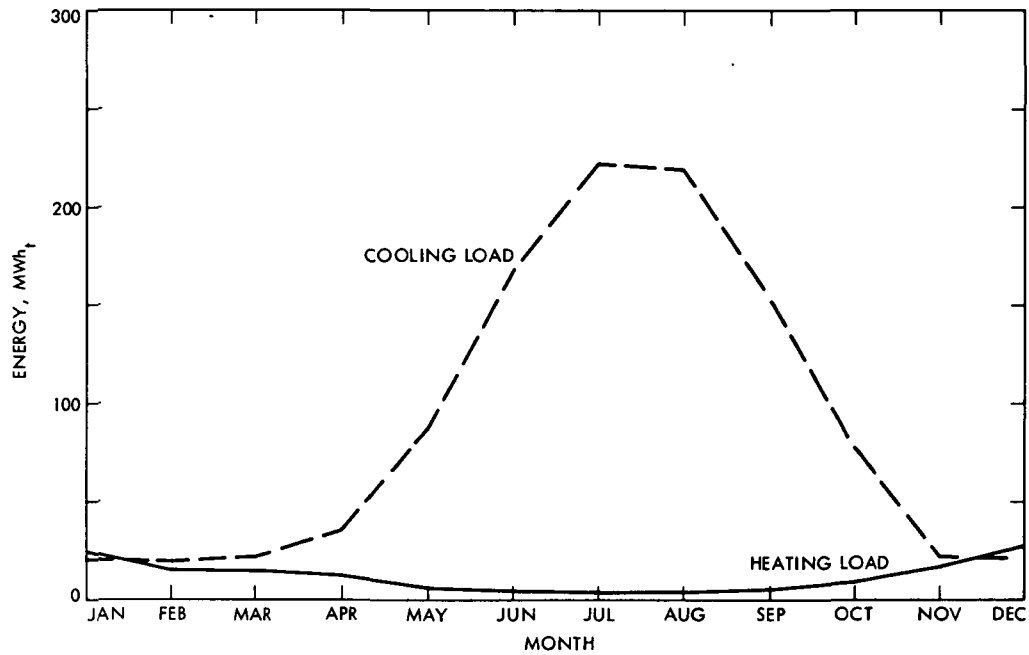


Fig. 2. Echo site heating and cooling loads

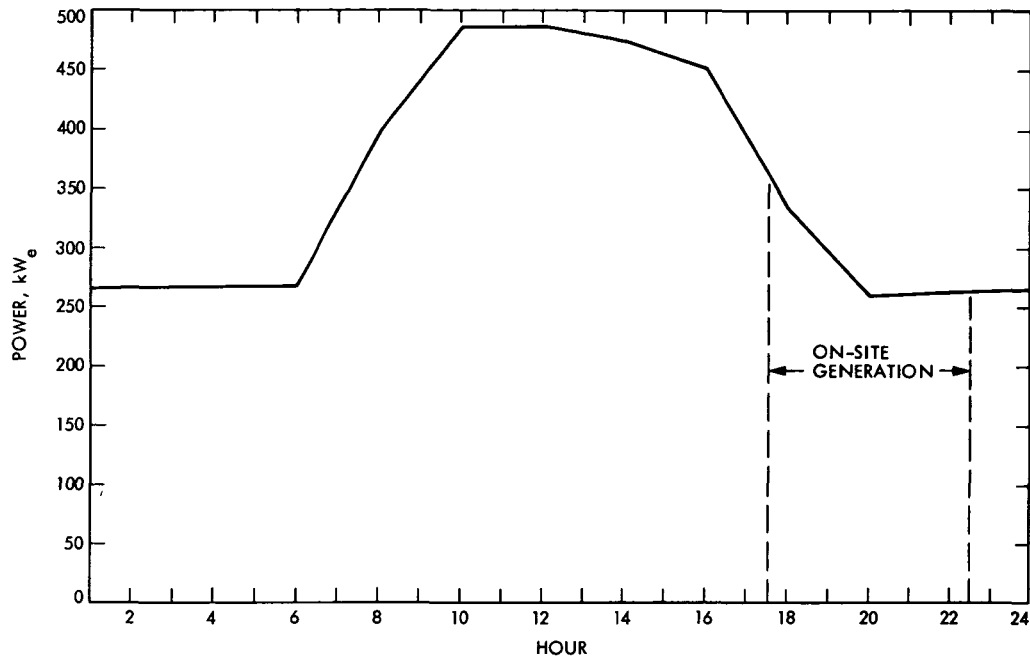


Fig. 3. Hourly electrical power for a typical day in January

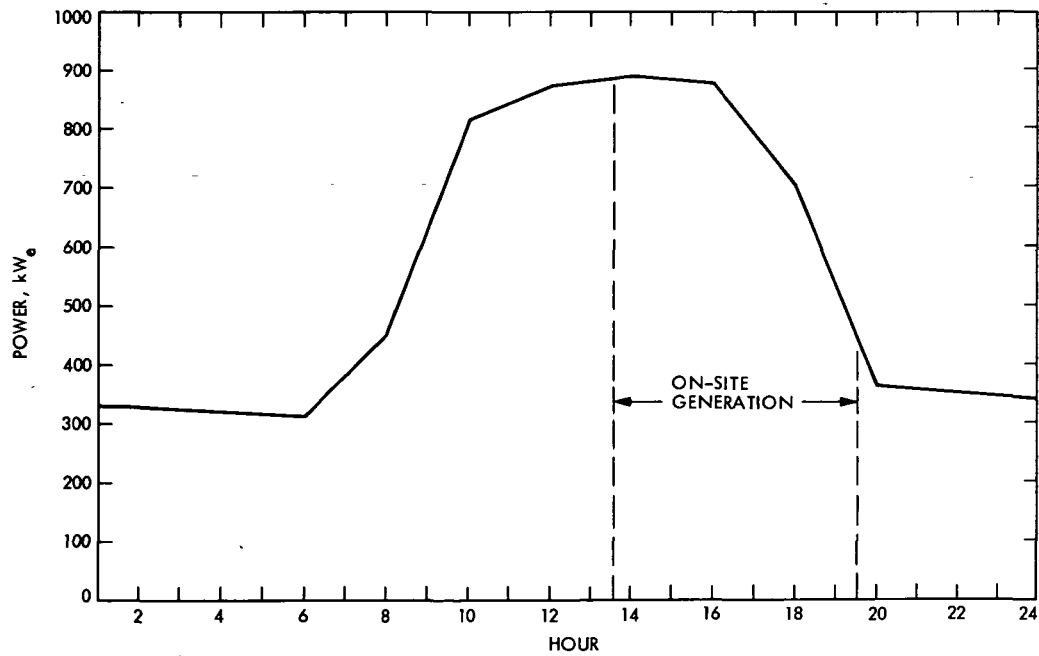
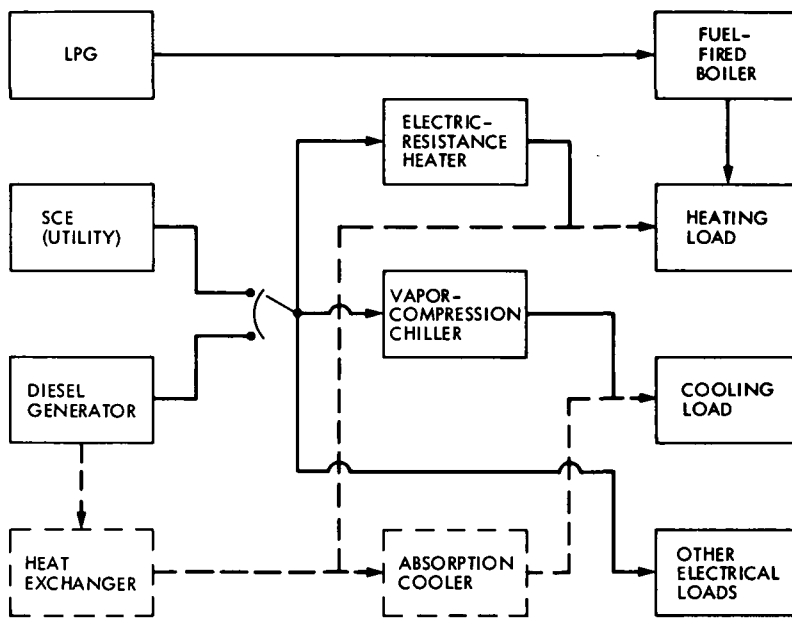


Fig. 4. Hourly electrical power for a typical day in August

ORIGINAL PAGE IS
OF POOR QUALITY



NOTE. DASHED LINES INDICATE COMPONENTS FROM WASTE-HEAT SYSTEM

Fig. 5. Available vs required thermal energy per month

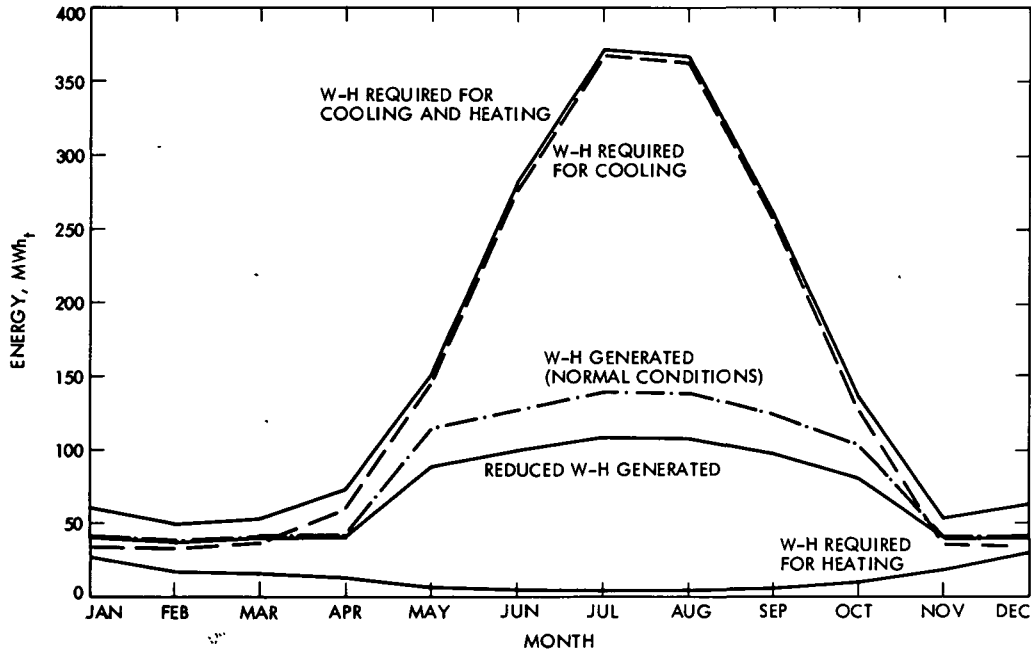


Fig. 6. Available vs required thermal power, January

ORIGINAL PAGE IS
OF POOR QUALITY

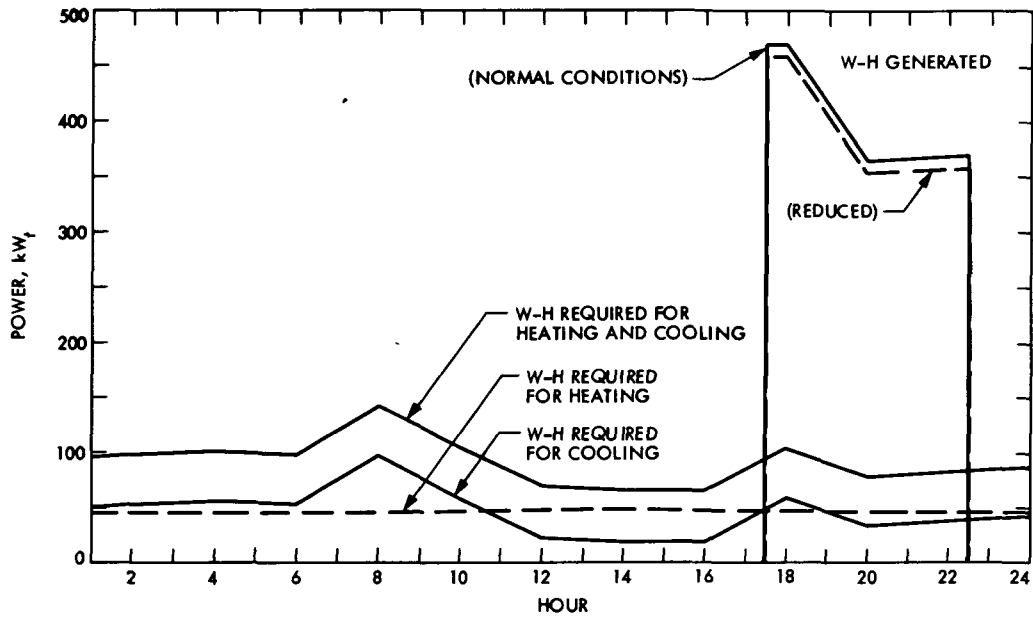


Fig. 7. Available vs required thermal power, August

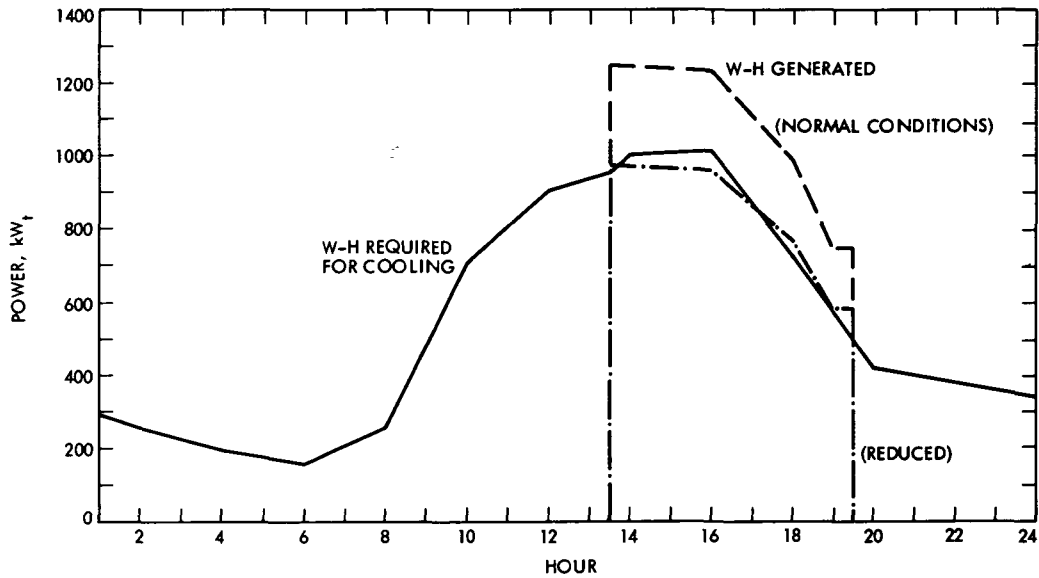


Fig. 8. Block diagram of energy flow in a waste-heat utilization system